博士論文

Researches on epi-fluorescence molecular tomography based on depth perturbation and spatially varying regularization

(深度摂動法及び空間変化正則化法に基づく
反射式蛍光トモグラフィーに関する研究)

Zhou Tuo
周　拓

Wings are a constraint that makes
it possible to fly.
— Robert Bringhurst

To my parents and fiancée…

Abstract

The main goal of fluorescence molecular tomography (FMT) is to recover the depth, size, and three-dimensional (3D) distribution of fluorophores in tissue from fluorescent signals measured on the tissue surface. FMT commonly works with fluorophore-loaded imaging agents that ideally only accumulate in diseased (or targeted) tissue. Preclinically, it has already been used in drug development. Clinically, it shows great potential in disease diagnosis, tumor staging, surgery margin and other applications. Epi-fluorescence molecular tomography works in epi-illumination geometry, which is clinically more practical than other geometries. Currently, the limitations of epi-fluorescence molecular tomography include but are not limited to inaccuracy in resolving depth, the ill-conditioned nature [1] of the optical inverse problem [2], and high computational cost.

To overcome the above limitations,

- a depth perturbation concept to estimate the depth and central location of fluorophore(s) inside tissue is proposed;
- the estimated fluorophore central location is then utilized as a new constraint during the reconstruction of 3D fluorophore distribution to ensure unbiased results;
- a piecewise spatially varying regularization method that achieves better estima-

---

[1] The solution is non-unique and vulnerable to measurement noise

[2] Reconstruction of fluorophore distribution from measured fluorescent signals

tion accuracy of fluorophore size compared with the conventional reconstruction method is proposed;

- In additional, potential issues that occur when the proposed methods are applied to biological tissues are discussed and quantitatively evaluated.

The proposed concepts are verified and evaluated by numerical simulations, phantom experiments, and ex vivo experiments using a custom-built epi-fluorescence tomography system. According to the results of the study, the proposed methods were successful in localizing fluorophore and estimating fluorophore size with relatively short computation time. I expect that the concepts and methods discussed in this thesis will extend the application scope of FMT in the near future.

Key words:

Fluorescent Imaging, Tomography, Epi-illumination, Depth Perturbation, Inverse Problem, Regularization;

Copyright Notice

Note that parts of this thesis have been published in the following manuscripts:

- Tuo Zhou, et, al. Piecewise Weighted Tikhonov Regularization for Reconstructing Fluorophore Distribution in Tissue using Mesoscopic Epifluorescence Tomography. Advanced Biomedical Engineering. Vol(2); 2013: 84-94. [176].
- Tuo Zhou, et, al. Localizing Fluorophore (Centroid) inside a Scattering Medium by Depth Perturbation. Journal of Biomedical Optics. 20(1), 017003 (2015).[178] doi:10.1117/1.JBO.20.1.017003
- Tuo Zhou, et, al. A Depth Perturbation Method for Determining Depth of Fluorophore in Tissue, Conference on Lasers and Electro-Optics (CLEO), San Jose, America, June, 2014. [177]

which are noted with citations in this thesis. Copyright for the parts included in these publications belongs to the Japanese Society for Medical and Biological Engineering, the Society of Photo-Optical Instrumenta¬tion Engineers, and the Optical Society of America, respectively. Systematic electronic or print reproduction and distribution, duplication of relating contents for a fee or for commercial purposes, or modification of the content of the parts require the permission from the respective publisher.

Additionally, a part of figures and tables are reprinted from other publications with permissions from the respective publishers including IEEE, Wiki, Elsevier, Springer, etc. The sources are cited behind the reprinted figures and tables, and listed in the bibliography.

Abbreviation List

Acronym	Definition
2D	two dimension
3D	three dimension
5-ALA	5-aminolevulinic acid
APD	avalanche photodiode
Appx.	Appendix
CCD	charge-coupled device
CPU	central processing unit
CT	computed tomography
CW	continuous wave
DCHM	dice coefficient at half the maximum
DM	dichroic mirror
DOT	diffuse optical tomography
ECW-FMT	epi-fluorescence continuous wave tomography
EMCCD	electron-multiplying charge-coupled device
EPR	enhanced permeability and retention
FD	frequency domain
FEM	finite elementmethod
FI	fluorescence imaging

Fig.	Figure
FMT	fluorescence molecular tomography
FOV	field of view
FWHM	full width half at maximum
GCV	generalized cross-validation
IAD	inverse adding doubling
ICG	indocyanine green
LD	laser diode
LED	light-emitting diode
LM	Levenberg-Marquardt
MEFT	mesoscopic epi-fluorescence tomography
MRI	magnetic resonance imaging
MC	Monte Carlo
N.A.	number aperture
NIR	near infrared red
OCT	optical coherent tomography
OIR	oblique incidence reflectometer
OPL	optical path length
OS	operation system
PA	photo acoustic
PAT	photo acoustic tomography
PBS	polarizing beam splitter
PDMS	polydimethylsiloxane
PET	positron emission tomography
PSVR	piecewise spatially varying regularization
PMT	photomultiplier tube

ROI	region of interest
SDS	source detector separation
Sec.	Section
SNR	signal to noise ratio
SPECT	single photon emission tomography
SWNT	single-walled carbon nanotube
SVR	spatially varying regularization
Tab.	Table
TBR	target to background ratio
TD	time domain
TV	total variation
US	ultrasound

Contents

Abstract i

Abbreviation List v

Contents ix

List of Figures xvii

List of Tables xxi

1 Introduction 1

- 1.1 Molecular Imaging 2
  - 1.1.1 Molecular Imaging in Diagnosis 3
  - 1.1.2 Molecular Imaging in Surgery 4
  - 1.1.3 Preclinical Molecular Imaging 6
- 1.2 Imaging Agent 7
  - 1.2.1 Targeting Component 8
  - 1.2.2 Signaling Component 8
- 1.3 Imaging Modality 9
  - 1.3.1 Positron Emission Tomography 9
  - 1.3.2 Computed Tomography 11
  - 1.3.3 Magnetic Resonance Imaging 12

1.3.4 Ultrasound 13
1.3.5 Fluorescent Imaging 15
1.3.6 Others Molecular Imaging Modalities 17
1.3.7 Sub-conclusion 17
1.4 Fluorescence Molecular Tomography 19
1.4.1 Photon Propagation Model 19
1.4.2 Common System Designs 21
1.5 Other Optical Volumetric Imaging Technologies 26
1.5.1 Photo Acoustic Tomography 26
1.5.2 Optical Coherent Tomography 28
1.6 Epi-fluorescence Continuous Wave Tomography 31
1.6.1 Why Epi-Fluorescence Continuous Wave Tomography? 31
1.6.2 Issues in ECW-FMT Technique 32
1.7 Objective of this Thesis 35
1.7.1 Outline 35

2 Overview of the Proposed Concepts 37

2.1 Essential Techniques Required by ECW-FMT 38
2.1.1 Fluorescent Measurement 38
2.1.2 Optical Properties Measurement 38
2.1.3 Forward Problem 40
2.1.4 Inverse Problem 40
2.1.5 Fluorescent Dyes 41
2.2 Development of ECW-FMT System 43
2.3 Resolving Depth by Depth Perturbation 43
2.3.1 Previous Research 43
2.3.2 Principle of Depth Perturbation 46

2.3.3 Perturbator 54
2.4 Coarse to Fine Strategy 55
2.4.1 Motivation 55
2.4.2 Method 56
2.5 Reconstruction with Prior Knowledge 58
2.5.1 Regularization 58
2.5.2 Incorporating the Centroid Constraint 65
2.5.3 Piecewise Spatially Varying Regularization 67
2.6 Conclusion 71

3 Epi-Fluorescence Continuous Wave Tomography System 73

3.1 Design 74
3.1.1 Source 75
3.1.2 Detector 75
3.1.3 Filtering 76
3.2 Realization 78
3.2.1 Source 81
3.2.2 Detector 82
3.2.3 Filtering 82
3.2.4 Other Components 83
3.3 Results 84
3.3.1 Scattered Fluorescent images 84
3.3.2 Excitation Leakage 84
3.3.3 Random Noise Level 86
3.3.4 Raster Scan Precision 87
3.4 Discussion 88

4 Estimating Fluorophore Centroid 91

4.1 Method 92

4.1.1 Depth Perturbation in 3D Space (Forward Process) 92

4.1.2 Estimating Fluorophore Centroid (Inverse Process) 94

4.1.3 Determining Fluorophore Number 95

4.2 Numerical Simulations 96

4.2.1 Basic Simulation Setting 97

4.2.2 Depth - Concentration Sensitivity 98

4.2.3 Effect of Optical Coefficients of the Perturbator 100

4.2.4 Effect of Perturbator Thickness 100

4.3 Experiments with Tissue-like Liquid Phantom 101

4.3.1 Tissue-like Liquid Phantom 101

4.3.2 Perturbator 102

4.3.3 Parameters Involved in the Inverse Process 103

4.3.4 Validation on Depth Determination 104

4.3.5 Validation on Fluorescent Object Localization 107

4.4 Discussion 113

5 Restoring Fluorophore Distribution 115

5.1 Technical Details in Reconstruction 116

5.1.1 Coarse Step 116

5.1.2 Region of Interest 117

5.1.3 Fine Step 117

5.2 Numerical Simulations 119

5.2.1 Simulation Setting 119

5.2.2 Fluorescent Model used in the Simulation 120

5.2.3 Results in the Single Object Case 123

5.2.4 Results in the Double Objects Case 130
5.3 Experiments with Tissue-like Solid Phantom 135
5.3.1 Solid Phantom 135
5.3.2 Experiments 136
5.3.3 Results 137
5.4 Discussion 139

6 Ex-vivo Evaluation 143

6.1 Purpose 144
6.2 Materials 144
6.3 Experiments 146
6.4 Results 148
6.4.1 Estimated Fluorophore Depth 148
6.4.2 Estimated Fluorophore Volume 149
6.5 Discussion 150

7 Discussion and Conclusion 155

7.1 Optical Heterogeneity 156
7.1.1 Simulation 157
7.1.2 Diffuse Optical Tomography 161
7.1.3 Multi-modality Imaging 163
7.2 Background Fluorescence 163
7.2.1 Introduction 163
7.2.2 Method 164
7.2.3 Experiments and Materials 165
7.2.4 Results 166
7.2.5 Sub-Dissusion 168

7.3 Tissue Shape 169

7.4 Crevices in Perturbator-tissue Interface 171

  7.4.1 Simulation 172

  7.4.2 Results 174

7.5 Measurement Errors in Tissue Optical Properties 175

  7.5.1 Method 176

  7.5.2 Results 176

  7.5.3 Sub-Discussion 177

7.6 Extension of the Depth Perturbation Method 179

7.7 Potential Application Scope 180

7.8 Conclusion 183

A Solid Perturbator 185

A.1 Introduction 186

A.2 Materials and Methods 186

A.3 Result 188

A.4 Discussion 189

B In situ Measurement of Biological Tissue Optical Properties 191

B.1 Introduction 192

B.2 Principle 192

B.3 Method and Material 193

  B.3.1 Oblique-incidence Reflectometry System 194

  B.3.2 Phantoms 195

  B.3.3 Tissue Samples 196

  B.3.4 Experiment Steps 196

  B.3.5 Data Processing 197

B.4 Results 197
B.4.1 Phantoms 199
B.4.2 Tissue Samples 199
B.5 Conclusion 200

Bibliography **217**

C Research Achievement **219**

D Acknowledgment **221**

List of Figures

1.1 Positron Emission Tomography 10

1.2 Computed Tomography 11

1.3 Magnetic Resonance Imaging 12

1.4 Ultrasound 14

1.5 Fluorescent Imaging 16

2.1 Essential Techniques Required by ECW-FMT 42

2.2 Measurement Sensitivity Distribution at Various Source-Detector Separations 44

2.3 Mean Penetration Depth at Various Source-Detector Separations . . . 45

2.4 Principle of The Spectra Change Method 46

2.5 Schematic of Depth Perturbation 47

2.6 Intensity Ratio owing to the Perturbation V.S. Fluorophore Depth . . . 49

2.7 Effects of Scattering on Excitation Light 51

2.8 Effects of Scattering on Emission Light 53

2.9 Solid Perturbator Made of Polydimethylsiloxane 55

2.10 Schematic of the Coarse to Fine Strategy 57

2.11 Comparison of Common Regularization Method 59

2.12 Effect of Regularization Parameter 61

2.13 Schematic of the L Curve Method 63

2.14 Dependency of the Centroid Deviation on the Regularization Parameter 66

2.15 Weighting for Spatially Varying Regularization 69

2.16 Overview of the Proposed Concepts 70

3.1 Schematic of the Epi-Fluorescence Continuous Wave Tomography System 74

3.2 Schematic of Electron Multiplying CCD Camera 76

3.3 Polarizing Beam Splitter 78

3.4 Setup of the Epi-Fluorescence Continuous Wave Tomography System . 79

3.5 Excitation Leakage of Specular Reflected Laser Beam 83

3.6 Scattered Fluorescent images 85

3.7 Excitation Leak 85

3.8 Typical Signal to Noise Ratio of the ECW-FMT System 87

3.9 Incident Points of 2D Raster Scan 88

4.1 Schematic of Depth Perturbation in 3D Space 92

4.2 Representative Distributions of Intensity Ratio Γ 94

4.3 Simulation Setting 97

4.4 Performance of the Proposed Method at Various Depthd and Concentrations 99

4.5 Simulation Results about the Effect of the Perturbator's Optical Properties 100

4.6 Simulation Results about the Effect of the Perturbator's Thickness . . . 101

4.7 Tissue-like Phantom 102

4.8 Typical Fluorescent Images Before and After the Perturbation 105

4.9 Measured Variation Ratio and Resolved Fluorophore Depths 106

4.10 Schematic of the Homogeneous Phantom 107

4.11 Typical Fluorescent Images After Pixel Binning 109

4.12 Relative residual used in the "Try From One" strategy 110

5.1 Method to Generate the ROI in the Fine Step 118
5.2 Environment of the Numerical Simulation 119
5.3 Simulated Single Object Models 121
5.4 Simulated Double Objects Models 122
5.5 Typical Distribution of Regularization Parameters 124
5.6 Representative Coarse Solutions for Model 1 – 7 125
5.7 Dice Coefficients of the Coarse Solutions for Model 1 – 7 126
5.8 Enclose Rates of the ROIs for the Models 1 – 7 127
5.9 ROI Sizes for Model 1 – 7 128
5.10 Representative Fine Solutions for Model 1 – 7 129
5.11 Dice Coefficients of the Fine Solutions for the Models 1 – 7 130
5.12 Size Ratios of the Fine Solutions for the Models 1 – 7 131
5.13 Representative Solution of the Models 8 – 10 132
5.14 Representative Solutions of the Models 10 – 13 133
5.15 Restored Relative Concentration Ratio of the Two Fluorescent Objects . 134
5.16 Solid Optical Phantom 136
5.17 Representative Restored Fluorophore Distribution 138
5.18 Effect of Piecewisely Spatially Varying Regularization 141

6.1 Materials used in the Ex-vivo Experiments 145
6.2 Steps of the Ex-vivo Experiments 147
6.3 Reconstructed Fluorophore 3D Distribution 150
6.4 Representative Fluorescent Data and Intensity Ratio 152

7.1 Setting of the Simulation on Optical Heterogeneity 157
7.2 Representative Results of the Simulation on Optical Heterogeneity . . . 160
7.3 Overall Results of the Simulation on Optical Heterogeneity 162

7.4 Schematic of the phantom 165

7.5 Perturbator Imposed on Tissues with Various Shapes 170

7.6 Adaptations of Fluorescence Measuring System for Irregular Tissue Shapes171

7.7 Crevices in Perturbator-tissue Interface 172

7.8 Simulations Setting for Crevices in Perturbator-tissue Interface 173

7.9 Effects of Inaccurate Measured Tissue Optical Properties 178

7.10 Depth Perturbation under Broad illumination 179

7.11 Intensity Ratio under Broad Illumination 181

A.1 Mold for the Solid Perturbator 187

A.2 Solid Perturbators 188

B.1 Schematic of OIR System 194

B.2 Setup of the OIR System 195

B.3 Ex-vivo Samples 196

B.4 Representative Images Captured by the Oblique-Incidence Reflectometry System 198

List of Tables

1.1 Molecular Imaging Modalities and Respective Agents 9

1.2 Characteristics of Molecular Imaging Modalities (partly referred to Ref.[62]) 18

3.1 Components in the Setup 80

3.2 Components in the Setup (cont.) 81

4.1 Parameters Involved in the Inverse Process 104

4.2 Results of the Single Object Group (all units in mm).[178] 111

4.3 Results of the Double Objects Group.[178] 112

5.1 Model Parameters in the Single Object Case 123

5.2 Properties of the Solid Optical Phantoms and the Perturbator 135

5.3 Results of Solid Phantoms Experiments (mm) 137

6.1 Optical Coefficients of Materials used in the Ex-vivo Experiments . . . 146

6.2 Estimated Central Depths of Ex-vivo Experiments 149

6.3 Estimated Volumes in Ex-vivo Experiments 150

7.1 Properties of the Simulated Medium, Vessel, and Perturbator 158

7.2 Results with Background Fluorescence (0.01 μM background ICG). . . 167

7.3 Localization Errors (mm) Contributed by Crevices 174

7.4 "Actual" and "Measured" Optical Coefficients (mm^{-1}) used in the Simulation 177

A.1 Scattering Coefficient of TiO_2 in PDMS 187
A.2 Properties of Solid Perturbators Shown in Fig. A.2 189

B.1 Phantom Composition 196
B.2 Estimated Optical Coefficient in Phantom Experiments 199
B.3 Estimated Optical Coefficient in Ex-vivo Experiments 199

1 Introduction

This chapter is organized as follows. Initially, a brief review of molecular imaging focusing on potential medical applications and various imaging modalities is provided. Thereafter, the development and principles of fluorescence molecular tomography (FMT) are introduced. The merits and demerits of FMT are compared with other optical volumetric tissue imaging modalities. Finally, the reason for focusing on epi-fluorescence molecular tomography (EFMT) is explained.

1.1 Molecular Imaging

Molecular imaging is defined as noninvasive visualization of biochemical events at cellular or molecular level within living cells, tissues and even human body[62, 159, 160]. It greatly broadens the way clinicians and researchers observe and track complex biomedical processes involved in physiology and diseases. In addition, it shows bright promise for diagnostics, therapy monitoring, and drug discovery and development [62].

Since its infancy, molecular imaging has been strongly tied to nuclear medicine[166]. An ^{18}F labeled imaging agent [^{18}F]-2-fluoro-2-deoxy-glucose ([^{18}F]FDG) was first synthesized In 1978. The agent was synthesized from glucose by replacing the 2-carbon hydroxyl group of glucose with a radioactive fluorine atom (^{18}F)[58]. Nuclear Imaging (i.e. positron emission tomography[40]) with [^{18}F]FDG is thought to reflect the glucose transporter activity of cells [56]. Due to stronger metabolic demands of cancer cells, glucose uptake is usually significantly higher than that of health cells. Consequently [^{18}F]FDG can serve as an effective marker for tumors [62]. However, the use of ionizing radiation and the high cost of nuclear imaging equipment restricts clinical applications of nuclear molecular imaging to a certain degree.

Fortunately, the idea of utilizing a targeting element to trace specific biochemical processes in living subjects has been generalized to many fields. A huge number of imaging agents, based on fluorescent dyes, microbubbles, gadolinium chelates, iron oxide nanoparticles, and X-ray absorbing nanoparticles, have been synthesized (Sec. 1.2). Such imaging agents are used in various imaging modalities, including but not limited to single photon emission tomography (SPECT), magnetic resonance imaging (MRI), ultrasound (US), computed tomography (CT), and optical imaging (Sec 1.3). Applications of molecular imaging have also expanded from diagnosis to surgery,and from cancer [2] to cardiovascular [19, 128], neuroscience[46], and even highly novel field such as gene therapy [65].

1.1.1 Molecular Imaging in Diagnosis

Diseases (e.g., cancer) always involve the alteration of numerous surface cell receptors, sustained angiogenesis, alterations in signaling pathways, vascular recruitment, hypoxia, metastasis, and other phenomena [62, 100]. Moreover, biochemical changes at a cellular level always occur much earlier than morphological changes at a tissue level. By examining these cellular functional properties, molecular imaging can detect carcinogenesis at an early stage [56]. Early detection of cancer is extremely crucial because successful therapeutic outcomes are directly related to the stage at which the disease is detected. According to clinical data, the five-year survival rate for non-small cell lung cancer patients is 60–80% for stage I detection and 40–50% for stage II detection[134], whereas the two-year survival rate for patients whose cancers are detected at stage III is less than 20% [133], while 2-year survival rate for patients of stage III is less than 20%[129]. Currently, numerous cancer-related agents are under development [172]. They show great promise in early identification of cancerous tissue and increasing patient survival rates.

Furthermore, biological information provided by molecular imaging can be a good complement to anatomical imaging techniques such as CT and MRI. Molecular imaging is applied in the cardiovascular field. Cardiovascular researchers use imaging agents to identify and assess the stage of vulnerable plaque [30], which is a common cause of myocardial infarction and sudden cardiac death [99]. Typically, a reduced vessel lumen is considered an indication of plaque deposition. However, for some patients, morphological variations are not noticeable prior to the occurrence of a cardiac event [62]. To solve this problem, Kietselaer, Bas LJH, et.al. synthesized a ^{99}mTc-labeled SPECT agent to image caps, which are considered as mature plaque [67]. Laitinen, et. al, have synthesized ^{18}F-galacto-RGD , a nuclear marker for PET imaging of vascular inflammation—a sign of the middle stage of plaque formation [74]. The combination of biological and morphological information will help cardiovascular patients in the process of risk management and can potentially prevent the occurrence of sudden cardiac events.

1.1.2 Molecular Imaging in Surgery

Intraoperative guidance is another crucial application of molecular imaging. Over the last several decades, minimally invasive surgery has been a popular alternative to conventional surgery. Further, minimally invasive surgery aims to resect diseased tissues completely while avoiding as much as possible damage to normal tissues. The current standard in differentiating diseased tissue from normal tissue relies on tissue color and texture under white light. However, its effect is limited, especially for diseased regions that are located at subsurface or deeper layers. Molecular imaging, especially optical molecular imaging, is a highly attractive potential alterna¬tive. Based on the concentration difference of fluorescent (or bioluminescent) molecules in diseased cells and normal cells, optical molecular imaging can provide an intrinsic contrast. The fluorescent molecule can be endogenous, i.e., bi¬ological structures such as mitochondria and lysosomes [105]; or exogenous, i.e., provided by fluorescent dyes such as Indocyanine green (ICG)[1] and 5-aminolevulinic acid (5-ALA)[126]. Owing to highly advanced contemporary optical techniques, a fluorescent contrast can be provided in real time with high resolution (in the order of 10 μm) and can be integrated with white light images. More specifically, surgery related applications of molecular imaging are as follows.

- **Surgery margin**. “Surgery margin” refers to the determination of the border of region to be removed surgically. Traditionally, the surgery margin is determined by an intraoperative biopsy, which extends operation time and whose result relies on the quality of the sample [56]. In cancer surgery 5-ALA, an imaging agent leading to the accumulation of porphyrins in malignant gliomas[139], has shown potential. Leblond et al. proved that a surgeon can remove a tumor more accurately with the assistance of 5-ALA illumination [80]. A previous research in our lab resulted in the successful development of an integrated diagnosis and therapeutic system for precision malignant resection of gliomas with the guidance of 5-ALA [4, 84, 85]. compared with the white light condition, a tumor is detected more easily in the 5-ALA-induced fluorescent image. Consequently, the surgery margin can be more accurate and efficient. However, note that due to the high scattering property of biological tissue, the fluorescent area is typically larger than the actual size of the tumor. In addition, this effect will be amplified when the tumor is located deep within tissue. This is the primary underlying motivation of FMT, as is discussed in Sec. 1.4.

- **Visualization of important structure**. Besides the removal of the entirety of a diseased region, it is extremely crucial to preserve healthy tissue while performing a surgery. Specifically, it is especially important to avoid hurting important structures, such as vessels, nerves, and functional areas in the brain. Nguyen’s group has been working on enhancing visualization of facial nerve during surgery in mice [168, 162]. Using fluorescent dye Cy5-NP41, a nerve branch as small as $\sim 50\mu$m can be easily observed[56]. ICG, an established clinical fluorescent probe that binds tightly to plasma proteins [150], has been widely used to make tiny vessels more visible, for instance in retinal angiography since the 1970s [37]. Enhanced visualization of important structures by molecular imaging can potentially help surgeons optimize surgical approaches.

- **Theranostics**. Theranostics is a combination of therapeutics and diagnostics [63]. Molecular imaging is becoming increasingly involved in this emerging field. For example, several agents that are dual-labeled with a magnetic substance and a fluorescent dye have been reported [112, 172, 72]. These agents allow both preoperative MRI and intraoperative guidance by optical imaging. Furthermore, postoperative imaging using the same agent can help surgeons evaluate therapeutic effects and determine the necessity of further therapy.

In summary, molecular imaging supports clinical stag¬ing, pre-surgical planning, and intraoperative guidance, and promises improved therapeutic outcomes for patients.

1.1.3 Preclinical Molecular Imaging

Here “preclinical” refers to the development of drugs and the investigation of com¬plex biological processes. Generally, researchers in this field perform numerous experiments on animals and obtain samples such as the cells, tissues, or organs of interest; then, they fix them and then finally perform an in vitro analysis. In contrast, molecular imaging has the following advantages [62] in

- Molecular imaging allows in situ observation of cells, tissue, and organs in their original environment. It can eliminate the need for sample preparation and avoids changes in physiological conditions. Consequently, research veracity is ensured.
- Molecular imaging allows continuous analysis in real time. The entire process rather than a static frame of a biological event can be scrutinized.

- • Molecular imaging allows repeated tests using only a single animal without causing physical harm, thereby reducing economic costs and mitigating ethical considerations.

In summary, the low invasive nature of molecular imaging makes it an excellent tool in pharmacy and biology research. For more details on its application on a preclinical level, see [79].

1.2 Imaging Agent

The main goal of a molecular imaging agent is to bind to (or interacting with) a cellular level target and then to feed back to an imaging device. Ideally, an agent should meet the following requirements[62]:

- High selectivity for the target of interest;
- Rapid binding to (or interacting with) the target;
- Low toxicity (especially for potential agents in clinical use)
- Sufficient signal intensity for the respective imaging equipment
- Synthesis of the agent should be efficient in terms of both time and cost

Although agents can be constructed on the basis of various chemical structures, such as small molecules, peptides, aptamers, antibodies, and nanoparticles, an imaging agent typically comprises a targeting component and a signaling component. The former is designed to be specific to some characteristics of the target of interest while the latter is traceable by the respective imaging modality.

1.2.1 Targeting Component

Diversity exists among the targeting methods of imaging agents. Agents that are not specific for a given cell type or biochemical event but make use of functional characteristics are classified as “nonspecific.” For instance, the aforementioned [^{18}F]FDG agent is transported into cells just like glucose. However, unlike glucose, the [^{18}F]FDG agent agent does not have a 2-carbon hydroxyl group (replaced by ^{18}F), thus the agent is not consumed in further metabolism. Consequently, [^{18}F]FDG accumulates in cells [58]. Some ultrasonic agents make use of augmented permeability of tumor vasculature [91] compared with a normal tissue. They cross the leaky vasculature of a tumor to enter in cancer cells, but do not interact healthy cells [76].

On the other hand, an agent designed for a certain target is called as a "specific" agent. For instance, Babich’s group developed radio-labeled small molecules (^{123}I-MIP-1072 and ^{123}I-MIP-1095) for binding to a prostate-specific membrane antigen which is a molecular marker for prostate cancer[92, 7]. Basically, a specific agent is more effective than a nonspecific agent, because the targeted functional characteristics may not always be reliable and unique. Of course, an intrinsic limitation of specific agents is their restricted application to only the designated target.

1.2.2 Signaling Component

According to the signaling strategy, imaging agents can also be classified as "continuous" and "activatable". Continuous agents, such as all radionuclide agents, are always active and signaling. Consequently, it is difficult to distinguish bound and unbound agents. In contrast, activatable agents only produce signals under given conditions, such as under for specific PH levels[70], or the presence of enzymes [123]. Compared with continuous agents, activatable agents provide lower background levels and thus stronger imaging contrasts.

The design and selection of a signal component must meet the characteristics of its respective imaging modality. Some molecular modalities and their common imaging agents are listed in Tab. 1.1 (for further discussion, see Sec. 1.3).

Table 1.1: Molecular Imaging Modality and Respective Agents [56]

Imaging Modality	Imaging Agents
PET/SPECT	Radionuclide
CT	Iodinated molecule
MRI	Gadolinium chelate
	Super Iron oxide nanoparticles
Ultrasound	Microbubble
Fluorescent Imaging	Fluorescent dyes
	Fluorescence inducing agents

1.3 Imaging Modality

In this section, a brief introduction of the principles, strengths, weak¬nesses, and clinical outlooks of representative molecular imaging modalities is provided.

1.3.1 Positron Emission Tomography

Positron Emission Tomography (PET) uses positrons released from the radioactive decay of a nuclear imaging agent. After encountering an electron in the surrounding tissue, a new positron produces two photons that travel in opposite direction within a body. The two photons are of high energy (511keV) and extremely short wavelength (i.e. in the gamma ray region)[134]. A PET scanner, usually in the form of a ring, is used to collect these photons (Fig.1.1(b)). Imaging agents for PET are all radionuclide related. The most common radionuclide agent is the aforementioned [^{18}F]FDG, which provides information about glucose metabolism and is widely used

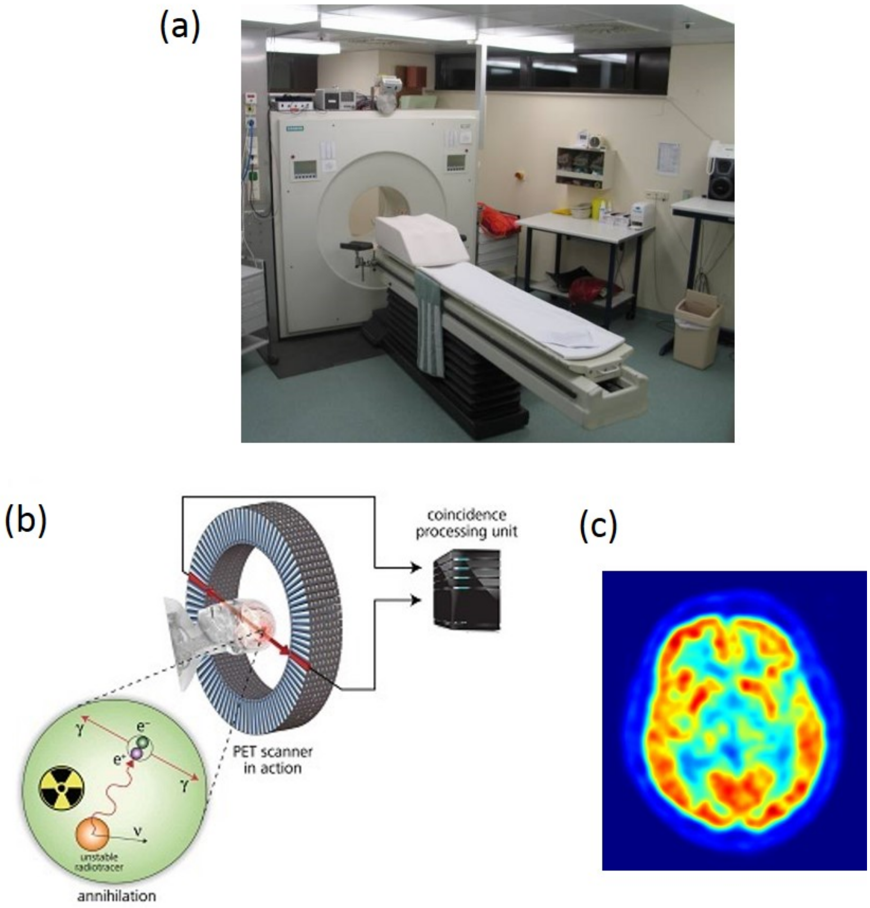

Figure 1.1: Positron Emission Tomography: (A) Outward Appearance of PET; (B) Imaging Principle; (C) PET images on human brain. [164]

in brain function monitoring (Fig. 1.1(c)) and cancer staging [15, 90].

The main strengths of PET include extremely high sensitivity and nearly limitless penetration depth [62], owing to the high energy of the emitted photons. On the other hand, exposure to radiation is its intrinsic limitation. Moreover, the necessity for a cyclotron which is used to synthesize nuclear agents, renders PET systems very expensive. In addition, its spatial resolution is relatively low (5–7 mm for a common clinical setting) [127]. Nevertheless, PET is still seen as the gold standard for clinical molecular imaging because of its molecular imaging history (dating back to the 1970s) and the large number of nuclear agents that have been approved for its

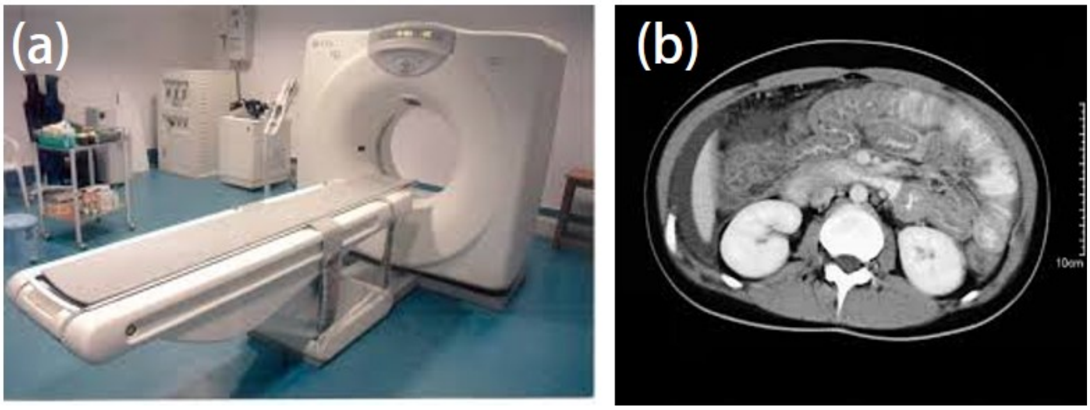

Figure 1.2: Computed Tomography: (a) outward appearance of CT; (b) CT image of eosinophilic gastroenteritis. [148]

clinical use[134].

1.3.2 Computed Tomography

Computed Tomography (CT) provides 3D tomographic images based on the X-ray attenuation differences of tissues [71]. An X-ray fan beam emerges from the source, passes through the subject, and is finally collected by a large number of detectors arranged in a fan shape. The differences in X-ray attenuations reflect the properties of tissue and are employed to reconstruct the anatomical images of the target(Fig. 1.2(c)).

Although CT has been one of the most used clinical imaging tools, its applica¬tion in molecular imaging is still in the early stage because a large dosage of iodinate molecules (common CT contrast agents) must be injected to alter the X-ray attenuation of a target. However, several groups have recently been working on gold nanoparticles, which can increase X-ray attenuation notably[83]. For example, Jon's group has functionalized gold nanoparticles with a prostate-specific membrane antigen RNA aptamer to target prostate cancer cells [68]. The inherent strengths of CT in

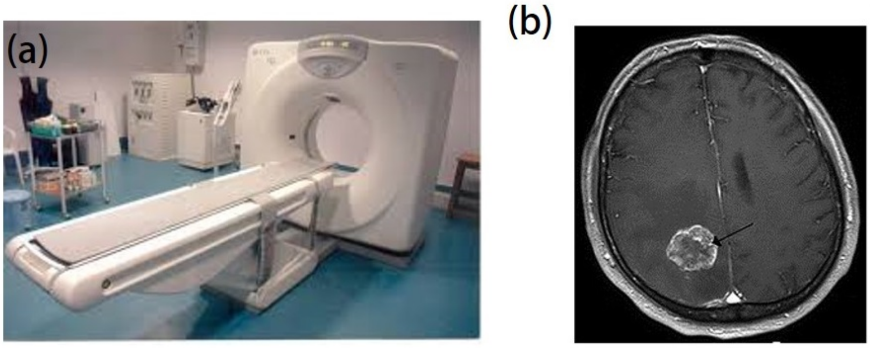

Figure 1.3: Magnetic Resonance Imaging: (a) outer appearance of MRI; (b) MRI image showing brain metastasis in the right cerebral hemisphere[148].

molecular imaging are high acquisition speed, good spatial resolution, and limitless penetration depth, whereas its primary weaknesses are exposure to X-rays and a shortage of imaging agents.

1.3.3 Magnetic Resonance Imaging

The phenomenon by which nuclear particles constantly spin around their axes and generate small magnetic fields on the application of an external field is the basis of MRI. Moreover, atomic nuclei have unique spin characteristics and magnetic properties. When an external magnetic field is applied, the spin axis aligns in a direction either parallel or anti-parallel to the external field. The magnetic resonance signal originates from the net difference between the field generated by the nucleus aligning itself parallel to the external field and the one generated by the nucleus aligning itself antiparallel to the external field. This difference1 is extremely small, typically in the order of one millionth [1]. Consequently, poor sensitivity and a weak signal are the key issues in MRI [62, 101].

In an MRI scanner, a static magnetic field is employed to align the spin axes

---

[1] In a 1.5 T external magnetic field at 37°C

of atoms (usually ^{1}H in water) within the subject. Then, a radiofrequency pulse is applied to temporally vary the orientation of the axes. After the application of the pulse, the orientation reverts via a process that includes two forms of relaxations, i.e., longitudinal (T1) relaxation and transverse (T2) relaxation. The relaxation times (either T1 or T2) are affected by the physiochemical environment (i.e., the surrounding tissue). For example, T1 time of 1H in water is longer than that in fat. Therefore, the relaxation times can in turn provide a contrast among different anatomical structures or pathologies [56, 101].

In molecular imaging, some MRI contrast agents are used as the signal component. Paramagnetic gadolinium chelate [123] is the most widely used for T1 weighted images [2], whereas super paramagnetic iron oxide nanoparticles [59] for T2 weighted images. These contrast agents are then functionalized with some specific targeting elements to detect cancer cells [49], endothelial vascular adhesion molecules [66] etc. The inherent advantages of MRI are high spatial resolution (1 mm in clinical application), limitless penetration depth, and most importantly no radiation. The disadvantages are poor sensitivity and relatively long acquisition time, both of which result from the weakness of the MR signal [62].

1.3.4 Ultrasound

US imaging detects sound waves reflected by different tissue inter¬faces within the body. Within an US equipment, a transducer is used to send sound waves into the body, which are then reflected gradually at tissue interfaces and returned to the transducer. The time of flight as well as the amplitude and frequency of the reflected sound wave are recorded to construct US images. Since the reflectance of sound waves

---

[2] a image showing the differences in the T1 relaxation time

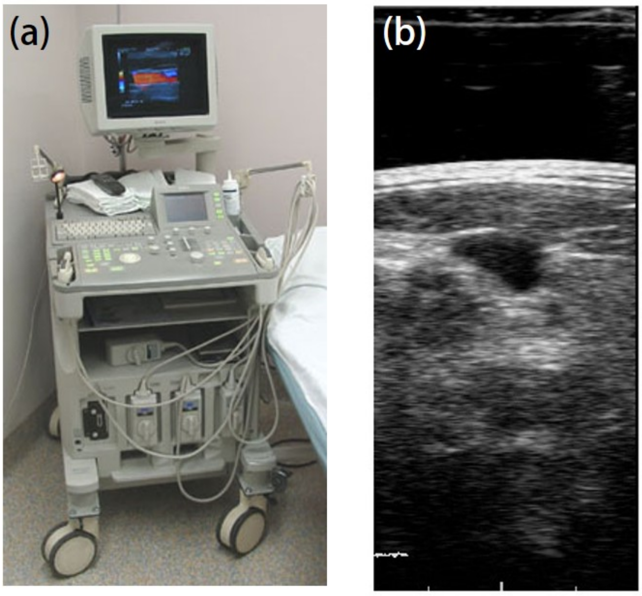

Figure 1.4: Ultrasound: (a) outer appearance of Ultrasound (US) machine [148]; (b) US image of the internal jugular vein measurement of a normal male.

depends on the density and compressibility of tissue [42], US imaging can provide internal morphological information of about subject [122].

A microbubble is the basis of most molecular imaging agents for US imaging. It has a gas core of several micrometers and can enhance the reflectance of sound waves by several orders [29]. The microbubble is typically coated with a targeting component which is selected on the basis of the properties of the target [76]. Owing to its large size, a microbubble cannot easily exit the vessel system. Consequently, its application primarily focuses on imaging angiogenesis, which is believed to be an indicator of carcinogenesis [10]. However, in some types of tumors, the permeability of vessels may be enhanced, thereby allowing the microbubble agents to move into the targets [91].

The advantages of US imaging include high cost-effectiveness, fast data acquisition, and no exposure to radiation. Compared to PET, MRI, and CT, US equipment is small and portable; thus, it is commonly available during surgery. Its primary limitations are relatively short penetration depth[3] as compared with other techniques, and a limited number of imaging agents.

1.3.5 Fluorescent Imaging

Typically, fluorescent imaging involves fluorescent dye, an excitation source, optical detector, and optical filter. There is a long list of fluorescent agents including 5-ALA[139], ICG [174], the Cyanine series [106], quantum dots [153], Alexa dye series [115], fluorescent proteins [22] and endogenous fluorophore such as nicotinamide adenine dinucleotide phosphate (NADPH)[48]. In the process of fluorescence, the agents absorb photons from an excitation source and fluoresce (emit) photons with longer wavelengths. Common excitation source includes lasers, light-emitting diodes, and lamps. An optical detector collects photons traveling back (or through) the subject. Charge-coupled device (CCD) cameras, photomultiplier tubes (PMT), and avalanche photodiodes (APD) are typical optical detectors. An optical filter is always set before the detector for filtering the excitation light.

The emergence of fluorescent imaging has enabled low-invasive, repetitive, and real-time observation of living cells, tissue samples, organs, and even the entire body (of small animals). In clinical applications, it has been used for tumor diagnosis [69], determination of the surgery margin [140], and removal of residual tumors [55]. Preclinically, owing to its low cost, fluorescent imaging serves as a tool to evaluate molecular imaging agents before the agents are moved to other expensive modalities, such as MRI [62]. High scattering and absorption of photons by the biological tissues is

---

[3] There is a trade-off between the spatial resolution and penetration depth of US. Using high frequency sound waves, US can realize high spatial resolution at the cost of penetration depth owing to the strong attenuation of high frequency sound waves within tissue, whereas low frequency waves are modestly attenuated by tissue but lead to decreased resolution.

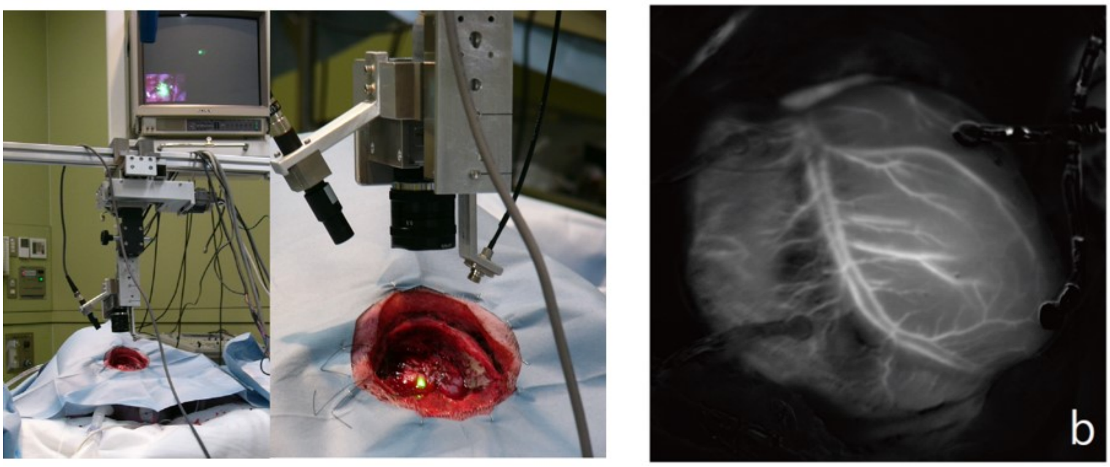

Figure 1.5: Fluorescent Imaging: (a) surgery with a NIR fluorescence imaging system [96]; (b) a cardiovascular fluorescence image captured using ICG[3].

the primary limitation of fluorescent imaging. Scattering leads to a blurred fluorescent image, and the resolution decreases with increasing tissue depth [79]. Cytochromes, hemoglobin, and water within a body contribute to photon absorption. Since the absorption of hemoglobin in the near infrared (NIR) wavelength band [4] is the lowest, the use of an NIR fluo¬rescent dye can yield a greater penetration depth [134]. Even though, the effective penetration region is approximately 1 cm, which limits the clinical applications of fluorescent imaging to environments where depth is not an issue.

Nevertheless, fluorescent imaging still has great clinical potential owing to real-time acquisition, portable nature, and low cost. Its potential applications include skin cancer staging [39], breast imaging [134, 146], endoscopy [158], and cranial surgery [140] etc. Another strength of fluorescent imaging is its multiplexing ability. Specifically, more than one biochemical events can be monitored simultaneously by using multiple fluorescent dyes, which emit light of different wavelengths. This ability is not available in the modalities discussed previously.

---

[4] Wavelength in the range around 800–1000 nm

1.3.6 Others Molecular Imaging Modalities

The aforementioned modalities are representative in their respective physical categories. Some other techniques such as single photon emission tomography (SPECT) [38], optical bioluminescence imaging [88] are also applied in the field of molecular imaging . However, the scope of this thesis does not allow an explicit introduction to all of them. For a description and comparison of these modalities, see Ref. [62].

1.3.7 Sub-conclusion

The characteristics of the aforementioned modalities are summarized in Table 1.2.

The large-scale modalities (PET, CT, and MRI) are good for whole-body imaging owing to their limitless penetration depth, which enables a wide range of applications in diagnosis. However, their large size, radiation (PET and CT), and long acquisition times (CT and MRI) obstruct intraoperative use. On the other hand, the limited penetration depth of US and fluorescent imaging only works well for superficial tissues. Consequently, their preoperative applications are restricted. In contrast, because of their real-time acquisition, good safety, and portability, they can be used during surgery for repetitive and low invasive detection of diseased foci. For fluorescent imaging, the availability of a greater number of targeted fluorescent dyes allows intraoperative use and diagnostic application for exterior tissues, such as skin and breast tissues. Moreover, if the effect of tissue attenuation in fluorescent imaging can be alleviated, fluorescent imaging can achieve better spatial resolution and greater penetration depth as well as restoration of the distribution of fluorescent dyes, which is the motivation for FMT.

Table 1.2: Characteristics of Molecular Imaging Modalities (partly referred to Ref.[62])

Modality	Equipment Scale	Acquisition Time	Spatial Resolution	Penetration Depth	Sensitivity[a] (mol/l)	Cost	Safety Profile	Multiplexing Ability
PET	large	~minutes	5 - 7 mm	limitless	$10^{-11} - 10^{-12}$	\$\$\$	radiation	No
CT	large	minutes	0.5 - 1 mm	limitless	ND[b]	\$\$	radiation	Possible
MRI	large	~hours	1 mm	limitless	$10^{-3} - 10^{-5}$	\$\$\$	good	No
US	medium	~minutes	1 - 2 mm[c]	mm - cm	[d]10^{-12}	\$	good	No
FI	small	~seconds	μm–cm[e]	~ 1 cm	$10^{-9} - 10^{-12}$	\$	good	Yes

---

[a] the concentration of imaging agent that can be detected in tissue

[b] Not determined

[c] for low frequency sound wave; for the high frequency wave, it can be less than 0.1 mm. but the penetration depth is limited to few millimeters

[d] using microbubble

[e] depends on depth and optical properties of tissue

1.4 Fluorescence Molecular Tomography

The main goal of FMT is recovery of the depth, size, and 3D distribution of fluorophores inside tissue from blurred fluorescent signals obtained from the tissue surface. The principle of FMT relies on the incorporation of a photon propagation model and a more delicate system design compared to conventional fluorescent imaging.

1.4.1 Photon Propagation Model

Typically, photon propagation is modeled on the basis of diffusion theory. It is simplified from the radiative transfer equation5 on the basis of the assumption that photon radiance is nearly isotropic [157], based on the assumption that photon radiance is nearly isotropic[157, 60]. The diffusion equation can be expressed as

$$\frac{\partial \Phi(\vec{r}, t)}{c \partial t} + \mu_a \Phi(\vec{r}, t) - \nabla \cdot [D \nabla \Phi(\vec{r}, t)] = S(\vec{r}, t) \tag{1.1}$$

where Φ denotes fluence rate[5], c denotes the speed of light, t denotes time, μ_a denotes the absorption coefficient of the medium, and $S(\vec{r}, t)$ denotes the light source. The constant D is the diffusion coefficient, which is defined as

$$D = \frac{1}{3(\mu_a + \mu_s')} \tag{1.2}$$

where μ_s' is the reduced scattering coefficient of the medium. For a time-independent light source, a simpler version of Eq. 1.1 is expressed as

$$\mu_a \Phi(\vec{r}) - \nabla \cdot [D \nabla \Phi(\vec{r})] = S(\vec{r}) \tag{1.3}$$

---

[5] Energy flow per unit area per unit time

In the field of FMT, researchers typically solve these equations at least two times: once for the fluence rate distribution of excitation light within the medium and once to calculate the fluorescence radiation intensity being emitted from the surface of the medium. Solving the equations may involve the finite element method (FEM), especially when μ_a or D is space variant. For details in solving the diffusion equation, see [132].

An alternative method in modeling photon propagation is Monte Carlo simulation. In the simulation, a huge number of photons [6] are subsequently launched off. Their trajectories within medium are considered as random walks. The scattering angle and step size of each step are sampled randomly from their probabilistic distribution which are affected by optical properties of the medium as well as boundary conditions. In each step, the direction of each step depends on the scattering angle and the direction of the previous step. After tracking and recording the trajectories of sufficient number of photons, physical quantities concerning photon propagation can be estimated [155, 157].

The diffusion equation and the Monte Carlo method have distinct advantages and disadvantages. The selection of either method depends on the application. Generally, the Monte Carlo method provides better accuracy with high computational cost because it must track a large number of photons. In contrast, solving the diffusion equation with the FEM is much more computationally efficient but is less accurate [157], because the diffusion assumption does not hold in the boundary or the region close to light source[7].

---

[6] Usually greater than the order of 10^5

[7] In biological tissue, the region is typically of approximately 1-mm radius

1.4.2 Common System Designs

There have been many recent attempts to develop FMT systems. Their design and considerations vary greatly to meet various preclinical and clinical needs. This subsection describes common types of FMT in terms of geometry, signal domain, incident mode, and detection mode, and discusses their strengths and weaknesses.

Geometry

Typically, an FMT system would possess either an epi-illumination geometry or a trans-illumination geometry. In the epi-illumination geometry, the light source and the detector are placed on the same side, whereas in the trans-illumination geometry, they are placed on opposite sides. For some certain cylindrical subjects (e.g., the entire body of a rat), the detectors and sources can be configured to surround the subject (circular geometry), which is actually a combination of epi- and trans-illumination geometry.

The main strength of a trans-illumination geometry is that the tissue region of interest (ROI) is sampled entirely because light passes through it [108], whereas whereas the information obtained by an epi-illumination geometry is surface weighted [8] [79]. This explains why research with small animals or ex vivo samples has typically used transmission geometry or circular geometry. However, owing to the limited optical penetration depth, trans-illumination is not available for large animals [12]. Similarly, it is impractical to insert a detector (e.g., optical fiber) into the human body; thus, clinical application of trans-illumination is effectively limited to breast imaging [23] wherein optical attenuation is relatively weak [151].

---

[8] The collected fluorescence signals mainly emit from the superficial region

As an alternative, FMT with reflectance geometry where the light source and detector are placed on the same side shows a greater clinical promise. First, it is available for some exterior organs, such as skin and the mouth. Second, during brain and thoracic surgeries, a reflectance geometry system can function without obstruction from the skull and chest; thus, penetration depth can be somewhat extended. Since all detectors and sources are placed on the same side as the observing doctor, only a few additional steps are required to set them up [9]. Finally, FMT with reflectance geometry shares the same illumination methods as endoscopy and microscopy, which makes it possible to integrate such methods. This will greatly extend its potential applications for imaging the colon and esophagus, whose wall thicknesses are normally less than 1 cm. [163, 170]

Signal Domain

In the field of FMT, common signal domains include the continuous wave (CW) domain, the time domain (TD) and the frequency domain (FD) [109].

The CW domain utilizes a light source that outputs constantly and continuously. The devices required for this method are simple and relatively inexpensive compared with other techniques. For instance, a laser diode, a CCD camera and an optical filter can fulfill the minimal requirements of this method. This method also has good potential to provide excellent signal to noise ratio (SNR), because fluorophore is continuously excited and emits fluorescent signal. The primary weakness of the CW method is the inability to image fluorescence lifetime [109, 28], a valuable tool in exploring tissue bio-chemical status [79], which is helpful in differentiating fluorophore type in multiplexed images.

---

[9] Such as attaching optical fibers to the opposite side of an organ

The TD method uses ultrafast photon pulses (10 fs to 100 ps [108]). The time of flight of the fluorescent photons to the tissue boundary reveals information about fluorophore depth and lifetime. By using early arrival photons, i.e., unscattered photons, theTD method can alleviate the effects of tissue scattering in optical imaging and improve resolution. A TD system typically involves a Ti:Sapphire laser and a high speed imager [20, 147], both of which are extremely complex and expensive. Moreover, because of the ultrafast switching and pulsing nature of the light source, the resultant signal is nosier and weaker than that obtained with the CW method [109].

In the FD method , the incident intensity of light source is modulated at a frequency of 100–1000 MHz[108]. Consequently, the excited fluorescent intensity vibrates at the same frequency. In addition, the fluorescence acts as a photon wave passing through the tissue. Since the phase shift of a wave depends on its pass length, the fluorophore location can thus be retrieved from measurements of the phase shift of the wavefront on the tissue boundary. Similar to the TD system, an FD system requires more complex equipment than the CW method, such as a frequency modulating light source [43]. It is also less robust because of the high frequency nature of the FD fluorescent signal [109].

To summarize, each method has its own distinct strengths and weaknesses. The CW method is simple, robust, and inexpensive but unable to offer information other than fluorescence intensity. The TD and FD methods can provide better spatial resolution and information concerning fluorophore lifetime at the cost of significantly increased complexity.

Incident Mode

Common incident modes of excitation light include broad illumination and point illumination . The former uses a broad light beam; thus, it can illuminate a large tissue area (several cm^2). In contrast, the latter focuses excitation light to a local region (~ 1 mm^2); thus, it must sample a given tissue region multiple times. Although time consuming, the point illumination mode is more common in the field of FMT. Compared to the broad illumination mode, its strengths include the following.

1. Point illumination can focus excitation power on a very limited area, resulting in a high energetic fluorescent signal when a fluorophore exists near the incident point.
2. Point illumination can potentially improve spatial resolution because the excitation light intensity over a volume close to the incident point is notably enhanced. Consequently, each incident position provides a locally emphasized image rather than a globally averaged image of broad illumination.

In my opinion, a hybrid illumination that combines point and broad illumination is better for epi-fluorescence tomography. One can first apply broad illumination to obtain the rough horizontal location of fluorophore inside tissue, and then apply fine 2D point illumination around the rough horizontal location. Such a method can reduce time cost, which is the primary weakness of point illumination.

There are two methods to realize point illumination, raster scan of a collimated beam, and an array of optical fiber together with an optical switch. The former typically requires motorized stages or a set of galvo mirrors. Since the speed, step size and range of the scan (either with stages or galvo mirrors) can be arranged by programming, the former is also more flexible than the latter. On the other hand, the main disadvantages of raster scan include mechanical vibration [10] and increased measurement time [11]. In contrast, the key problems of the fiber array mode include inflexibility and difficulty in arranging a very dense array.

Detection Mode

As mentioned before, CCD cameras, photomultiplier tubes (PMT), and avalanche photodiode (APD) are typical optical detectors used in fluorescent imaging. CCD cameras can offer detection over an entire region of interest (ROI), whereas the latter two are typically arranged in a detector array to collect light from some isolated detection positions. Apparently, the detection of the entire region ensures more complete and abundant fluorescent information than isolated point detection. Some research has asserted that CCD detection results in too many sample points, which increases computational cost in the subsequent reconstruction of the fluorophore biodistribution [53]. However, this issue can be solved easily by selecting a ROI on the CCD images and binning several pixels into a single virtual detector.

The main strength of isolated point detection is that the gain of each PMT or APD can be tuned independently according to the expected signal intensity at its respective detection position. For instance, the gain of a detector corresponding to a point far away from the incident point can be set to a larger value than that of a point closer to the incident point to ensure that the dynamic range of a PMT or APD is used effectively [53]. Its weaknesses include shortage of fluorescent data and additional complexity of the optical system.

---

[10] Optics is sensitive to mechanical vibration

[11] Time for the mechanical motion should be taken into consideration, especially for a system using stages

1.5 Other Optical Volumetric Imaging Technologies

On the basis of the contrast provided by the fluorescent imaging agents, FMT realizes 3D imaging within a tissue. Fluorescent imaging agents always bind to chemical substances or biological processes in tissue; thus, FMT results reflect the biochemical information of the investigated tissue. Besides fluorescent contrast, other tissue optical properties, such as optical absorption and internal reflectivity, can be used for bio-optic imaging. In this section, with the exception of FMT, two representative optical volumetric tissue imaging technologies are briefly introduced and compared with FMT.

1.5.1 Photo Acoustic Tomography

The photo-acoustic effect is the basis of Photo Acoustic Tomography (PAT) [171, 136]. Optical absorption by tissue leads to a local temperature rise which induces pressure jump and then ultrasonic waves [156]. The amplitude of these ultrasonic waves is proportional to the energy of the absorbed light. Furthermore, the detected temporal acoustic signal (i.e., the time that the ultrasonic wave passes through tissue) can indicate the depth of signal source because the speed of ultrasonic wave within tissue has been well determined and acoustic scattering in tissue is extremely low [12]. Therefore, PAT images can present a volumetric distribution of optical absorbers in tissues, such as hemoglobin, DNA/RNA, and melanin. A typical PAT system includes a pulse laser (the light source), an acoustic transducer, and optical and acoustic lenses. Further, PAT is most commonly used in localizing shallow and tiny vessels, and it is on this basis that this technique has been applied to various biomedical fields, including vascular oncology, neurology, ophthalmology, and dermatology.

---

[12] Approximately three orders less than optical scattering[156]

The main merit of PAT comes from its "light in sound out" nature. Comparing conventional "light in light out" pure optical imaging, it is less affected by tissue scattering. Consequently, PAT has better performance in terms of penetration depth and spatial resolution than FMT. Varying with the configuration, the penetration depth of PAT ranges from several mm–cm. Note that its spatial resolution can be of 100-μm order, even at a 10-mm depth, which is difficult to obtain in pure optical imaging[13]. In addition, excitation leakage and autofluorescence, which are troublesome in fluorescence imaging, do not contribute to the PA signal; thus, the effort required to eliminate such background noise can be avoided.

However, although having been extensively studied for several decades, there are still a number of challenges to be addressed with PAT. The challenges come from both the PAT technique itself and the photoacoustic imaging agents. For example, the lack of suitable laser systems is considered a critical issue in translating this technique to clinical applications. The Ti:Sapphire laser system has been proved effective in laboratory settings; however, its large size, necessity for external cooling systems, and the need for re-alignment obstruct its practical application, especially in a surgical environment. On the other hand, owing to the use of ultrasound, some intrinsic ultrasonic issues also appear in PAT. For example, it is not feasible for bone or air structures. In addition, coupling is required between the detector and the target tissue. Its failure in non-contact imaging will result in significant inconvenience, especially in clinical environments [82, 156, 124].

The more important challenge is the shortage of PAT imaging agents compared with fluorescent imaging. In some applications, such as detecting early cancer, endogenous optical absorption cannot provide sufficient contrast; thus, it requires ex-

---

[13] As a rule of thumb, the achievable spatial resolution of PAT is on the order of 1/200 of the penetration depth [156]

ogenous contrast-enhancing agents. Until now, most PAT targeting agents have been based on nanoparticles, which exhibit high and tunable absorption spectra [82]. However, compared with agents synthesized from small molecules, fewer nanoparticles can be delivered to the target because they accumulate rapidly in the reticuloendothelial system (liver, spleen, and bone marrow) after administration. Thus, only some of the nanoparticles are available for delivery. In addition, it is also challenging for nanoparticles to extravasate and reach their target owing to their large sizes (100 nm), unless the target is vessel itself or the enhanced permeability and retention (EPR) effect resulting from cancer has already been notable. Furthermore, for PAT nanoparticle agents synthesized from single-walled carbon nanotubes, their biodegradability and toxicity limit their use in humans [62]. Finally, some investigators have attempted to use fluorescent agents as absorbers of excitation light to provide a PA contrast [124]. However, the limited absorption ability of fluorescent agents is a potential issue. In addition, more effort is required to render the agents stable under the high peak power of the incident laser pulse of a PAT system [9].

To summarize, relative to agent availability and system cost, compared with PAT, the CW mode FMT is more appropriate for volumetric tissue imaging up to depths of several millimeters in a clinical environment. For PAT, after the aforementioned issues are addressed, I believe it will have much more promising for imaging applications in future.

1.5.2 Optical Coherent Tomography

Optical coherence tomography (OCT) is an interferometric technique that detects reflected or backscattered light from a scattering media and maps internal reflectiv¬ity within the media as a function of depth [95]. Internal reflections typically occur on the interfaces of different tissue components or substances; thus, OCT can vi¬sualize the morphology of the media of interest. An OCT system is typically built on the basis of the Michelson interferometer. A laser beam is split to a sample arm and a reference arm. Interference of the back-reflections from both arms is measured by a photo detector [31]. According to the amplitude of the interference signal and the phase delay between the reflections of the two arms, one can resolve the local reflectivity and the depth where the reflection event occurred. Furthermore, by scanning along the depth, the reflectivity-depth profile can be acquired. The depth scan can be realized in several ways, including mechanically moving the reference mirror (time-domain OCT) and splitting the interference signals into different optical frequencies (spectral domain OCT), etc. For technical details of OCT, see Review [95, 31] and Book [157].

Currently, OCT has been commercialized and widely applied in biomedical fields. It has been accepted as a clinical standard within ophthalmology [167], and demonstrates great potential in dermatology [161] and cardiology [144]. The attractiveness of OCT comes from its high spatial resolution which is typically on the order of 10 μm [95]. Another reason for the acceptance and adoption of OCT is the fact that it is in vivo real-time imaging. Using state-of-the-art light sources, current OCT can realize five million depth scans per second [31]. High-speed in vivo imaging implies that the motion of a specific substance and the time variation of tissue properties can be traced by OCT. In addition, unlike fluorescence imaging, OCT has intrinsic depth resolving ability, thereby avoiding the annoying optical inverse problem required by FMT.

However, the weaknesses of OCT are also significant. Multiple scattered laser light loses its coherence, i.e., it is thus unable to interfere with the reference beam. In principle, only single back-scattered (reflected) photons contribute to the OCT signals.

However, the high scattering nature of tissues makes the potential OCT signal (i.e. single scattered photons) decreases extremely quickly with the depth. Consequently, the typical penetration depth of OCT in biological tissue is 1–2 mm. The application scope of OCT is thus greatly restricted. In addition, similar to US imaging, speckles are always observed in OCT images. Such speckles potentially affect the tiny features of OCT images, and and ruin the high-resolution strength of the OCT to a certain degree. Finally, the lack of chemical selectivity is another drawback of OCT. This results in difficulty in differentiating between a pathological and normal tissue with similar morphology [31].

Therefore, multi-modality imaging is always a hot issue in the field of OCT. By combining a biochemical contrast imaging modality, the tissue status or the targeted lesion can be understood and diagnosed from both morphologic and biochemical perspectives. Among this, many efforts have been made in combining OCT with fluorescence imaging. Such efforts have proved that fluorescence imaging guided OCT can achieve better accuracy and specification in early determination of cancer [114], atherosclerotic plague [116], etc. Yu et, al. even built a co-registered OCT and FMT system for simultaneous morphological and molecular volumetric imaging [21]. The combination of OCT and FMT is especially interesting because the structure information provided by OCT can be incorporated into the computation of the FMT forward problem, thereby allowing a more realistic sensitivity matrix and thus more accurate estimations for fluorophore bio-distribution inside tissues. Therefore, rather than being a rival imaging technique, OCT can be a good candidate to be used in conjunction with FMT.

1.6 Epi-fluorescence Continuous Wave Tomography

This thesis describes my work on FMT, especially on **epi-fluorescence continuous wave tomography (ECW-FMT)**. I have studied several key issues that this technique faces and have attempted to improve performance by improving SNR, resolving depth, and reconstruction of the fluorophore distribution. I have built an ECW-FMT system and tested the proposed concepts and methods by numerical simulation, phantom experiments, and ex vivo experiments.

1.6.1 Why Epi-Fluorescence Continuous Wave Tomography?

FMT has already become a common and valuable research tool in preclinical situations. How¬ever, its clinical and large animal applications remain restricted. Thus, I have selected the most clinically promising type of FMT as my research focus. As described in Sec. 1.3.5, fluorescent imaging's clinical potential is supported by its strengths, including low cost, fast acquisition time, simplicity, small scale, and good safety. It is my hope that the target FMT type can inherit as many of these traits as possible. Furthermore, the robustness and convenience are considered to fulfill more strict requirements in intraoperative environments.

In terms of geometry, epi-illumination FMT has wider potential applications compared to trans-illumination FMT because of its simplicity, operability, and compatibility with endoscopy. In terms of the signal domain, the prime clinical requirement is to localize the fluorescent imaging agents inside tissue; thus, the CW method is sufficient to realize this and is considered the optimal method owing to its low cost, simplicity, and robustness. In terms of methods to realize point illumination, handling a bundle of optical fibers is inconvenient and lacks robustness. Finally, in terms of detection mode, camera-based detection is preferred because it offers a large amount of data and requires a relatively simple optical system. Moreover, the use of a camera enables rapid switching between fluorescent images and white light images. Consequently, a fluorescent image and a reconstructed fluorophore distribution can be registered directly onto the white light image for surgery navigation.

In a word, in my opinion, ECW is the most promising type of FMT for clinical application.

1.6.2 Issues in ECW-FMT Technique

In this section, key issues concerning ECW-FMT are enumerated, parts of which are actually the objectives of this research.

1. How to obtain depth information ?

Resolving depth is crucial to any tomography technique. Unlike circular geometry where depth information can be extracted from intensity differences among detectors[14], and differing from the time or frequency domain methods where time of flight or phase shift reveals distance from fluorophore to the surface, in epi-illumination and the CW domain, there is no direct way to obtain depth information. Most previous research has used different source-detector distances to determine fluorophore depth under the assumption that a greater distance from detector to source will result in a deeper (average) light collected by the detector. However, it owns poor depth sensitivity [79]. Thus, a more accurate method to determine fluorophore depth is required.

---

[14] For example, it is very likely that a fluorophore is closest to the detector with the strongest signal

2. How to further improve spatial resolution ?

FMT makes use of the light propagation model and measured fluorescent data to recover fluorophore distribution, which is a typical inverse problem. In practice, the propagation model is typically expressed as a large-scale matrix[15] that is usually ill-posed[16], meaning that the FMT solution is non-unique and that any small perturbation (e.g., random noise, and a leak of excitation light) in the fluorescent data may result in a much larger error in the solution. Solving such an ill-posed inverse problem always requires a numerical treatment, for example, the incorporation of an additional assumption or prior knowledge, to select the optimized solution—a process known as regularization. The most commonly used regularization method is Tikhonov regularization [145], which prefers to select the smoothest solution as the final answer. This method indeed stabilizes the solution; however, it significantly worsens the spatial resolution. Consequently, a regularization method that does not affect spatial resolution is desirable.

3. How to reduce computational cost ?

Relative to the last issue, the reconstruction of fluorophore bio-distribution typically involves inversion of a large-scale matrix. Consequently, the inversion is extremely time consuming. Considering that the raster-scan illumination mode has already increased acquisition time to some degree, an overly long reconstruction time is unacceptable.

---

[15] The number of elements is usually larger than 10^7.

[16] A well posed mathematical model should have the characteristics of [45]

1. There is a solution
2. The solution is unique
3. The solution changes continuously with the initial condition or input data

4. How to enhance detecting sensitivity ?

Here sensitivity refers to the minimal fluorophore concentration that makes fluorophore bio-distribution reconstruction possible with acceptable accuracy. In epi-illumination, both excitation optical pass length [17] and emission optical pass length [18] increase with fluorophore depth and emitted fluorescent intensity; thus, the sensitivity rapidly decreases with depth. This problem cannot be solved by simply increasing the incident power or dosage of the fluorescent dyes because an overly strong laser beam may damage the tissue and a strong dosage potentially means more toxicity. Therefore, a better way to enhance detection sensitivity is to eliminate noise or perform background subtraction, as explained later, in fluorescent data as much as possible

5. How to handle potential issues in clinical applications ?

Optical heterogeneity is common in practical biological tissue, meaning the optical properties of tissue are spatially and even temporally variant. Ideally, this should be considered when building a light propagation model. However, since in vivo measurement of the 3D distribution of the optical properties is a difficult task, many previous studies in this field have omitted this heterogeneity and used average or representative values [11, 111]. Herve et al. used measurements of excitation light passing through tissue to reconstruct the tissue's optical properties [52]. Another group has utilized the Born ratio (intensity ratio of fluorescence on excitation light at the same detection position) to alleviate the effects of heterogeneity [110] and then treated the subject as homogeneous. However, the availability of this method is limited in a trans-illumination geometry. In an epi-illumination geometry, most

---

[17] average of the distances that all excitation photons passed till they arrive at a fluorophore

[18] average of the distances that all fluorescent photons passed till they emit away from surface

of the back-scattered excitation light passes through superficial tissue only, whereas fluorescence may emit from a deeper region if the fluorophore is located deeply. This mismatch renders these ideas unavailable in the epi-illumination mode.

Besides optical heterogeneity, the irregularity of tissue shape and crevices on the tissue surface can also be observed. These affect light propagation inside tissue, thereby affecting the detection efficiency of the optical system. In addition, current imaging agents are still imperfect, i.e., presence of residual agents in normal tissues, which leads to background noise. Therefore, it is necessary to evaluate the effects of these issues and discuss potential solutions.

1.7 Objective of this Thesis

The main goal of this study is to improve some essential techniques of ECW-FMT to recover the depth, size, and distribution of fluorophore within tissues more accurately and stably. Specifically, in this thesis, I

1. attempt to estimate fluorophore depth more accurately;
2. improve established methods for obtaining an unbiased, and not overly smoothed fluorophore bio-distribution;
3. evaluate the effects of several practical issues once the proposed methods and system are applied to realistic tissue, and discuss potential strategies.

1.7.1 Outline

This thesis is organized as follows.

Chapter 1 provides a brief review of molecular imaging. The development and principles of FMT are then introduced, and the reason for my focus on EFMT is explained.

Chapter 2 offers an overview of the proposed concepts to solve the key issues of ECW-FMT. The essential techniques required by an ECW-FMT system are described. Then, the principles of the proposed concepts are examined. Note that details and evaluations are given in later chapters.

Chapter 3 describes the custom ECW-FMT system. In reference to a previous study [12], an NIR light source and a pair of polarizing beam splitters (PBS) are utilized to improve penetration depth and detection sensitivity.

Chapter 4 describes the detailed steps required to localize fluorophore (centroid) on the basis of intensity variations resulting from perturbation. Here a fluorophore of finite size is treated as a fluorescent point source located at its initial weighted centroid. The method is validated by experiments using tissue-like homogeneous phantoms and numerical simulations.

Chapter 5 provides further technical details about the proposed framework for restoring fluorophore distribution. The performance of the proposed methods are evaluated by a series of numerical simulations and phantom experiments.

Chapter 6 evaluates the depth perturbation concept as well as the reconstruction framework proposed by this thesis in an ex vivo environment. Meat, which has slight optical heterogeneity, is utilized as the subject, and a solid optical phantom is utilized as the depth perturbator.

Chapter 7 describes the influences of remaining issues and their potential solutions. The extension and potential applications of the proposed methods are discussed.

2 Overview of the Proposed Concepts

This chapter present an overview of the concepts proposed to resolve some key issues associated with the ECW-FMT technique described in Sec. 1.6.2. First, the essential techniques required by an ECW-FMT system are described and the issues of my interest are identified. Then, the principles of the proposed concepts are explained in detail.

2.1 Essential Techniques Required by ECW-FMT

The essential techniques required by ECW-FMT are listed in Fig. 2.1. Some techniques are well established while others remain challenging.

2.1.1 Fluorescent Measurement

Measuring fluorescent signals requires only an optical de¬tector, an excitation source, and an optical filter and thus is relatively easy. However, in epi-illumination geometry, auto-fluorescence [1] and leakage of the excitation light [2] is typically stronger than other geometries, resulting in low contrast in fluorescent images [79]. In particular, for fluorescence of fluorophores in deep tissues, the weakness of emitted fluorescence amplifies the effects of those unexpected ingredients. Therefore, special attention should be paid to enhancing the contrast of fluorescent images.

2.1.2 Optical Properties Measurement

In this thesis, optical properties include to absorption coefficient μ_a, reduced scattering coefficient μ_s', and the refractive index n of a subject. Several mature techniques exist to measure the optical properties of a sliced sample or superficial tissue. Prahl et al. used a pair of integrating spheres to detect reflectance and transmission of a sample simultaneously [117], and then applied the measured values to an inverse adding doubling (IAD) algorithm [120] to solve the absorption and scattering coefficient. Dam et al. developed a handheld fiber-based optic probe to collect light reflection on tissue surface and estimated the optical properties by fitting the measured fluorescent signals to the diffusion equation [25]. An oblique-incidence reflectometer

---

[1] fluorescence emitted from endogenous fluorophore in tissue

[2] A part of reflected excitation light passes through the optical filter

is also capable of rapidly calculating the reduced scattering coefficient μ_s' [3] [94]. In the phantom and ex-vivo experiments described in this thesis, the oblique-incidence reflectometer was used to measure optical properties of the phantom.

However, measuring optical properties of deep region of tissue in the reflectance (epi-illumination) geometry is still challenging. One possible technique is diffuse optical tomography (DOT), which is the predecessor of FMT and is employed in locating some regions with optical properties that differ from the background (e.g., high absorption regions, such as vessels and blood) [81, 14]. Like FMT, DOT typically involves a complex source-detector configuration (beam scan or a bundle of optic fibers) and the optical inverse problem [135, 77, 53, 107, 118]. For circular or transmission geometry, DOT can effectively reconstruct the distribution of optical coefficients over the sampled tissue because the collected light passes throughout the entire sample. However, in reflectance geometry, the reflected light is primarily backscattered from shallow tissue layers and therefore does not include significant deep tissue information. Consequently, DOT's ability to probe deep tissue effectively is limited. PAT may be a better alternative. PAT has deeper probing depth owing to its "light in sound out" nature as elaborated in Sec. 1.5.1. Razansky et al. utilized PAT to reconstruct a quantitative optical absorption map of tested tissue and incorporated the map into the FMT computation [125]. In addition, some studies [16, 57, 169] have attempted to integrate a non-optical modality, such as CT and MRI into DOT or FMT. The morphological prior provided by these non-optical modalities can mitigate the ill-conditioned issue of the optical inverse problem, thereby resulting in a better 3D reconstruction of tissue optical coefficients.

---

[3] $\mu_s' = \mu_s(1-g)$

2.1.3 Forward Problem

The forward problem is a modelling problem that involves light propagation from a light source via tissue and fluorophores to detectors. The model is always expressed as a sensitive matrix. This process relies on knowledge of the distribution of tissue optical properties. As mentioned in Sec. 1.4.1, techniques to model light propagation in tissue are well established. The state of the art modeling techniques in this field are adequate to handle tissue with irregular structure and optical heterogeneity, where finite element method (FEM) and parallel computing techniques are widely used. Some sample code packages such as MCML [155], MCC [33], MCX [34], NIRFAST [26], Toast++ [131] are freely available. In this thesis,I used the Monte Carol method (adapted from the MCML software package) and an accelerated Monte Carol model proposed by [142] are used without special annotation.

2.1.4 Inverse Problem

The determination of unknown florescence distribution from experimentally measured data, i.e., the inverse problem, is the core technique of FMT. Since 2000, the inverse problem has been extensively studied. However, most of the previous research has focused on FMT acquisitions in transmission or circular geometry. A typical method to solve the inverse problem involves the inversion of a sensitivity matrix and an appropriate regularization [4] method, where the depth resolving step is usually not treated independently from the fluorophore distribution reconstruction step. The sensitive matrix is always ill-posed, meaning that there is no unique solution and that the solution is extremely sensitive to noise in the measured data.

In the reflectance (epi-illumination) geometry, solving the inverse problem ac-

---

[4] A numerical treatment to stabilize and select the final solution of the inverse problem

curately is more difficult because of the intrinsic weakness of epi-FMT in obtaining depth information, as described in Sec. 1.6.2. On the other hand, the low SNR in reflectance geometry also intensifies the effect of the ill-posed nature of the matrix, causing notable instability and inaccuracy of the reconstructed result. As reported previously [12], accurately estimating fluorophore depth was only realized when the true depth was less than 0.7 mm. In this thesis, I propose an algorithm that includes the following two steps:

1. use of a depth perturbation method to obtain accurate fluorophore depth and centroid;
2. addition of this prior knowledge of fluorophore depth and centroid into the regularization process as a new constraint to ensure an unbiased result.

2.1.5 Fluorescent Dyes

Although out of scope, the development of nontoxic, high target-to-background ratio (TBR) fluorescent dye is crucial for the clinical availability of all fluorophore-related imaging modalities. For details about fluorescent dye, see Review [62].

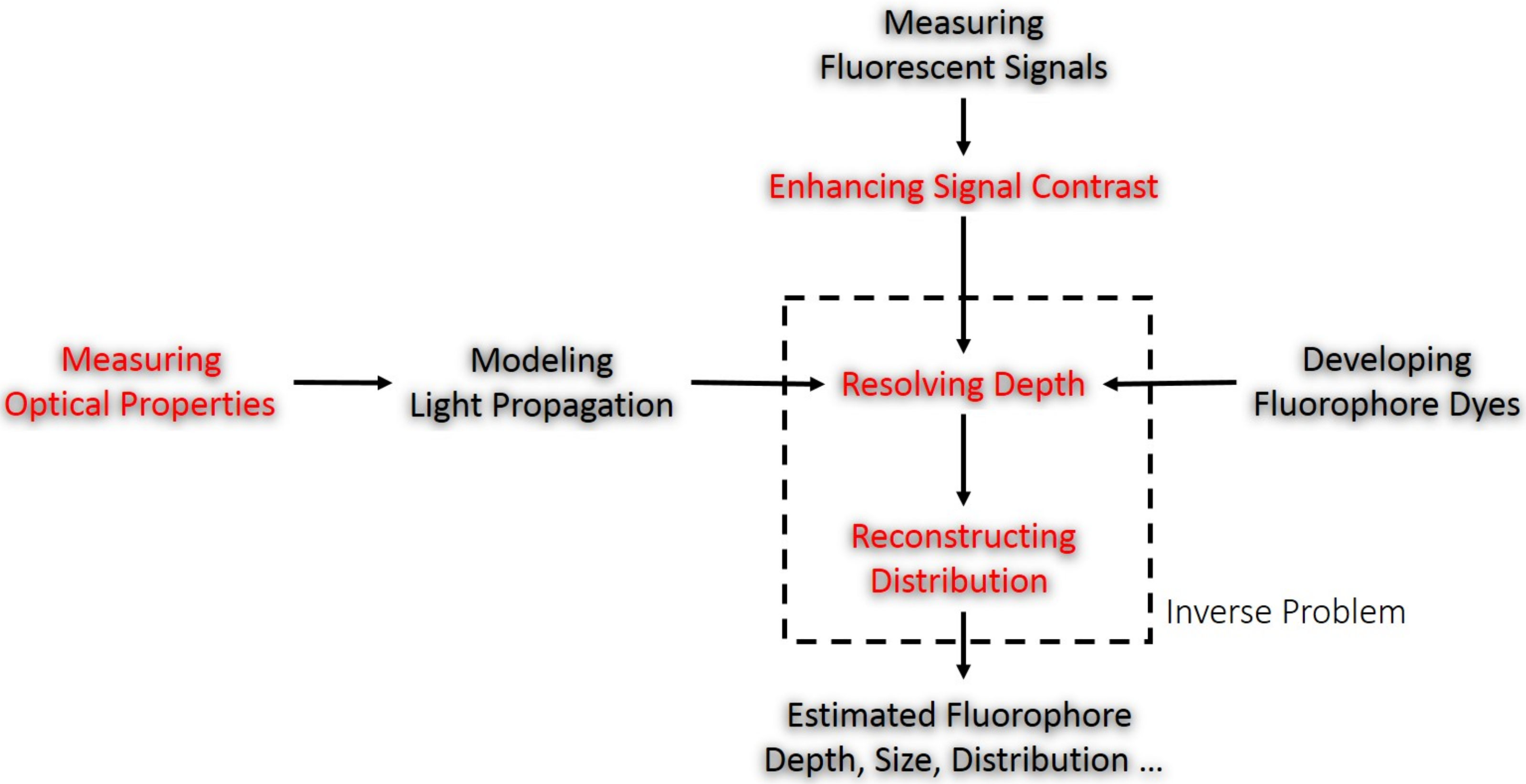

Figure 2.1: Essential Techniques Required by ECW-FMT: modules in red are the key points in the scope of this thesis. The red fonts show the focus of my interest.

2.2 Development of ECW-FMT System

The custom ECW-FMT system inherits the idea of mesoscopic epifluorescence tomography (MEFT) proposed by Björn et al.[12]. However, I noticed that in their setup the leakage of excitation lighta part of excitation light is reflected by tissue surface and passes through the optical filters, finally enter the detector was too strong to obtain meaningful measurements when the fluorophore is deeply embedded inside tissue. was too strong to obtain meaningful measurements when the fluorophore is deeply embedded within a tissue. A pair of PBSs is thus added to the proposed system to suppress excitation leakage. In addition, a NIR light source is used to increase penetration depth.

2.3 Resolving Depth by Depth Perturbation

2.3.1 Previous Research

This subsection describes two established methods to obtain depth information.

Source Detector Separation

The source detector separation method is most commonly used in the field of epi-fluorescence tomography [54]. This method is based on the hypothesis that scattered light detected further from the incident position has, on average, traveled more deeply into tissue [173]. Therefore, depth-dependent information can be retrieved from measurements at multiple source-detector distances [21]. Typical measurement sensitivity distributions of various source-detector separations are shown in Fig. 2.2. One can easily find that the sensitivity profile notably varies in the horizontal direction, whereas such a trend along the depth is not that clear. Actually, I performed a similar

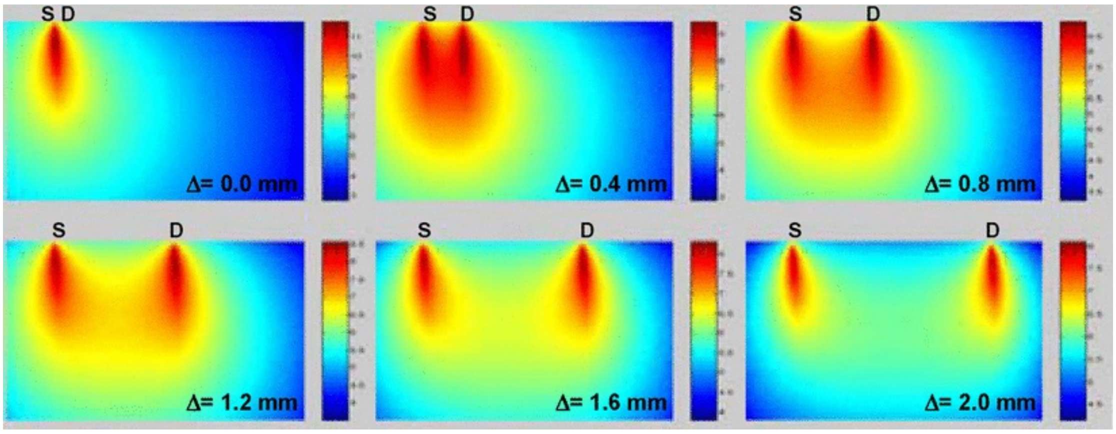

Figure 2.2: Measurement Sensitivity Distribution at Various Source-Detector Separations. These distribution are simulated by the Monte Carlo Method with scattering coefficient $\mu_s = 8mm^{-1}$ for excitation wavelength and $\mu_s = 7mm^{-1}$ for emission wavelength (g = 0.9). The simulated space is 3 × 2 mm ^{2}. The source detector separation varies from 0 to 2 mm. Reprinted from [21] with permission © 2010 IEEE

simulation as Ref. [21], and found that even if the separation increases to 20 mm, the mean depth[5] scattered light passed is as shallow as 4 mm (Fig. 2.3). Besides the poor sensitivity in depth, the signal strength becomes weaker for a larger separation, causing a lower SNR, which potentially contributes to a worse estimation for fluorophore depth.

Spectra Change

The phenomenon of fluorescence involves radiation being emitted in various wavelengths rather than at a single wavelength. Since optical attenuation of light in tissue depends on its wavelength, when fluorescence radiation passes through a tissue the intensity of a con¬stituent with a higher attenuation coefficient decreases

---

[5] The depth was defined as the weighted average depth of light passing the middle cross-section between source and detector

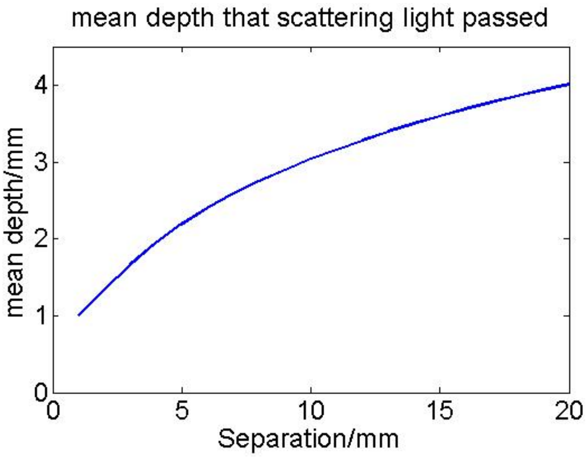

Figure 2.3: Mean Penetration Depth at Various Source-Detector Separations (Simulation performed with the same optical coefficients as Fig. 2.2)

faster than that of a constituent with a lower attenuation coefficient. The spectrum of fluorescence thus varies according to the tissue amount traversed (Fig. 2.4) [175]. Accordingly, Stefan et al. proposed that fluorescence spectra can provide depth information [143] and proved its effect in a trans-illumination FMT [6].

I agree with the results reported in that study but notice that its feasibility is restricted in the wavelength band where tissue optical properties change drastically with wavelength. However, the dependency of optical coefficients on wavelength is extremely complicated; in some wavelength bands, scattering decreases with wavelength while absorption increases. Therefore, the total optical attenuation may not change with wavelength. On the other hand, in multi-spectral fluorescence imaging, fluorescence is independently measured at several isolated wavelength bands (the band width is 10 nm in Ref. [78]). The fluorescent strength over a narrow band is apparently much weaker than that of the integrated fluorescence. Therefore, low detection sensitivity is another issue in multi-spectral fluorescence imaging. In addition, the original fluorophore emission spectra are necessary for the multi-spectral method to calculate how much the measured emission spectra have changed. In clinical

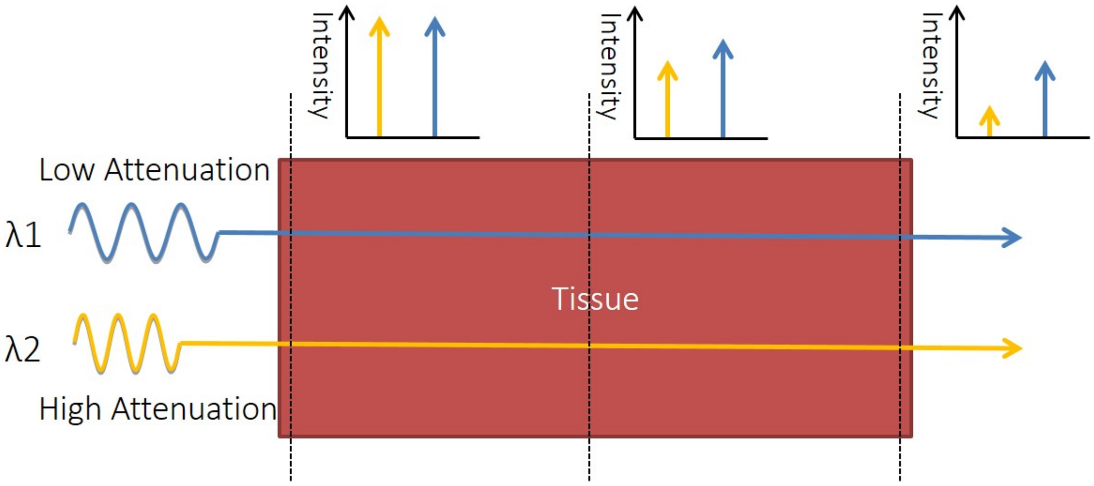

Figure 2.4: Principle of The Spectra Change Method.

conditions, it may be difficult to acquire the original spectra accu¬rately because the initial spectra vary according to the chemical environment of the tissue surrounding the fluorophore. For instance, the emission peak of ICG is 780 nm in water, 810 nm in plasma [75], and 830 nm [174] in intralipid solution [178].

2.3.2 Principle of Depth Perturbation

To overcome the limitations of the previous methods, a depth perturbation method was proposed to resolve the fluorophore depth. To the best of my knowledge, this is the first time the concept of depth perturbation has been proposed and verified in the FMT field of.

Method

A thin optical phantom with known optical properties is used as a depth perturbator (Fig. 2.5). By superposing the perturbator onto a sample, the depth of a fluorescent object inside the sample is deliberately changed. Fluorescent signals are measured before and after the perturbation. I believe that the fluorophore depth can

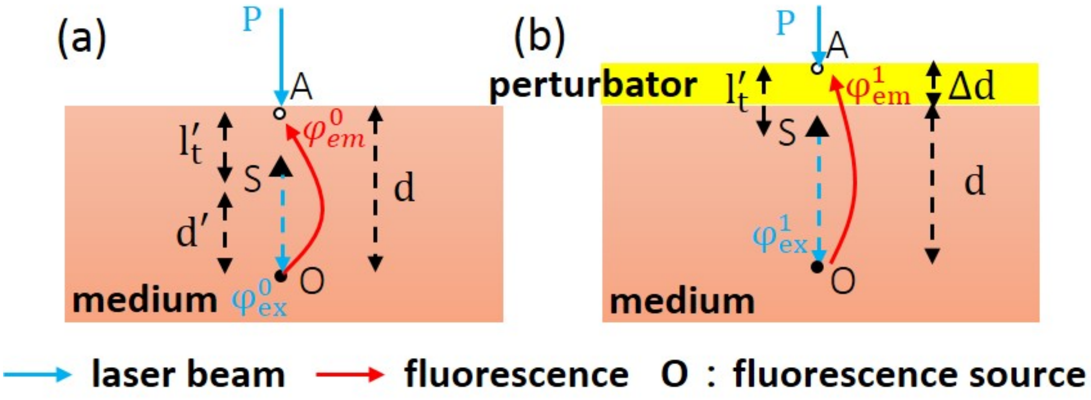

Figure 2.5: Schematic of Depth Perturbation: (a) initial status, (b) after perturbation. Solid dots denote fluorophore s, circles denote observation points, and triangles denote a virtual point source corresponding to the laser beam [177].

be determined according to the variations of the measurements. [177, 178]

Mathematical Explanation[178]

The concept of depth perturbation originates from the diffusion equation [157] that describes light propagation within a scattering medium (such as tissue). First, consider the situation shown in Fig. 2.5(a), a pencil laser beam is incident on a semi-infinite scattering medium. If the refractive index mismatch at the air-medium boundary is ignored, the fluence rate of excitation light at point O, i.e., d beneath the incident point can be expressed as:

$$\varphi_{\mathrm{ex}}^{0}(\mathrm{d}) = \mathrm{C}_{\mathrm{ex}}\exp(-\mu_{\mathrm{eff}}^{\mathrm{ex}}\mathrm{d}')/\mathrm{d}' \tag{2.1}$$

where $\mu_{\mathrm{eff}}^{\mathrm{ex}}$ [6]denotes the effective attenuation coefficient at the excitation wavelength; $\mathrm{C}_{\mathrm{ex}} = \alpha' P/(4\pi D_{ex})$ is a constant comprising incident power P, light diffusion coefficient $D_{ex} = 1/(3\mu_{a,ex} + 3\mu'_{s,ex})$, albedo $\alpha' = \mu'_{s,ex}/(\mu_{a,ex} + \mu'_{s,ex})$; and $\mathrm{d}' = \mathrm{d} - \mathrm{l}_t'$ is

---

[6] $\mu_{eff} = \sqrt{3\mu_a(\mu_a + \mu_s')}$

the distance from virtual excitation source S (approximation of the pencil beam) to O, where $\mathrm{l}_t^{\prime}$ denotes the transport mean free path. Assuming a fluorescent source with unit power at O and ignoring the refractive index mismatch at the air–medium boundary, emission fluence rate at point A can be solved as:

$$\varphi^0_{\mathrm{em}}(\mathrm{d}) = \mathrm{C_{em}} \exp(-\mu^{\mathrm{em}}_{\mathrm{eff}}\mathrm{d})/\mathrm{d} \tag{2.2}$$

where $\mu^{\mathrm{em}}_{\mathrm{eff}}$ denotes the effective attenuation coefficient at the emission wavelength and $\mathrm{C_{em}} = c\kappa\eta/(4\pi D_{em})$ is another constant consisting of fluorophore amount c, extinction coefficient κ, quantum yield η and the diffusion coefficient at emission wavelength $D_{em} = 1/(3\mu_{a,em} + 3\mu^{\prime}_{s,em})$. Therefore, fluorescence intensity at point A is expressed as

$$\Phi_0 = \varphi^0_{\mathrm{ex}}(\mathrm{d})\,\varphi^0_{\mathrm{em}}(\mathrm{d}) \tag{2.3}$$

Thereafter, a perturbator of thickness Δd is superposed onto the medium (Fig. 1(b)). For simplicity, I assume that the optical properties of the perturbator are identical to those of the medium. Fluorescence intensity at A can thus be expressed as

$$\Phi_1 = \varphi^0_{\mathrm{ex}}(\mathrm{d}+\Delta\mathrm{d})\,\varphi^0_{\mathrm{em}}(\mathrm{d}+\Delta\mathrm{d}) \tag{2.4}$$

Consequently, at A, the ratio of fluorescence intensity after the perturbation to that before can be calculated as:

$$\Gamma = \frac{\Phi_1}{\Phi_0} = \exp\left[-(\mu^{\mathrm{ex}}_{\mathrm{eff}} + \mu^{\mathrm{em}}_{\mathrm{eff}})\Delta\mathrm{d}\right] \frac{\mathrm{d} - \mathrm{l}^{\prime}_t}{\mathrm{d} - \mathrm{l}^{\prime}_t + \Delta\mathrm{d}} \frac{\mathrm{d}}{\mathrm{d} + \Delta\mathrm{d}} \tag{2.5}$$

where constants C_{em} and C_{ex} (as well as other factors like the sensitivity of the measuring system) are canceled out. Although analytically complex, Γ **is actually a monotonic increasing function of d**, as shown in Fig. 2.6. For a given Δd, the larger

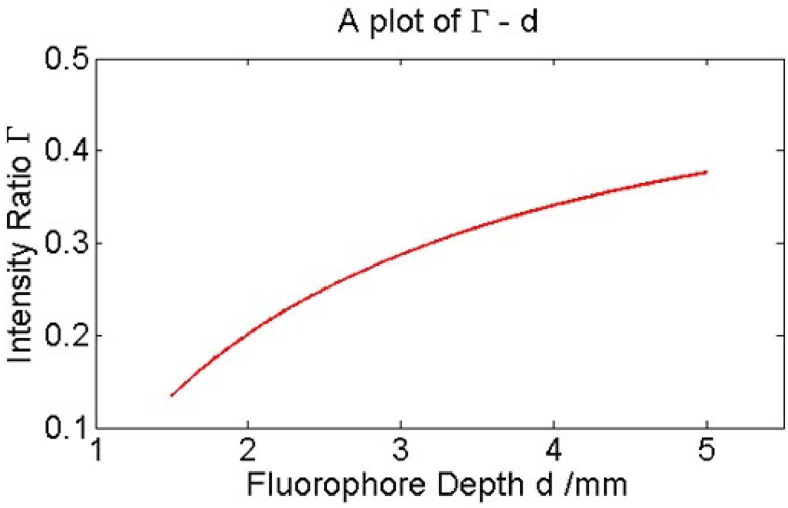

Figure 2.6: Intensity Ratio owing to the Perturbation VS Fluorophore Depth: the ratio is calculated with Eq. 2.5 and biological tissue like optical coefficients: in the excitation wavelength: $\mu_s' = 11.7cm^{-1}$, $\mu_s' = 0.2cm^{-1}$; in the excitation wavelength: $\mu_s' = 10.5cm^{-1}$, $\mu_a' = 0.1cm^{-1}$; the thickness of the perturbator $\Delta d = 1mm$. [178]

the initial fluorophore depth, the smaller the relative variation of the distance $\mathrm{\Delta d/d}$ ($\mathrm{\Delta d/d'}$) from fluorophore to detector (excitation source), resulting in smaller variation (attenuation) in the intensity, i.e. a larger part of intensity is retained. On the basis of this dependency of Γ on fluorophore depth, one can in turn obtain depth information by observing the intensity variation owing to the perturbation.

Physical Explanation

In this subsection, the effects of depth perturbation are explained from a physical perspective. In essence, the perturbation prolongs the optical path lengths from incident points via fluorophore to observation points and results in intensity attenuations of the measured fluorescent signals. Light attenuation in tissue is attributable to both absorption and scattering. According to the Beer–Lambert law [7] , optical attenuation

---

[7] Beer–Lambert law: $T = \dfrac{I}{I_0} = e^{-\mu_a l}$, where T denotes transmittance (i.e. residual rate after absorption), I_0 and I denotes initial intensity and residual intensity respectively, μ_a denotes absorption coefficient and l denotes light propagation length.

resulting from absorption depends on only the tissue absorption coefficient and the amount of tissue light has passed through, which provides a baseline attenuation rate [8]. Compared with absorption, the effects of scattering are more complicated and spatially variant, because scattering transfers, rather than eliminates, optical energy to another direction or location.

First, consider the scattering of an incident laser beam. A representative distribution of excitation light intensity within tissue is shown in Fig.2.7 (a). Here, the region just below the incident is called the "center" region, whereas regions horizontally separated are defined the "side" regions. Assuming the average scattering angle (Defined by the scattering anisotropy g) is spatially invariant within a medium, the possibility of one center-region photon scattered to the side region is thus the same as that of one side-region photon scattered to the center. On the other hand, at the surface and sub-surface of tissue, the laser beam does not completely lose its directionality, and the intensity in the center region is significantly larger than that in the side regions. Consequently, when excitation photons move downward [9], the number of photons scattered to the side regions will also be significantly greater than the number scattered in the center region. In terms of net flow, in shallow tissue, center-region photons not only flow to deeper tissue but also flow to the two sides. The excitation intensity thus decreases very quickly along the depth (Z) direction. Conversely, at deep tissue, owing to multiple scatterings, the difference between the center and the side regions become insignificant. In this case, the net flow from the center region to the side becomes smaller, and the energy in the center region essentially flows to the deeper tissue, leading to higher energy remaining along the depth direction. Figure 2.7(b) shows the Z-direction residual rate Γ_{ex} of the distribution shown in Fig. 2.7(a),

---

[8] defined as intensity relative decrease per unit propagation length

[9] In biological tissues, forward scattering events are probabilistically far more in number than back scattering events. Therefore, only forward scattering is discussed here

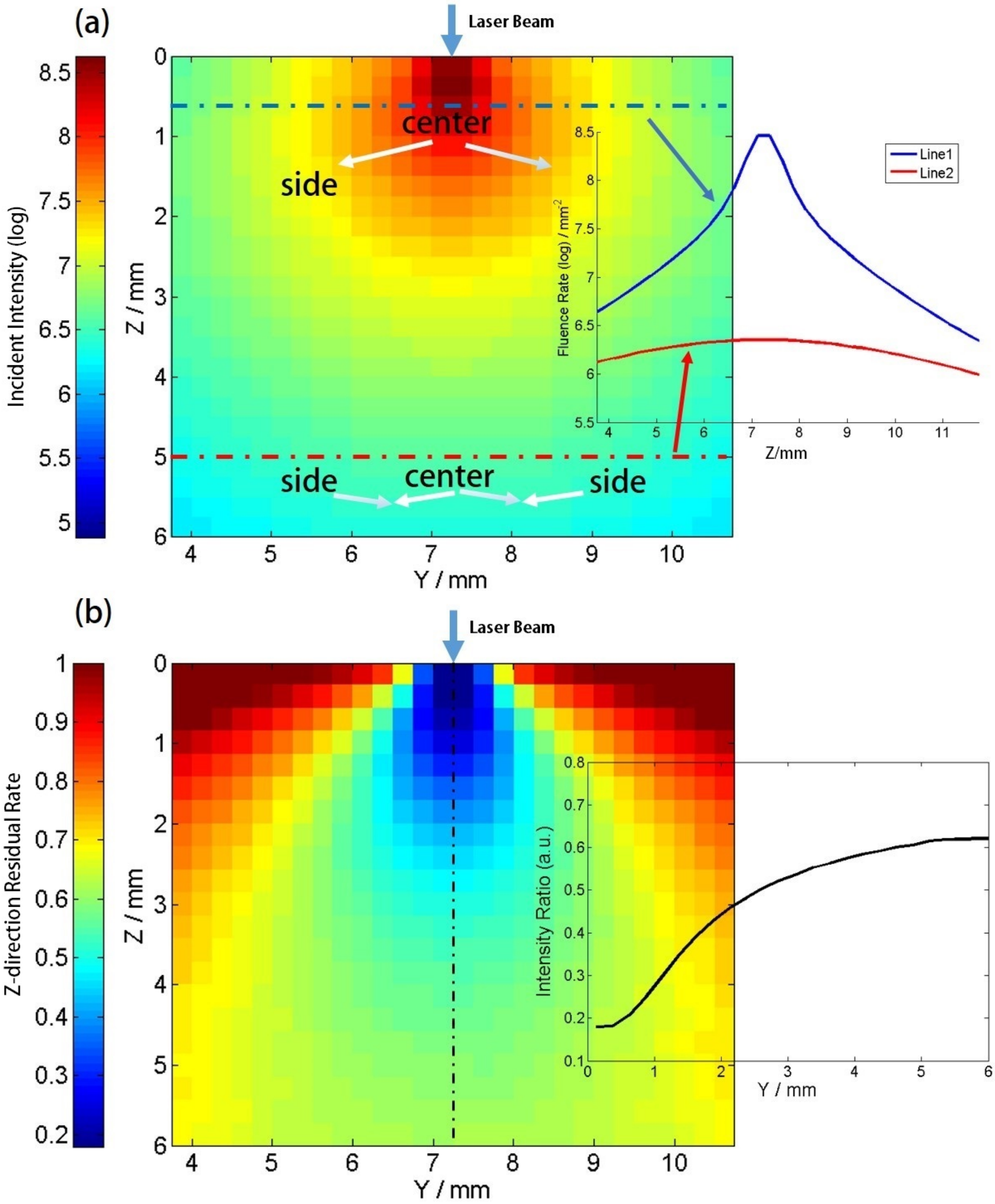

Figure 2.7: Effects of Scattering on Excitation Light: (a) representative distribution of excitation light intensity within tissue. The insert shows the intensity profiles at shallow and deep tissue respectively; (b) Z-direction residual rate of (a). The insert shows the values along the dot-dash line.

which is defined as

$$\Gamma_{ex} = \frac{\Phi_{ex}(y, z + \Delta d)}{\Phi_{ex}(y, z)}, \tag{2.6}$$

where $\Phi_{ex}(y, z)$ denotes excitation intensity at location (y, z), and $\Delta d = 1$ mm. Along with the vertical center line (also the initial incident direction), the residual rate monotonically increases with depth.

Furthermore, for a fluorescent point source located inside a scattering medium, the emission intensity has a concentric distribution and decreases with distance from the source (Fig. 2.8). If the boundary condition and detector collection efficiency are ignored, measuring fluorescence on the medium surface is equivalent to sampling a horizontal surface from the distribution. Note that on a surface close to the source (i.e., the source is shallow to the surface), the intensity in the center region (the points just above the source) is much higher than that on the side, which is similar to the horizontal excitation profile at shallow tissue as aforementioned. This is attributable to the distance of the center region to the source being one order smaller than the distance of the side regions to the source. Conversely, on a surface distant from the source (i.e., the source is deep relative to the surface), the intensity profile is flatter because the source distance of the center region and those of the side regions are comparable. Thereafter, as previously discussed, owing to differences on the intensity profile, the relative upward net photon flow will differ. The insert in of Fig. 2.8(b) shows the residual rate Γ_{em} (defined similar to Eq. 2.6) of the emission intensity along the Z direction, which is also a monotonically increasing function of the vertical distance from the sampling surface to the source, i.e. the depth of fluorophore source.

Finally, return to the effect of depth perturbation. Because the perturbator is also a scattering medium, to superpose a perturbator on the medium is nearly equivalent to moving the fluorescent source downward inside the medium. After the perturbation,

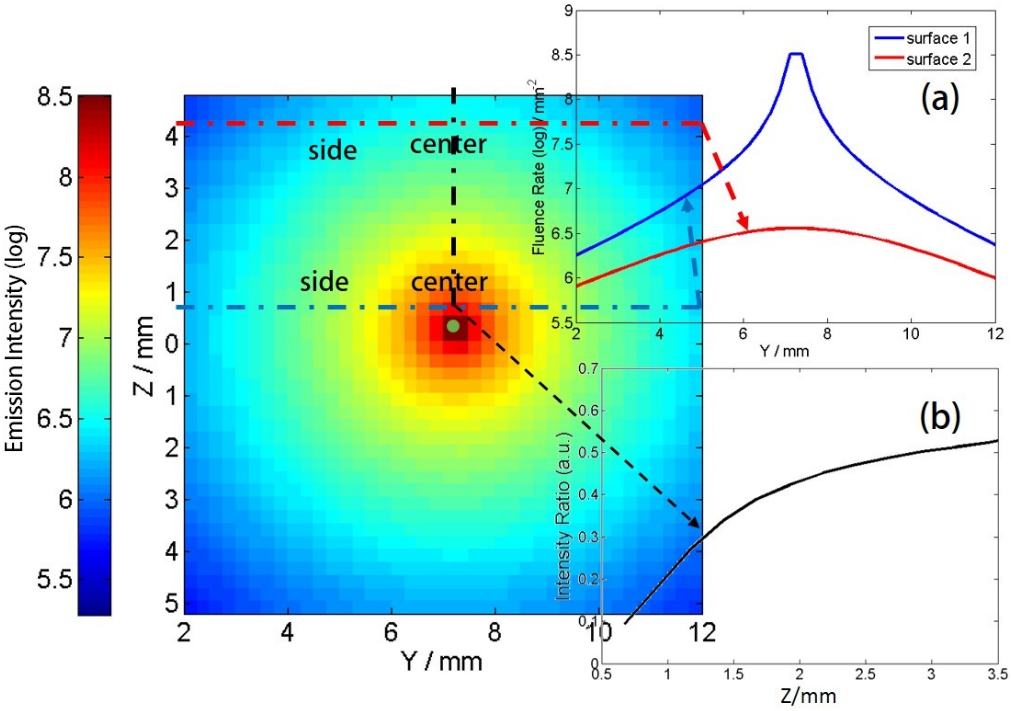

Figure 2.8: Effects of Scattering on Emission Light: a representative intensity distribution of light emitted from a fluorophore point source. The insert (a) shows the intensity profiles at a close sampling surface and at a far one respectively. The insert (b) shows the residual rates along the dot-dash line.

only Γ_{ex} times the initial excitation photons remain. Likewise, for a given emission energy, owing to a more distant sampling surface, the number of detected emission photons will be Γ_{em} times the previous number. Therefore, the ratio Γ of intensity with perturbation to that without perturbation is the product of Γ_{ex} and Γ_{em}. Because both Γ_{ex} and Γ_{em} are monotonically increasing functions of fluorophore depth, the intensity ratio Γ increases with the depth, which is why this perturbation method can be used to resolve depth

2.3.3 Perturbator

In this thesis, two types of perturbators are used: one is liquid and the other is solid.

When an experiment involves a liquid phantom such as intralipid aqueous solution [10], the same subject as the phantom is used as the perturbator. Specifically, a few volumes of the same solution are added to the phantom to perturb the fluorophore depth.

I also produced a solid perturbator for experiments with biological tissues or a solid phantom. The solid perturbator was made using polydimethylsiloxane (PDMS). As a widely used silicon-based organic polymer, PDMS is optically clear, nontoxic, and flexible [97] . Therefore, a perturbator made of PDMS could be tightly attached to biological tissue, even at a non-planar irregular surface. The scattering properties of the perturbator are provided by mixing TiO2 [141] into PDMS[178]. Figure 2.9 shows a representative solid perturbator. The manual to produce the solid perturbator is given in Appx. A.

---

[10] A type of emulsion, commonly used in optical experiments to mimic tissue's scattering properties

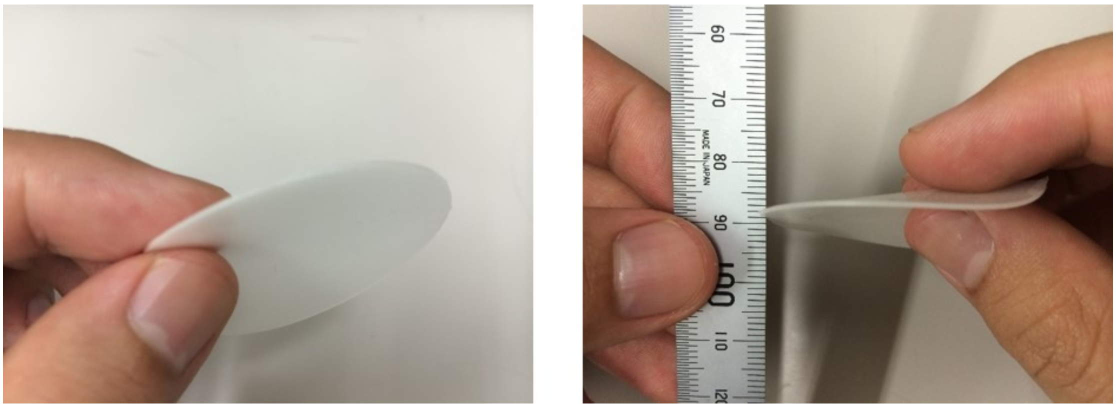

Figure 2.9: A solid perturbator made of polydimethylsiloxane with a thickness less than 1 mm

2.4 Coarse to Fine Strategy

In the depth perturbation process, a fluorescent object is treated as a point source, while the ultimate goal of FMT is to restore both size and location of the fluorescent imaging agent. In this thesis, a framework of fluorophore bio-distribution reconstruction is built on the basis of a coarse to fine strategy. Herein, fluorophore bio-distribution refers to the concentration distribution of fluorescent molecules. Since quantification of the concentration requires extremely complicated calibration and quantification's meaning is still unclear from a clinical perspective, this thesis focuses on the recovery of the relative concentration distribution over the examined region and the effective size of the fluorescent object, i.e., the size of the diseased region.

2.4.1 Motivation

A common step in the reconstruction is to divide the reconstructed space into a large number of small voxels. Then for each voxel, an appropriate relative concentration value is calculated by solving the inverse problem. The size of the voxel determines the accuracy of the restored distribution because 1) a local distribution within a voxel is averaged as a uniform value; and 2) a fluorescent object with size less than the voxel size may be considered as zero or one voxel (e.g., quantization error).

Therefore, a group of finely divided voxels theoretically yield about more accurate results. However, it also means significantly increasing computational cost. For instance if one divides a 5×5×5 mm^3 volume with a voxel size of 0.25×0.25×0.25 mm^3 in to 5 × 5 × 5 = 8000 voxels, and uses measured data as many as the voxels in the reconstruction process [11], the transfer matrix will scale to 8000 × 8000 comprising 64,000,000 elements, and requires 512 MB memory with a 64-bit operating system (OS). Moreover, only the inversion of the transfer matrix, a computation that is typically repeated more than 10 times in one reconstruction process, takes more than 2 min [12] with a high performance personal computer. This results in an unacceptable reconstruction time and diminishes the real-time imaging advantage fluorescent imaging.

As an alternative, if the voxel size is changed from 0.25×0.25×0.25 mm^3 to 0.5×0.5×0.5 mm^3, the transfer matrix scales down to 1000 × 1000[13]. Moreover, the computation time of the inversion decreases to only 0.34 s under the same conditions, which is close to 0.3% of the previous value. This huge gap shows that, relative to the matrix scale, the computation time decreases sharply rather than linearly.

2.4.2 Method

To achieve both accuracy and fastness of the reconstruction process, a coarse to fine strategy was taken, that is, to implement the reconstruction in more than one

---

[11] That is, let the number of knowns equals to the number of unknowns.

[12] This time is measured using a computer with a Inter(R) Core i7 2.80GHz CPU, 8 GB memory and 64-bit OS

[13] Keeping the known number equal to the unknown.

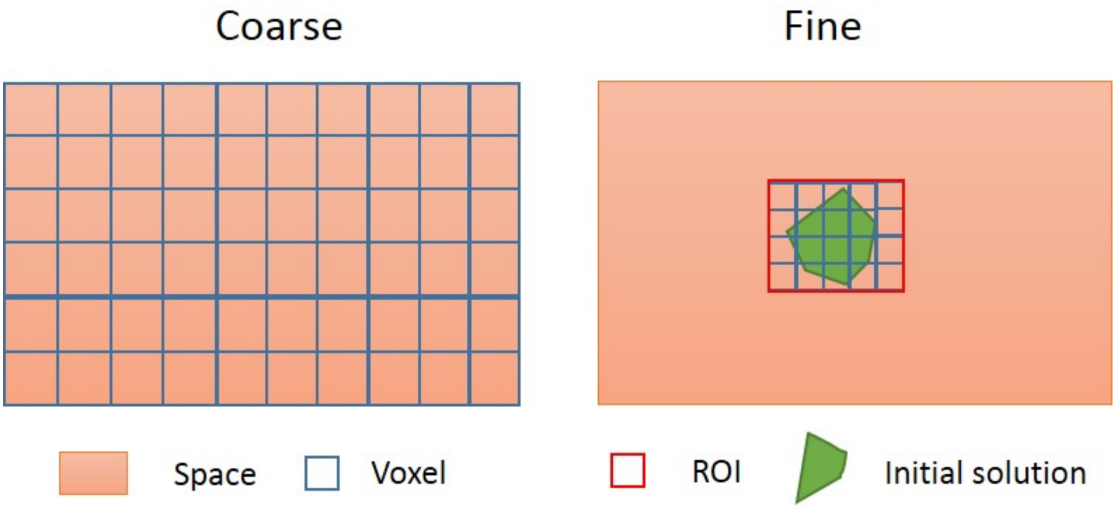

Figure 2.10: Schematic of the Coarse to Fine Strategy: although this strategy is actually applied in 3D volume, here we only show a cross section for better visibility.

steps:

Coarse Step: solving the inverse problem over the entire space but with a large voxel size to obtain a coarse result(Fig. 2.10(a));

Fine Step: set a ROI according to the coarse result, then reconstruct within the ROI with finer voxels(Fig. 2.10(b)).

In each step, the involved number of voxels is suppressed [14] o realize fast computation. If necessary, the fine step can be repeated several times. Consequently, a fine and more accurate recovery of the fluorescent distribution can be achieved within an acceptable time. Realization and evaluation of this strategy are described in detail in Chapter 5.

---

[14] For instance, not allow it larger than 1000

2.5 Reconstruction with Prior Knowledge

The optical inverse problem in FMT is a typical ill-posed problem (see Footnote 3 in Chapter 1), , which means that there is more than one solution. For instance, owing to the high scattering of tissue, a broad profile of fluorescent signals may be generated by either a small but deep fluorophore source or a broad and shallow source. Therefore, an additional assumption or constraint is required to select a solution from potential solutions; this process is referred to as regularization.

2.5.1 Regularization

Mathematically, regularization is the process to minimize an object function of

$$\|\mathbf{Gm}-\mathbf{d}\|_2^2+\alpha F(\mathbf{m}) \tag{2.7}$$

where **G** denotes the sensitivity matrix [15], **m** denotes the unknown fluorescent concentration distribution [16], and **d** denotes measured fluorescent signals. The left half of the object function is a standard least square term to fit the measured data to the light propagation model. In the right half, $F(\mathbf{m})$ is a regularization term that represents the aforementioned assumption or constraint, and α is regularization parameter.

Regularization Term

The most commonly used assumption is smoothness of the solution, which is realized by a regularization term of norm 2 ($\|\mathbf{m}\|_2^2$). This method is also called Tikhonov regularization [145]. Other common methods include sparsity regularization [50] and total variation (TV) regularization [35]. The former assumes the solution is isolated

---

[15] Describing light propagation from source via any voxel in reconstructed volume to detector

[16] Although as a 3D distribution, in this computation it is always reshaped to a vector

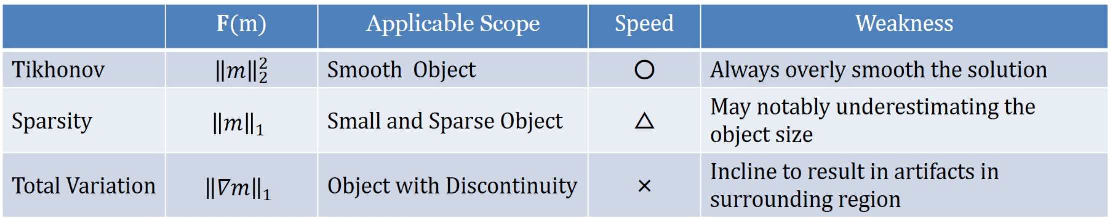

	F(m)	Applicable Scope	Speed	Weakness
Tikhonov	$\|\|m\|\|_2^2$	Smooth Object	○	Always overly smooth the solution
Sparsity	$\|\|m\|\|_1$	Small and Sparse Object	△	May notably underestimating the object size
Total Variation	$\|\|\nabla m\|\|_1$	Object with Discontinuity	×	Incline to result in artifacts in surrounding region

Figure 2.11: Comparison of Common Regularization Method.

and sparse[17], corresponding to a norm 1 ($\|\mathbf{m}\|_1$) regularization term. The latter prefers a solution with discontinuous jumps with a regularization term of $\|\nabla\mathbf{m}\|_1$. Here the ∇ refers to discretization of the gradient operator [5].

According to the assumption content, the applicable scopes of the three methods are different. Tikhonov regularization works well with smooth distribution; sparsity regularization performs well when object size is small and in the same order as the voxel size. Note that TV regularization can maintain sharp changes in the distribution. All these methods have been used to solve the optical inverse problem [32, 35, 8, 17, 21, 111].

In this thesis, since diseased cells, such as cancer cells, are assumed to emerge from one site and then penetrate into surrounding tissue, the practical profile of number of diseased cell, and thus the number of accumulated fluorescent molecules, is considered to vary smoothly within a tissue. On the other hand, because current imaging agent techniques cannot ensure that all fluorescent dyes bind to their target, a condition of zero background concentration (preferred by sparsity regularization) or a sharp boundary between normal and diseased tissue (preferred by TV regularization) is impractical. Furthermore, Only Tikhonov regularization can be realized by non-iterative algorithm, thus with a notably faster speed. Accordingly, I selected Tikhonov regularization as the basis of the proposed reconstruction framework, although its

---

[17] A status that the values of most voxels is zero

result is sometimes biased in the depth direction and is always overly smoothed which results in poor resolution and size overestimation [135]. To overcome this two weaknesses, I introduced the centroid knowledge obtained from the depth perturbation method to constrain the solution, and a piecewise spatially varying regularization method to compress the estimated distribution.

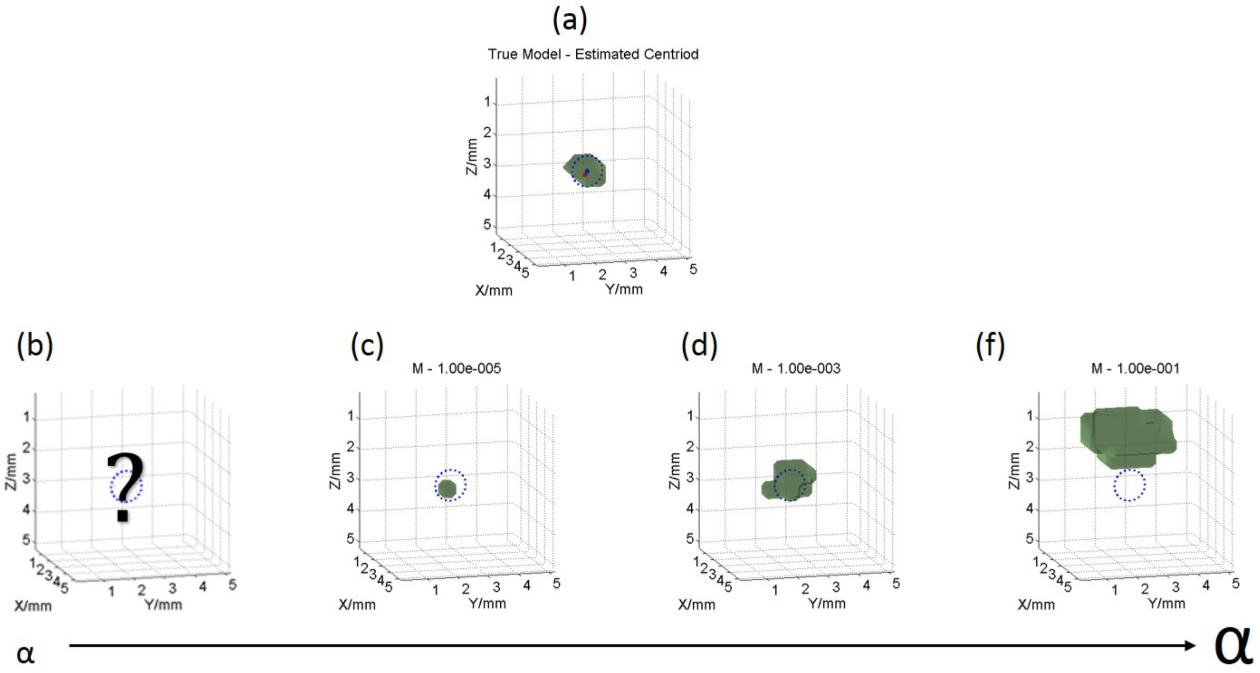

Figure 2.12: Effect of Regularization Parameter: The top shows the true model (a) which is a uniform concentration distribution within the green surface; the bottom show FWHM [18] of the restored models with regularization parameter of, extremely small value (e.g. 10^{-7}) (b), 10^{-5}(c), 10^{-3}(d), 10^{-1}(f). The question mark denotes the result does not converge. The dash circles denote the actual boundary of the fluorophore inclusion.

Regularization Parameter

The regularization parameter α determines the weight of the regularization term in the entire inverse problem and significantly influences the final solution. For Tikhonov regularization in an epi-fluorescence tomography environment, the following statements hold true:

- for extremely small α, the solution is sensitive to noise (Footnote 3, Chapter 1), unstable, and even does not converge (Fig. 2.12(b)), because the ill condition is rarely alleviated by the regularization;
- when α increases to a certain value, the solution begins to converge around its actual location (Fig. 2.12(c));
- with increasing α, the solution becomes smoother (broader in size), and its central depth generally deviates from the truth (become shallower) because the regularization term plays a more important role(Fig. 2.12(d));
- for excessively large α, the solution is notably biased from the actual fluorescent region (Fig. 2.12(e)).

That the solution becomes shallower with increasing α can be attributed to the fact that in the transfer matrix **G**, corresponding values of voxels in shallower layers are higher (since the optical path to both incident position and observation position are shorter) than those in deep layers. Consequently, values of a solution at shallow layers will be smaller [19]. For larger α, $\|\mathbf{m}\|_2^2$ is more dominant in the inverse problem. Therefore, a shallower solution is more easily selected as the final result.

---

[19] Consider $\mathbf{m} \approx \mathbf{G}^{-1}\mathbf{d}$

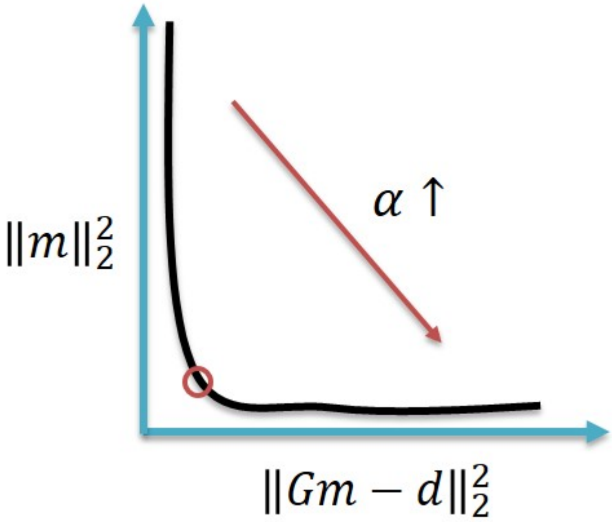

Figure 2.13: Schematic of the L Curve Method

In previous researches [118, 107, 87] in the field of optical inverse problem, the regularization parameter is manually or empirically determined. However, this heuristic choice of the parameter will be impractical in clinical applications and may cause unwanted bias in the restored fluorophore. Therefore, a method to optimize the regularization parameter automatically is preferred. To date, the methods most frequently reported in the literature include the L-curve and the generalized cross-validation (GCV) methods [61, 24].

The L-Curve method selects a few of parameters from a large range (e.g. 10^{-10} – 10^{0}), and solves the inverse problem using each parameter. Their respective solutions are substituted into the least square term $\|\mathbf{Gm} - \mathbf{d}\|_2^2$ and the regularization term $\|\mathbf{m}\|_2^2$, whose values are plotted in pairs as Fig. 2.13 and expected to be an L-like form [47]. The parameter corresponding to the turn point is usually selected as the best regularization parameter. However, the L-Curve method is intrinsically an empirical method. It was reported to always provide an overly smooth solution [121], and not to always exhibit a clear corner to determine an optimal regularization parameter [61].

he GCV method works on the principle that when the current regularization parameter is appropriate, if one measured data point is ignored in the fitting process and a regularized solution is found using the remaining data set, then the ignored data point should be accurately restored by substituting the regularized solution back to the theoretical model. Consequently, the regularization parameter can be optimized by minimizing the differences between the restored values and the measured value [24, 5]. Algorithmically, this can be realized by minimizing the function $g(\alpha)$, defined as

$$g(\alpha) = \frac{||\mathbf{Gm}_\alpha - \mathbf{d}||_2}{\mathbf{TR}(\mathbf{I} - \mathbf{GG}_\alpha^\dagger)}, \tag{2.8}$$

where $\mathbf{G}_\alpha^\dagger$ denotes the Tikhonov regularized pseudo-inverse of the sensitivity matrix $\mathbf{G}$ at the regularization parameter α, and $\mathbf{TR}$ denotes the trace of a matrix [24]. Golub et al. [44] further proposed a singular value decomposition (SVD) based accelerating algorithm, thus allowing GCV to be applied to large scale problems, e.g. FMT and DOT. However, recently some studies have reported that the selection made by the GCV method is sub-optimal [121, 61]. It does not work well when the function $g(\alpha)$ is flat or has multiple minima. This method is also reported to be unable to offer an appropriate solution when noise in measured data is correlated [20]. Even without correlated noises, the GCV method slightly overestimate the regularization parameter, thus potentially leading to an over-smoothed reconstruction result [24].

In summary, although the widely used L-Curve and GCV methods can provide an automatic choice of the regularization parameter, they are not always feasible in any condition. Depending the conditions the results are not always optimal.

---

[20] Correlated noises can be produced by some in-vivo factors such as motion artifacts [24].

2.5.2 Incorporating the Centroid Constraint

As an alternative to the previously described methods, I proposed using centroid prior knowledge obtained from the aforementioned depth perturbation to determine an appropriate regularization parameter. The basic idea is using the estimated fluorophore central depth to reject any α that results in the solution deviating significantly from its true centroid.

Method

Similar to the L-Curve method, the proposed method also selects a group of α values [21] from a predefined range and minimizes Eq. 2.7 with each selected value. The weighted central depth z_α of each solution is calculated using Eq. 2.9. Then the central depth is compared with the depth of the estimated fluorophore centroid z_0 by $\|z_\alpha - z_0\|$.

$$z_\alpha = \frac{\sum z_i m_i^\alpha}{\sum m_i^\alpha} \tag{2.9}$$

where m_i^α denotes the reconstructed value at the ith voxel with a regularization parameter of α and z_i denotes the Z coordinate of the ith voxel.

A typical dependency of the centroid deviation $\|z_\alpha - z_0\|_2$ on the regularization parameter α is shown in Fig. 2.14. By taking a threshold δ (e.g. half of the voxel length), a range of α whose solutions are unbiased in depth can be determined. However, if α is too small, the solution will not be sufficiently smoothed, i.e., the fluorophore size will be underestimated (Fig. 2.12(c)). Achieving a balance between the smoothness constraint and the centroid (depth) constraint is necessary. In the proposed reconstruction framework, this centroid constraint is used in the coarse step to retrieve an initial solution. Then, a ROI will be identified on the basis of the

---

[21] Usually, 10–40 points in a logarithmic manner.

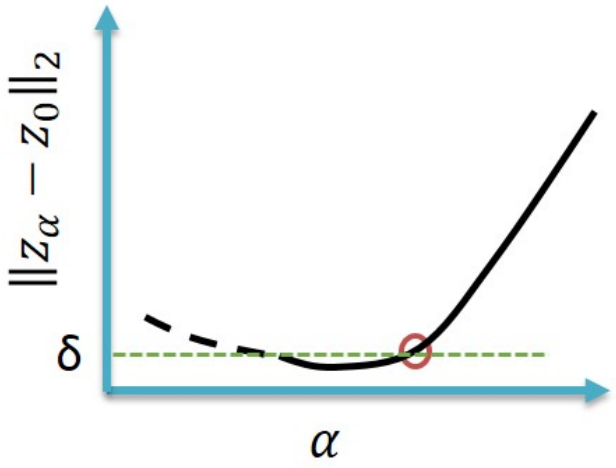

Figure 2.14: Dependency of the Centroid Deviation on the Regularization Parameter: the initial part of the curve is plotted with dash line because for a very small α the solution is unstable. The red circle denotes the regularization parameter of choice

initial solution. The ROI is expected to include the entire volume of the fluorophore. Therefore, an initial solution that is slightly broader than the actual distribution is preferred. selecting the largest value for α in the unbiased range is thus recommended.

Discussion

This is not the first FMT study to include more than one constraint in the objective function. For example, Dutta et al. used a sparsity constraint and a TV constraint simultaneously [32]. They realized it by adding two regularization terms and thus two regularization parameters into the objective function. They realized the use of two constraints by adding two regularization terms and thus two regularization parameters into the objective function. It is evident that this would increase the inverse problem solution complexity; determining a single regularization parameter without prior knowledge is already challenging. Therefore, automatically tuning two regularization parameters would be extremely difficult. In the proposed method, determining the regularization parameter and incorporating a new constraint are realized simply and simultaneously. With the centroid prior, the proposed method improves reconstruction accuracy without increasing computational complexity.

2.5.3 Piecewise Spatially Varying Regularization

Spatially varying regularization in piecewise weighting manner is proposed to improve conventional Tikhonov regularization.

Spatially Varying Regularization

In optical inverse problems, spatially varying regularization (SVR) is widely used to compensate reconstruction results in regions of low detection sensitivity [22] where respective restored values are always underestimated and overly smoothed [27, 107]. For SVR the uniform regularization parameter α is replaced by a spatially varying parameter matrix $\alpha\mathbf{W}$ [118]. As a result, the objective function changes to

$$\|\mathbf{Gm}-\mathbf{d}\|_2^2+\alpha\mathbf{W}\,\|\mathbf{m}\|_2^2 \tag{2.10}$$

Generally, a locally small regularization parameter enhances the restored value and resolution in the corresponding region, whereas a large regularization parameter leads to suppressed local values. For any voxel i, if its regularization parameter αw_i is very small, then even its restored value m_i is relatively large, $\alpha w_i m_i$ (the corresponding element in the regularization term $\alpha\mathbf{W}$) may be not large. Therefore, a solution in which large values appears in the region with smaller regularization parameter will result in a smaller $\alpha\mathbf{W}\,\|\mathbf{m}\|_2^2$ term, i.e., easily selected by the regularization process.

In this thesis, I place small regularization parameters in the region surrounding the estimated centroid. However, larger parameters are placed in the region far from

---

[22] Region distant from sources and detectors.

the centroid to (1) locally enhance the restored values around the centroid and (2) to suppress artifacts that usually appear in boundary regions. Consequently, the solution is forced to converge around the centroid more compactly.

Piecewise Weighting

This SVR method is applied in the fine step. The weight matrix is generated on the basis of the initial solution from the coarse step in a piecewise manner (Fig.2.15(a)). A given initial solution m0 is first normalized by its maximum as $\mathbf{m}' = \mathbf{m_0}/\max(\mathbf{m_0})$. Then, W is determined by the following equations [176]:

$$W = \begin{pmatrix} {}^{1}/_{w_1} & 0 & \cdots & 0 \\ 0 & {}^{1}/_{w_2} & \cdots & 0 \\ \vdots & \vdots & \ddots & \vdots \\ 0 & 0 & \cdots & {}^{1}/_{w_n} \end{pmatrix} \tag{2.11}$$

$$w_i = \begin{cases} \beta, & \text{for } m'_i > \beta \\ m'_i & \text{for } \beta \geq m'_i > \epsilon \\ \epsilon, & \text{for } m'_i \leq \epsilon \end{cases} \tag{2.12}$$

where w_i and m'_i are the weight and normalized initial value, respectively, for the ith voxel. n is the number of voxels, ϵ is a very small positive value to avoid dividing a zero or a very small non-zero value in Eq. 2.11, the weight of a voxel with a value smaller than ϵ is set as ϵ. β is an empirical threshold [176].

Discussion

By this piecewise weighting, the region with larger initial values than $\beta \bullet \max(\mathbf{m_0})$ will be further enhanced in the fine reconstruction, whereas others are suppressed to

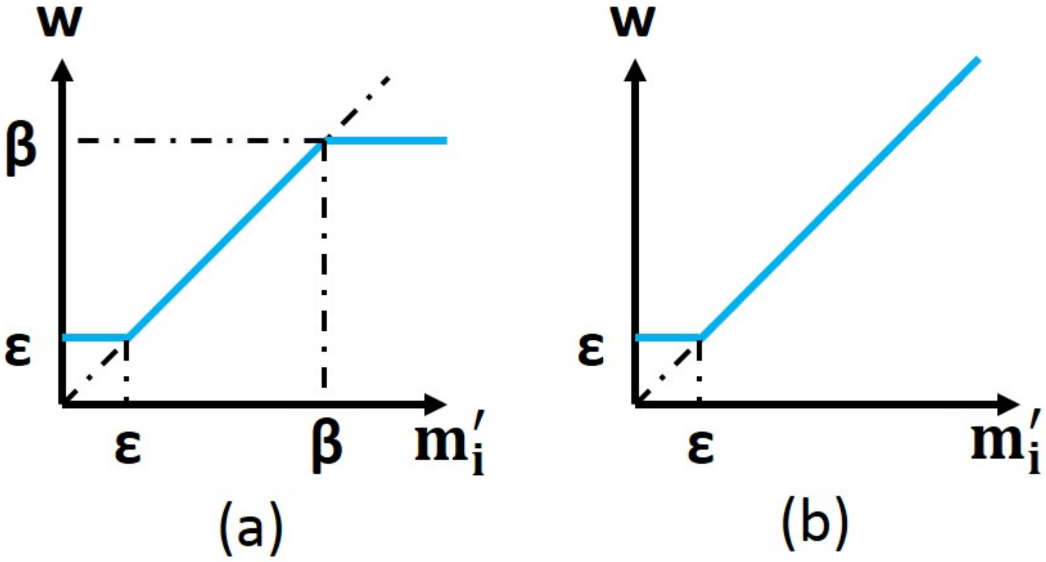

Figure 2.15: Weighting for Spatially Varying Regularization: (a) piecewise manner (b) linear manner. (reprinted from [176] with permission)

slightly compress the estimated fluorophore volume.

In previous research, w_i was set as continuously linear (Fig.2.15(b)) [87] or logarithmic function [6] of m_i'. However, in the enhanced region, the larger initial value a voxel has the smaller the corresponding regularization parameter will be, i.e., the voxel's value will be strengthened to a greater extent. Consequently, the profile of fluorescent distribution may be destroyed and concentration values at several voxels (those with the largest values in the initial solution) may be over exaggerated. For the piecewise manner, voxels inside the ROI share the same regularization parameter; thus, they are enhanced to the same extent. Therefore, the original profile of the fluorophore distribution can be retained [176].

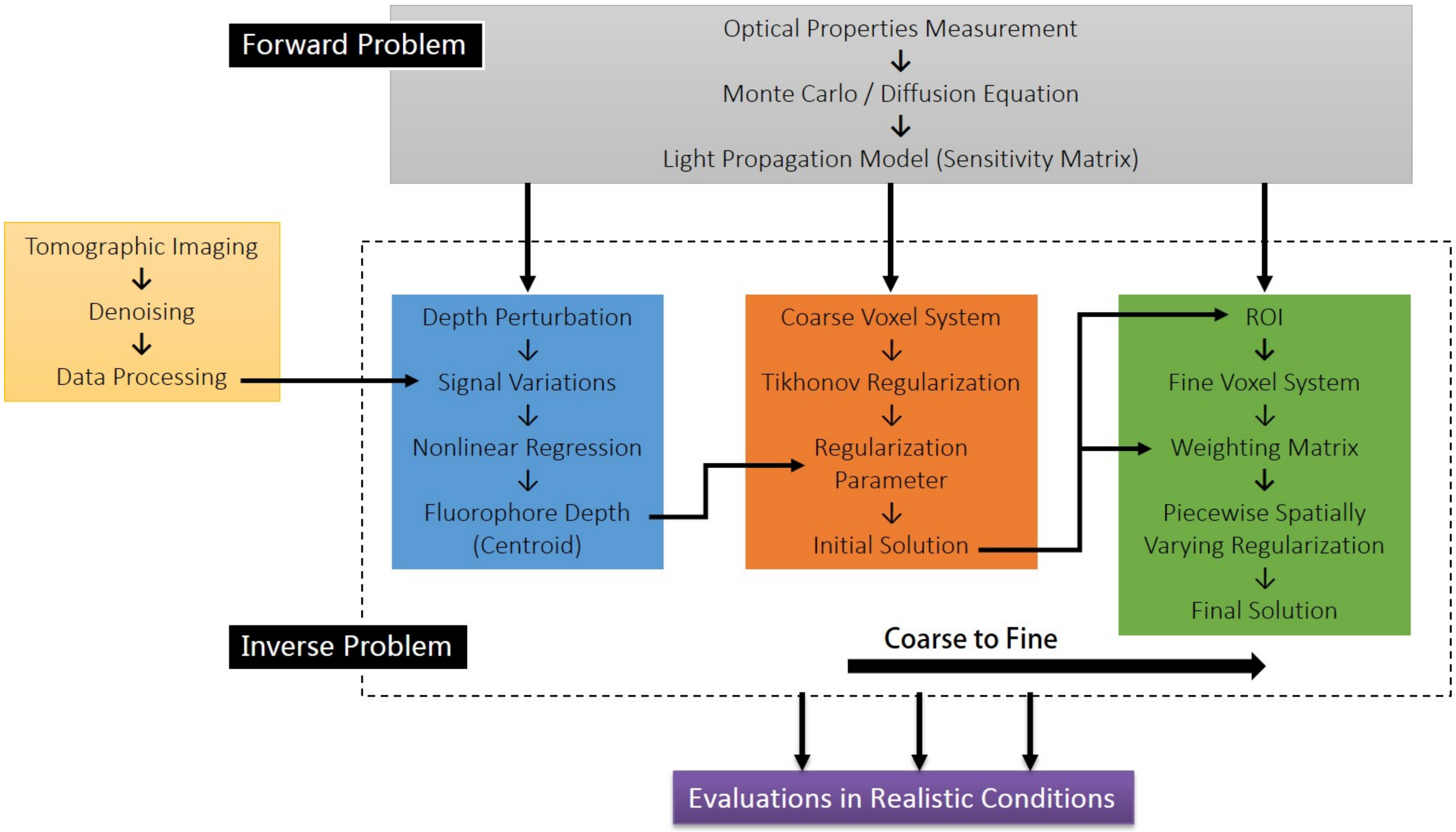

Figure 2.16: Overview of the Proposed Concepts and a framework for the ECW-FMT system: the arrows denote the transfer of information.

2.6 Conclusion

A framework for the ECW-FMT system, including all concepts and methods proposed in this thesis, is described in Fig. 2.16.

For fluorescence imaging, I developed an ECW-FMT system. The system works with reflectance geometry; therefore, it is feasible for large animals and has many clinical applications. Note that particular attention is paid to noise suppression. The system uses a pair of PBSs to reduce excitation leakage, and a NIR excitation light source is used to avoid tissue autofluorescence.

For the forward problem, optical coefficients of the tissue and perturbator are measured in advance. In the in vivo condition, I recommend the oblique-incidence reflectometry technique (see Appx. B), which can easily be combined with the ECW-FMT system. Using the measured optical coefficients and based on the Monte Carlo method or diffusion equation, the sensitivity matrix relating the source-detector positions to the potential fluorophore position are computed.

Relative to the inverse problem, the framework first localizes the fluorophore centroid by the depth perturbation method. In the depth perturbation method, a membrane-like perturbator is superposed as a scattering optical phantom onto the tissue. On the basis of the dependency of the light attenuation rate on propagation depth, depth information (centroid location) for the included fluorophore can be estimated from the variations of the fluorescent measurements that result from perturbation. The central depth information is then used as a new constraint in the later reconstruction of fluorophore bio-distribution.

The reconstruction process is divided into coarse and fine steps. In the coarse step, Tikhonov regularization is used to restore an initial fluorescent distribution over the entire space. In this step, the regularization parameter is determined by prior depth knowledge. The initial fluorescent contributes to the fine step as the basis of ROI determination and weighting matrix generation. The space inside the ROI is then split to finer voxels. The piecewise spatially varying regularization (PSVR) is utilized to solve the inverse problem within the ROI and retrieve a fine and locally smooth solution. Owing to the relatively low number of unknowns involved in each computation, this algorithm is time efficient and ensures fast reconstruction. Moreover, because the final bio-distribution is reconstructed in a ROI centered by the estimated centroid and that estimated centroid has been proved to be close to the true centroid, the reconstructed bio-distribution is thus unbiased from the actual location.

Dividing the framework into two steps also reduces computational costs; the computational cost of a nonlinear inverse problem is considerably more than the cost of a linear inverse problem. In the proposed framework, only centroid location and relative concentration, i.e., no more than four unknowns for one fluorescent object, are estimated by the nonlinear regression. Thus, computation time is minimized. In contrast, the bio-distribution reconstruction involves solving a linear inverse problem. The problem typically involves thousands of unknowns [23]. Fortunately, the linearity reduces computation cost, thereby ensuring acceptable total computation time. If one finds all knowns, including the fluorophore centroid, size, and the spatial distribution, by solving a single nonlinear problem, the process will be highly time consuming.

To summarize, the key points of the proposed methods include the depth perturbation method to roughly localize fluorophore (centroid), and the use of the rough location to constrain the reconstruction of bio-distribution. These two points effectively eliminate the ill-conditioned nature of the optical inverse problem and thus yield more accurate estimates for the location, size, and distribution of fluorophore.

---

[23] Relative concentration values for each voxel in the reconstructed space

3 Epi-Fluorescence Continuous Wave Tomography System

In this chapter, the custom ECW-FMT system is described. The system uses an NIR light source and a pair of PBSs to improve penetration depth and detection sensitivity.

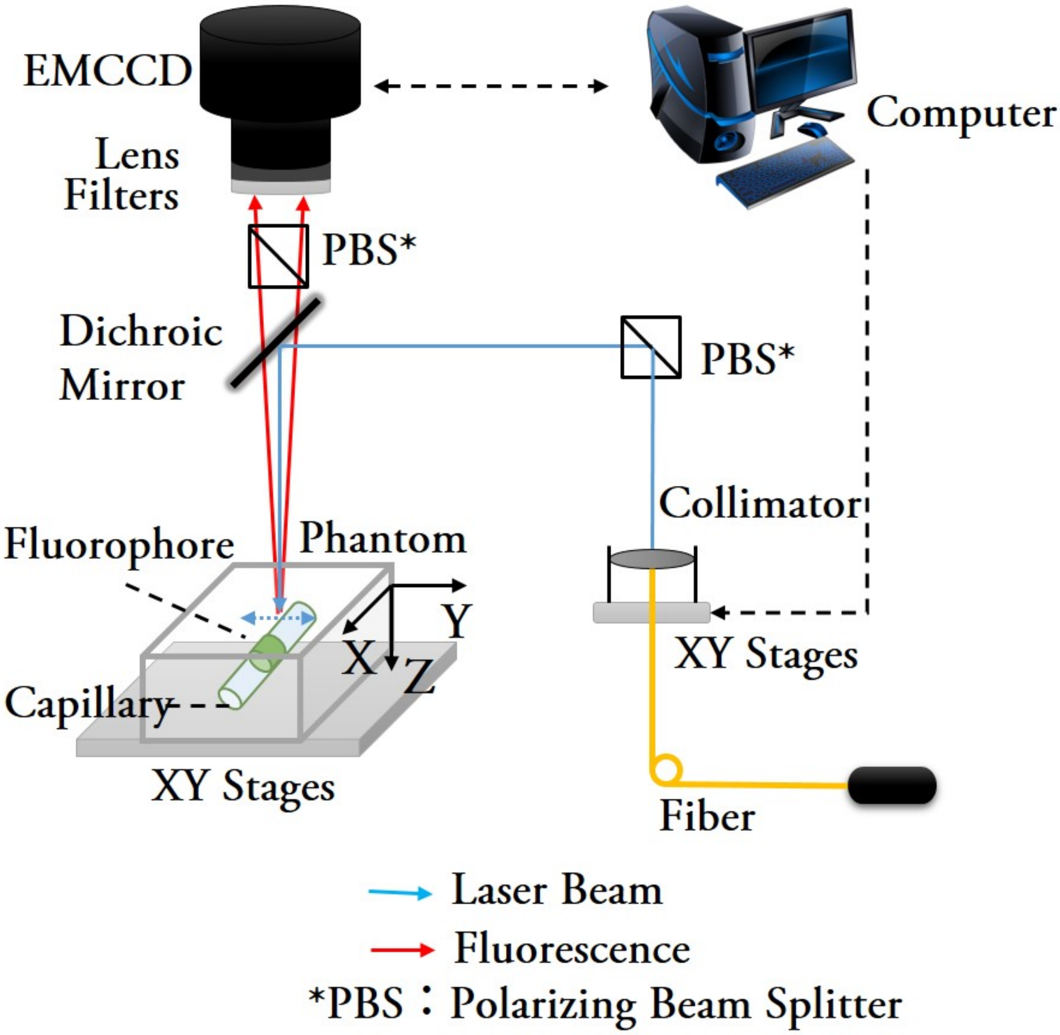

Figure 3.1: Schematic of the Epi-Fluorescence Continuous Wave Tomography System [178]

3.1 Design

As mentioned in Sec. 1.6.1, I selected an epi-illumination geometry for the FMT system, CW domain, raster scan incident mode, and a camera-based entire region detection mode. The basic design of the custom system is shown in Fig. 3.1.

3.1.1 Source

In this system, a laser system with current and temperature control is used as the light source because of its good directionality and stable power. Its wavelength is selected from the NIR region for three reasons: (1) optical absorption of hemoglobin and water is low in this range; (2) tissue scattering is relatively moderate compared to the visible region [151]; (3) autofluorescence in the NIR region rarely exists [79]. The first two points ensure greater penetration depth while the last point results in lower background noise. The laser light is coupled with an optical fiber and collimated to form a light beam. Generally, there are two strategies for a beam scan, a stage-based and galvo mirror-based scan. The latter involves less mechanical motion and a faster scan speed but increases cost and system complexity [1]. The proposed system uses a pair of motorized stages, and the collimate lens is fixed to these stages. When the stages move, the laser beam scans over the sample surface after being reflected by a PBS and a dichroic mirror (DM).

3.1.2 Detector

High sensitivity is the primary requirement for the detector. Here an electron-multiplying CCD (EMCCD) camera is used, whereby one incident photon may result in generation of several thousands of electrons. This is achieved by adding a multiplication register to the end of a normal CCD camera (Fig. 3.2), which includes a large number of gain stages [2]. each incident photon results in generation of electrons by impact ionization in a manner that is similar to an avalanche diode. The use of the EMCCD camera reduces measurement time effectively. With the EMCCD camera, short exposure time can be maintained, and the electron multiplying function can be

---

[1] Such as the necessity for a scan lens [173]

[2] Usually more than 500

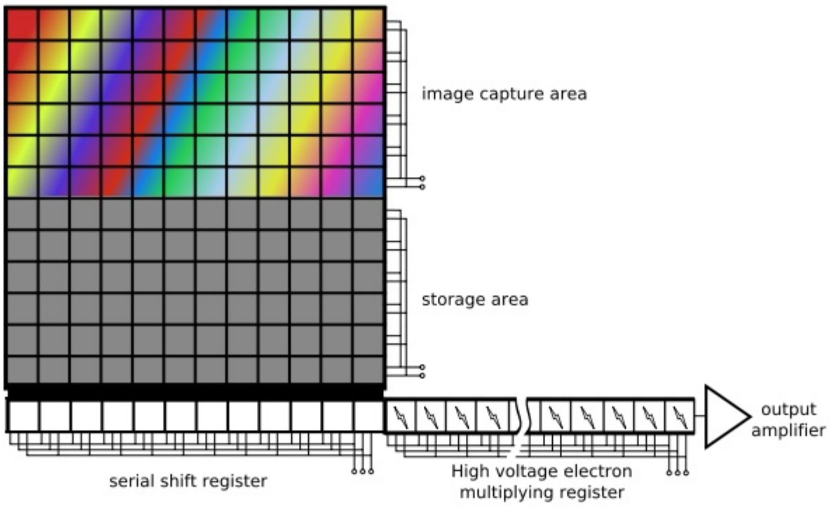

Figure 3.2: Schematic of Electron Multiplying CCD Camera: photons are transformed to photoelectrons in the image area, stored in the storage area, then transferred serially through the gain stages.[64]

used to amplify the signal if necessary.

Similarly, to collect as many photons as possible, a camera lens with low f-number [3] and short work distance is used to achieve a large numerical aperture [4].

3.1.3 Filtering

Excitation light leakage is problematic in any reflectance geometry and laser-based optical system. A part of the laser beam is reflected directly to the detector. Owing to its high and focused power, the reflected laser beam may saturate the detector and thus render the measurements meaningless. Similar to a conventional fluorescent imaging system, the proposed system includes a DM, notch filter, and band pass filter, each of which can theoretically attenuate the excitation light by more than 90%. However, their actual effects are limited. This can be attributed to

---

[3] The ratio of the lens's focal length to the diameter of the entrance pupil[51]

[4] The solid angle over which an optical system can accept or emit light

the optical filter, which is typically designed for light perpendicularly incident to its surface. For obliquely incident light, the effective attenuation is notably lower than the designed value. For the camera-based detection used in this study, incident light from most detection positions is not exactly perpendicular on average (see the optical paths in Fig. 3.1).

In the proposed system, the polarization of excitation light further suppresses the exci-tation leakage. Polarization is a property of electromagnetic waves in which the electric and magnetic fields oscillate simultaneously but in different orientations. Specifically, for a light beam, electric and magnetic field components that oscillate in a direction parallel to each other are referred to as the S-polarized components while the components that oscillate in a direction perpendicular to each other are referred to as the P-polarized components. A PBS can split these two components into two beams (Fig. 3.3). Many optics systems demonstrate polarization dependent properties. For example, the DM used in this system more strongly reflects S-polarized light than P-polarized light. In addition, the reflected laser beam includes two parts, specular reflection[5] and diffuse reflection[6]. Specular reflection never changes the polarization state of light, whereas the polarization state will become ran¬dom after diffuse reflection [51].Since the laser beam is collimated, the specular reflected laser light is also a collimated beam, which results in a very bright point on the captured image and may potentially saturate the CCD imaging sensor. In contrast, diffuse reflection emits in all directions; thus, it contributes to background noise.

A pair of PBSs in the same orientation is added to the system. The first (right in Fig. 3.1) ensures that the incident laser beam is pure S-polarized light. Consequently, the effective reflectance of the DM increases; thus, less of the reflected laser beam

---

[5] Direct reflection on the surface, just like a reflection on a mirror.

[6] Light enters the subject once, is backscattered within the subject, and finally emitted from the surface.

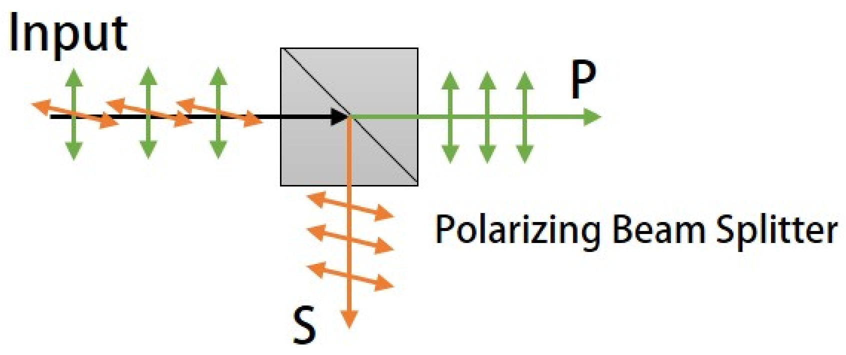

Figure 3.3: Polarizing Beam Splitter: the orange beam denotes the S polarization component and the green beam denotes the P polarization component.

passes through the DM. The second PBS (left in Fig. 3.1) rejects all S-polarized light, which includes the whole specular reflection and one-half of the diffuse reflection [7]. Although the second PBS also obstructs one-half [8] of fluorescence, it is beneficial because the excitation leakage is reduced more greatly and the imaging contrast is enhanced. The remaining diffuse reflection of excitation light can be eliminated by capturing a control image without a fluorophore and subtracting it from the fluorescent images. This process is known as background removal.

3.2 Realization

The setup of the aforementioned design is shown in Fig. 3.4. The specifications of all components used in the setup are given in Tabs. 3.1 and 3.2.

---

[7] Assuming its polarization is completely random, powers of S polarization and that of P polarization are half to half

[8] also assuming the polarization of fluorescence is random

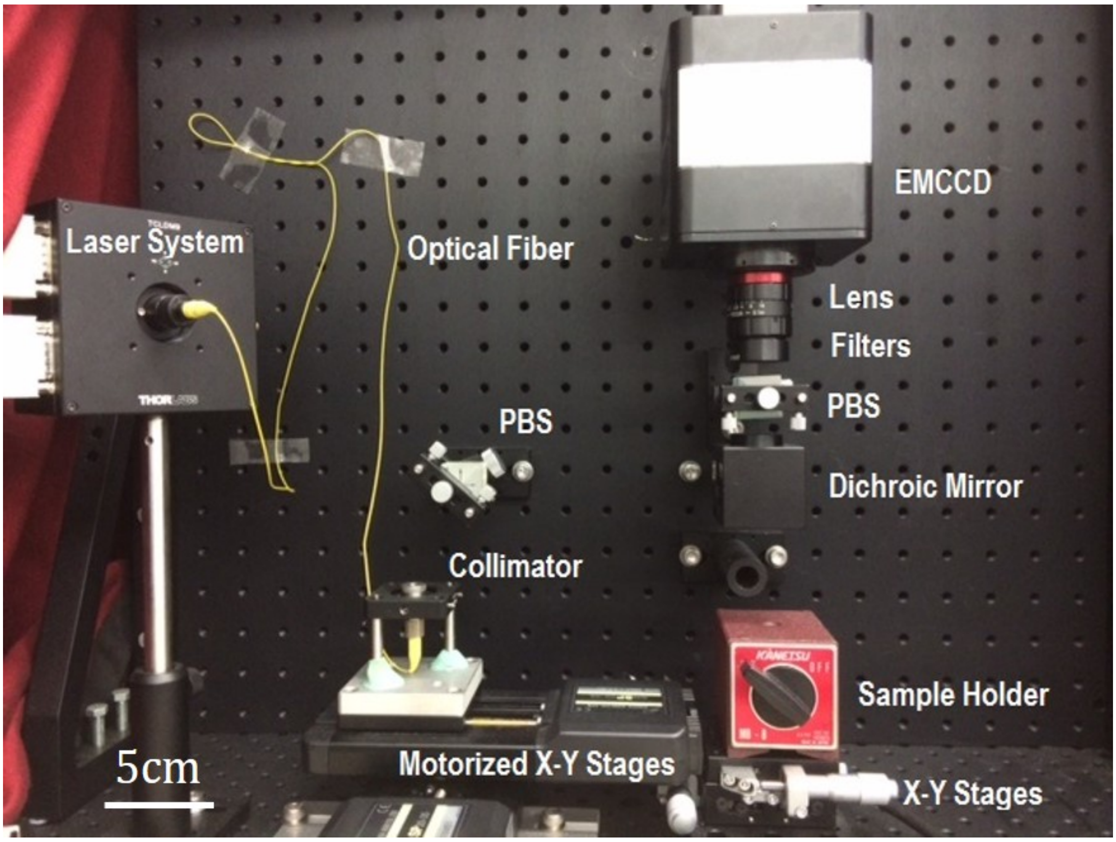

Figure 3.4: Setup of the Epi-Fluorescence Continuous Wave Tomography System: some components, such as the current controller for the laser diode, are not shown.

Table 3.1: Components in the Setup

Component	Producer	Product No.	Specifications
Laser Diode	Thorlabs	LP785-SF20	Fiber-Pigtailed Laser [a] Wavelength: 785 nm Maximal Output Power: 25 mW
Laser Controller Kit (not shown in Figure 3.4)	Thorlabs	LTC100-B	Including: a Laser Mount a Current Controller a Temperature Controller
Optical Fiber	Thorlabs	780HP	Single Mode Fiber Wavelength Range: 780 ~ 970 nm
Collimator	Thorlabs	CFC-2X-B	Adjustable FC/PC collimator Wavelength: 600 ~ 1050 nm Effective Focus Length: 2.0 mm
Motorized Stages	Sigma Koki	SGSP20-35	Stepping Motor Driven Stages Travel Range: 35 mm Maximal Speed: 25 mm/s Resolution: 2 μm
Stages Controller	Sigma Koki	SHOT-602	2-Axis Stages Controller via Serial Communication
Camera	Flovel	ADT-100	Electron Multiplying CCD Imaging Sensor: 2/3 inch Maximal Gain: 1600 Monochrome Resolution: 1000×1000 Bit Number: 10
Lens	Edmund	59-871	Fixed Focal Length Lens Focal Length: 25 mm Aperture: f/1.4 - f/17 Field of View: 19.8° Working Distance: 100 ~
Polarizing Beam Splitters	Thorlabs	PBS102	Broadband PBS Cubes Wavelength Range: 620 - 1000 nm Cube Size: $10\times10\times10$ mm^3 Reflection: > 99.5% Transmission: > 90%

---

[a] a optical fiber has already been coupled to the laser diode

Table 3.2: Components in the Setup (cont.)

Component	Producer	Product No.	Specifications
Notch Filter	Thorlabs	NF785-33	Center Wavelength: 785±2 nm Blocking FWHM[a]: 35 nm Maximal Optical Density [b]: > 6
Band Pass Filter	Semrocks	FF01-832/37-25	Center Wavelength: 832 nm Pass Bandwidth: 37 nm Optical Density: > 10 [c] Transmission : > 93% [d]
Dichroic Mirror	Semrocks	LPD01-785RU-25	edge wavelength: 792.9 nm Longer Pass Reflection(P-pol): > 90% [e] Reflection(S-pol) : > 98% [f]
X-Y Stages	Sigma Koki	TSDS-602	Travel Range: 13 mm Resolution: 2 μm

[a] full width at half maximum
[b] in blocking region
[c] at 785 nm
[d] in passing region
[e] at 785 nm
[f] at 785 nm

3.2.1 Source

In this setup, the light source is a fiber-pigtailed laser diode (LD) of wavelength 785 nm. A single mode fiber has already been coupled to the LD, which greatly facilitates the coupling of laser light into the optical fiber. The 785-nm wavelength is close to the peak absorption spectrum of ICG [174], which is the primary fluorescent dye used in our experiments. The LD current and temperature are monitored and controlled by a controller kit to ensure stable output power. The laser light is collimated to a 460-μm diameter and 10-mW power[9] Gaussian beam.

The motorized X–Y stage can move the collimator in both X and Y directions,

---

[9] Changeable if necessary

allowing the beam to scan over a sample. Their travel ranges are 35 mm. This range is limited to the size of the optics used in this setup (diameter of approximately 25 mm); therefore, the effective scan range is approximately 20×20 mm. The scan can be run at a resolution of 2 μm and a maximal speed of 25 mm/s. Thus, the system can finish one line scan in one direction in less than a second.

3.2.2 Detector

A 10-bit monochrome EMCCD camera functions as the detector. This camera provides an image of size 1000×1000 pixels and a maximum magnification of 1600. A compact fixed focus length lens is equipped in front of the camera. Its angle of view is 19.8°, and the shortest working distance is 100 mm. Consequently, the field of view (FOV) is approximately 25×25 mm^2 at the shortest working distance. The aperture is always set to f/1.4 to collect as much fluorescence as possible. The camera is adjusted and calibrated carefully such that the lens plane is parallel to the top surface of the sample holder. The vertical distance between the camera and the top surface of the sample is approximately 13 cm (depending on the height of sample).

3.2.3 Filtering

Besides the conventional notch filter, band pass filter, and DM, the system includes a pair of PBSs. The first PBS is placed at the laser side to allow the S polarization component of the laser beam to arrive at the DM, which notably decreases the amount of specularly reflected laser beam leaked from the DM. Assuming the specular reflectance of a sample is α, and the reflectance of the DM to a given polarization is β, the specular leakage rate [10] can be expressed as $\alpha\beta(1-\beta)$, as shown in Fig. 3.5. For

---

[10] The ratio of the power of leaked specular reflected light to the initial power when the laser beam first arrives at the DM.

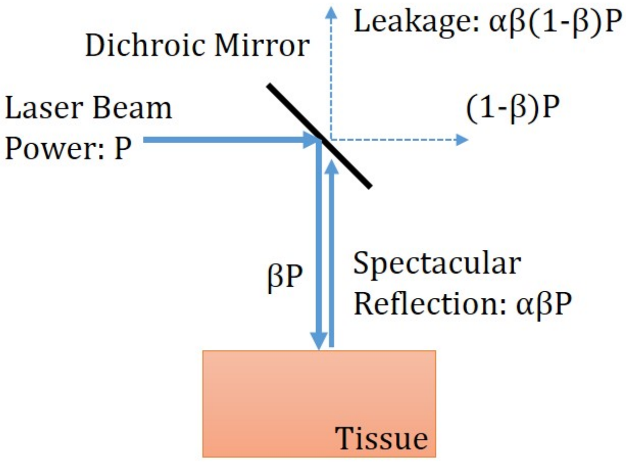

Figure 3.5: Excitation Leakage of Specular Reflected Laser Beam.

the DM used in the setup, the quoted reflectance for P-polarized light is 90% while that for S-polarized is 98%. Consequently, the leakage rate for P-polarized light is 0.09α. In contrast, the leakage rate for S-polarized is 0.02α, i.e., only 22% of the former. Theoretically, the second PBS rejects 99.5% S-polarized light from the camera, i.e., the leakage rate (specular light) after traversing through the second PBS becomes 0.0001α. As mentioned previously, the second PBS also eliminates one-half of the diffusion reflection of the laser light. Thus, the pair of PBSs effectively reduces unexpected light and enhances the contrast in fluorescent images.

3.2.4 Other Components

A test subject is typically placed on the sample holder, below which the X–Y stages allows fine adjustment of the horizontal position of the subject. The image capturing and beam scan are controlled by a personal computer using a camera link and serial communication, respectively.

Finally, as mentioned in Sec. 1.4.2, occasionally a high power laser diode (780 nm, 1W, not shown in Fig.3.4) is used to provide broad illumination over the sample.

An image captured under broad illumination may show the rough planar position of a fluorophore object, which can be used to determine an appropriate initial position and area of the collimated beam scan.

3.3 Results

This section provides an example fluorescent image captured by the proposed system and gives evaluations of the system's performance.

3.3.1 Scattered Fluorescent images

Figure 3.6 (a) shows a typical fluorescent image after being strongly scattered. The fluorescence signals were emitted from a glass tube (diameter: 1.1 mm) filled with the ICG solution. The tube was inserted into an optical phantom (Fig. 3.6(b), reduced scattering coefficient, 0.65 mm^{-1}) made of PDMS (silicon) and TiO2 (optical scatters). Its central depth was approximately 4.0 mm. Along the Y direction the ICG object is as narrow as 1 mm, and the full width at half maximum (FWHM) of the fluorescent signal profile along the Y direction is approximately 9.4 mm. This shows the effect of light scattering and the difficultly in estimating fluorophore size from a fluorescent image on the surface.

3.3.2 Excitation Leakage

Using the same PDMS phantom, the effect of the second PBS was also tested. The laser beam was moved to nearly the center of the FOV. Its power was set to 20 mW, and the exposure time of the camera was set to 60 ms. Images were captured when the left PBS (just below the camera) was removed. As can be seen in Fig. 3.7(a),

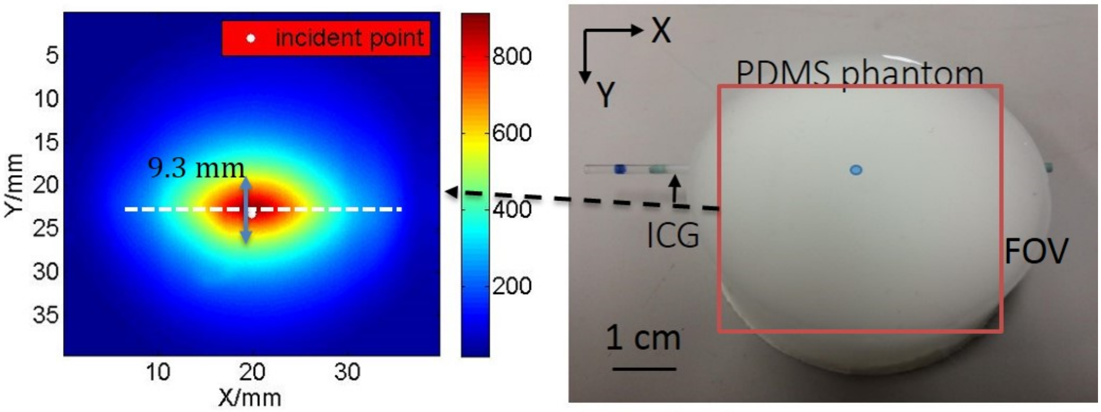

Figure 3.6: Scattered Fluorescent images: (a) image captured on phantom surface (white point = relative incident position, white dash line = center line of included tube); (b) PDMS phantom (blue spot = rough incident position)

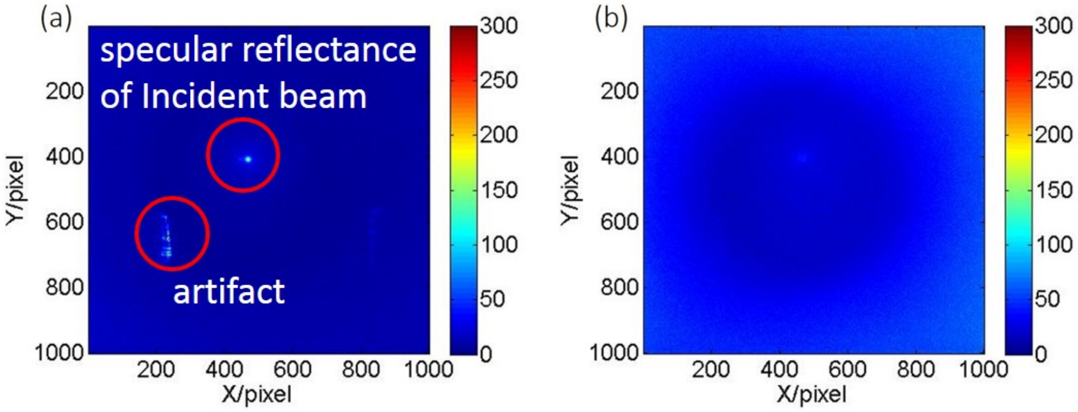

Figure 3.7: Excitation Leak: (a) without the second PBS; (b) with the second PBS

an obvious light spot and some artifacts resulted from the reflected laser light on the image captured without the left PBS. In contrast, on the image captured with the left PBS (Fig. 3.7(b)), the light spot and artifacts are nearly invisible. Quantitatively, the total intensity (brightness) as observed in Fig. 3.7(a) is 3.6×10^7,, whereas that in Fig. 3.7(b) is 8.4×10^6 (23% of the former). The effect of the PBS pair is more notable than the data shown here because the right PBS was retained. Note that the right PBS was not removed because it also functions as a mirror.

3.3.3 Random Noise Level

Typically, there are two types of noise in fluorescent images. One is background noise, including autofluorescence, excitation leakage, and ambient light. Background noise can be removed by subtracting an image obtained with a fluorophore with a control image, which is obtained without targeted fluorophore. The other type of noise is random noise, which is attributable to camera image noise and the random nature of fluorescing [11].

Herein, A series of phantom experiments were performed to obtain the rough SNR range [12] of the ECW-FMT system. A glass tube, including ICG object (concentration, 1μM; length, 1.5 mm; diameter, 1 mm) was submerged into intralipid solution (scattering medium, reduced scattering coefficient at 785 nm: 0.66 mm^{-1}). The central depth of the ICG object was fixed at 2.8 mm, 3.8 mm and 4.8 mm sequentially. For each depth, the laser beam started from a position just above the ICG object, and scanned along the tube in 0.5-mm step. The maximal horizontal distance from the incident positions to the ICG was 3 mm. At each incident position, 10 fluorescent images and 1 control image were captured. Here the SNR at the ith pixel on the fluorescent images is defined as $20log_{10}(A_i/\delta_j)$, where A_i denotes average brightness and δ_j denotes standard deviation. The average SNR of the images [13] captured at each depth and each incident position are shown in Fig. 3.8. The average SNR was 20–35 dB and decreased with the separation of incident position to fluorophore. This is attributable to the fact that the camera exposure time was set to a fixed value for each beam scan. As a result, the signal amplitude, i.e., image brightness, decreased when the incident

---

[11] Absorbing and emitting fluorescent photons by fluorophore are random processes

[12] The SNR may vary with fluorophore concentration, size, depth and other factor. The range obtained here is for a reference

[13] Pixels with weak brightness (e.g., < 10% of camera dynamic range) were excluded because they are usually not used in later calculation such as inverse problem.

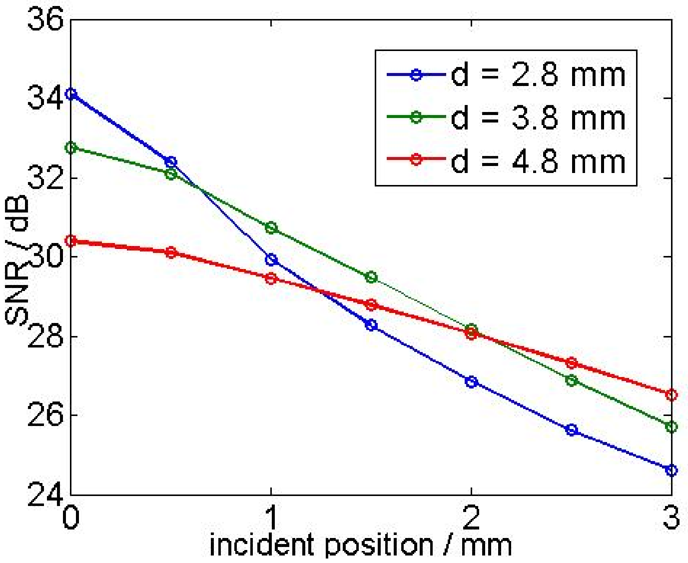

Figure 3.8: Typical Signal to Noise Ratio of the ECW-FMT System

position moved away from the fluorophore object.

3.3.4 Raster Scan Precision

To evaluate the precision of the incident positions produced by the 2D raster scan, a white reflectance standard (reflectance 99% in plate shape) was placed on the sample holder holder and all optics were temporally removed, with the exception of the DM between the sample and the lens. A 10×15 X-Y scan was then performed. The step length was 1 mm. For each incident position, an image of the reflected laser beam was captured (Fig. 3.9(a)). Herein, the centroid of the light spot resulting from the reflected light is defined as the respective incident position. An array of the 10×15 scans and their positions [14] are shown in Fig. 3.9(b). The array looks neat, the standard deviation of the X coordinates of each column is 0.014 mm on average, and that of the Y coordinates of each row is 0.017 mm on average. This demonstrates the excellent scan precision is provided by this stage-based beam scan.

---

[14] After calibration from pixels to physical coordinates

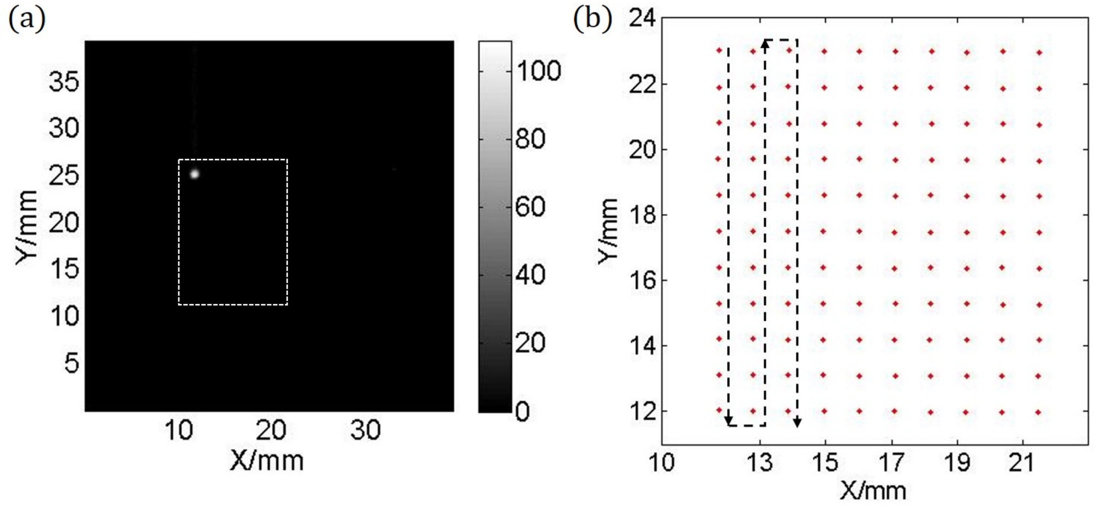

Figure 3.9: Incident Points of 2D Raster Scan: (a) reflected light spot at the initial position of the scan (white dash rectangle denotes scan area); (b) light spot centroids of all incident position (red points) and sequence of the 2D scan (black arrows)

3.4 Discussion

The above results show that this system has particular strengths, including low excitation leakage, good scan precision, and high signal amplification. The SNR is approximately 30 dB, which can be improved by pixel binning or averaging. Cooling the EMCCD camera can also facilitate a better SNR. In addition, this system structure is similar to that employed in fluorescent microscopy; thus, it has the potential to be combined with microscopy and thus can be applied to surgeries conducted under microscopes.

In the custom ECW-FMT system, the camera-sample height (13 cm) appears to be large. However, it is actually nearly the shortest possible for the current system configuration because a lens, two optical filters (5 mm height for each), a PBS (25 mm) and a DM cube box (36 mm) are vertically arranged in this space. With a larger camera-sample height, the numerical aperture of the system (i.e., the light-collecting efficiency) would decrease. However, the light-collecting efficiency of the target fluorescent signals is nearly the same as that of the main background noise (background fluorescence and diffuse reflection of excitation light). Therefore, signals and background noise will decrease to a similar degree with an increasing height, i.e., variation of the target-to-background ratio will be insignificant. Similarly, in the proposed system, the random noise level is nearly a linear function of the mean signal amplitude. The effects of height on the signal amplitude can be canceled by adjusting the exposure time; thus, the random noise level and the SNR are not affected significantly by the height. Note that an intralipid phantom (with a small fluorophore fixed at 2.8 mm depth) was tested sequentially at 13 cm and 20 cm below the camera. The total target fluorescent intensity at 20 cm was decreased by approximately 75% compared to that at 13 cm; however, the variation of the average SNR was approximately 1 dB after exposure at 20 cm was increased threefold. To summarize, the camera-sample height (in a reasonable range, e.g., 10–30 cm) rarely affects the results of the proposed method. However, camera-sample height has notable effect on measurement time [178].

Actually, measurement time may be an issue with the current system. A single run of a 2D beam scan typically requires 10–100 s relative to the exposure time and the number of incident positions. Therefore, the current system is more appropriate for localizing a stable target, such as imaging agents accumulated in a tumor, rather than tracking fast biomedical processes.

Another potential issue of FMT is the power of the incident laser beam. A high-powered incident beam may damage the illuminated tissue, whereas a weak beam will not result in sufficient fluorescence. In the current system, the laser power is controlled by the laser controller kit and can be varied within 0–20 mW. The incident power can be adjusted according to fluorescence intensities. Note that tissue safety was tested preliminarily under this current power range. A block of chicken breast was illuminated by a 20-mW laser beam with the same beam size as the ECW-FMT system. After one minute of illumination, the temperature of the illuminated spot was measured by a thermocouple (Sanwa Inc, Japan), showing a temperature variance of less than 1°C[15]. In contrast, in our experiments, the exposure times for each incident position are typically in the order of 100 ms. Thus, the current incident power range and incident mode will not result in thermal damage to the sample.

---

[15] The precision of the thermocouple is 1°C, and the output of the thermocouple did not actually vary after illumination.

4 Estimating Fluorophore Centroid

In this chapter, the depth perturbation concept is first mathematically extended to 3D space. Then, the method to localize fluorophore (centroid) on the basis of intensity variations resulting from the perturbation is described. Here a fluorophore of finite size is treated as a fluorescent point source located at its centroid. The method has been validated by numerical simulations and experiments using tissue-like[1] homogeneous phantoms.

Note that this chapter has been partly published in the following paper.

- Tuo Zhou, et, al. Localizing Fluorophore (Centroid) inside a Scattering Medium by Depth Perturbation. Journal of Biomedical Optics. 20(1), 017003 (2015).[178] doi:10.1117/1.JBO.20.1.017003

Copyright of related content was transferred to the Society of Photo-Optical Instrumentation Engineers.

---

[1] Whose optical properties are close to those of tissue

4.1 Method

As mentioned in Sec. 2.1.4, the FMT inverse problem is solved by two steps, i.e., localizing the fluorophore centroid and reconstructing the fluorophore distribution with the centroid prior. In this section, the methodology of the first step is described.

4.1.1 Depth Perturbation in 3D Space (Forward Process)

Section 2.3.2 describes the mathematical model of the perturbation behavior under the condition that both the detector $\mathbf{r_d}$ and the excitation source $\mathbf{r_s}$ are just above the fluorophore $\mathbf{r_f}$ (Fig. 2.5). This condition is an extreme case and may be impractical when the horizontal location of the fluorophore is also unknown. For more generality, I generalized Eq. 2.5 from the single depth dimension to any given excitation source point or observation point (Fig. 4.1) in a 3D volume, by replacing

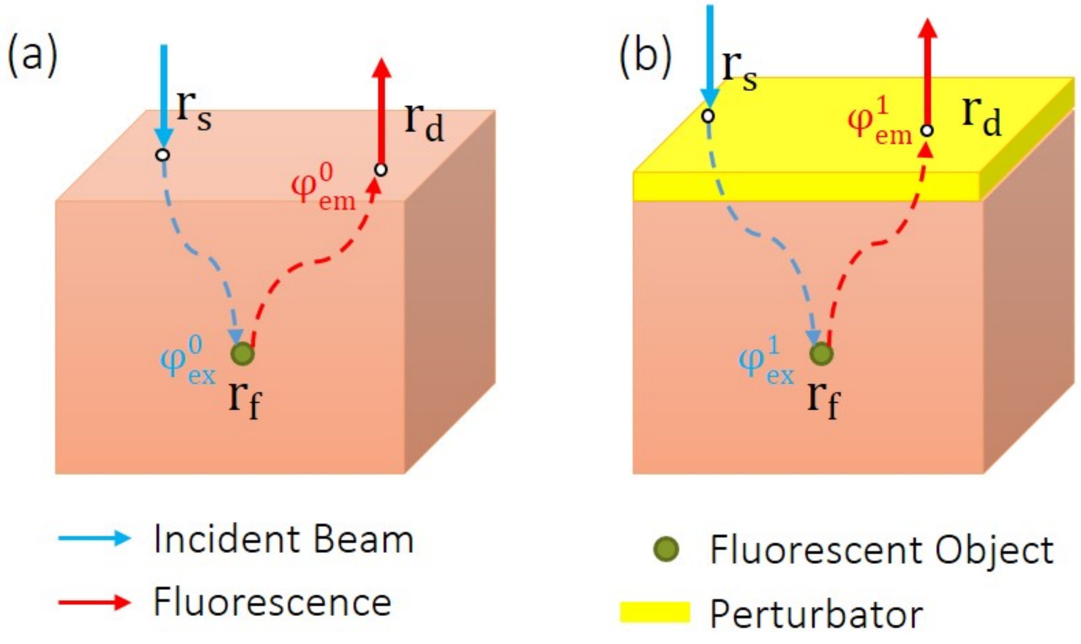

Figure 4.1: Schematic of Depth Perturbation in 3D Space.[178]

$\mathbf{d}'$ with $|\mathbf{r_s} - \mathbf{r_f}|$, and $\mathbf{d}$ with $|\mathbf{r_d} - \mathbf{r_f}|$ as well as some other modifications. Therefore, Γ actually depends on perturbator thickness Δd and the relative positions among detection point $\mathbf{r_d}$, incident point $\mathbf{r_s}$, and fluorophore $\mathbf{r_f}$. Modeling this dependency is referred to the forward process.

In the forward process, a fluorescent object of finite size is approximated as a point source at the object centroid. This approximation is valid because this study focuses on localizing fluorophore of small size.To consider factors such as boundary condition, optical mismatch between the perturbator and medium, and laser beam size, numerical simulations are used to calculate the theoretical fluorescent intensity before perturbation Φ_0 and that after perturbation Φ_1 for any given $\mathbf{r_s}$, $\mathbf{r_d}$, $\mathbf{r_f}$ and Δd. The numerical simulations can be executed on the basis of either the diffusion equation or the Monte Carlo method. Simulation based on the diffusion equation is faster but inaccurate in the region near the air-medium boundary whereas the Monte Carlo method is time-consuming but accurate as mentioned in Sec. 1.4.1.

If there is only one fluorescent object inside the medium, the forward model can be expressed as:

$$\Gamma(\mathbf{r_s}, \mathbf{r_d}, \mathbf{r_f}, \Delta \mathrm{d}) = \frac{\Phi_1(\mathbf{r_s}, \mathbf{r_d}, \mathbf{r_f}, \Delta \mathrm{d})}{\Phi_0(\mathbf{r_s}, \mathbf{r_d}, \mathbf{r_f})} \tag{4.1}$$

If there are multiple objects in the examined region simultaneously, Γ can be calculated as:

$$\Gamma(\mathbf{r_s}, \mathbf{r_d}, \mathbf{m}, \Delta \mathrm{d}) = \frac{\sum_{i=1}^{n} c_i \Phi_1\left(\mathbf{r_s}, \mathbf{r_d}, \mathbf{r}_f^i, \Delta \mathrm{d}\right)}{\sum_{i=1}^{n} c_i \Phi_0\left(\mathbf{r_s}, \mathbf{r_d}, \mathbf{r}_f^i\right)} \tag{4.2}$$

where $\mathbf{m} = (\mathrm{c}_1, \mathbf{r_f^1}, \ldots \mathrm{c_i}, \mathbf{r_f^i} \ldots \mathrm{c_n}, \mathbf{r_f^n})$; $\mathrm{c_i}$ and $\mathbf{r_f^i} = (x_i, y_i, z_i)$ denote the amount of fluorescent molecules and position vector of the ith object, respectively; and n denotes the number of objects inside the medium.

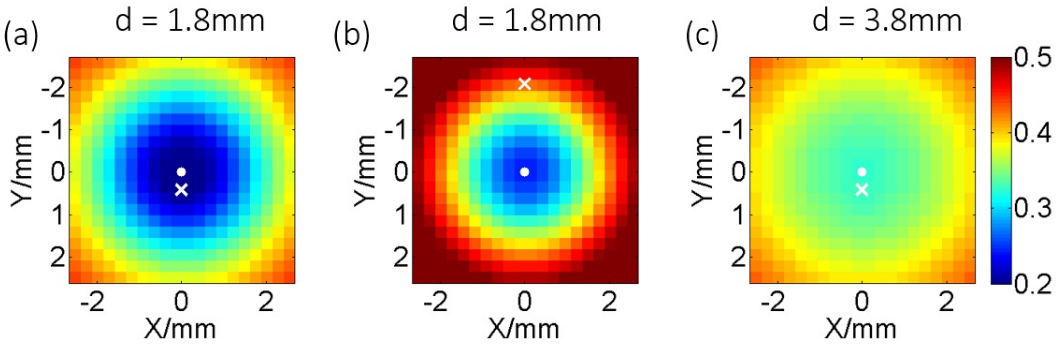

Figure 4.2: Representative Distributions of $\Gamma\left(\mathbf{r_s}, \mathbf{r_d}, \mathbf{m}, \Delta d\right)$: (a)when the laser incident position is horizontally close to a fluorescent point source; (b)when the incident position is moved far from the source; (c) when the point source is more deeply fixed. In each subfigure, the • denotes the horizontal position of a fluorescent point source and its initial depth d is shown in the title. The × denotes the laser incident point. Each pixel in the figures represents an observation point. Optical coefficients and perturbator thickness (1 mm) are same as those of the phantom experiments (described later). The three subfigures share the same color bar. [178]

Representative theoretical distributions of Γ are shown in Fig. 4.2. Note that the ratio increases with increasing distance from the observation point to the fluorophore (Fig. 4.2(a)). Similarly, when the incident point moves away from the fluorophore (Fig. 4.2(b)) or when the fluorophore is located more deeply (Fig. 4.2(c)), the ratios over the image increase notably. All of this can be attributed to the fact that a longer initial optical path length (OPL, the path of incident point → fluorophore → observation point) results in less relative variation of OPL for a given perturbation.

4.1.2 Estimating Fluorophore Centroid (Inverse Process)

In the inverse process, the measured ratio is calculated as

$$\mathbf{R}\left(\mathbf{r_s}, \mathbf{r_d}, \Delta d\right) = \mathbf{I}_1\left(\mathbf{r_s}, \mathbf{r_d}, \Delta d\right) / \mathbf{I}_0\left(\mathbf{r_s}, \mathbf{r_d}\right) \tag{4.3}$$

where $\mathbf{I}_0$ and $\mathbf{I}_1$ are fluorescent images before and after the perturbation respectively. Then, the fluorophore location $\mathbf{r_f}$ and the relative fluorescent amount c can be estimated by fitting the measured intensity ratios **R** to the forward model Γ as follows,

$$\min \left\| \begin{bmatrix} \mathbf{R}(\mathbf{r_s}^1,\mathbf{r_d}^1) \\ \mathbf{R}(\mathbf{r_s}^1,\mathbf{r_d}^2) \\ \vdots \\ \mathbf{R}(\mathbf{r_s}^i,\mathbf{r_d}^j) \\ \vdots \\ \mathbf{R}(\mathbf{r_s}^{N_s},\mathbf{r_d}^{N_d}) \end{bmatrix} - \begin{bmatrix} \Gamma(\mathbf{r_s}^1,\mathbf{r_d}^1,\mathbf{m}) \\ \Gamma(\mathbf{r_s}^1,\mathbf{r_d}^2,\mathbf{m}) \\ \vdots \\ \Gamma(\mathbf{r_s}^i,\mathbf{r_d}^j,\mathbf{m}) \\ \vdots \\ \Gamma(\mathbf{r_s}^{N_s},\mathbf{r_d}^{N_d},\mathbf{m}) \end{bmatrix} \right\|_2 \tag{4.4}$$

,where N_s and N_d are the number of sources and detectors, respectively, and $\mathbf{r_s}^i$ and $\mathbf{r_d}^j$ denote the i'th source position and the j'th observation position respectively. The Levenberg–Marquardt (LM) nonlinear regression method is utilized for the fitting, and a multistart strategy is employed to avoid convergence to a local minimum. In the multistart strategy, a large number of initial solutions are first generated. The LM method is initiated with each of these initial solutions and converges to a group of local minimum solutions. Finally, the most statistically likely solution is selected from the local minimum solutions as the final result. For further details of the LM method and the multistart strategy, see Ref. [5].

4.1.3 Determining Fluorophore Number

For improved generality, I proposed a "try from one" strategy to handle an unknown number of fluorescent objects in the examined region. First, the strategy assumes the number as n, ranging from 1 to N (i.e., N = 5). Second, nonlinear regression is performed. Third, the solution $\mathbf{m_n}$ is substituted back to the theoretical ratio model $\Gamma(\mathbf{m})$ to calculate the relative residuals as follows

$$\mathrm{Res}\,(\mathrm{n}) = \frac{\|\Gamma(\mathbf{m_n}) - \mathbf{R}\|}{\|\mathbf{R}\|} \tag{4.5}$$

When the assumed number n is less than the true value, the residual is large. In contrast, if n is greater than or equal to the true value, it decreases to a relatively lower and stable level. For underestimated n, the parameters used in the regression are too few to achieve good fitting, and for overestimated n, the overestimated object(s) usually appear as a small number of object(s) or those present at a large depth, i.e., they rarely contribute to the fitting result. By detecting the turning point on Res (n), the number of objects can be estimated. The turning point is defined as the first n (from 1 to N) whose residual variation rate

$$\mathrm{rate}\,(\mathrm{n}) = \frac{|\mathrm{Res}\,(\mathrm{n}) - \mathrm{Res}\,(\mathrm{n}+1)|}{\mathrm{Res}\,(\mathrm{n})} \tag{4.6}$$

is less than threshold ϵ. Herein I empirically selected the threshold as $\epsilon = \frac{1.2\sum_{n=1}^{N} rate(n)}{N}$ (i.e., 1.2 times the mean value of rate(n) over n = 1 ~ N). After this "try from one" strategy, other hard limits are set to eliminate some obviously incorrect estimates. For instance, an object at very large depth (> 10 mm) was ignored; two estimated objects located extremely close to each other (distance ≤ 0.1 mm) are counted as one object.

4.2 Numerical Simulations

Numerical simulations were conducted to evaluate the depth sensitivity and fluorophore concentration sensitivity of the proposed method. The effects of the perturbator's optical coefficients and thickness were also investigated.

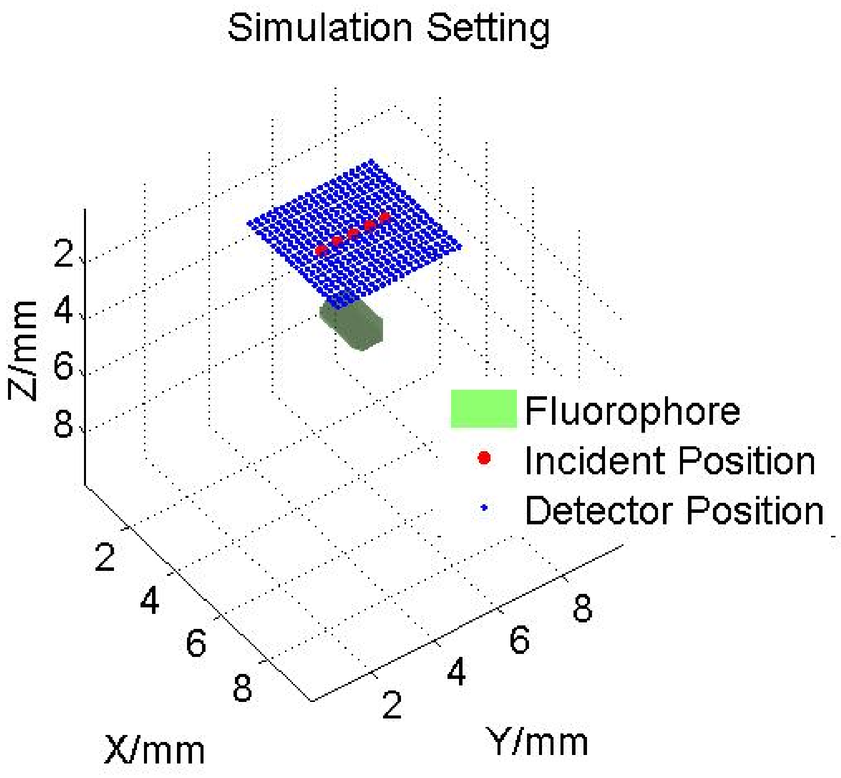

Figure 4.3: Simulation Setting.

4.2.1 Basic Simulation Setting

The simulations were implemented in a 10×10× mm^3 volume. The optical coefficients of the volume were set the same as those of the liquid phantom described in Sec. 4.3. The thickness of the perturbator was defined as 1 mm, and its optical coefficients were 80% of those of the volume. One fluorescent object (length, 1.5 mm; diameter, 1 mm) was set inside the volume. Its horizontal position was fixed at (5, 5) mm. On the top of the volume's surface, I selected a ROI (4×4 mm) just above the fluorophore and defined a 20×20 observation positions (0.2-mm intervals) and five incident positions (0.5-mm intervals), as shown in Fig. 4.3.

For each incident position, two fluorescent images (before and after perturbation) were produced. The simulated fluorescent intensities were generated on the basis of the Monte Carol method. Note that random Gaussian noise was added to the simulated data. The level of random Gaussian noise approximated the noise level of the proposed ECW-FMT system2 [2].

4.2.2 Depth - Concentration Sensitivity

To investigate the algorithm's performance at different depths and noise levels, the fluorophore (central) depth was varied from 1 mm to 9 mm, and its concentration was set to 2μM, and 0.2 μM sequentially [3]. The emission efficiency of fluorophore was calibrated by phantom experiments with the same optical coefficients and fluorophore concentrations. The simulations were repeated five times for each depth-concentration pair.

Figure 4.4 shows the estimated depths and total errors (norm of errors in all directions) from the estimated centroids to the true values. As can be seen, the accuracy of the proposed method (blue points) in resolving depth decreases with increasing depth or decreasing concentration. If a total estimation error of less than 0.5 mm is acceptable, then the maximal feasible depth limit of the proposed method is 7 mm for the 2μM object, 5 mm for the 0.2μM object. I believe that bad SNR is the primary reason for the deterioration of accuracy. The average SNRs (before perturbation) under the conditions of (2μM, 7 mm) and (0.2μM, 5 mm) are 20.3 dB and 16.8 dB, respectively, whereas, those for (2μM, 8 mm) and (0.2μM, 6 mm) are 13.8 dB are 9.3 dB, respectively. This suggests that for the proposed method, the average SNR of fluorescent images should be greater than 16 dB.

In addition, a source-detector separation (SDS) method was tested under the

---

[2] Linear interpolation and extrapolation was used here to determine the specific noise level for each observation position according to certain conditions including fluorophore depth, fluorophore concentration, incident position, exposure time, etc.

[3] The two values fall in the common concentration range used in previous researches of this field

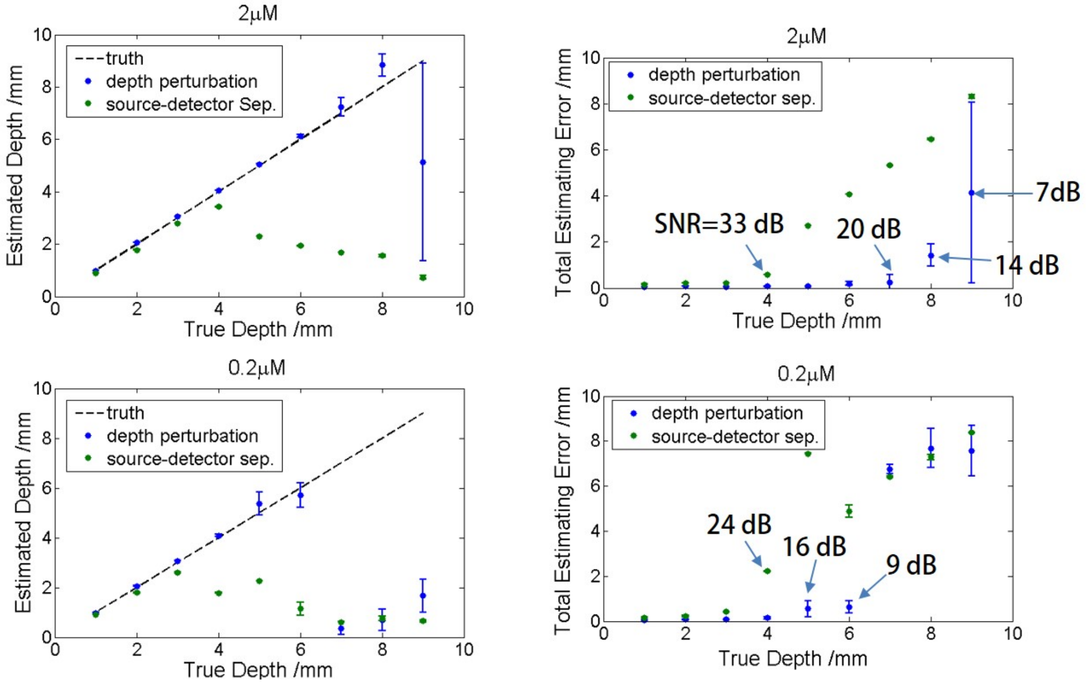

Figure 4.4: Performance of the Proposed Method at Various Depth and Concentration: The left column shows the estimated depths and the right column shows the root square error of the estimated centroids to the true values. The first and second rows show results of 2μM and 0.2 μM, respectively. SNR for a part of the data points are denoted by blue arrows.

same conditions. First, the sensitivity matrix of the source-detector pairs over the reconstructed space was modeled, and the fluorophore bio-distribution was reconstructed with the LSQR algorithm [113]. Finally, weighted center of the reconstructed distribution was seen as the estimated centroid. The green points on Fig. 4.4 show the results. Under most conditions, the errors of the SDS method are significantly larger than the proposed method. As can be seen, the error of the SDS method is obvious at 33 dB. In contrast, the proposed method works well at 20 dB. This proves that the proposed method is less sensitive to noise than the SDS method.

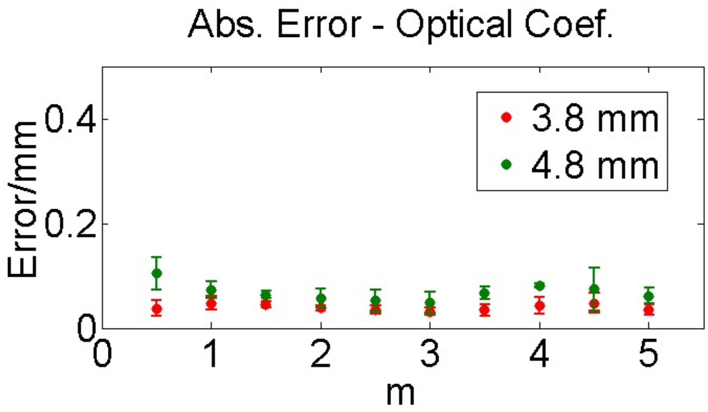

Figure 4.5: Simulation Results about the Effect of the Perturbator's Optical Properties. [178]

4.2.3 Effect of Optical Coefficients of the Perturbator

Here the influence of the perturbator's optical coefficients are evaluated. The scattering and absorption coefficient of the perturbator were changed to m times (from 0.5 to 5) those of the volume. The fluorophore central depths were predefined at 3.8 mm and 4.8 mm, which are two of the central depths used in the liquid phantom experiments (Sec. 4.3).

The results show that the total estimation error did not vary significantly with m in the tested range (Fig.4.5). This suggests that if the optical properties of the perturbator are in the same order as those of the medium, the proposed method will work well.

4.2.4 Effect of Perturbator Thickness

The effects of perturbator thickness on estimation accuracy were also examined with the same simulation settings. In this simulation, perturbator thickness varied from 0.1 mm to 10 mm, whereas the perturbator's optical properties were fixed to

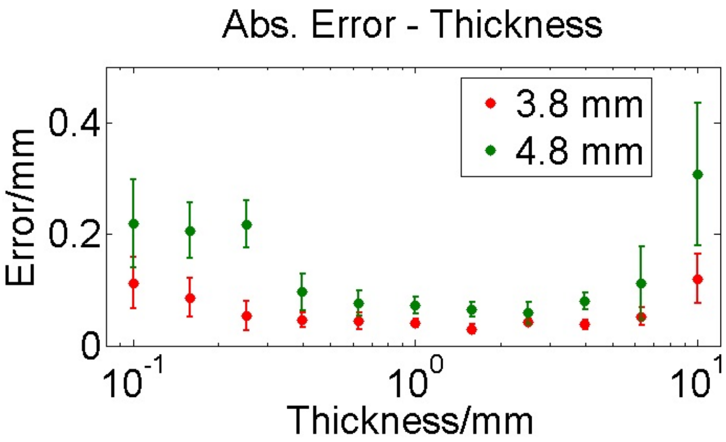

Figure 4.6: Simulation Results about the Effect of the Perturbator's Thickness: note that the X axis is in log scale. [178]

those of the medium.

The results (Fig. 4.6) show that an overly thick perturbator (> 4.0 mm) results in a relatively large estimation error because the fluorescent signals are weakened greatly by the perturbation, resulting in poor SNR. In contrast, a thin perturbator (≤ 0.4 mm) also caused a large error because the intensity variations due to the perturbation were too small to apply the proposed method.

4.3 Experiments with Tissue-like Liquid Phantom

The proposed methods were then tested with the ECW-FMT system described in Chapter 3 and a tissue-like optical phantom.

4.3.1 Tissue-like Liquid Phantom

In the phantom, a mixture of intralipid, ink, and water was used to mimic scattering and absorption properties of biological tissues. Optical coefficients of the mixture are close to those of the brain cortex [151]: reduced scattering coefficient $\mu_s' = 11.7$

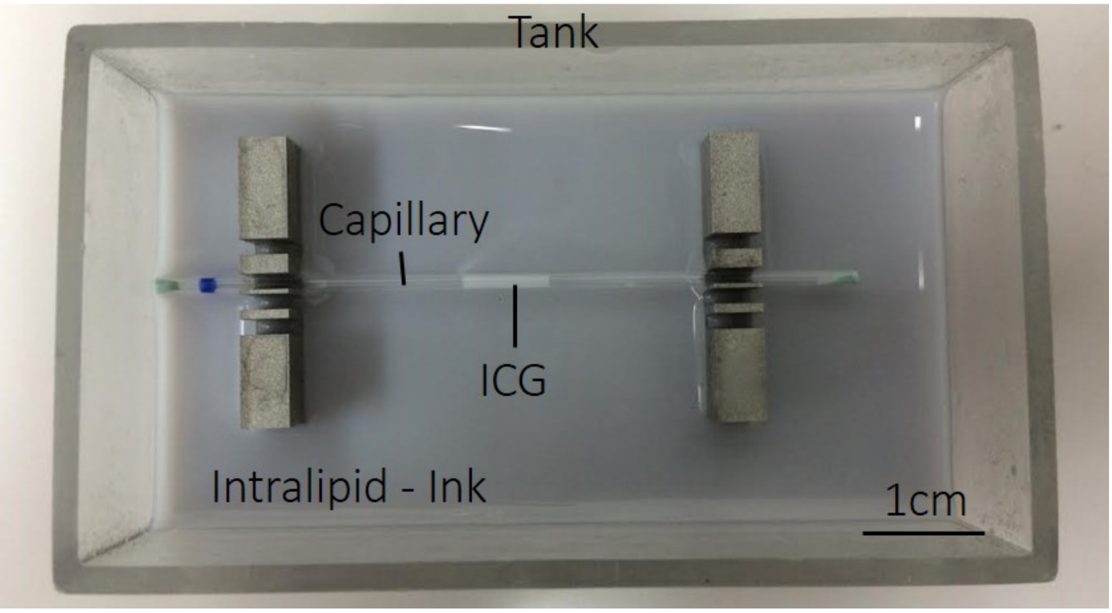

Figure 4.7: Tissue-like Phantom: for a clear view of the ICG object, we did not submerge the capillary into the mixture. The volume of ICG in this figure is also far greater than the actual volume.

cm^{-1}, absorption coefficient μ_a = 0.2 cm^{-1} at excitation wavelength 785 nm; μ_s' =10.5 cm^{-1}, μ_a' = 0.2 cm^{-1} at the emission peak wavelength 830 nm of ICG (the fluorophore used herein, absorption maximum 780 nm, emission maximum 830 nm [174], Keisei, Japan). A small volume (around 1 μL) of ICG solution (2 μM), diluted with the mixture, was injected in a capillary tube (inner diameter: Φ 1.0 mm, outer diameter: Φ 1.6 mm) to make an isolated ICG object. The capillary was then submerged and fixed inside a plastic tank filled by the tissue-like mixture. By arranging the volume of the mixture, the depth of the ICG object could be varied. The tissue-like phantom is shown in Fig. 4.7.

4.3.2 Perturbator

The same mixture with a 1-mm fixed thickness was used as the depth perturbator.Owing to the liquid nature of this phantom, it is difficult to fix a solid perturbator onto a liquid surface. In addition, a liquid perturbator with different optical properties from the initial medium would mix with the medium, thus changing the optical properties of the initial medium.

4.3.3 Parameters Involved in the Inverse Process

FMT computations involve a large number of parameters and factors. Some of them are known or measurable thus can be used directly in the computation. However, others are unknown; thus, they must be estimated by the inverse process. The involved parameters and their states before the inverse process are listed in Tab. 4.1. The central locations are always unknown and must be estimated in the inverse process. For multiple objects, the number of fluorescent objects and their relative concentrations are considered knowns of non-linear regression. Fluorophore size and concentration distribution are treated as a point in the inverse process. Note that these are restored in the reconstruction process described in Chapter 5. In contrast, the laser beam size, numerical aperture (N.A.) of the detector, and the perturbator properties can be measured beforehand. The incident and detection positions depend on the predefined area of the beam scan and the SNR of the captured fluorescent images, respectively. Thus, they are usually determined after fluorescence imaging by some simple calibrations (Sec. 3.3.4). Finally, the optical coefficients of the sample are relatively complex. For this phantom experiment, the phantom optical coefficients were measured beforehand. The optical properties of biological tissue are usually measured immediately after fluorescence imaging to avoid temporal variation. Here the oblique-incidence reflectometry technique, which allows in situ and in vivo optical coefficients, was used. These measured and calibrated parameters are treated as knowns in the inverse process.

Table 4.1: Parameters Involved in the Inverse Process

Status	Parameter	Remark
Unknown	central coordinates	$\mathbf{r_f} = (x, y, z)$
	fluorophore concentration	multiple fluo. objects
	No. of fluorescent object	multiple fluo. objects
	inclusion size	treated as a point
	concentration distribution	treated as a point
Prior Knowledge	incident beam size	
	detector N.A.	
	optical coefficients of perturbator	μ_s', μ_a, n
	thickness of perturbator	Δd
	optical coefficients of phantom	μ_s', μ_a, n
Calibration	incident position	$\mathbf{r_s}$
	detecting position	$\mathbf{r_d}$
Measurable	optical coefficients of tissue	μ_s', μ_a, n

4.3.4 Validation on Depth Determination

First, the hypothesis that depth perturbation can provide depth information (Sec. 2.3.2) was tested [177].

Measurement Setting

In this experiment, the laser beam was translated to a position just above the ICG object, whose length was approximately 1.5 mm. Experiments were conducted at five fluorophore depths, from 1.8 mm to 5.8 mm at 1-mm intervals. The steps of the experiment are as follows:

1. pour the mixture into the tank until the fluorophore depth reaches the predefined value
2. obtain a fluorescent image with the ECW-FMT system

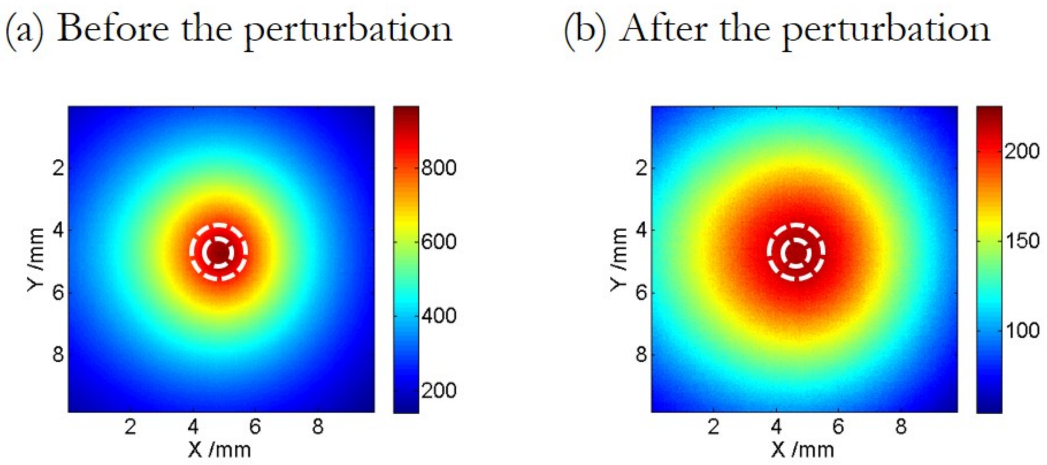

Figure 4.8: Typical Fluorescent Images (a) Before and (b) After the Perturbation: The fluorophore depth is 3.8 mm; The white dash lines denote annular ROI.[177]

3. pour into a given volume (3.9 mL) of the mixture again to increase fluorophore depth by 1 mm;

4. take an image again.

5. Experiment was repeated nine times for each depth.

Data Processing

Figure 4.8 shows typical fluorescent images before and after the perturbation with the ICG object set at a depth of 3.8 mm and approximately centered in the images. As can be seen, the fluorescent profile after perturbation (Fig. 4.8(b)) is weaker and broader than that before perturbation ((Fig. 4.8(a))) owing to additional scattering of the perturbator. A ROI surrounding the laser incident point was then selected. The center of this ROI was set as the incident point, and its inner and outer diameters were approximately 1 mm in the object plane and 2 mm, respectively. The central region was not used because the reflected laser beam is occasionally notably overlaid in this

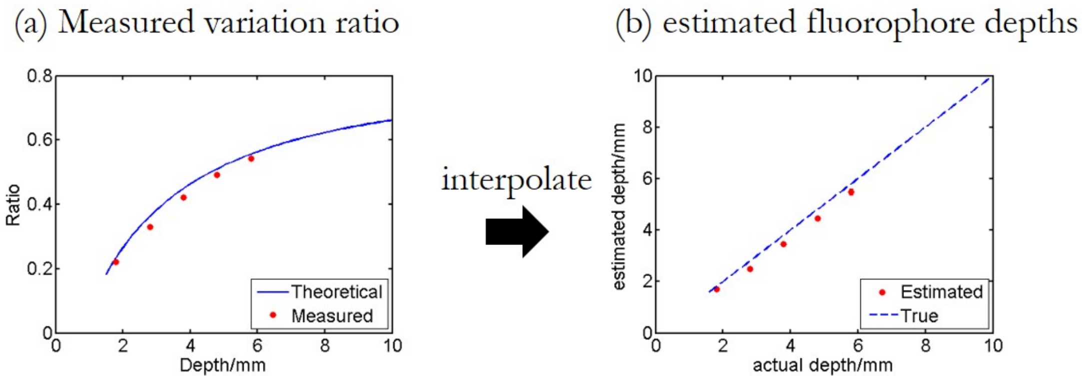

Figure 4.9: Measured Variation Ratio and Resolved Fluorophore Depths:(a) Measured variation ratio due to the perturbation and their theoretical values, (b) estimated fluorophore depths.[177]

region [4]. For each image, fluorescence intensities (image brightness) were summed over the annular ROI, and the ratio of the total intensity after perturbation to the initial intensity was determined.

Results

The average ratio for each depth is shown in Fig.4.9. As can be seen, the ratio increases with the depth of the fluorophore. Note that theoretical variation ratios at depths of 1.5–10 mm were calculated to generate the theoretical curve shown in Fig.4.9(a). Furthermore, fluorophore depth can be estimated by interpolating the measured values to the theoretical curve. As shown in Fig.4.9(b), the estimated fluorophore depths well match the true values. The most significant deviation occurs at the fourth point, where the estimated value is 4.44 ± 0.04 mm and the true value is 4.8 mm.

---

[4] The parallel polarization technique was not applied in the ECW-FMT system during this experiment

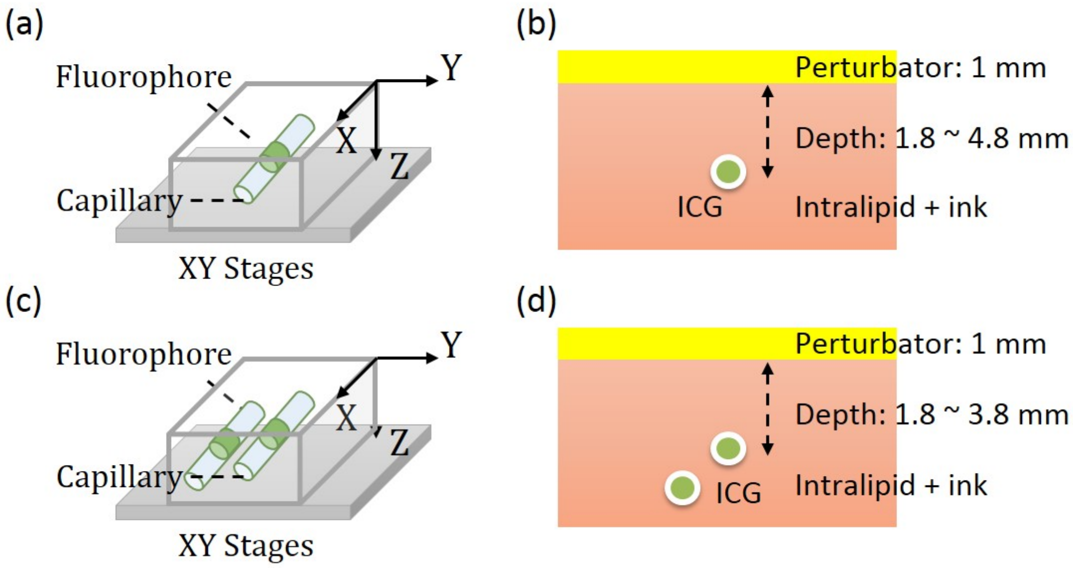

Figure 4.10: Schematic of the Homogeneous Phantom: (a) one tube was fixed in the tank; (b) the Y-Z cross-section of (a); (c) two tubes were fixed in the tank at different depths; (d) the Y-Z cross-section of (c). [178]

4.3.5 Validation on Fluorescent Object Localization

The proposed method was then evaluated in a more general manner (in 3D space) with the “try from one” strategy with two groups of phantom experiments. In the first group, a single ICG object (filled in a capillary tube) was fixed in the tank (Fig. 4.10(a,b)). The initial central depth of the tube was changed from 1.8 mm to 4.8 mm in 1-mm interval. The ICG probe had a length of 1.5 mm and a concentration of 1 μM. In the second group, two tubes were immersed into the phantom. The ICG concentration in tube T1 was fixed at 1 μM, whereas that of T2 was 2 μM, 1 μM sequentially. Thus, the ratio of fluorophore amount c_{T2}/c_{T1} was 2 and 1, respectively. The ICG sizes in the two tubes were as the same as that in the first group. The initial depth of T1 varied from 1.8 mm to 3.8 mm, whereas T2 was vertically 1 mm deeper than T1. The horizontal separation (edge-to-edge) between T1 and T2 was 1 mm(Fig. 4.10(c-d)).

Ground Truth

To obtain a ground truth of the fluorophore location, all optics between the camera and phantom were removed temporally (fluorophore only, no mixture), and an image of the fixed fluorophore was obtained. From the image, the X–Y coordinates of the fluorophore centroid could be determined with a precision of 0.03 mm. In addition, a height gauge (precision, 0.01 mm; Mitutoyo, Japan) with a pin was used to measure the absolute heights of the surface and the tube to calculate the tube's depth from the surface.

Measurement Setting

The steps of these two groups of experiments were the same as described in 4.3.4. However, in these experiments the laser beam was translated in the Y direction with a 0.5-mm spacing and 4.5-mm travel range to produce 10 × 1 incident points. Fluorescent imaging was performed for each incident point. On one captured fluorescent image, a sampling of 20 × 20 virtual detectors over a 5.3 × 5.3 mm^2 FOV was assumed. Each detector used 8 × 8 camera pixel binning [5] to reduce random noise and computational cost. The top left of the image and the initial height of the medium surface were set as the X–Y and Z origins of the coordinates, respectively.

Representative Fluorescent Images

Figure4.11 shows a pair of fluorescent measurements after pixel binning where a fluorescent object was set at 3.8 mm depth and approximately centered in the FOV. Their intensity ratio map (Fig.4.11(c)) shows a similar distribution as the theoretical models (Fig. 4.2).

---

[5] Pixels values are averaged.

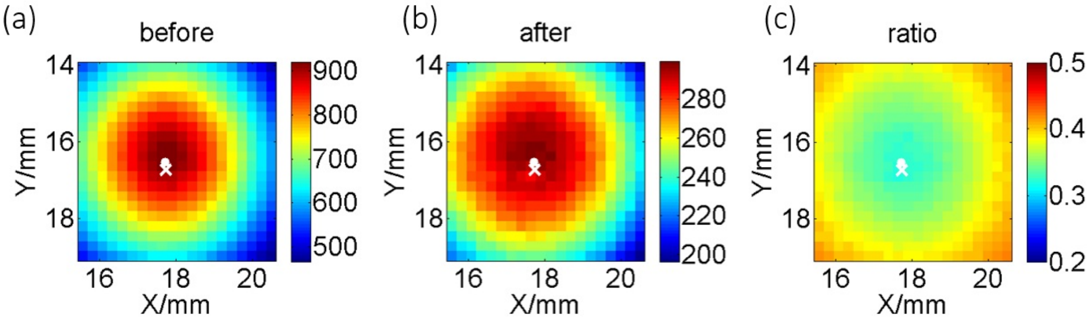

Figure 4.11: Typical Fluorescent Images After Pixel Binning: (a) before and (b) after the perturbation; (c) intensity ratio of (b) to (a). The • denotes horizontal position of the fluorescent point source and the × denotes the laser incident point. [178]

Number of Fluorescent Object

In the inverse process, the object number n was estimated first. Figure. 4.12 shows the normalized residuals (Res(n)/Res(1), i.e., normalized by the respective value at $n = 1$) of the experiments. The residuals among the single object configuration experiments are almost invariant when n was assumed to be 1–5 (Fig. 4.12(a)), whereas among the double objects configuration experiments (Fig. 4.12(b,c)), the residuals at $n = 1$ were significantly larger than those at $n \geq 2$ ($p < 0.01$). Using the aforementioned strategy and limits, the number of objects was identified correctly in all experiments. The solutions of the nonlinear regression corresponding to the determined fluorophore number were selected as the final results.

Results of the Single Object Group

Table 4.2 shows the performance of the proposed methods under the single object configuration. The localization error Δ_{tot} is defined as the Euclidean distance from the estimated centroid to the actual centroid. Δ_Z and Δ_Y are the error's vertical and horizontal component, respectively. For depths of 1.8 – 4.8 mm, Δ_{tot} of the proposed method is in the range of 0.20 – 0.30 mm (on average). A previous method [12, 11]

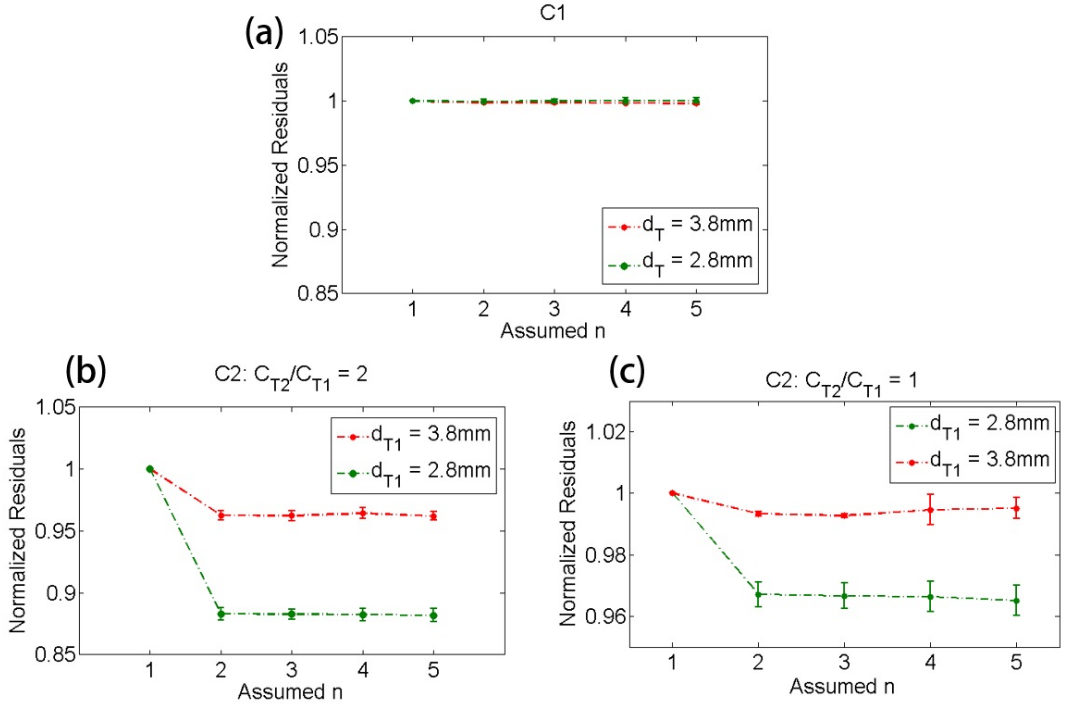

Figure 4.12: Relative residual used in the "Try From One" strategy: normalized relative residual (a) in the single object configuration (tube depth = 2.8, 3.8 mm); (b) in the double objects configuration ($c_{T2}/c_{T1} = 2$, T1 depth = 2.8, 3.8 mm); (c) in the double objects configuration ($c_{T2}/c_{T1} = 1$, T1 depth = 2.8, 3.8 mm). The Y axis scale of (c) is smaller than that of (a) and (b). Other data are not included because most overlap the shown data and deteriorate clarity. [178]

based on the SDS concept using the same data sets, whose algorithm was described in Sec. 4.2.2, was examined for comparison. For this SDS based method, Δ_Z increases rapidly with fluorophore depth and was significantly greater than that obtained in the proposed method ($p < 0.01$), whereas the Δ_{XY} values of the two methods are similar [6] As a result, the total localization errors of the SDS method are also significantly greater than the proposed method ($p < 0.01$). This is attributable to the severe ill-condition of the sensitivity matrix whose condition number is in an order of 10^{18}. These results suggest that the proposed method has better accuracy in resolving depth and localizing the fluorophore centroid.

Table 4.2: Results of the Single Object Group (all units in mm).[178]

	on Depth Perturbation			on Source-Detector Sep.		
Depth	Δ_{tot}	Δ_Z	Δ_{XY}	Δ_{tot}	Δ_Z	Δ_{XY}
1.80	**0.22±0.07**	0.20±0.06	0.09±0.04	**0.27±0.03**	0.26±0.02	0.05±0.02
2.80	**0.18±0.02**	0.09±0.01	0.16±0.06	**0.53±0.01**	0.52±0.01	0.07±0.01
3.80	**0.28±0.06**	0.22±0.04	0.16±0.08	**0.71±0.02**	0.70±0.01	0.08±0.01
4.80	**0.28±0.04**	0.24±0.05	0.12±0.06	**1.03±0.01**	1.02±0.01	0.11±0.01

Result of the Double Objects Group

In double objects group experiment, the localization estimation errors for T1 Δ_{tot1} and T2 Δ_{tot2} are listed in Tab. 4.3 (the vertical and horizontal components are omitted for brevity). The averages are around 0.3 mm and increase slightly with depth. On the other hand, the percentage error of restored fluorophore amount ratio to the

---

[6] Although the averages of Δ_{XY} of the SDS method are lower, statistically the Δ_{XY} values of the SDS method are not significantly less than those of the proposed method ($p > 0.01$).

actual is defined as

$$\Delta_c = 100\% * \frac{|(c_{T2}/c_{T1})_{est} - (c_{T2}/c_{T1})_{true}|}{(c_{T2}/c_{T1})_{true}}, \tag{4.7}$$

where $(c_{T2}/c_{T1})_{est}$ and $(c_{T2}/c_{T1})_{true}$ denotes the restored and true amount ratios respectively. As listed in Tab. 4.3, the percentage errors of Δ_c are less than 20% (on average) for all tested cases.

Table 4.3: Results of the Double Objects Group.[178]

	$c_{T2}/c_{T1} = 2$			$c_{T2}/c_{T1} = 1$		
Depth (mm)	Δ_{tot1} (mm)	Δ_{tot2} (mm)	Δ_c (%)	Δ_{tot1} (mm)	Δ_{tot2} (mm)	Δ_c (%)
1.8 mm	0.20±0.02	0.18±0.02	9±7%	0.18±0.02	0.19±0.02	7±6%
2.8 mm	0.20±0.04	0.21±0.04	18±12%	0.20±0.03	0.24±0.06	16±12%
3.8 mm	0.23±0.06	0.27±0.08	18±11%	0.24±0.05	0.32±0.09	13±9%

Sub-Conclusion

The results of these two group of experiments verified the proposed method and strategy. The estimation errors are around 0.3 mm which may a result of the measurement errors, the effects of the glass wall of the capillary tube, etc. As proof-of-concept experiments, the same liquid mixture was used to mimic the medium and the perturbator. However, in practice, it is difficult to ensure that the tissue and perturbator share the same properties. Further validations implemented on solid optical phantoms (Fig. 3.6(a)) and biological tissue using a solid perturbator (Fig. 2.9) are described in Chapter 5 and 6, respectively.

4.4 Discussion

This chapter has verified the depth perturbation concept and extended its application to the localization of fluorophore (centroid) inside a scattering medium. Compared with the commonly used SDS method, the proposed method is more accurate in resolving depth (Tab. 4.2). Note that a comparison with the multi-spectral imaging method is not provided, partly because the phantom used does not show obvious optical attenuation variation over 800–850 nm (the main wavelength range of ICG emission). It is considered that the multi-spectral method is primarily feasible in hemoglobin-rich tissues and over the wavelength range of 500–700 nm where optical absorption of hemoglobin varies drastically [130]. The proposed method uses an integrated wavelength and is thus available at any wavelength.

A "try from one" strategy was employed to identify the number of fluorophore to enable the potential of localizing multiple fluorescent objects. The results imply that the strategy can achieve a 1-mm spatial resolution up to 3.8 mm depth. However, this strategy has two limitations. Neighboring is that neighboring objects may affect each other: an object of lower sensitivity or of smaller amount may be missed owing to the effect of a notably neighboring object of higher sensitivity or larger amount. The other limitation is that the deeper the two objects of a given separation are fixed the smaller are their relative distance to the depths. Owing to the high scattering nature of tissue, the pattern of fluorescent images of the two objects appear as those of a single object when seen from the surface. As a result, variation of the residual signal becomes smoother, as shown in Fig. 4.12. A smooth variation is vulnerable to measurement noise or estimation error. Therefore, the strategy may fail to detect the turning point correctly. In other words, the spatial resolution achieved by the "try from one" strategy potentially decreases with the depth, which is a common issue of

FMT. These two limitations suggest that the "try from one" strategy must be further improved. This is the reason some hard limits have been set after the "try from one" strategy.

Another potential issue with the proposed method is that additional time is required to collect data after the perturbation. Therefore, the use of broad illu¬mination or a coarse 2D beam scan is recommended to obtain a rough fluorophore location before applying the tomography technique and perturbation. The use of an EMCCD camera is also effective in reducing measurement time. With an EMCCD camera, short exposure time can be maintained, and its electron multiplying function can amplify the signal if necessary. In our exper¬iments, the exposure time per image is less than 200 ms. Consequently, one measurement, including two 10×10 raster scans (one for the initial state and one for after the perturbation), can be completed in one minute (including time for mechanical movement of the stages). Note that this time can be further reduced for a single object case. One image, including several hundreds of virtual detectors, is theoretically sufficient to retrieve fluorophore location because the number of unknown coordinates is only three. However, for more than one object, additional data are required to identify the number of fluorophores. Optimizing the quantity and position of incident points is planned for future work.

As a conclusion, this chapter has proposed a depth perturbation concept to resolve depth information of the FMT technique, and its excellent ability to localize fluorophors and potential to handle multiple fluorescent objects has been demonstrated.

5 Restoring Fluorophore Distribution

This chapter provides technical details about the proposed framework to restore the fluorophore distribution. The performance and feasibility of the proposed methods are evaluated by a series of numerical simulations and phantom experiments.

5.1 Technical Details in Reconstruction

The principles and concepts of the reconstruction process have already been discussed in Sec. 2.4 and 2.5. Herein, some technical details are provided for better understanding.

5.1.1 Coarse Step

In this chapter, if not specifically indicated, the volume involved in reconstructing fluorophore bio-distribution is always approximately $5\times5\times5$ mm^3. In the coarse step, a relatively large voxel size, $0.5\times0.5\times0.5$ mm^3, is used. This means the voxel number N (i.e., unknown number) in this step is 1000. The number of fluorescent data M, which is a product of incident point number N_i and virtual detector number N_d, is always set close to the unknown number.

The objective function used in this step is standard Tikhonov regularization plus with a non-negative constraint, which is expressed as

$$\min[\|\mathbf{Gm}-\mathbf{d}\|_2^2+\alpha\,\|\mathbf{m}\|_2^2] \qquad \text{s.t.} \quad \mathbf{m}\geq 0 \tag{5.1}$$

The non-negative constraint s.t.[1] $\mathbf{m}\geq 0$ is added because a negative concentration is physically impossible. This optimization problem is equivalent to a nonnegative ordinary least squares problem when Eq.5.1 is transformed as

$$\min\left\|\begin{bmatrix}\mathbf{G}\\ \sqrt{\alpha}\mathbf{I}\end{bmatrix}\mathbf{m}-\begin{bmatrix}\mathbf{d}\\ \mathbf{0}\end{bmatrix}\right\|_2^2 \qquad \text{s.t.} \quad \mathbf{m}\geq 0 \tag{5.2}$$

where $\mathbf{I}$ is an $N\times N$ identity matrix. Note that a block principal pivoting algorithm is

---

[1] subject to

used to solve this nonnegative least squares problem. For details about the algorithm, see Ref. [119]. Sample code for this algorithm (in MATLAB) can be freely downloaded from the following link:

www.mathworks.co.jp/matlabcentral/fileexchange/8157-nnls/content/blocknnls.m

5.1.2 Region of Interest

Here to simplify the division of space, a cubic ROI is selected. The center of the ROI is set the same as the estimated centroid provided by the depth perturbation. The width of the ROI in each direction is set as the full width at quarter (25%) maximum [2] of the initial coarse solution in the respective direction, as shown in Fig.5.1(b).

5.1.3 Fine Step

In the fine reconstruction step, the voxel size is typically downscaled to $0.25 \times 0.25 \times 0.25$ mm^3. The voxel number depends on the size of the ROI. However, if the voxel number is greater than 1000, the voxel size will be reset to ensure that the number of voxel number does not exceed 1000.

The objective function in this step is modified to the SVR from expressed as

$$\|\mathbf{Gm} - \mathbf{d}\|_2^2 + \alpha \mathbf{W} \|\mathbf{m}\|_2^2 \qquad \text{s.t.} \quad \mathbf{m} \geq 0 \tag{5.3}$$

which is also transformed to a ordinary least squares problem as

$$\min \left\| \begin{bmatrix} \mathbf{G} \\ \sqrt{\alpha}\mathbf{W} \end{bmatrix} \mathbf{m} - \begin{bmatrix} \mathbf{d} \\ \mathbf{0} \end{bmatrix} \right\|_2^2 \qquad \text{s.t.} \quad \mathbf{m} \geq 0 \tag{5.4}$$

---

[2] Distance from one quarter maximum value to the other in the opposite side

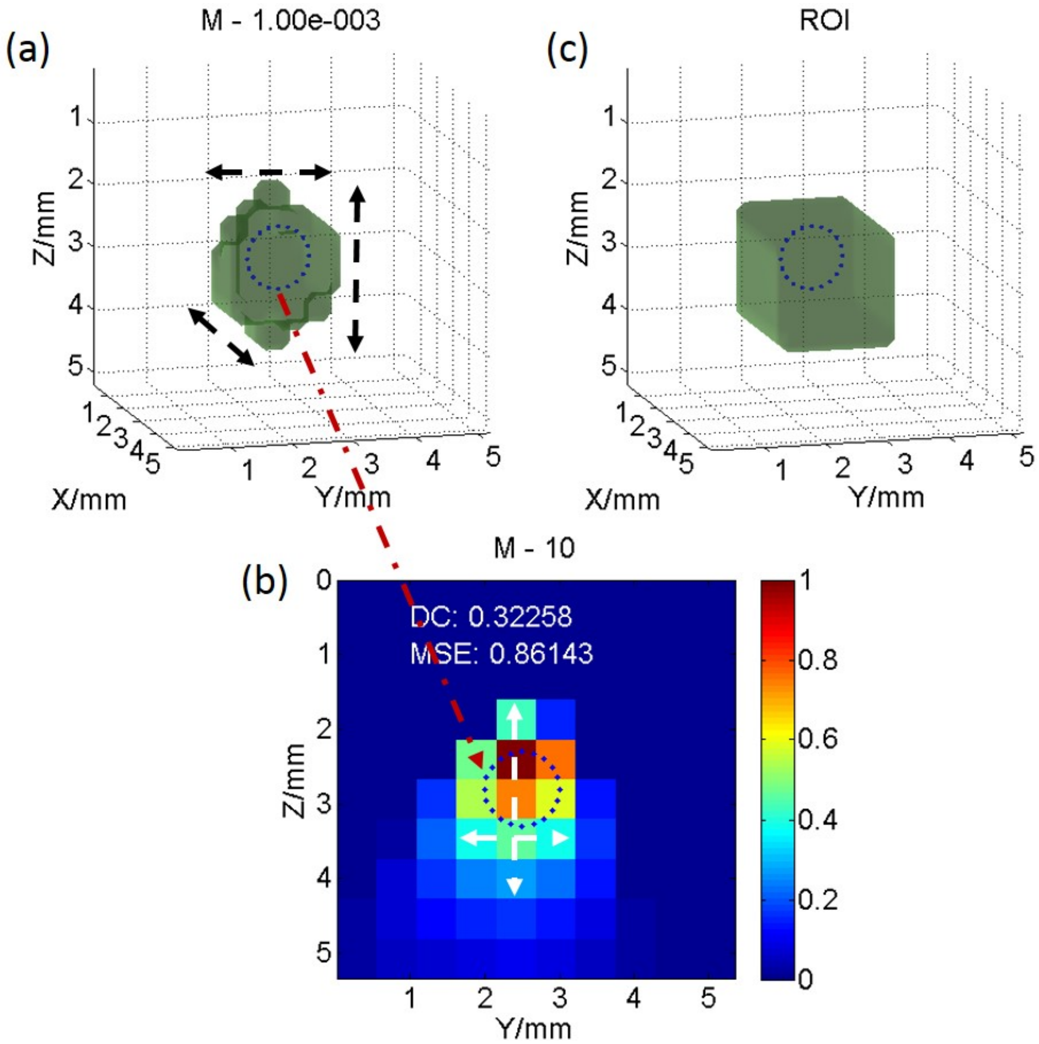

Figure 5.1: Method to Select the ROI in the Fine Step: (a)25 % iso-surface[3] of the initial solution; (b) a Y-Z cross-section of (a) where the white arrows denote the ROI widths in Y and Z directions respectively; (c) cuboid ROI generated from the initial solution (a).

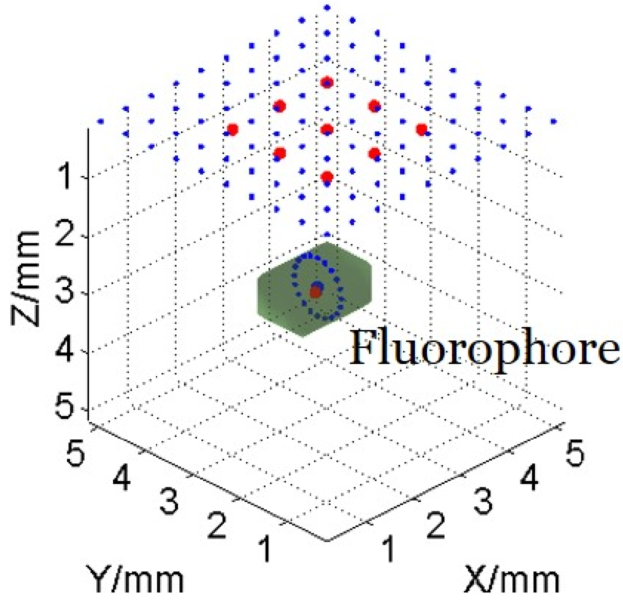

Figure 5.2: Environment of the Numerical Simulation: blue dots on the top denote virtual observation points; red dots on the top denote incident points of laser beam; green object denotes the pre-defined fluorophore model.

and solved by the block principal pivoting algorithm. The weighting matrix **W** is determined in a piecewise manner as mentioned in Sec. 2.5.3. The two parameters ϵ and β involved in Eq.2.11 and Eq.2.12 are fixed at 0.01 and 0.5 respectively.

5.2 Numerical Simulations

A series of numerical simulations were performed to evaluate the performance of the proposed method.

5.2.1 Simulation Setting

These simulations involve a 5×5×5 mm^3 volume, which is assumed to be filled with scattering medium of tissue like properties ($\mu_s' = 11.7cm^{-1}$, $\mu_a = 0.2cm^{-1}$). As shown in Fig.5.2, 10×10 detection positions with 0.5-mm interval and 3×3 incident positions are arranged on the top of the medium. As a result, the number of fluorescent data M is 900. The perturbator used for the depth perturbation was set as the same medium of 1 mm thickness. Fluorophore was predefined as an isolated object with a locally uniform concentration distribution. Fluorescent signals on the medium surface were simulated on the basis of the diffusion equation. Random noise was added to the simulated signals. The SNR was approximated to the measured values of the custom ECW-FMT system (see Sec. 3.3.3).

5.2.2 Fluorescent Model used in the Simulation

As described in Chapter 4, both a single object case and a double object case were considered in these simulations. The former simulation was primarily used to evaluate the reconstruction accuracy of the proposed method, whereas the latter was used to assess its ability to improve reconstruction resolution.

Models in the Single Object Case

Seven single object fluorescent models were tested in the simulations. All objects were cylindrical and aligned along the X direction. Models 1,2,3 varied in depth; models 4,2,5 varied in horizontal length; and models 6,2,7 varied in cross-section diameter (Fig. 5.3). Note that models 5 and 6 are the smallest. The model parameters used in the single object case are detailed in Tab. 5.1.

Models in the Double Objects Case

In the double object case, two fluorescent objects of the same size as that of model 2 were predefined inside the medium. These objects were positioned at the same depth 1 mm (edge to edge) apart (Fig. 5.4). Among the models 8 – 10, central

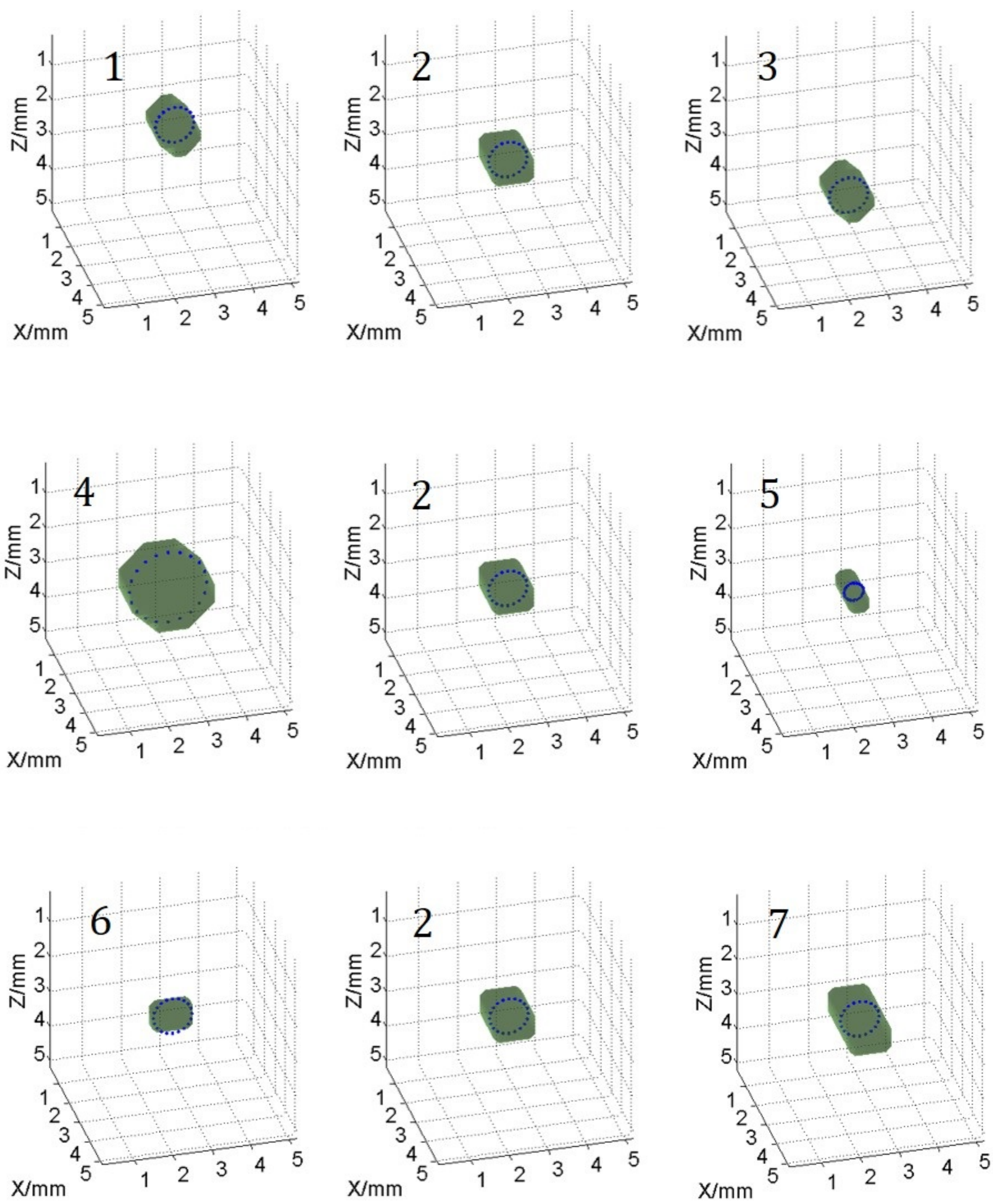

Figure 5.3: Simulated Single Object Models: the model 2 is pictured three times to provide better comparison.

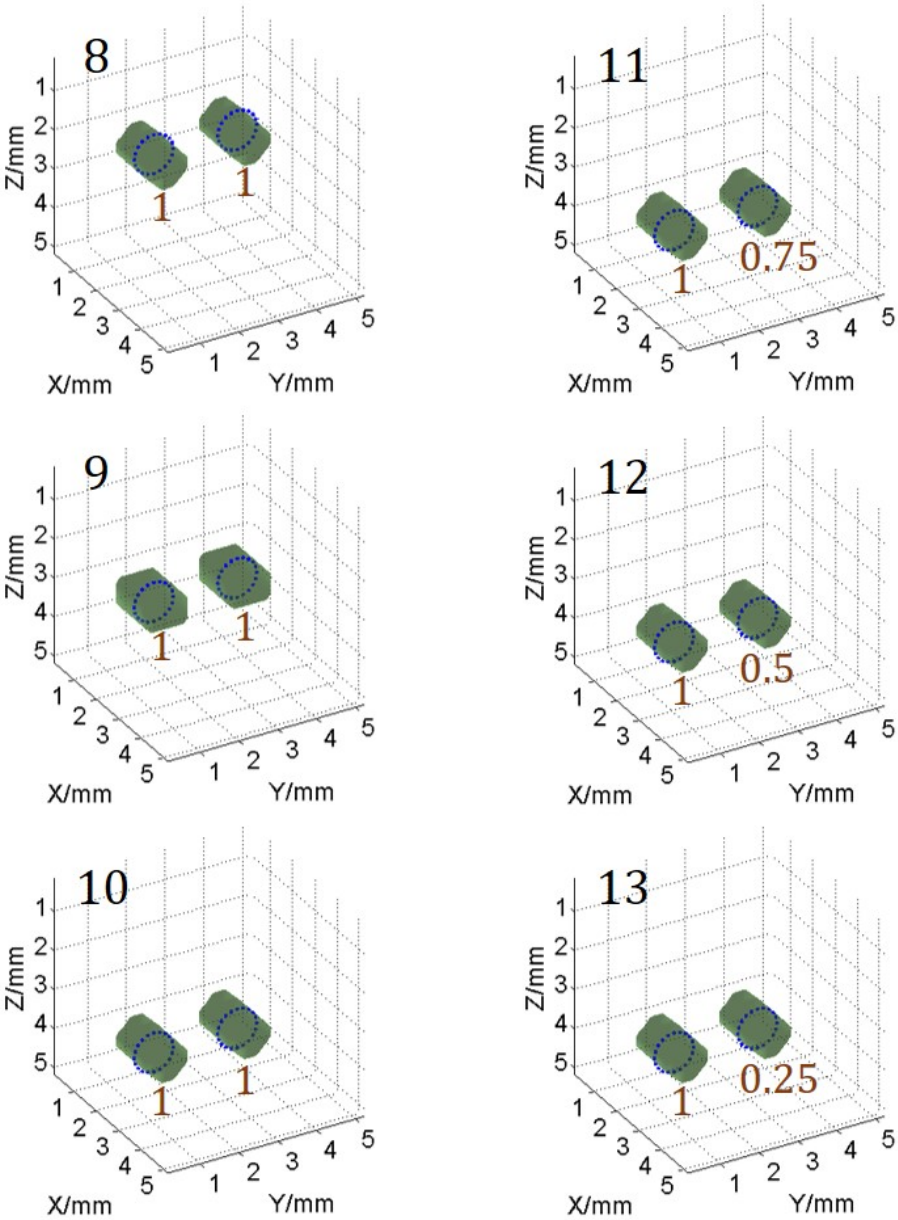

Figure 5.4: Simulated Double Objects Models: the orange number below the green fluorescent object denotes the relative concentration.

Table 5.1: Model Parameters in the Single Object Case

Model No.	Central Depth (mm)	Length (mm)	Diameter (mm)	Volume (mm^3)
1	1.8	1.5	1	1.4
2	2.8	1.5	1	1.4
3	3.8	1.5	1	1.4
4	2.8	1.5	2	5.0
5	2.8	1.5	0.5	0.3
6	2.8	0.5	1	0.5
7	2.8	2.5	1	2.0

depths varied from 1.8 mm to 3.8 mm at 1-mm interval. Among models 10 – 13, depths were fixed at 3.8 mm; however, their concentration ratios (right object to left object) decreased from 1 to 0.25.

5.2.3 Results in the Single Object Case

The simulation was repeated 10 times for each model. The results for each step are provided here. The restored fluorescent distributions were compared with the true models using the dice coefficient at half maximum (DCHM), which shows the conjugation between the pixels occupied by the restored distribution and that by the true value which is defined as [137]:

$$DCHM = \frac{2\,|\mathbf{m}_{0.5+} \cap \mathbf{m}_{true}|}{|\mathbf{m}_{0.5+}| + |\mathbf{m}_{true}|} \tag{5.5}$$

where $\mathbf{m}_{0.5+}$ denotes the component of $\mathbf{m}$ whose values are greater than half the maximum. $\mathbf{m}_{true}$ denotes the true distribution, and $|\quad|$ denotes the number of elements.

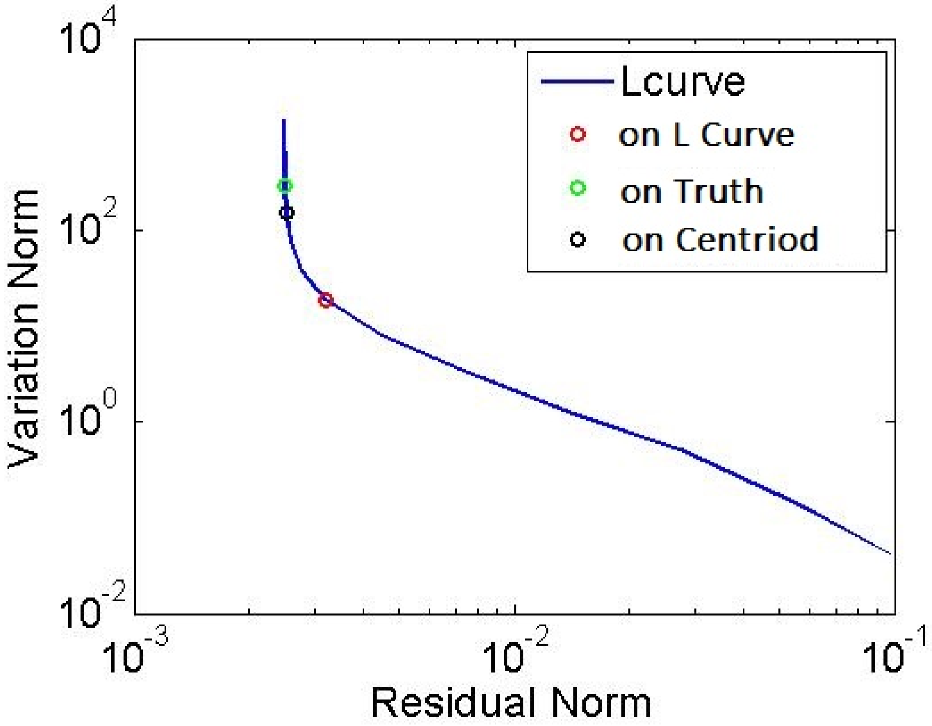

Figure 5.5: Typical Distribution of Regularization Parameters: the red circle denotes the value decided by the turn point at the L-Curve; the blue circle denotes the value decided by the proposed method; the green circle denotes the best value compared with the truth.

Regularization Parameter

In this thesis, the centroid constraint is used to determine the regularization parameter. A typical selection of the proposed method and that of the L-Curve method are shown in Fig. 5.5. Since the true model is known in the simulations, solutions were compared with the ground truth to determine the best parameter, i.e., the parameter that achieves the highest DCHM. The value returned by the L-Curve method is notably larger than the best parameter which explains why its solution is always overly smoothed (Fig. 5.6(a-b)). In contrast, the proposed method provides a value closer to the best. It is usually slightly larger than the best because the largest value in the unbiased range is selected according to the centroid constraint (see Sec. 2.5.2).

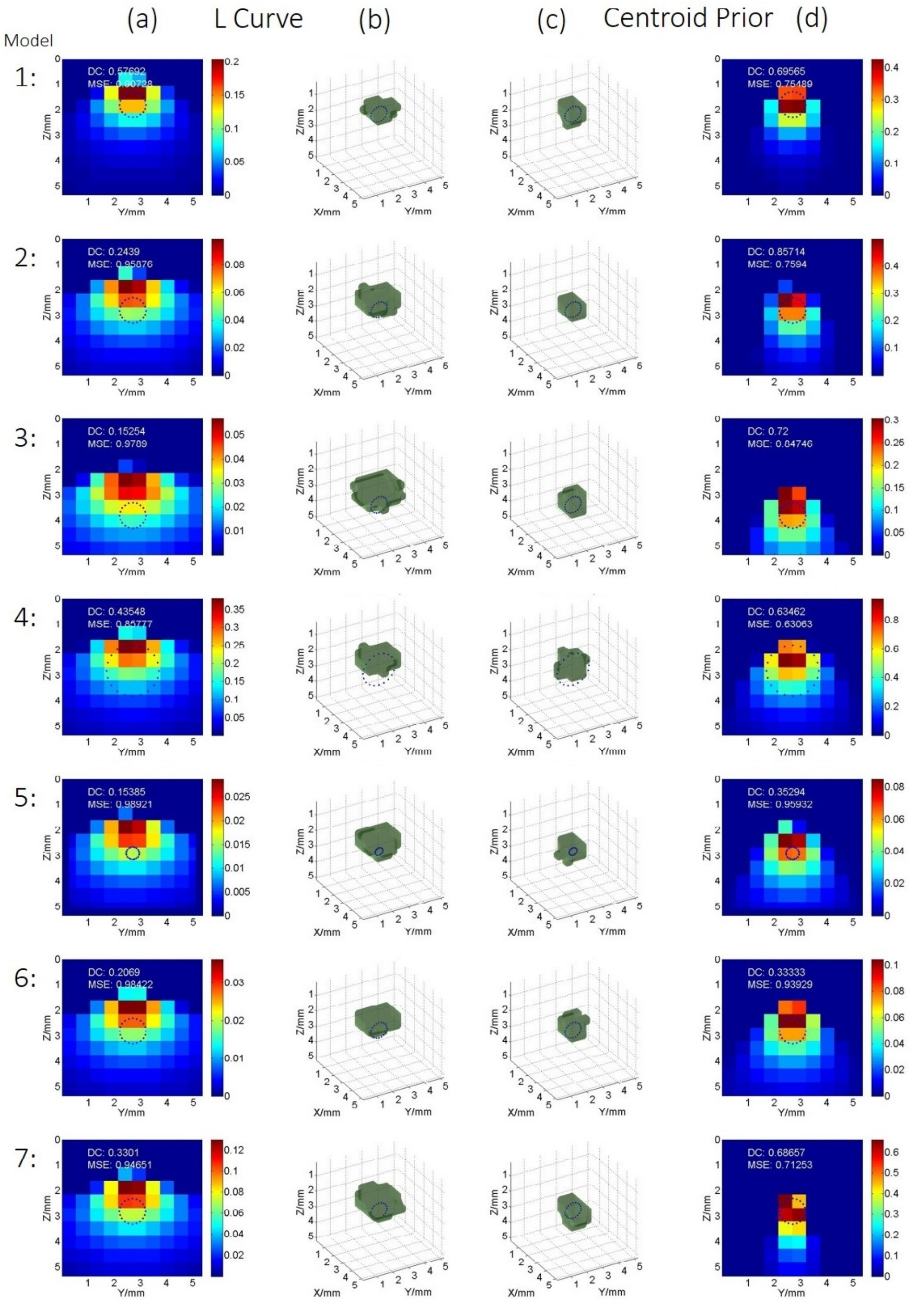

Figure 5.6: Representative Coarse Solutions for Model 1 – 7: (b) column: the restored results with regularization parameter decided by the L Curve method; (a) column: Y-Z cross-section (X = 2.5 mm) of (b); (c) column: the restored results with regularization parameter decided based on the estimated centroids; (d) column: Y-Z cross-section (X = 2.5 mm) of (c); The blue dots circles denote the actual fluorescent region.

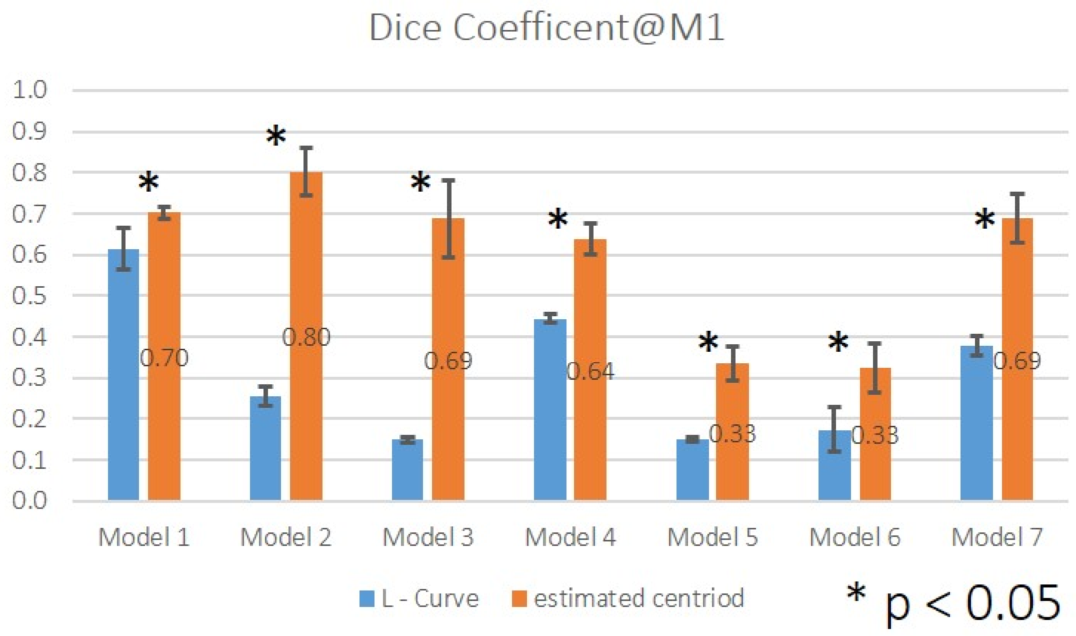

Figure 5.7: Dice Coefficients of the Coarse Solutions for Model 1 – 7: the ⋆ refers that a significant difference exists between the dice coefficient of L-Curve based solution and that of centroid prior based solution; the number on the bars denotes respective mean values.

Coarse Solutions

Fig. 5.6 shows representative coarse solutions for all the models 1 ~ 7. Compared with the conventional L Curve method, the centroid constraint ensure the solutions unbiased from their actual location. In the term of DCHM, for all the single object models, the proposed method offered significantly ($p < 0.05$) higher values than those by the L Curve (Fig. 5.7). However, the average DCHM for the two small models, the model 5 and 6, are less than 0.4. It is attributed to the fact that the object size is comparable, even smaller than the voxel size of this step. As a result the quantization errors greatly affect the solutions.

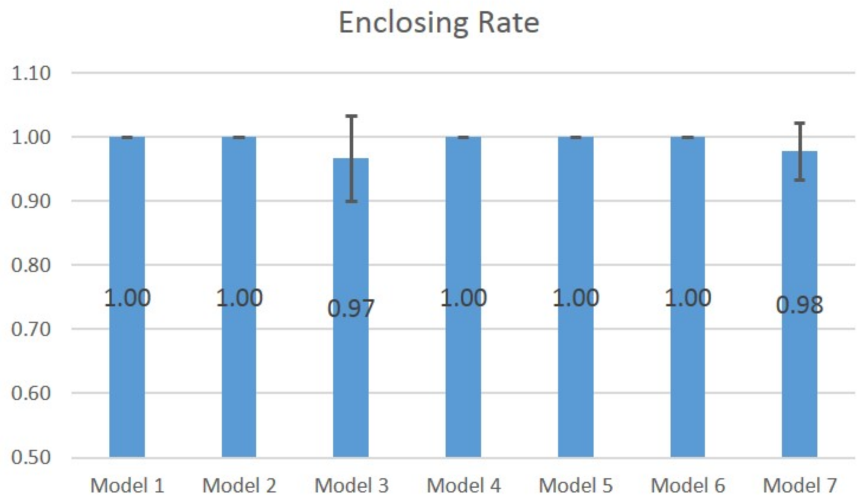

Figure 5.8: Enclose Rates of the ROIs for the Models 1 – 7

Region of Interest

Two indexes were used to evaluate the ROI chosen for the coarse solution, i.e., the enclosing rate and the number of voxels within the ROI. The former is defined as the percentage of the part enclosed by the ROI of the true model compared with its total volume. Ideally, it is preferable that the true model is totally enclosed by the ROI, thus the expected rate is 100%.

In this series of simulations, the enclosing rate of most models equals 100%. Only the models 3 and 7 show slightly lower values: 0.97 ± 0.07 and 0.98 ± 0.04 respectively (Fig. 5.8). On the other hand, the number of voxels (fine voxel) within the ROI is less than 1000 for all models (Fig. 5.9). This is consistent with the aforementioned expectation and and ensures that each inversion of the transfer matrix requires no more than 0.5 s. However, their size is notably larger than those of the respective actual models. This suggests that the proposed method for setting ROI widths requires improvement because a larger ROI incurs higher computational costs.

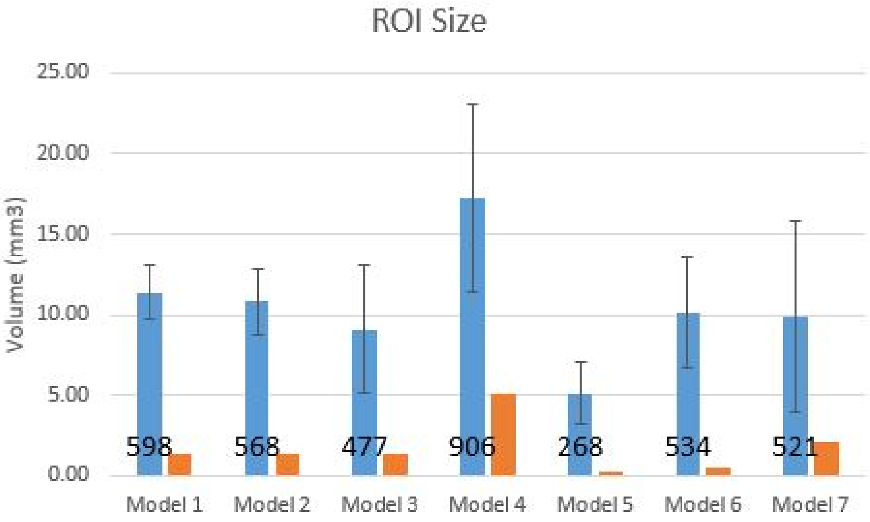

Figure 5.9: ROI Sizes for Model 1 – 7: the blue bars denote the sizes of the ROIs, the orange bars denote the sizes of the respective models, and the number denotes the average voxel number in the ROIs

Fine Solutions

Representative solutions for the fine steps are shown in Fig. 5.10. With finer voxels, the solutions better reflect the actual voxel distributions. To be more specific, the DCHMs of the fine solutions for models 1, 4, 5, and 6 increase significantly compared with the coefficients of the coarse solutions. For other models, the average DCHM also becomes larger (Fig. 5.11).

The size of the reconstructed fluorescent distribution was then compared to the actual size using a size ratio index, which is defined as

$$SR = \frac{V(\mathbf{m}_{0.5+})}{V_{true}} \tag{5.6}$$

where $\mathbf{m}_{0.5+}$ denotes component of a reconstruction distribution $\mathbf{m}$ that is larger than half the maximum, and V_{true} denotes the actual volume of the predefined fluorophore model. As shown in Fig. 5.12, the size ratios of the coarse solutions are typically

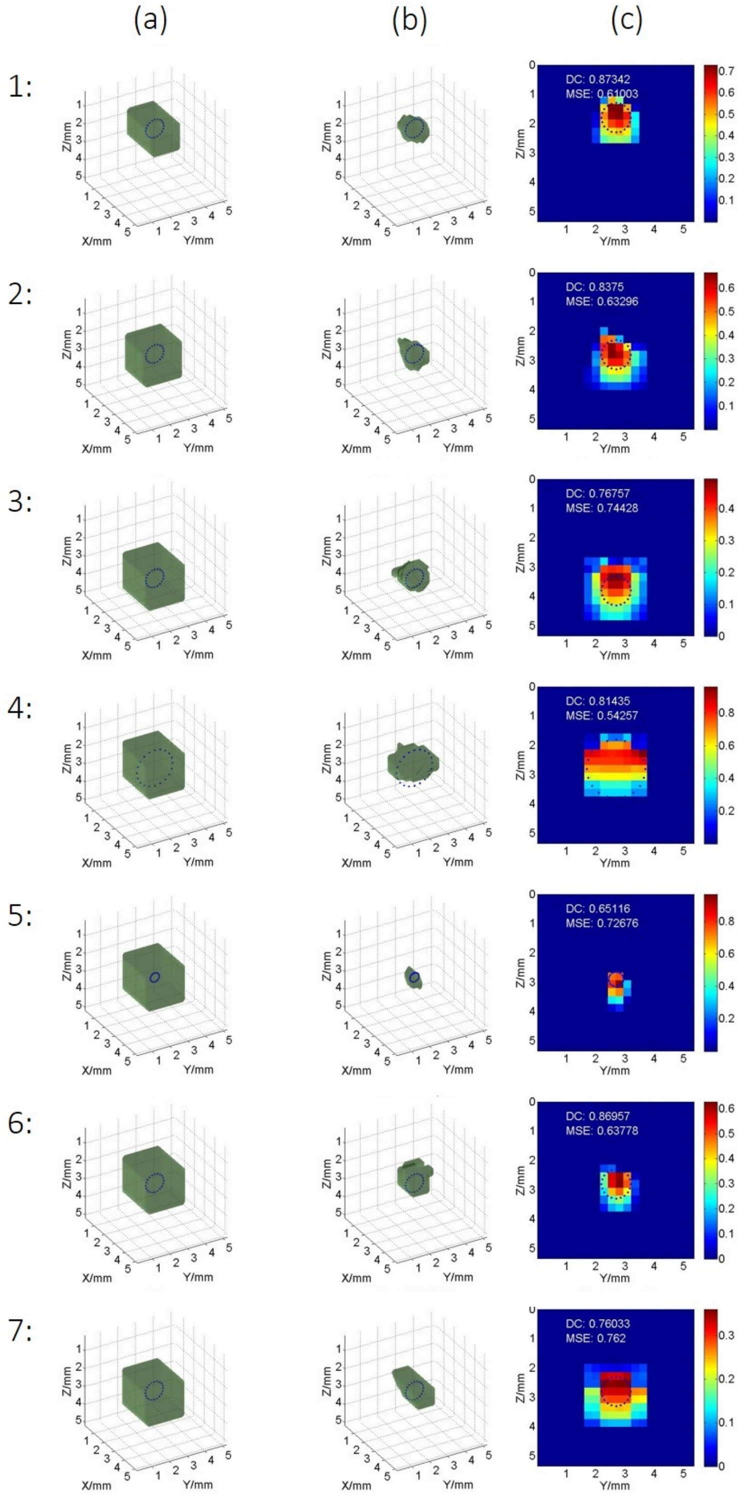

Figure 5.10: Representative Fine Solutions for Model 1 – 7: (a) column: ROI chosen based on the coarse solutions; (b) column: 50% iso-surface of the fine solutions; (c) Y-Z cross-section (X = 2.5 mm) of (b).

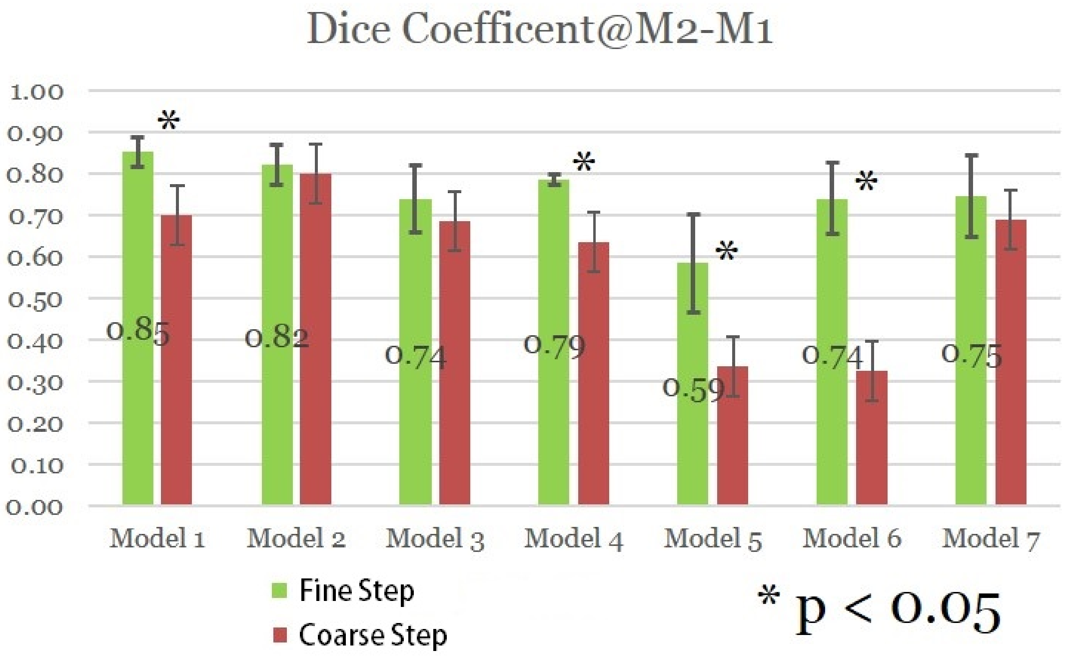

Figure 5.11: Dice Coefficients of the Fine Solutions (green bars) and the Coarse Solutions (red bars) for the Models 1 – 7.

approximately 2.0, indicating that fluorophore size is greatly overestimated. After the fine step, owing to the compression effect of PSVR, the estimated sizes better converge to their truths; the ratios decease to values in the range of 0.8 – 1.5.

5.2.4 Results in the Double Objects Case

The procedure to handle the double object case is nearly the same as in the single case, except that two ROIs must be determined. Therefore, rather than proving intermediate results, this sub-section focuses on other issues, such as whether the spatial resolution is improved or the concentration difference of the two objects can be reflected correctly.

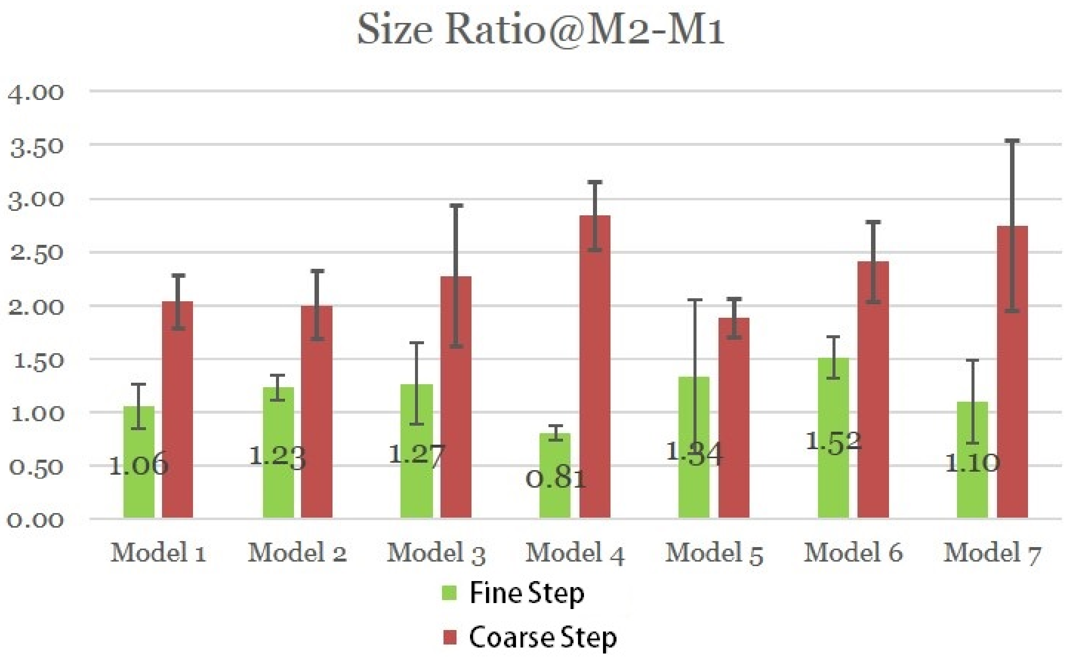

Figure 5.12: Size Ratios of the Fine Solutions (green bars) and the Coarse Solutions (red bars) for the Models 1 – 7.

Improved Resolution

As mentioned previously, the double object models 8 – 10 are positioned at depths of 1.8 mm, 2.8 mm, and 3.8 mm, respectively. As shown in Fig. 5.13, using conventional Tikhonov regularization, the solution appears as one object even at depth of 1.8 mm. In contrast, the results provided by the proposed method maintain two independent objects in all three models. This indicates that spatial resolution is notably improved and that the proposed method can attain 1-mm resolution at depths up to 3.8 mm.

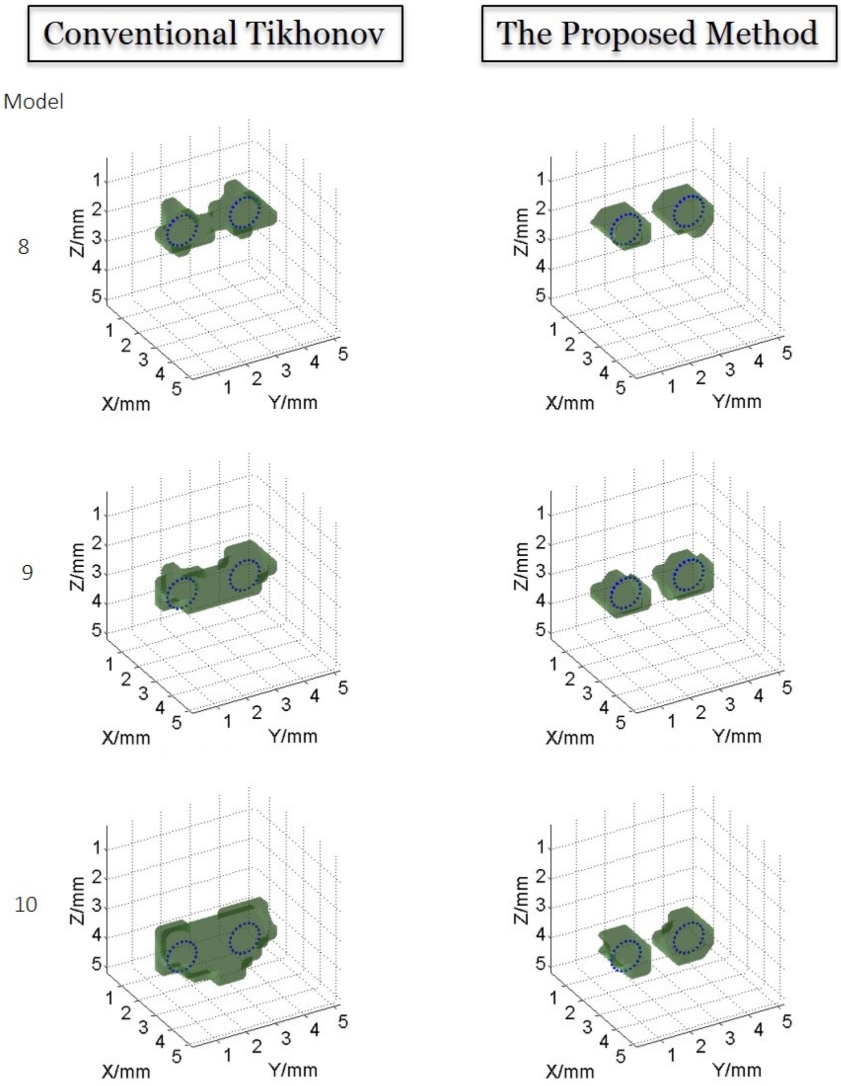

Figure 5.13: Representative Solution of the Models 8 – 10: the left column is the 50% iso-surface of results reconstructed with conventional Tikhonov regularization; the right column is those reconstructed with the proposed methods.

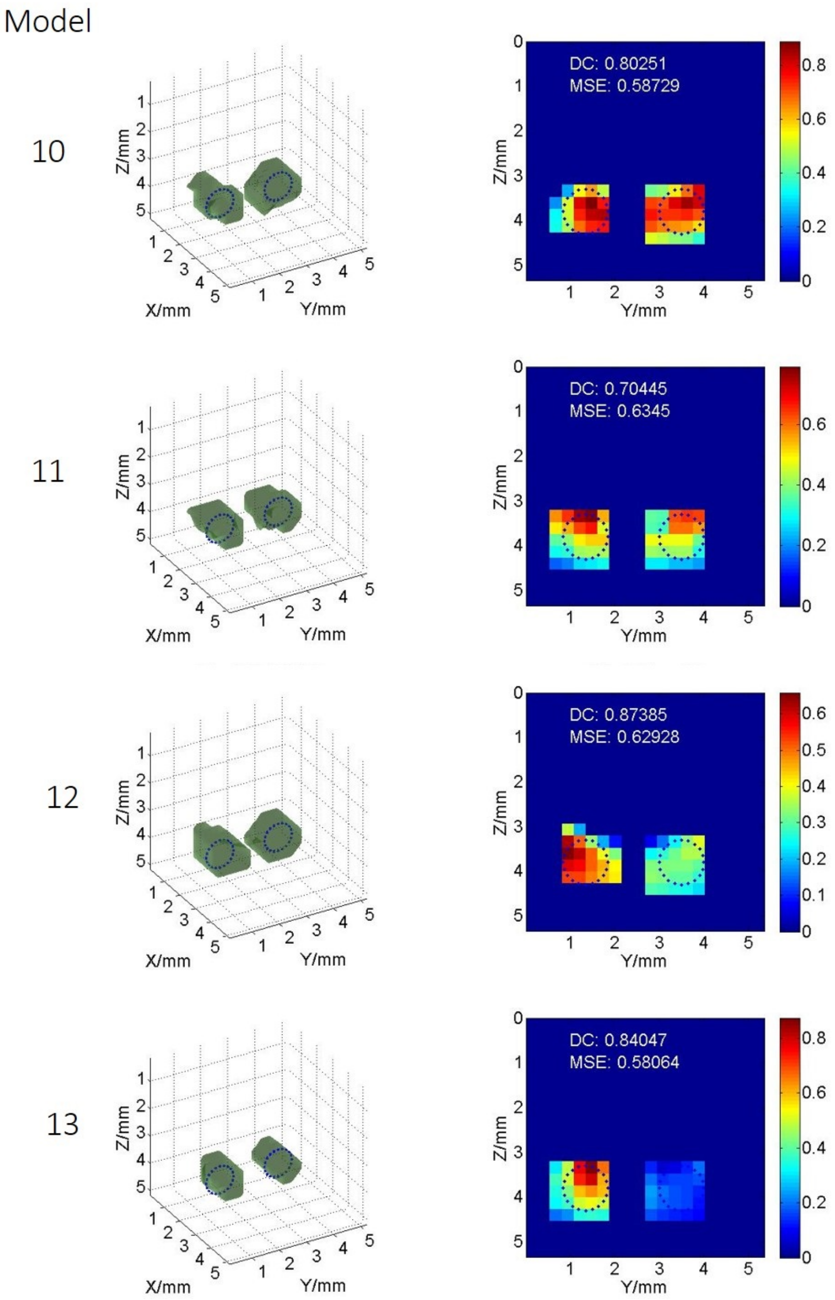

Figure 5.14: Representative Solution of the Models 10 ~ 13: left column: 50% iso-surface of the reconstructed distribution with the proposed methods; right column: Y-Z cross section of respective 3D solution (X = 2.5 mm). Note that the 50% value is calculated independently for each object.

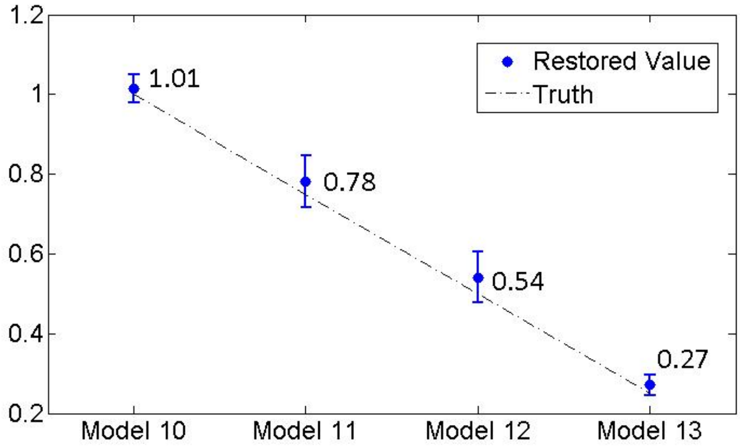

Figure 5.15: Restored Relative Concentration Ratio of the two Fluorescent Objects: The ground truths are denoted by the dash line.

Relative Concentration

Representative Solutions of models 10 – 13 are shown in Fig. 5.14. For all four models, the solutions are in the form of two objects. In the cross-sectional view, the left object maintains high-level values, whereas the values within the right object subsequently decrease. This is consistent with the predefined configurations (Fig. 5.4). Fig. 5.15 shows the ratio of the mean concentration of the right object to that of the left for the four models. Compared with the ground truth, the restored values do not show a large deviation. This proves the potential of the proposed method to retrieve concentration differences between multiple fluorophore objects.

5.3 Experiments with Tissue-like Solid Phantom

Unlike the experiments described in Chapter 4, here solid optical phantoms were used to evaluate the proposed reconstruction framework. Compared with the liquid phantom, a solid optical phantom is more realistic, and facilitates the use of a solid and optically mismatched [4] perturbator.

5.3.1 Solid Phantom

The solid phantoms were made of PDMS. TiO2 (scatter) and ink (absorber) were mixed into the phantoms to provide tissue-like scattering and absorption coefficients. A horizontal channel (diameter, 1.1 mm) was left in the phantom to allow for a capillary tube including fluorophore. In this study, two solid phantoms (phantom 1 and phantom 2) with different optical coefficients and central channel depth were tested. The properties of the phantoms and the solid perturbator (made of PDMS; 1 mm thickness; detailedly described in Appx. A) used in later phantom experiments are listed in Tab. 5.2.

---

[4] Mismatched means the optical properties of the perturbator differ from those of a sample

Table 5.2: Properties of the Solid Optical Phantoms and the Perturbator

	Scattering Coef. [a]	Absorption Coef. [b]	Channel Depth
Phantom 1	0.44 mm^{-1}	0.04 mm^{-1}	3.4 mm
Phantom 2	0.65 mm^{-1}	0.02 mm^{-1}	5.2 mm
Perturbator	0.43 mm^{-1}	0	–

---

[a] at the excitation wavelength (785 nm), values at the emission wavelength are omitted for brevity

[b] same as *a*

5.3.2 Experiments

Small ICG objects, included in a capillary tube (diameter, 1.1 mm), were fixed in the phantom channels. The inclusion length in the experiments using phantom 1 was approximately 2.0 mm, whereas the inclusion length in experiments using phantom 2 was approximately 1.4 mm. Tomographic fluorescence measurements were conducted using the ECW-FMT system. The laser beam scanned the phantom surface (horizontally close to the inclusion), providing 5×5 incident positions (1-mm

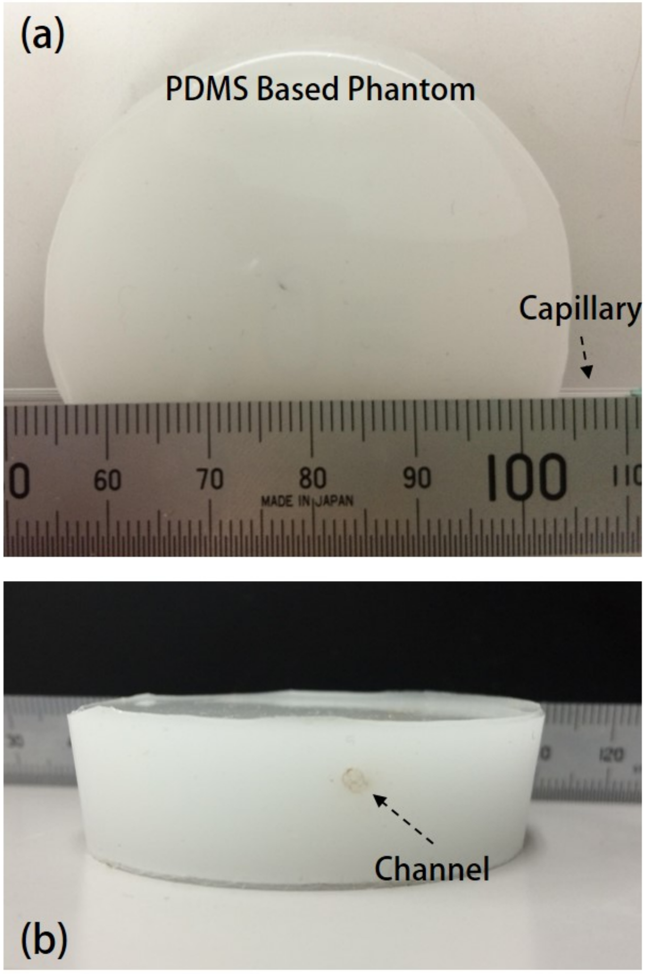

Figure 5.16: Solid Optical Phantom Made of PDMS, TiO2, and ink: (a) top view, (b) side view.

intervals). Fluorescence measurements were performed twice, the first to determine the initial superficial fluorescence distribution and the second to determine the distribution after the depth perturbation. Control images (no ICG inclusion) were also captured to remove the background. The experiments were repeated 10 times for each condition.

5.3.3 Results

On the basis of the methods and algorithms described in Chapter 4, the fluorophore centroid was first estimated from the measured data. Table 5.3 shows estimations and percentage absolute errors of the estimated fluorophore central depth. The estimated values are well consistent with the expected values, with less than 10% errors (on average). Errors of horizontal centroid are not provided, because it is difficult to determine the ground truth of the fluorophore inclusion exactly after it is embedded into the phantom. [5]

Then, using the centroid prior and the fluorophore reconstruction framework discussed in this chapter, the fluorophore distribution was stored and the FWHM

Table 5.3: Results of Solid Phantoms Experiments (mm)

		Central Depth	Width@X	Width@Y	Width@Z
Phantom 1	Expected Val.	3.4	2.0	1.1	1.1
	Estimation	3.2±0.2	1.8±0.1	1.2±0.1	1.2±0.1
	Perc. Error	6±4%	12±2%	11±2%	8±3%
Phantom 2	Expected Val.	5.2	1.1	1.4	1.1
	Estimation	5.2±0.4	1.4±0.2	1.5±0.2	1.2±0.2
	Perc. Error	5±5%	25±15%	9±10%	13±17%

---

[5] In the experiment using the liquid phantom, the horizontal centroid can be determined before tissue-like liquid is poured into the tank.

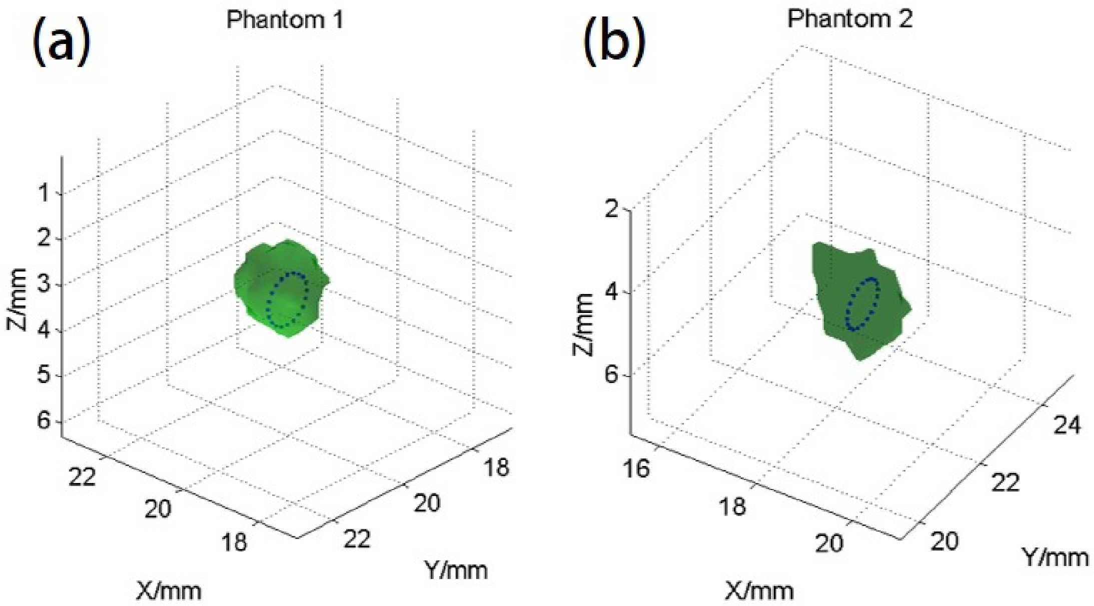

Figure 5.17: Representative Fluorophore Distribution: (a) restored from phantom 1 data; (b) restored from phantom 2 data. The green surface denotes the 50% value isosurface and the blue dash circle denotes the expected fluorophore boundary (central cross-section).

of the restored distribution was calculated [6]. Representative restored fluorophore distributions of the two phantoms were shown in Fig. 5.17. They appear around the actual fluorophore location, indicating that the centroid prior works well. However the surface of restored distribution is not smooth as expected. Table 5.3. also provides the FWHM along the X, Y, Z axes of the restored distributions, showing that estimation errors are in the range of 10 – 25% (on average). These results verify the feasibility of the proposed methods to restore fluorophore distribution.

---

[6] Because the restored distributions are not always in regular shapes, the average FWHMs along the Y direction of all Y-Z and X-Y cross sections within the 50 % isosurface were used as the width along the Y direction. A similar method was also applied to the calculations of X, and Z widths

5.4 Discussion

The two-step coarse-to-fine strategy greatly accelerates the reconstruction process. For example, consider model 4, which has the largest ROI among all simulated models and therefore requires the longest computation time. In the reconstruction process of model 4, centroid estimation typically takes less than 0.1 s. The coarse step requires approximately 40 s, and the fine step requires approximately 18 s on average. [7]. Therefore, the computations require approximately one minute. In contrast, if fine reconstruction is performed over the entire space, it would require more than one hour.

These simulations require only one coarse step and one fine step. The strategy can be extended progressively, i.e., coarse, fine, finer, etc. A progressive strategy may be more efficient for larger fluorophore than those tested here because a larger size means a larger ROI. Using a progressively downscaled voxel size helps control the number of voxels involved in each computation. In addition, for a very small fluorophore, a finer voxel system than those used in these simulations will potentially provide a better reconstruction.

In the simulation results for the single object case, the DCHM of the final solutions for most models is greater than 0.7 on average; only that of model 5 is less than 0.6. Similarly, the size ratio for the two small models, i.e., models 5 and 6, is 1.34 ± 0.72 and 1.52 ± 0.19 respectively. Accuracy when determining fluorophore size for very small fluorophore is modest. This can be attributed to the smooth nature of the solution offered by Tikhonov regularization. Piecewise SVR was applied to compress the solution; however, the compression force, which is controlled by the threshold β in Eq. 2.12, was fixed as 0.5 in these simulations. Generally, Generally, smaller

---

[7] Depend on ROI size

fluorophore requires stronger force (i.e., greater β). Therefore, effectively tuning β can further improve size estimation accuracy.

Another issue about PSVR is how well it maintains the original profile of the fluorophore bio-distribution. Consider the restored results of model 2 (Fig. 5.18(b)). This model has a locally uniform distribution within the fluorescent region. The result restored with the piecewise weighting manner shows a nearly flat distribution inside the true fluorescent region (Fig. 5.18(d)). Om contrast, if weighting in a linear manner (Fig.2.15), values on some voxels (such as the right top two voxels in the fluorescent region, Fig. 5.18(f)) are overly enhanced, because their restored values of the coarse solution is the greatest. Consequently, the flat profile is changed significantly. Furthermore, the FWHM size of the restored distribution shrinks because the profile becomes steep (see the defect in Fig. 5.18(e)). For 10 simulations of model 2, the DCHM of the linearly weighted results is 0.70 ± 0.09, whereas that of the piecewise weighted result is 0.82 ± 0.05. The piecewise weighted manner shows better performance($p < 0.01$). However, this thesis focuses on locally uniform fluorophore bio-distribution. Further evaluation of the performance of PSVR and the entire reconstruction framework under a more complex fluorophore bio-distribution is planned for the future work.

In the double object simulations, the number of fluorescent objects was treated as an unknown and estimated by the "try from one" strategy described in Sec. 4.1.3. The strategy provided correct estimation for most models, with the exception of two runs of model 13 (the concentration ratio = 1:0.25), where the number of objects was incorrectly determined as one. Owing to difficulty with comparisons, the results of these runs were excluded when the relative concentration ratio shown in Fig. 5.15 was calculated. Further evaluations of concentration sensitivity and the limits of the “try from one” strategy under more realistic conditions, e.g., phantom experiments, are

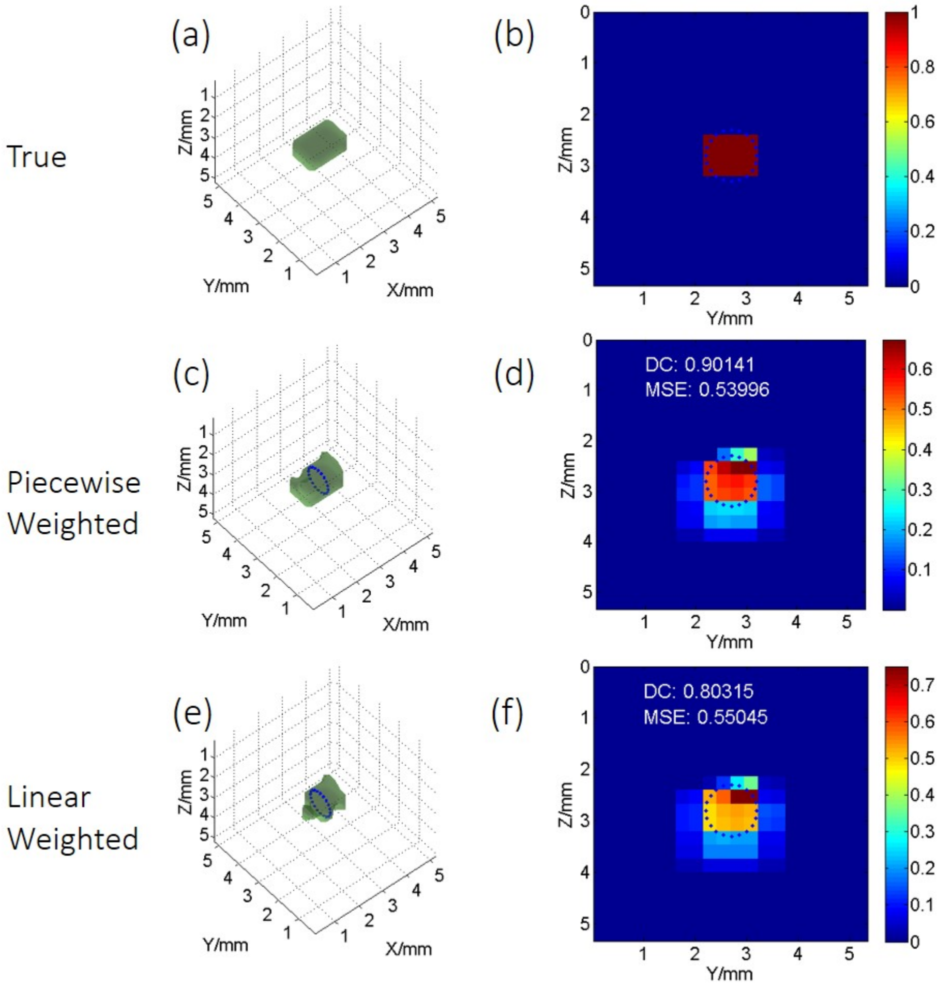

Figure 5.18: Effect of Piecewisely Spatially Varying Regularization: (a) the true model (model 2), (b) Y-Z cross-section (X = 2.5 mm) of the true model; (c) 50% isosurface and (d) Y-Z cross-section (X = 2.5 mm) of the reconstructed distribution by piecewisely weighted manner; (e) 50% isosurface and (f) Y-Z cross-section (X = 2.5 mm) of the reconstructed distribution by linearly weighted manner. The blue dots circles denote the actual fluorescent region.

planned for future work.

Finally, in the results of the phantom experiments, although the inclusions are actually of a cylindrical shape, the 50% surface of the reconstructed distribution is extremely irregular and not as smooth as expected. This is partly attributable to the relatively large voxel size. Even in the fine step, the cubic voxel length is set to approximately 0.3 mm, which is the same order of the inclusion size. A smaller voxel size may allow for a finer restored fluorophore distribution shape at the cost of computation time. In addition, noise and errors in measured data and the effects of the capillary tube are also potential reasons for such deformations

In conclusion, this chapter has described and evaluated the proposed framework for fluorophore reconstruction in the proposed ECW-FMT system. The framework incorporates a coarse-to-fine strategy, regularization parameter determination based on centroid constraints, and PSVR. The results of numerical simulations and phantom experiments indicated that although slightly complicated, the proposed framework demonstrates improved speed, better accuracy, and higher spatial resolution than conventional Tikhonov regularization.

6 Ex-vivo Evaluation

In this chapter, the depth perturbation concept and the reconstruction framework proposed in this thesis are evaluated in an ex vivo environment. The experiments utilized pork chuck meat, which has slight optical heterogeneity, as the subject and a solid optical phantom as the depth perturbator.

6.1 Purpose

The main goal of the ex vivo evaluation was to verify the depth perturbation con-cept as well as the other proposed methods in a realistic environment. This chapter focuses on various issues, including whether slight optical heterogeneity and surface crevices in biological tissue lead to unacceptable reconstruction results. Compared with an actual clinical environment, for simplicity, some potential issues are ignored, including irregular tissue shape, complex anatomical structure [1] and temporal variance of tissue properties.

6.2 Materials

Pork meat was used as the subject in these ex-vivo experiments. As shown in Fig. 6.1 (a), it was composed of a large amount of muscle fibers and a few fat tissues; thus it is not exactly a homogeneous medium. For depth perturbation, a silicon perturbator made of PDMS and TiO_2 (Fig. 6.1 (b)) was used. The perturbator (diameter, 45 mm; thickness, 1.0 mm) was used. To avoid the effect of the capillary wall, a solidified ICG probe was employed. The ICG powder was first diluted with intralipid aqueous solution, and then mixed into liquid PDMS. The liquid PDMS hardened at high temperature (60°) in several hours with the assistance of a hardening material. The volume concentration of ICG in the hardened PDMS was approximately 10μM. Intralipid was used to (1) provide lipid without binding to which ICG cannot fluoresce; (2) provide scattering properties similar to the background medium. A small-size (approximately $1.5\times2\times1.5 = 4.5$ mm^3) PDMS-based ICG probe (Fig. 6.1(c)) was fixed inside the tissue as the fluorophore inclusion.

---

[1] Such as multiple layers and vessels which may produce significant optical heterogeneity

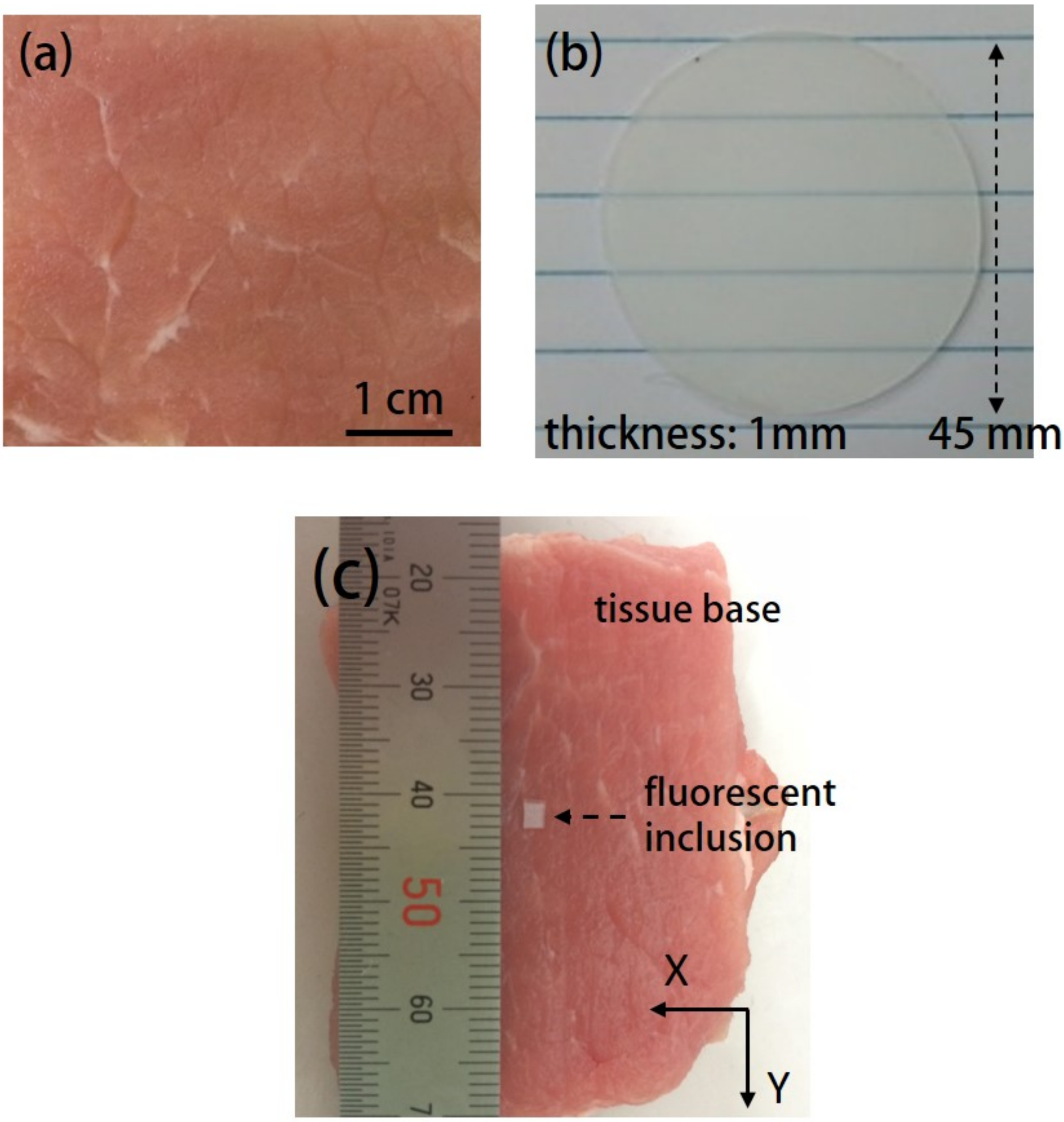

Figure 6.1: Materials used in the Ex-vivo Experiments: (a) pork chuck meat; (b) depth perturbator; (c) fluorophore inclusion and tissue base.

Table 6.1: Optical Coefficients of Materials used in the Ex-vivo Experiments: each value is the average of measurements on five randomly selected locations.

	Perturbator		Pork Chuck	
Wavelength	785 nm	830 nm	785 nm	830 nm
μ'_s (mm^{-1})	0.44	0.37	0.25	0.22
μ_a (mm^{-1})	0	0	0.02	0.02

The optical coefficients of the materials were measured using an oblique-incidence reflectometry technique that allows in situ and noninvasive measurements of optical properties of biological tissue. Details of this technique are described in Appx. B. The measured absorption and reduced scattering coefficients at wavelengths of 785 nm and 830 nm [2] are listed in Table 6.1.

6.3 Experiments

A part of the meat was sliced to thin pieces of 1.5 – 2.5 mm thickness. The remaining part ($5 \times 4 \times 2$ cm^3) was used as a base (Fig. 6.1(c)) to ensure the validity of the assumption that incident light and fluorescence only propagate within the examined subject or emit from the top surface. The ex-vivo experiments were performed as follows.

1. The ICG inclusion was placed on the base and pushed down slightly to ensure the top of the inclusion was at the same height as the top surface of the base [3] (Fig. 6.2(a)).
2. A pieces of sliced meat were covered onto the base [4] (Fig. 6.2(a)).
3. The prepared sample was moved to the ECW-FMT system and the subject was

---

[2] The excitation wavelength and emission peak wavelength

[3] The tissue just below the inclusion was slightly crushed

[4] The number of covered meat pieces determined the fluorophore depth

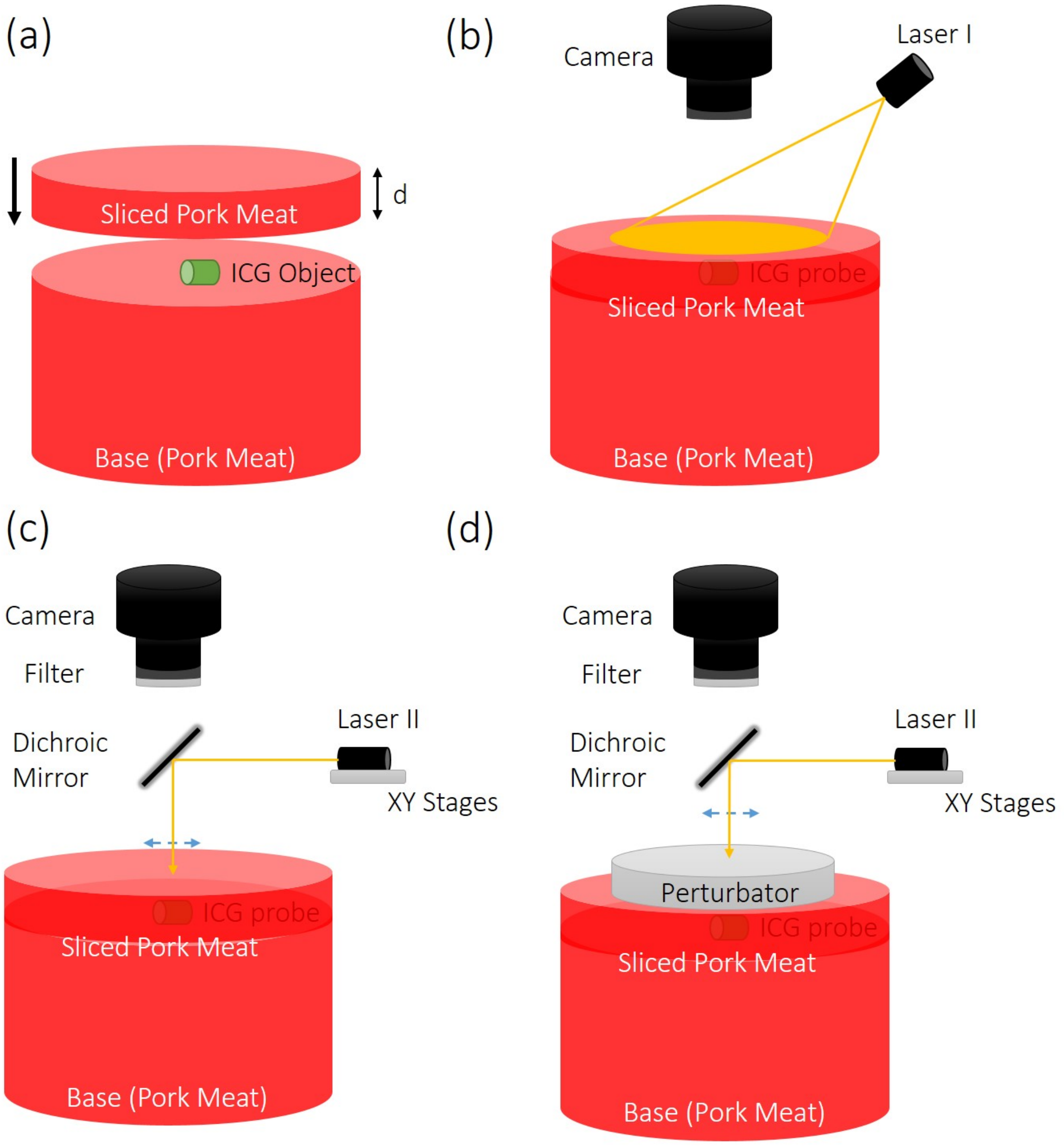

Figure 6.2: Steps of the Ex-vivo Experiments: (a) fixing the fluorophore inclusion at an expected depth inside the tissue; (b) broad illumination; (c) raster beam scan; (d) depth perturbation.

illuminated with a broad laser beam (wavelength, 790 nm; power, 100 mW; illumination area, 4× 4 cm^2) (Fig. 6.2(b));

4. The rough horizontal position of the fluorophore inclusion was determined on the basis of the fluorescent image obtained under broad illumination.
5. The area around the rough horizontal position was raster scanned using a narrow laser beam (wavelength, 785 nm; power, 10 mW; beam size, 0.46 mm) (Fig. 6.2(c));
6. The perturbator was superimposed onto the sample and the depth perturbed sample was raster scanned again with the same incident positions as in step 5 (Fig. 6.2(d)).

Here broad illumination was applied prior to the beam scan to reduce the scan area and time. The approximate horizontal position of the inclusion was assumed to be located at the point that emitted the strongest fluorescence. In these ex vivo experiments, the number of slices of meat covering the base was 1, 2, 3, and 4. The resultant fluorophore central depth was 2.6 mm, 4.7 mm, 6.4 mm, and 8.8 mm, respectively. For each depth, the measurements were repeated five times.

6.4 Results

6.4.1 Estimated Fluorophore Depth

Fluorescent data obtained at all incident points were denoised and down sampled. Then, nonlinear regression was applied to estimate the fluorescent centroid, as described in Chapter 4. As shown in Tab. 6.2, the estimated fluorophore central depths are essentially consistent with the expected values. Absolute estimation errors are 0.3

– 0.5 mm (on average). Since Obtaining the exact fluorophore horizontal position after the inclusion is concealed under the sliced meat is difficult, I did not calculate the error to the horizontal centroid.

Table 6.2: Estimated Central Depths of Ex-vivo Experiments

	Expected Depth (mm)			
	2.6	4.7	6.4	8.8
Estimation (mm)	3.0±0.1	4.2±0.2	6.3±0.3	8.5±0.4
Abs. Error (mm)	0.4±0.1	0.5±0.2	0.3±0.1	0.3±0.4

6.4.2 Estimated Fluorophore Volume

3D fluorophore distributions were reconstructed in a $5\times 5 \times 5$ cm^3 space. The reconstruction process was implemented as described in Chapter 5. Representative examples of the restored fluorophore distributions are shown in Fig. 6.3. The restored distributions appear at reasonable locations. However, they are typically irregular and have notable deformations because the actual shape of the fluorophore inclusion is close to a cuboid. These deformations are attributable to the smooth effect of the Tikhonov regularization and the optical heterogeneity of the meat.

Because of the irregularity of the restored shapes and the difficulty in determining the true fluorophore distribution, estimated volumes were calculated to evaluate the proposed reconstruction framework. The estimated volumes were defined as the volume inside the 50% iso-surface of the restored fluorophore distributions. Table 6.3 shows the estimated volumes, volume error and percentage errors at the four depths. On average, the percentage volume (absolute) errors are in the range of 10 – 30 %, indicating that the fluorophore size was relatively well reconstructed.

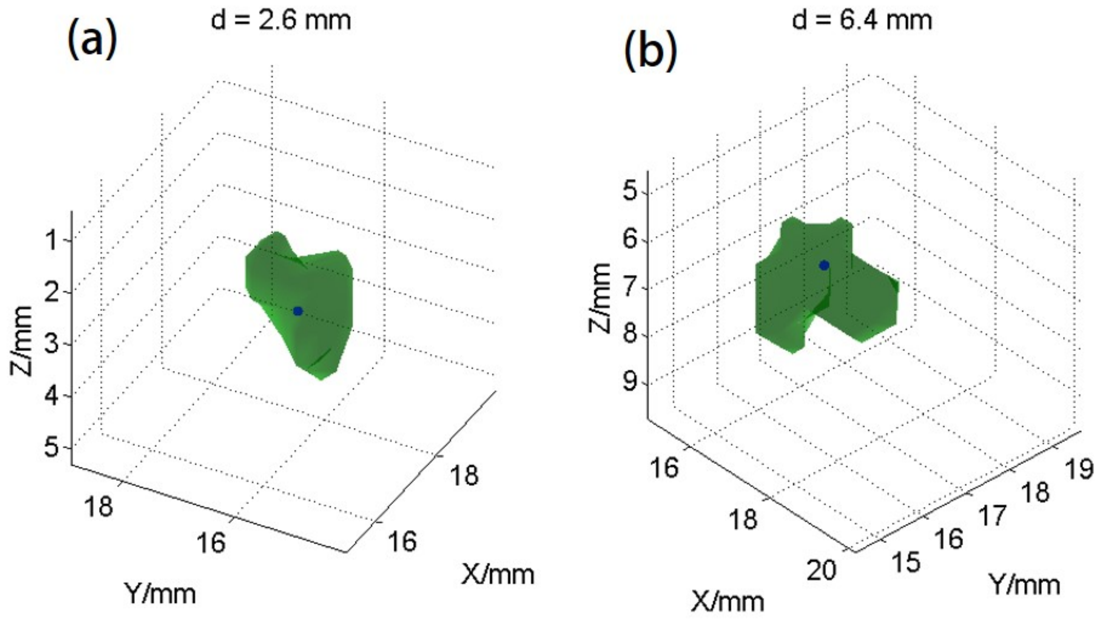

Figure 6.3: Reconstructed Fluorophore 3D Distribution: expected fluorophore central depth (a) d = 2.6 mm; (b) d = 6.4 mm. The green surface denotes the 50% iso-surface, and the blue point denotes the estimated fluorophore centroid. Note that the Z-axis range differs on (a) and (b).

Table 6.3: Estimated Volumes in Ex-vivo Experiments

	Expected Depth (mm)			
	2.6	4.7	6.4	8.8
Expected Vol. (mm^3)	4.5	4.5	4.5	4.5
Estimation (mm^3)	3.4 ± 0.4	4.6 ± 0.5	4.1 ± 0.9	5.7 ± 1.1
Abs. Error (mm^3)	1.1 ± 0.4	0.5 ± 0.3	0.9 ± 0.2	1.3 ± 1.0
Perc. Error (%)	25 ± 9	11 ± 6	21 ± 5	30 ± 22

6.5 Discussion

In this chapter, the depth perturbation concept and the reconstruction framework proposed in this thesis are evaluated in an ex vivo environment. The errors in localizing fluorophore depth are approximately 0.3–0.5 mm, which is slightly larger than those of the phantom experiments. These increases in errors are attributable to the optical heterogeneity of the tested sample. As shown in Fig. 6.1(a), a small amount of fat and tiny slits can be seen on the tissue surface. These heterogeneities apparently lead to unexpected light propagation. Fig. 6.4 compares fluorescent images captured in the ex vivo experiments and in the liquid phan¬tom (intralipid) experiments. The liquid phantom is completely flat and homogeneous. The profile of the measured fluorescent signal (Fig. 6.4(c)) is nearly concentric. In contrast, the profile of the ex-vivo fluorescent image (Fig. 6.4(a)) is obviously distorted. Similarly, the distribution of intensity ratios resulting from depth perturbation also deviates from the theoretical ratio model illustrated by Fig. 4.3. Fortunately, in the centroid estimation process, thousands of data points are applied to data fitting. Therefore, owing to the averaging effect, the slight distortions reduce accuracy but do not lead to unacceptable results. Further studies on the effect of strong optical heterogeneity and uneven tissue surface are provided in Chapter 7.

In terms of estimated volume, for some measurements where the central depths are underestimated (e.g., 8.8 mm), the volumes are significantly overestimated. In contrast, when depths are overestimated (e.g., 4.5 mm), the estimated volumes are less than the expected values. These results show that the errors in localizing fluorophore centroid are transferred to the reconstruction process because prior knowledge of central depth was used to determine the regularization parameter in the proposed reconstruction framework. If the effect of the regularization parameter on the reconstructed fluorophore distribution is considered (Sec. 2.5.1), it is reasonable to conclude that an underestimated central depth results in an over-smoothed distribution and vice versa.

Finally, to image a deep region (i.e., 8.8-mm depth), in these ex vivo experiments the ICG concentration was diluted to 10 μM, which is one order greater than that in

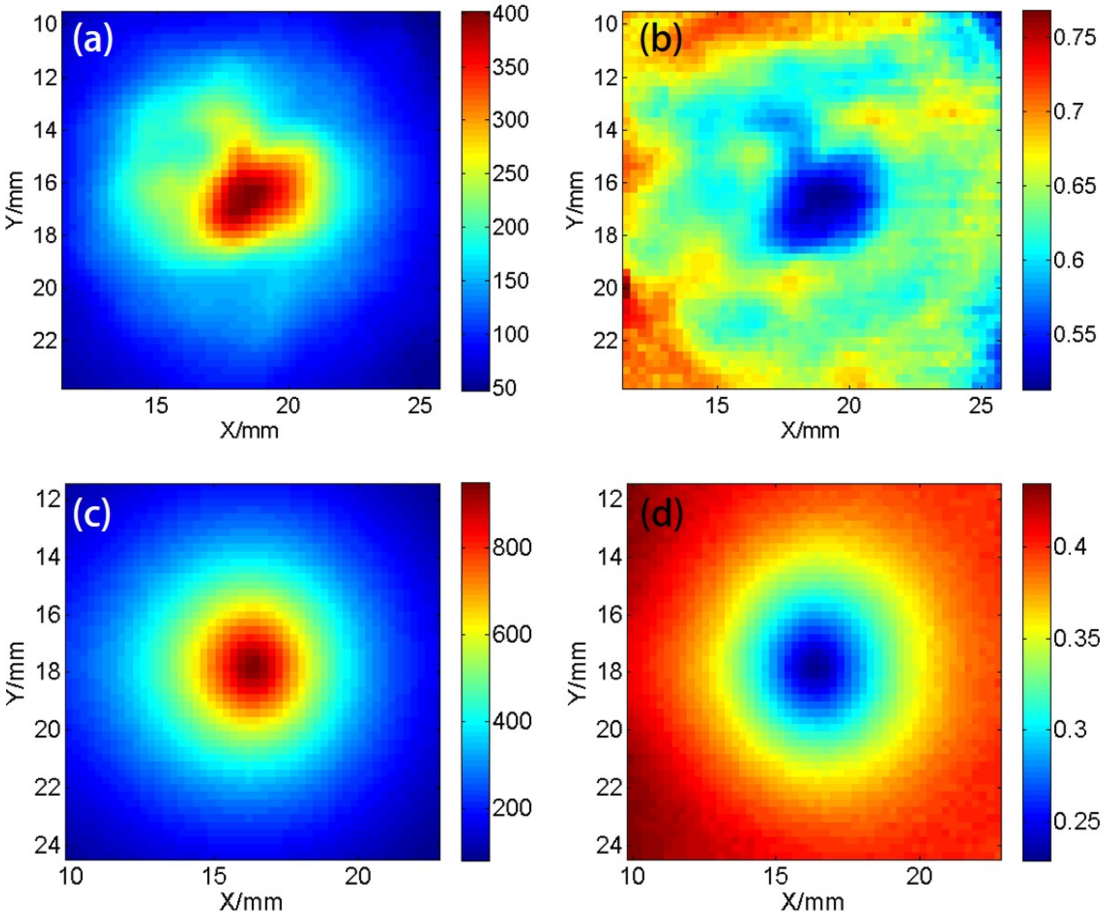

Figure 6.4: Representative Fluorescent Data and Intensity Ratio: (a) initial data from one ex-vivo experiment; (b) intensity ratio corresponding to (a); (c) initial data from one liquid phantom experiment; (d) intensity ratio corresponding to (c).

the phantom experiments. A higher concentration enhances the SNR of the captured images. The results show that the proposed methods are theoretically feasible for the localization and reconstruction of a small fluorophore located inside the tissue at a depth of approximately 1 cm only if the SNR is sufficient. Note that an ICG dosage of 10 μM is not high. According to a clinical report [98], the local concentration of ICG accumulated in human tissues can be as high as 200 μM within 60 minutes after administration and can maintain a concentration greater than 10 μM for 240 minutes.

In summary, on the basis of the results of the ex vivo experiments, the proposed methods exhibited potential feasibility in imaging of biological tissues. Slight optical heterogeneity does not result in large estimation errors. More realistic biological tissue conditions will be discussed in Chapter 7.

7 Discussion and Conclusion

In section 1.6.2, the critical issues about the epi-fluorescence tomography technique were identified. Time limitations do not allow extensive study of each issue. This chapter describes the effects of remaining issues and their potential solutions. The extension and potential applications of the proposed methods are also dis-cussed.

In Chapters 4 and 5, the proposed framework was evaluated through a series of simulations and experiments. Their main limitations were that the testing conditions were not sufficiently realistic compared to actual clinical practices, where the potential influencing factors include but are limited to tissue optical heterogeneity, background fluorescence, tissue surface shape, and crevices at the tissue–perturbator interface. This chapter discusses the effects of these factors and attempts to determine potential strategies.

7.1 Optical Heterogeneity

Optical heterogeneity is considered a nonuniform 3D distribution of tissue optical properties. This distribution is the basis of the forward process, which models the sensitivity matrix between a fluorophore, source positions, and detector positions. Thus, it may affect the estimation accuracy of FMT because the matrix is involved in all inverse processes. Many factors influence optical heterogeneity, including tissue components and biochemical environments. Among them, anatomical differences are the most significant factor. For example, in human skin (around 800 nm), scattering of the epidermis is approximately 2.5 times that of the dermis and eight times that of subcutaneous fat. The absorption of vessels (blood) is 59 times that of fat [151].

In this thesis, the simulated medium defined in the simulations and optical phantoms are all homogeneous. In the ex vivo evaluation, slight optical heterogeneity can be observed in the tested sample. Under this slight heterogeneous condition, the estimation errors increased slightly. Therefore, the extent to which more notable heterogeneity affects the performance of the proposed methods and framework is examined in this section. The effects of optical heterogeneity are first quantitatively evaluated by numerical simulation. Potential strategies are then discussed.

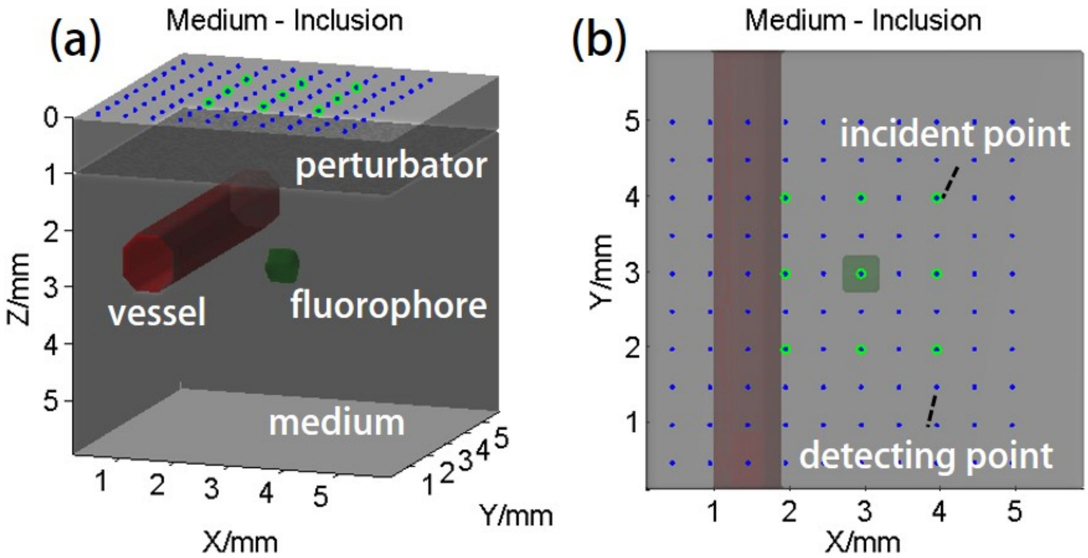

Figure 7.1: Setting of the Simulation on Optical Heterogeneity: (a) side view, (b) top view.

7.1.1 Simulation

Setting

The simulations were conducted in a 6×6×6 mm^3 medium. The optical coefficients of the medium were set to the literature values for human subcutaneous fat[1]. A small fluorophore inclusion was fixed in the center of the medium (3 mm, 3 mm, 3 mm). Thereafter, a vessel (diameter, 1 mm) filled with blood was assumed inside the medium. As shown in Fig. 7.1, the vessel transverses the medium horizontally along the Y axis. Its absorption coefficient was set to 59 times that of the background medium, thereby providing notable optical heterogeneity. The central depth of the vessel was varied from 0.5 to 5.5 mm, and its central X coordinate was set to 0.5, 1.5 and 3 mm. In other words, the center-to-center displacement of the vessel relative to the fluorophore varied vertically from –2.5 mm to 2.5 mm along the depth and varied from –2.5 mm to 0 mm along the horizontal direction. The perturbator thickness was

---

[1] at 800 nm

Table 7.1: Properties of the Simulated Medium, Vessel, and Perturbator

	Scattering Coef. [a]	Absorption Coef.	Refractive Index
Medium	0.83 mm^{-1}	0.011 mm^{-1}	1.37
Vessel	0.76 mm^{-1}	0.65 mm^{-1}	1.37
Perturbator	0.65 mm^{-1}	0	1.4

---

[a] optical properties at the emission and excitation wavelength were set as same for simplicity.

set to 1 mm. The optical coefficients of the perturbator, vessel, and medium are given in Tab. 7.1. To evaluate the effects of the optical heterogeneity, random noise was not introduced to the simulated data.

On the medium surface, 10 × 10 detector positions and 3 × 3 incident positions were assumed. For each simulated condition, fluorescent images before and after perturbation were generated by the Monte Carol method [34]. The existence of the vessel was considered in the forward process, but ignored in the inverse process. In other words, in the inverse process, the medium was considered homogeneous. On the basis of the generated data and using the aforementioned methods, the fluorophore inclusion's centroid and distribution were restored.

Results

In a preliminary evaluation of the effects of the vessel, two indexes were calculated, localization errors for the fluorophore centroid and normalized DCHM values of the restored distributions. The former was defined as the Euclidean distance from the estimated centroid to the actual centroid. The definition of DCHM is given in Sec. 5.2.3. Here to cancel out the intrinsic error contributed by regularization, the DCHM values of all simulated conditions were normalized by DCHM under the homogeneous condition (no vessel).

Figure 7.2 illustrates the representative results of these simulations. For the configuration shown in Fig. 7.2(a), the central coordinates of the vessel are (3, 3, 0.5 mm), i.e., it is close to the surface and located just 2.5 mm above the fluorophore inclusion. In the simulated fluorescent image (before perturbation, Fig. 7.2(c)), a significant intensity decrease can be observed on its central region along the Y-axis. Normally, this region is just above the fluorophore inclusion, thus should demonstrate the greatest intensity. This decrease shows that fluorescence is notably absorbed by the vessel. A similar phenomenon also occurs on the simulated images after perturbation. Consequently, the distributions of the intensity ratio resulting from the perturbation are distorted, which is expected in a concentric profile. This obvious distortion leads to a large localization error (2 mm) and an unexpected restored distribution (normalized DCHM = 0) as shown in Fig. 7.2(c).

In contrast, for the configuration shown in Fig. 7.2(e), the central coordinates of the vessel are (1.5, 3, 3.5) mm, i.e., it is deep inside the medium and horizontally distant from the fluorophore inclusion. Under this condition, both the simulated fluorescence image (Fig. 7.2(g)) and intensity (ratio Fig. 7.2(h)) demonstrate the expected single peak and concentric profile. Quantitatively, compared to the no vessel condition, the total intensity of the simulated fluorescence signals before and after perturbation decreases by only 7% owing to the presence of the deep vessel. For the shallow vessel configuration, this decrease is as large as 34%. Consequently, the localization error with the deep configuration is only 0.1 mm, and the normalized DCHM is 0.95. In other words, the deep vessel does not affect the accuracy of the proposed methods significantly.

Figure 7.3 shows the overall results of these simulations. As can be seen, large localization errors appear only when the vessel is above the inclusion. For the other

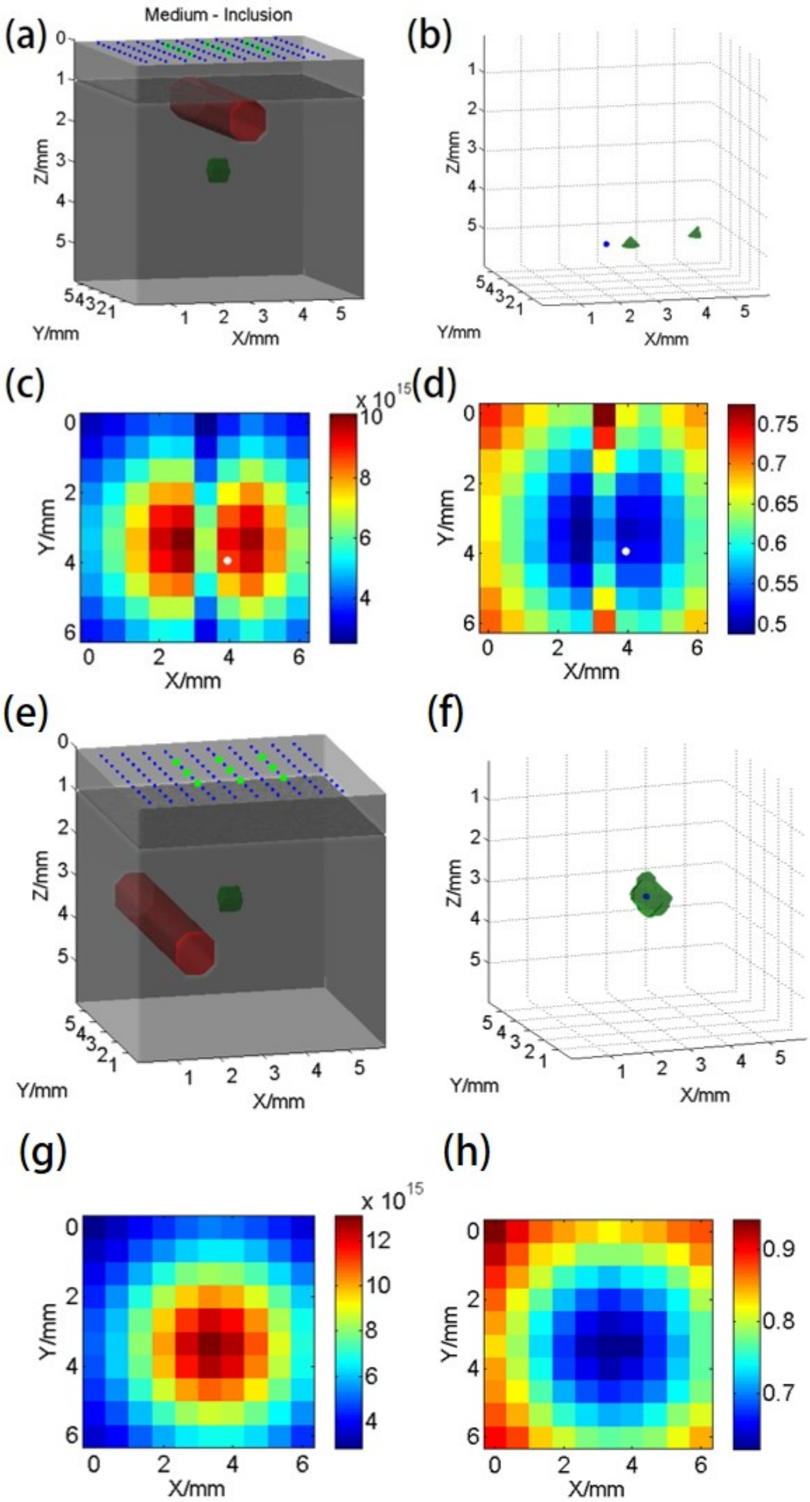

Figure 7.2: Representative Results of the Simulation on Optical Heterogeneity: (a) a shallow-vessel configuration, (b) 50% isosurface of restored distribution, (c) simulated data before perturbation, (d) intensity ratio for configuration (a); (e) a deep-vessel configuration, (f) 50% isosurface of restored distribution, (g) simulated data before perturbation, (h) intensity ratio for configuration (e).

positions, the errors are significantly smaller. For example, the error for positions 1.5 mm left of the inclusion are approximately 0.2 mm. Furthermore, errors for positions below the inclusion are in the order of 0.01 mm. Similarly, in terms of the dice coefficients, the normalized DCHM is close to zero when the vessel is close to the surface, whereas for the deep position, the values are close to one. These results suggest that optical heterogeneity in superficial tissue greatly affects the estimation accuracy of the proposed method, while the effects of optical heterogeneity in deep tissue are limited. Consider the effects of the vessel on light propagation in tissue. If an incident point (observation point) exists just above a shallow vessel, i.e., in a high absorption region, most incident (emitted) photons must pass through the vessel and are thus attenuated significantly. In contrast, after multiple scattering events, light propagation in deep tissue becomes diffusive, i.e., countless optical "paths" exist deep within tissues. A deep vessel only influences a few of the "paths", thereby having less effect on light propagation between the incident beam via the fluorophore inclusion to the detector. Therefore, when applying the ECW-FMT technique to notably heterogeneous tissues, measuring the volumetric distribution of optical coefficients in the surface and sub-surface regions is extremely important.

7.1.2 Diffuse Optical Tomography

A straightforward method to realize volumetric measurement of tissue optical coefficients in superficial tissue is DOT. As discussed in Section 2.1.2, DOT detects the reflectance or transmittance of incident light. Its main goal is to investigate local optical coefficient contrast within biological tissue, especially absorption variation resulting from blood activities. Normally, the primary issue with DOT arises from its ill-conditioned nature, similar to FMT. Its resolution and accuracy in reconstructing optical heterogeneity decrease with depth. However, according to these simulation

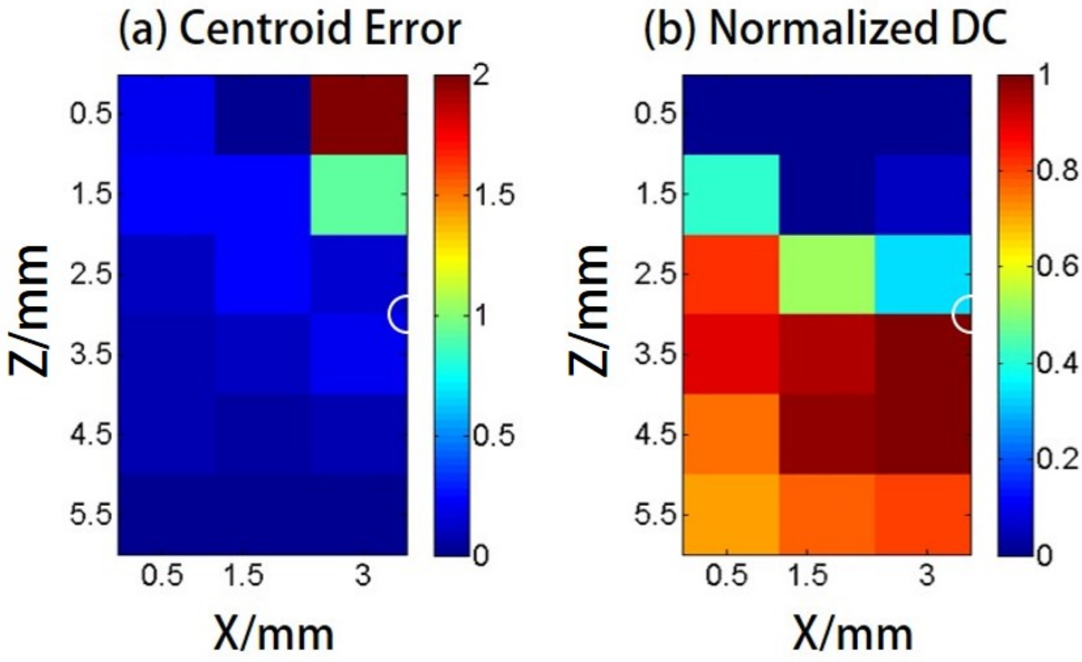

Figure 7.3: Overall Results of the Simulation on Optical Heterogeneity: (a) localization error, (b) normalized dice coefficient at half maximum. The white half circle denotes the boundary of the fluorophore inclusion.

results, the effects of optical heterogeneity in deep tissue are limited. Therefore, it may be reasonable to assume that deep tissue can be considered a homogeneous background medium. In other words, DOT is only required to restore the background optical coefficients and heterogeneity in relatively superficial tissues (e.g., up to 3-mm depth), which is the region DOT is adequate.

On the basis of the current ECW-FMT system, a DOT system can be realized easily by replacing the DM (Fig.3.1) with a half mirror and changing the wavelength band of the optical filters. Therefore, it is feasible to first set the system to DOT mode to measure 3D optical coefficient distribution and then set it to FMT mode for fluorescent imaging. The result of DOT, i.e., the tissue optical coefficients distribution, can then be used in the FMT computations to handle the optical heterogeneity issue.

7.1.3 Multi-modality Imaging

Another idea is to relate morphological information to optical heterogeneity. As mentioned above, anatomical differences are one of the most significant contributors to optical heterogeneity. Therefore, combining a morphological imaging technique to DOT or FMT is natural and has already been discussed. Brooksby et al. developed a DOT-MRI system for breast imaging [16]. Further, very recently, Wu et al. developed a structural-prior-based DOT method to reconstruct optical heterogeneity. In structural-prior-based DOT, the distributions of the optical coefficients of the phantom are restored with the aid of X-ray CT [169]. These studies employed prior morphological knowledge to mitigate the ill-conditioned nature of DOT, thereby allowing high resolution and good accuracy for DOT even in deep tissue. I strongly agree with the effects of these multi-modal studies and expect that such multi-modality imaging can be extended to clinical application of FMT.

To summarize, optical heterogeneity, especially when appearing in shallow tissue, potentially deteriorates the performance of the proposed methods. An effective strategy to solve this problem is to combine DOT, or even a morphological imaging modality, with FMT.

7.2 Background Fluorescence

7.2.1 Introduction

Herein, background fluorescence refers to fluorescence not emitted from the targeted tissue. Reasons for background fluorescence include endogenous fluorophore (auto-fluorescence) or the distribution of exogenous fluorescent dyes outside the targeted tissue. Although fluorescent dyes are supposed to accumulate in the targeted tissue, owing to the imperfect current fluorescent imaging agents, they are more or less residual in the background tissue. [138].

In the presence of background fluorescence, raw measured fluorescent images before the perturbation (after the perturbation) can be expressed as $\mathbf{I}_0 = \mathbf{I}_0^{tar} + \mathbf{I}_0^{back}$ ($\mathbf{I}_1 = \mathbf{I}_1^{tar} + \mathbf{I}_1^{back}$), where $\mathbf{I}_0^{tar}$ ($\mathbf{I}_1^{tar}$) denotes intensity contributions from the fluorescent object before (after) the perturbation, and $\mathbf{I}_0^{back}$ ($\mathbf{I}_1^{back}$) denotes intensity contributions from background fluorophore before (after) the perturbation. As a result, the raw intensity ratios $\mathbf{I}_1/\mathbf{I}_0$ may significantly differ from the target intensity ratio $\mathbf{I}_1^{tar}/\mathbf{I}_0^{tar}$. When applying $\mathbf{I}_1/\mathbf{I}_0$ to the inverse process, the weighted centroid of the fluorophore over the entire tissue can be obtained. However, to localize the fluorophore target, the background fluorescence component must to be removed first.

7.2.2 Method

As a preliminary evaluation, herein I only considered the condition that the background concentration is homogeneous within the tissue of interest. In this condition, to obtain background fluorescence images, one can simply transferred the laser beam to an incident position distant (i.e., 10 mm away) from the fluorophore object [2], and assumed that the image captured in this condition included background fluorescence only. Thereafter, after spatial registration and data interpolation, the background fluorescence components can be subtracted from the raw fluorescent images (captured under the usual beam scan) to obtain the target fluorescence components[3]. A similar method was used previously in Ref. [41] where the effect of background fluorescence

---

[2] The rough horizontal location of a fluorescent object can be determined by coarsely scanning the laser beam over the sample and comparing the brightness of images captured at all incident positions

[3] Light-collecting efficiencies of the system at different observation positions (corresponding to pixels on the camera) were calibrated beforehand using an optical phantom with known a homogeneous background fluorophore distribution (no additional fluorophore inclusion).

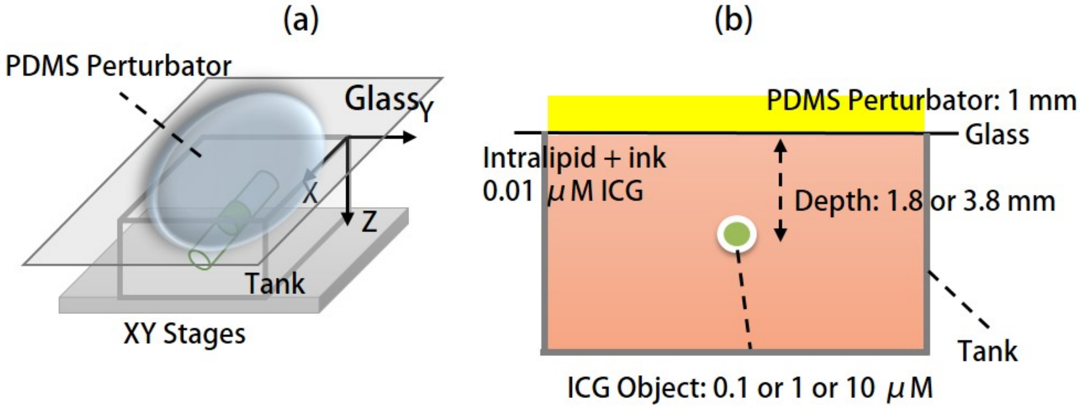

Figure 7.4: Schematic of the Phantom: (a) schematic of phantom configuration: one tube, 0.01μM ICG background fluorescence, and solid perturbator; (b) the Y-Z cross section of (a).

on transmission geometry FMT was investigated.

7.2.3 Experiments and Materials

Herein, a group of phantom experiments were performed. The configuration of the phantom was modified from that of the single object configuration described in Sec. 4.3.5. A single ICG object was submerged and fixed inside a plastic tank ($40 \times 90 \times 50$ mm^3) filled with the tissue-like (intralipid and ink) mixture. 0.01 μM ICG background fluorophore was added into the mixture (see Fig. 7.4). I set the ICG concentration inside the tube as 10, 1, and 0.1 μM sequentially. Thus, the target to background concentration ratio c_T/c_B was 1000, 100, and 10 respectively.

To simulate practical applications more realistically a PDMS perturbator was used, rather than the liquid perturbator in phantom experiments used of Chapter 4. To support the PDMS perturbator, a very thin glass slide was covered onto the tank which was initially filled with the tissue-like mixture. For the depth perturbation, the PDMS perturbator was superposed on the glass slide. Note that, the effect of the glass was considered in the forward process.

The experiments were conducted with the following steps:

1. fixed the tube to the predefined depth;
2. measured background signals;
3. measured fluorescent signals with beam scan;
4. superposed the PDMS perturbator onto the phantom (the glass slide);
5. measured fluorescent signals again;
6. repeated steps 1–4 for each condition N = 10 times.

For data preprocessing and centroid estimation, the same algorithms as described in Chapter 4 were used, except that the measured target intensity ratios $\mathbf{I}_1^{tar}/\mathbf{I}_0^{tar}$ rather than raw intensity ratio $\mathbf{I}_1/\mathbf{I}_0$ were applied to the inverse process.

7.2.4 Results

To show the effects of background fluorophore quantitatively, relative intensity contributions of the fluorophore target within the raw images for different target to background concentration ratio ($\mathrm{c}_T/\mathrm{c}_B$) were calculated. The relative contribution before the perturbation was defined as $t_0 = \sum_{ROI}\mathbf{I}_0^{tar}/\sum_{ROI}\mathbf{I}_0^{raw}$, where $\sum_{ROI}$ denotes brightness summation over the aforementioned ROI. Similarly, the relative contribution of the fluorescence target after the perturbation was defined as $t_1 = \sum_{ROI}\mathbf{I}_1^{tar}/\sum_{ROI}\mathbf{I}_1^{raw}$.

Measured values of t_0 and t_1 are given in Tab. 7.2 (standard deviation of all t_0 and t_1 values are of the order of 0.001). Notably, both decrease with a decreasing $\mathrm{c}_T/\mathrm{c}_B$,

Table 7.2: Results with Background Fluorescence (0.01 μM background ICG).

Depth (mm)	c_T/c_B (a.u.)	t_0 (a.u.)	t_1 (a.u.)	Δ_{tot} (mm)
1.8	1000	0.94	0.91	0.14±0.01
	100	0.59	0.52	0.08±0.02
	10	0.21	0.19	0.48±0.01
3.8	1000	0.76	0.71	0.13±0.06
	100	0.35	0.32	0.47±0.05
	10	0.06	0.04	2.02±0.10
blank	–	0	0	not converge

indicating that the target fluorescence components shrank greatly. In particular, for the 3.8 mm depth and $c_T/c_B = 10$ case, t_0 and t_1 were less than 0.1. In other words, background fluorescence played a dominant role. The values of t_1 were only slightly lower than those of t_0 indicating the perturbation did not result in an obvious decrease of the target's relative contribution.

On the other hand, the localization errors Δ_{tot} [4] basically increase with a decreasing target to background ratio (Tab. 7.2). This is attributable to the worsening SNR after the background removal. For a high background concentration the signal amplitude decreased significantly after background images were subtracted, whereas random noises and measuring errors remained. Furthermore, subtracting a background image cannot remove the background fluorescence completely because background measurement is also affected by various noises and errors. These noises and errors might be transferred to the data after background removal by the subtraction. If it is assumed that a localization error of less than 0.5 mm is acceptable, at 1.8 mm depth the concentration sensitivity limit would be approximately 0.1 μM (or $c_T/c_B \geq 10$); at 3.8 mm depth it would be approximately 1 μM (or $c_T/c_B \geq 100$).

---

[4] Defined as the Euclidean distance from the estimated centroid to the actual centroid

7.2.5 Sub-Dissusion

These results show that the background fluorescence level is an important factor for FMT. The $100--10:1$ lower limit for c_T/c_B is higher than the results provided in some previous researches [138, 41] in which transmission geometry FMT was studied. This high limit arises owing to the reflectance geometry of the MEFT system, rather than the depth perturbation, because depth perturbation does not worsen the relative contribution of the target greatly (see Tab. 7.2). Under reflectance geometry, the detection sensitivity is known to be surface weighted. That is, excitation light intensity at the surface or sub-surface is much higher than that in the deep region, and background fluorescence emitted from the surface is rarely attenuated by the tissue. As a result, if the concentration of a deep target is not one or two orders higher than the background level, the signal from the object may be buried in background fluorescence emitted from the surface or sub-surface. In addition, the small size (around 1.2 μL) of the ICG object is another reason for the high c_T/c_B lower limit. In many previous reports [138, 6] the fluorescent inclusion is usually a tube (tens of mm length) filled by fluorophore rather than an object with a short length (1.5 mm). A smaller fluorophore inclusion will apparently result in less target contribution, and thus a higher concentration sensitivity limit.

Currently, many technologies have been employed to eliminate background fluorescence. Some advanced methods to subtract background fluorescence have been established for FMT of transmission geometry [138, 41, 18]. However, because the effects of background fluorescence on the reflectance geometry is more significant than those of the transmission geometry, the feasibility of these methods needs further investigation. Furthermore, I believe that developing fluorophore imaging agents with extremely high target to background ratio, rather than the background removal methods, are the fundamental solution for this background fluorescence issue. Numerous dyes are synthesized to fluoresce in NIR wavelength range [89], where auto-fluorescence is known to be negligible [79]. In addition, unlike non-specific dyes that always fluoresce, some "activatable" dyes are engineered to be dark (or extremely weak) in base states but to strongly fluoresce only after interaction with targeted proteins or enzymes. For instance, Volkova et al. developed a protein-sensitive dye whose emission intensity increases up to 190 times after binding to bovine serum albumin [152]; Messerli et al. imaged apoptosis in cells using an enzyme selective dye that releases NIR fluorochrome (Cy5.5) after being activated by the targeted enzyme and allows 78-fold signal enhancement[102]. The increasing availability of such fluorescent dyes promise a bright outlook for the epi-fluorescence tomography technique.

7.3 Tissue Shape

The depth perturbation method superimposes a thin optical perturbator onto the tissue surface. Although our simulations and experiments were implemented on the basis of media with flat and horizontal surfaces, the silicon-based perturbator is actually sufficiently flexible to be tightly attached to most uneven tissue surfaces. As shown in Fig. 7.5(c), a PDMS perturbator can well match with a convex tissue surface with an approximately 90° turning angle. Similarly, for a deeply recessed surface, the perturbator can be inserted into the hollow and remain tight to the surface, as shown in Fig. 7.5(d).

However, for such extremely uneven surfaces, optical measurements may be challenging. For example, it is difficult for a camera fixed above the sample to observe the vertical side in Fig. 7.5(c) and the inner sides of the hollow in Fig. 7.5(d). For the convex condition, I recommend moving the camera along the curved surface or to use

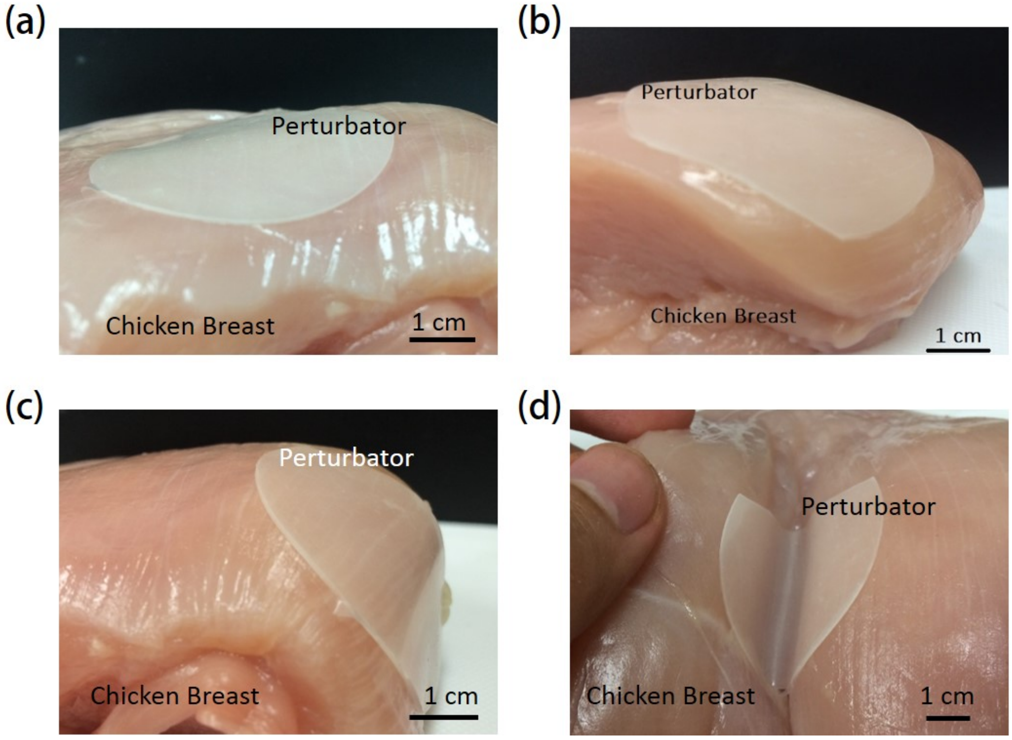

Figure 7.5: Perturbator Imposed on Uneven Tissue Surface: (a) on a relatively flat surface; (b) on a convex surface; (c) on a convex surface with almost 90 ° turning angle; (d) on a concave surface.

a mirror to reflect fluorescence emitted from the region outside the FOV of the camera (Fig. 7.6(a)). For the concave condition, if the hollow is sufficiently large, inserting a side-viewing endoscope [5] is a potential solution (Fig. 7.6(b)). Otherwise, the tissue surface must be artificially leveled, if that is permitted.

Another issue with irregular tissue surface is the forward problem: (1) incident and detector positions may not be on the same horizontal plane and (2) tissue volume cannot be simply divided into cubic voxels. Fortunately, there are already a large number of established techniques for simulating light propagation in realistic biological tissue [73, 13]. For example, by projecting a line pattern light onto tissue surface, the surface shape can be calculated on the basis of deformation of the lines [175]. There-

---

[5] A 45° mirror is fixed to the tip of the endoscope, allowing the observation of tissue parallel to the endoscope body.

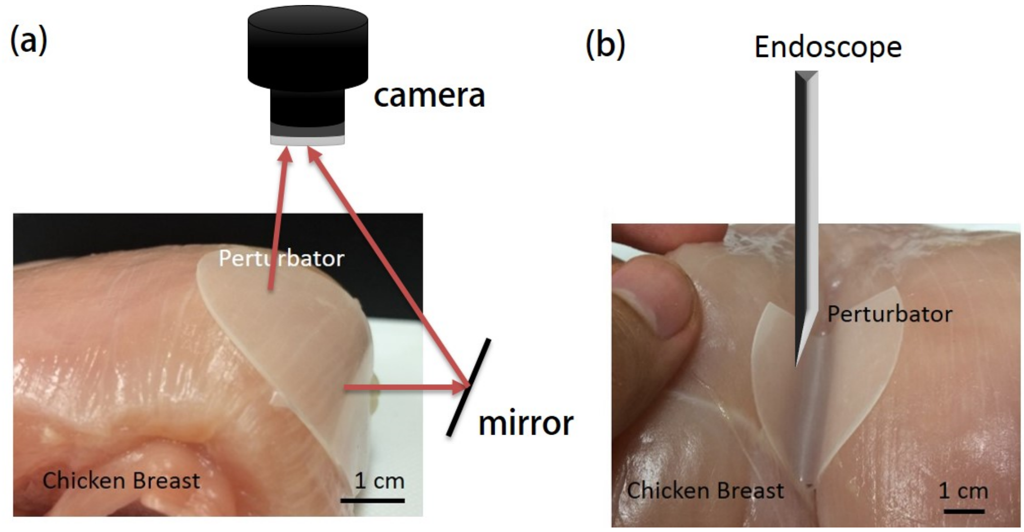

Figure 7.6: Adaptations of Fluorescence Measuring System for Irregular Tissue Shapes: (a) using mirror for the convex condition, (b) using endoscope for the concave condition.

after, the irregular tissue volume can be divided into triangular meshes and vertexes by the FEM. Finally, both the Monte Carlo method [33] and diffusion equation [132] have been proven compatible with the FEM and irregular tissue surfaces. Therefore, irregularity of tissue surface should not be a great obstacle in the development of epi-fluorescence tomography.

7.4 Crevices in Perturbator-tissue Interface

Some microstructures exist on tissue surfaces (e.g., skin textures and fingerprints), thereby making the surface uneven. Consequently, when a flat perturbator is superposed onto the surface, crevices may appear at the perturbator-tissue interface. When a crevice is sufficiently large (e.g., its diameter is close to 1 cm), it can be handled using a small perturbator, as shown in Fig.7.7 (a). However, for crevices ≤ 1 mm, producing a large number of very small perturbators to fill them is impractical. Here the effect of such crevices on the localization accuracy of the depth perturbation method is

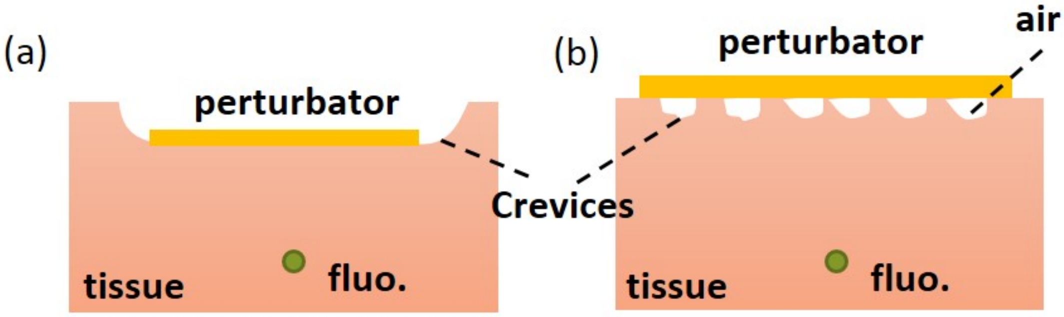

Figure 7.7: Crevices in Perturbator-tissue Interface: (a) a large crevice; (b) small crevices

examined.

For simplicity, I assume only air exists in the crevices and ignore crevice deformation owing to the weight of the perturbator. The air inside the crevices increases the internal reflection at the perturbator–tissue interface. The reflective indexes of air, common tissues, and the PDMS perturbator are 1.0, 1.37, and 1.4, respectively. For normally incident light, the reflectance of the PDMS-tissue interface is only 5e-5, whereas that of the PDMS–air interface and air–tissue interface are 2.7e-2 and 2.6e-2, respectively, increased by two orders. On the other hand, compared with biological tissues, the absorption and scattering of air is negligible. Light is thus rarely attenuated when propagating through air in crevices. The increased reflectance and lack of optical attenuation complicates the effects of the crevices. Thus, a simulation was performed to evaluate them quantitatively.

7.4.1 Simulation

The simulations were implemented in a 6×6×6 mm^3 medium. Optical coefficients of the medium and the perturbator (1-mm thick) were set as the same as those of the solid phantom and the solid perturbator described in Sec. 5.3. On the medium

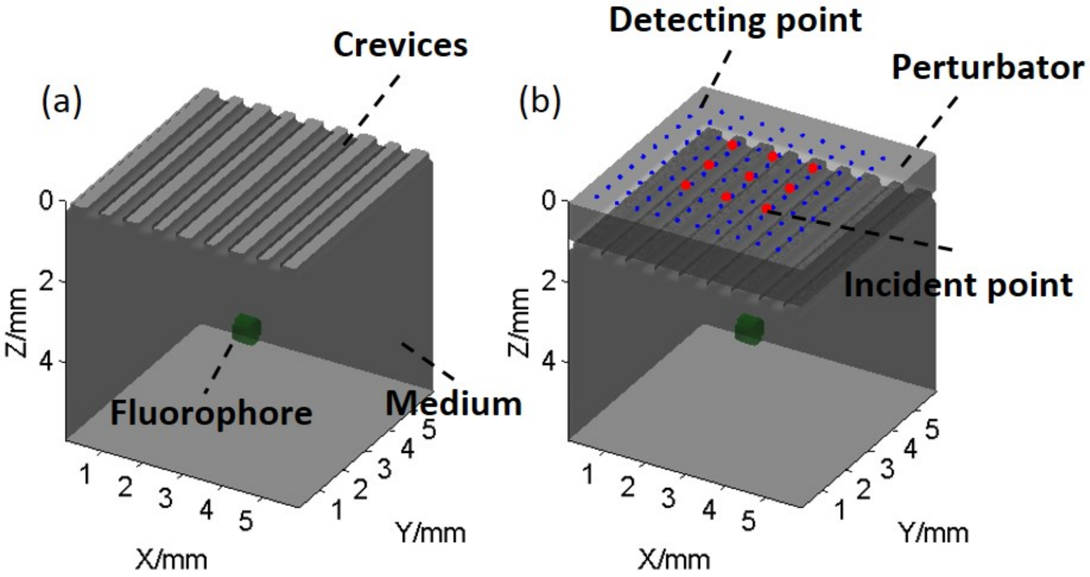

Figure 7.8: Setting of Simulations for Crevices in Perturbator-tissue Interface: (a) initial state when crevice cross-section radius is 150 μm; (b) after-perturbation of (a).

surface, 10 crevices aligned along the Y direction were defined, as shown in Fig. 7.8(a). The X direction separation (center-to-center) of two neighborhood crevices was 0.5 mm. Their cross-section radius varied from 50 to 250 μm [6]. One small fluorescent object (length, 0.5 mm; diameter, 0.6 mm) was fixed inside the medium. Its horizontal position was fixed at (3, 3) mm, and the central depth varied from 1.8 mm to 3.8 mm in 1-mm steps. Further, 10×10 observation positions (0.5-mm interval) and 3×3 incident positions (1-mm interval) were defined on the surface, as shown in Fig. 7.8 (b).

For each simulated condition, fluorescent images before and after perturbation were produced by the Monte Carol method using the MCX toolbox provided by Fang et al. [34]. In this forward process, the existence of crevices was considered. To evaluate the effects of the crevices independently, random noise was not introduced to the simulated data. The simulated data were then applied to the inverse process

---

[6] I did not consider a larger radius because the center-to-center separation between two crevices is only 0.5 mm. A radius greater than 250 μm will let all crevices connect and let the perturbator float above the medium which is physically impractical

Table 7.3: Localization Errors (mm) Contributed by Crevices

depth (mm)	cross-section radius (μm)		
	50	150	250
1.8	0.02	0.2	0.24
2.8	0.02	0.14	0.24
3.8	0.04	0.17	0.5

described in Chapter 4. Unlike the forward process, the crevices were not considered in the inverse process computations because in practice it is difficult to measure the micro-structures of tissue surfaces because of limited time and cost constraints. By investigating the localization error resulting from ignoring the crevices, the effects of crevices can be understood roughly.

7.4.2 Results

The localization errors for all simulated conditions are given in Tab. 7.3. For all tested conditions, errors are no greater than 0.5 mm. The errors increase with cross-section radius as expected because as crevice size increases more photons passing through the perturbator-tissue interface are affected. The errors also increase with fluorophore depth. This is attributable to the dependency of the intensity ratio Γ on the fluorophore depth d. As shown in Fig. 2.6, the slope of the Γ-d curve decreases with fluorophore depth. In other words, even for the same variation of intensity ratios resulting from the crevices, the resultant localization error will be large for a large fluorophore depth d.

These results suggest that crevices with cross-sectional radius less than 200 μm do not result in a very large localization error. Therefore, tissue with relatively small crevices is more appropriate for the depth perturbation method. For example, the radiuses of crevices in the skin is commonly less than 100 μm[104]. The early diagnosis of skin cancer can thus be considered a potential application of the proposed method.

7.5 Measurement Errors in Tissue Optical Properties

In Chapters 4 and 5, the location, concentration, and bio-distribution of fluorophore were treated as unknowns in the computation. In contrast, a large number of parameters (Tab. 4.1) are considered known prior to the fluorescence measurements. Some, including laser-beam size and the optical coefficients of the perturbator, can be measured carefully ahead of time and are thus reliable. Others, including incident positions, detector positions, detector numerical aperture, and FOV size, can be determined accurately by simple calibrations in the field. Compared with these parameters, measuring tissue optical properties is more complex. As described in Sec. 2.1.2, some techniques have been established to determine absorption coefficient μ_a and reduced scattering coefficient μ_s' of tissue even under in-vivo conditions. These techniques typically involve multiple-point diffuse reflectance measurements, data calibration, and parameter estimation. The complexity of these steps may yield measurement errors in the determined optical coefficients. In addition, in many studies, including this thesis, the refractive index n of tissue is simply set to 1.37. This is partly valid because, for most biological tissues the n ranges from 1.37~1.40 and is nearly invariant with optical wavelength. However, a few tissue types, such as skin stratum corneum ($n = 1.55$) and calcified aorta ($n = 1.53$), have notably higher refractive indexes [151]. In this subsection, the effects of inaccurate μ_a, μ_s' and n on fluorophore localization are examined through numerical simulations.

7.5.1 Method

The simulations were implemented with the same setting described in the Sec. 7.4.1, except that the simulated tissue has an even surface. In these simulations, two groups of tissue optical coefficients were used: " actual" optical coefficients and "measured" optical coefficients. The former ones were used in the forward process to generate the simulated fluorescent signals. The latter were considered as measured values with potential errors, and applied to the inverse process to localize fluorophore. To evaluate the effects of measurement errors on tissue optical coefficients, the measured group was intentionally different from the actual group. Three configurations of measured tissue optical coefficients were considered. In configuration S1 (S2), the measured μ_s' (μ_a) was varied 0.5 – 2 times the actual value (i.e. percentage measurement error: -50% – +100%), while others were set as same as the actual values. In configuration S3, the measured n was varied 0.9 – 1.4 times the actual (i.e. percentage measuring error: -10% – +40%), whereas others were unchanged. Table 7.4 shows the values of the "actual" optical coefficient and the variation ranges of "measured" optical coefficients. The subscript $_{ex}$ and $_{ex}$ denote the excitation and the emission wavelength, respectively. For each condition, the inverse process was executed and the localization error, defined as the distance from the estimated fluorophore centroid to the actual central location, was calculated. In these simulations, the fluorescent object was set at a depth of 3.8 mm and 4.8 mm, sequentially.

7.5.2 Results

Localization errors contributed by the inaccuracies of tissue optical properties are shown in Fig. 7.9. For both 3.8- and 4.8-mm fluorophore depths, the errors are notable and increase with the inaccuracy. For the case in which μ_s' is underestimated

Table 7.4: "Actual" and "Measured" Optical Coefficients (mm^{-1}) used in the Simulation

	$\mu'_{s,ex}$	$\mu_{a,ex}$	$\mu'_{s,em}$	$\mu_{a,em}$	n
Actual	0.65	0.02	0.56	0.02	1.37
Measured - S1	0.33 ~ 1.3	0.02	0.28 ~ 1.2	0.02	1.37
Measured - S2	0.65	0.01 ~ 0.04	0.56	0.01 ~ 0.04	1.37
Measured - S3	0.65	0.02	0.56	0.02	1.23 ~ 2.74

by 50%, the resultant errors are approximately 3 mm. For the worst conditions (100% overestimation) of S2 and S3, the errors are also greater than 1 mm.

7.5.3 Sub-Discussion

Of course, for a effective tissue optical coefficients measurement technique, the potential error range should be notably smaller than the values used in these simulations. For the oblique-incidence reflectometry technique used in this thesis, which is proposed by Wang et al., the relative estimation errors of μ_a were reported as in the range of -11.8 – 5.1 %, and those of μ'_s were -4.8 –3.9 %. When interpolating these ranges into the simulation results, resultant errors should be less than 0.3 mm [7]. On the other hand, when the inaccuracy of n is less than ±5%, the localization errors are not obvious. In other words, for most biological tissues in which n falls in the range of 1.30 – 1.44, directly using a value of 1.37 will be acceptable. In contrast, when some specific tissue types (e.g., skin stratum corneum) with higher n are involved, n must be measured in field or referenced from literatures.

---

[7] If applying the μ'_s error range to S1 results, the largest error is 0.28 mm for 4.8-mm fluorophore depth, and 0.23 mm for 3.8-mm fluorophore depth. Similarly, the If applying the μ_a error range to S2 results, the largest error is 0.24 mm for 4.8-mm fluorophore depth, and 0.26 mm for 3.8-mm fluorophore depth.

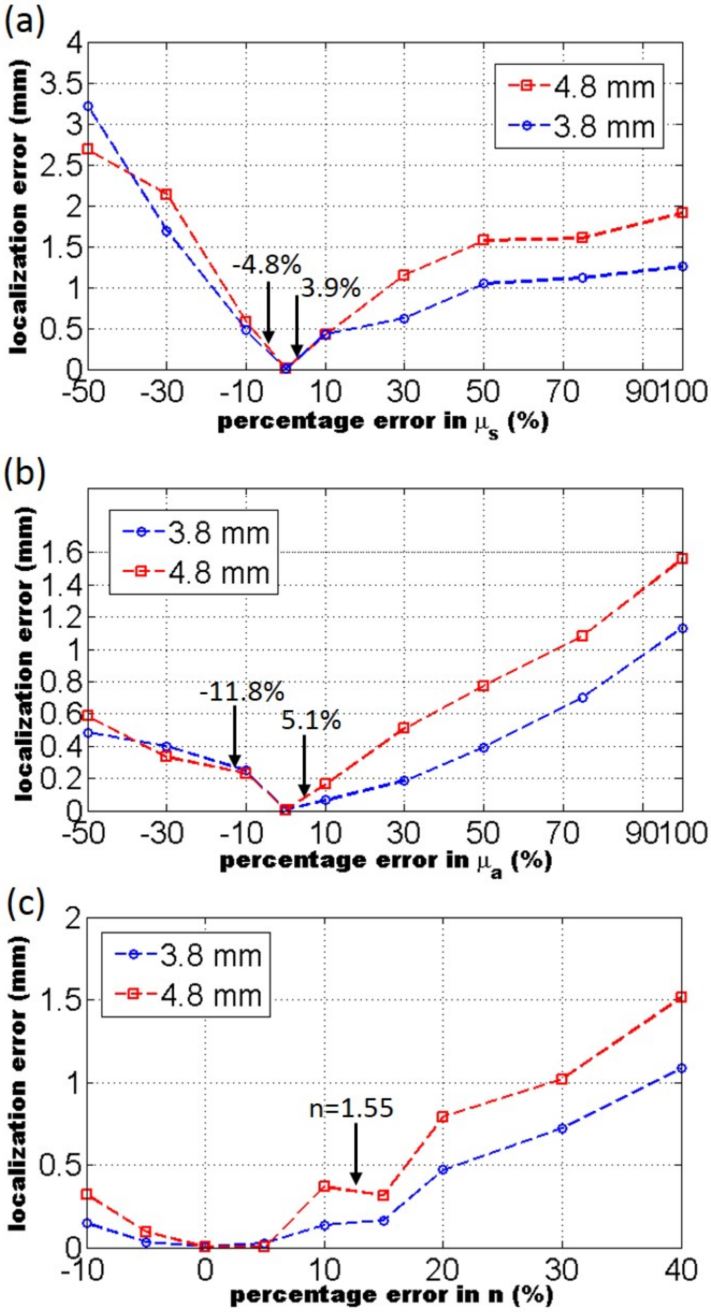

Figure 7.9: Effects of Inaccurate Measured Tissue Optical Properties: (a) S1 results (inaccurate μ_s'); (b) S2 results (inaccurate μ_a); (c) S3 results (inaccurate n). The arrows in (a) and (b) show the reported error ranges [86] of the OIR technique (see Appx. B). The arrow in (c) indicates the n of skin stratum corneum which has the highest n among biological tissues as far as I know. The results of 3.8-mm (4.8-mm) fluorophore depth are shown in blue (red).

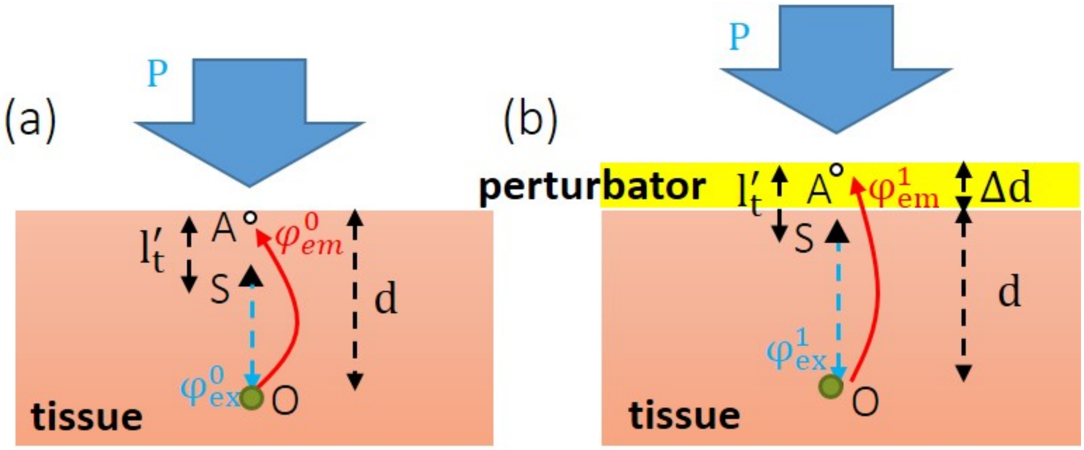

Figure 7.10: Depth Perturbation under Board illumination: (a) the initial state, (b) after perturbation

7.6 Extension of the Depth Perturbation Method

In this thesis, the depth perturbation method was mainly verified and evaluated under narrow beam illumination. Theoretically, the proposed depth perturbation method is also viable when a broad incident light beam is used.

Consider the condition shown in Fig. 7.10. For simplicity, it is assumed that the incident light is an infinitely broad top flat beam [8]. The refractive index mismatch at the air-tissue boundary is also ignored. The expression for excitation fluence rate at point O changes from Eq.2.1 to

$$\varphi_{\mathrm{ex}}^0(\mathrm{d}) = \mathrm{C'}_{\mathrm{ex}}\exp(-\mu_{\mathrm{eff}}^{\mathrm{ex}}\mathrm{d}), \tag{7.1}$$

where $\mu_{\mathrm{eff}}^{\mathrm{ex}}$ denotes the effective attenuation coefficient at the excitation wavelength; $\mathrm{C'}_{\mathrm{ex}}$ is a constant, and d is the depth of the fluorophore point source. By contrast, the

---

[8] The intensity on the top is uniform

expression for emission fluence rate at point A is the same as the Eq.2.2

$$\varphi^0_{\mathrm{em}}(\mathrm{d}) = \mathrm{C}_{\mathrm{em}}\exp(-\mu^{\mathrm{em}}_{\mathrm{eff}}\mathrm{d})/\mathrm{d}, \tag{7.2}$$

where $\mu^{\mathrm{em}}_{\mathrm{eff}}$ denotes the effective attenuation coefficient at the emission wavelength and C_{em} is another constant.

As a result, the ratio of fluorescence intensity with perturbation to the initial status at point A can be expressed as:

$$\Gamma = \frac{\Phi_1}{\Phi_0} = \exp\left[-(\mu^{\mathrm{ex}}_{\mathrm{eff}} + \mu^{\mathrm{em}}_{\mathrm{eff}})\Delta\mathrm{d}\right]\frac{\mathrm{d}}{\mathrm{d}+\Delta\mathrm{d}}. \tag{7.3}$$

Compared to the same expression under pencil beam illumination (Eq. 2.5) this expression is simpler but also a monotonic increasing function of d. For comparison, the dependencies of Γ on fluorophore depth *d* under broad illumination (top flat light beam) and under a pencil beam illumination are shown in Fig. 7.11 [9]. The viability of the depth perturbation method under broad illumination means that the use of depth perturbation can be extended from FMT to conventional fluorescent imaging. In other words, even without a beam scan, the depth perturbation method can resolve the fluorophore depth.

7.7 Potential Application Scope

In this study, a reflectance geometry FMT system has been developed to restore the location and size of fluorophore located inside biological tissue, and a depth perturbation method has been proposed to localize the fluorophore centroid, which alleviates the severely ill-conditioned traditional optical inverse problem and con-

---

[9] Calculated using the same optical properties as Fig. 2.6

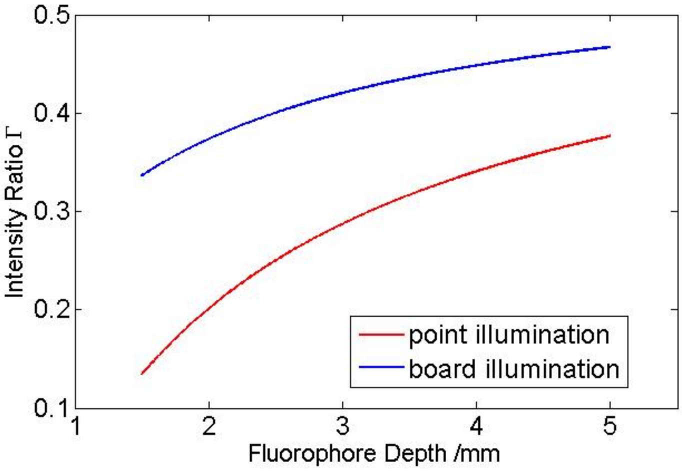

Figure 7.11: Intensity Ratio under Broad Illumination

tributes to unbiased recovery of fluorophore distribution.

As described in Chapter 1, fluorescent imaging has great potential in angiography, early disease diagnosis, and the determination of the surgery margin. With the assistance of the proposed system and methods, the applications of fluorescent imaging can be extended from surface or subsurface tissues to deep tissue (up to 1 cm). However, the implementation of the proposed methods brings new limitations.

First, owing to the necessity of a 2D beam scan, it is difficult for the current system to track biomedical processes that change quickly. For example, monitoring blood activity may be inappropriate for the proposed system. However, localizing stable targets, e.g., a florescent dye accumulated in a tumor, is a desirable application.

Second, as discussed in Sec. 7.2, owing to the surface-weighted sensitivity matrix, imaging agents with high TBR are preferred; otherwise, signals from a deep target may be buried in background noise. Consequently, I recommend the use of targeted or activatable fluorescent imaging agents rather than conventional unspecific dyes in epi-fluorescence tomographic imaging.

Third, because too many crevices on a tissue surface increase the localization error (Sec.7.4), and tomographic imaging on an extremely uneven tissue surface is challenging and requires complex calibrations for surface shape and light-collecting efficiency (Sec.7.3), relatively flat and smooth surface is preferred for the proposed system and depth perturbation method. Therefore, skin, breast, and inner organs, such as the lungs and stomach (under thoracic or abdominal surgery), are appropriate subjects. In contrast, since the surface of the brain is wrinkled, superimposing a depth perturbator onto the surface and ensuring good contact may be challenging. A small and extremely flexible perturbator will be helpful under such conditions.

To summarize, the proposed system and methods are appropriate for tissues with a relatively flat surface for imaging time invariant (or slowly variant) targets, with the assistance of advanced high TBR florescent imaging agents. Under such conditions, the proposed depth perturbation method can determine the fluorophore centroid quickly and effectively, thereby providing the depth information of a targeted lesion. Furthermore, on the basis of prior centroid knowledge, the proposed reconstruction framework partly overcomes the ill-conditioned nature of the FMT inverse problem, thereby ensuring that the restored fluorophore size is unbiased. Thus, the proposed framework can be applied to disease staging and the determination of the surgery margin. Finally, although the proposed depth perturbation method can determine depth more accurately, it does not extend the intrinsic penetration depth of light (approximately 1 cm). Consequently, it is difficult for the proposed system and methods to detect disease foci that are deeper than this limit. However , even for deeply located disease foci, the proposed system and methods can be used to confirm whether the disease foci have been completely removed by surgery. Thus, optical measurement of tissues after the foci have been removed becomes feasible.

7.8 Conclusion

In this thesis, I have discussed on several critical issues about epi-fluorescence tomog¬raphy, including the depth resolution, the ill-conditioned optical inverse problem, and high computational cost. A depth perturbation concept has been proposed to localize a fluorophore (centroid) within tissues, by which the probing depth of ECW-FMT is extended from 1–2 mm [12] to around 1 cm [10]. This centroid prior was added to the reconstruction process of fluorophore bio-distribution as a new constraint, which ensures that the restored bio-distribution is unbiased. I have also proposed a PSVR method to avoid overly smoothed distributions, which decreases the percentage error of estimated fluorophore size to approximately 30%. Using the same method, the profile of fluorophore distribution can be better restored than the conventional SVR method.

The proposed methods were evaluated by numerical simulations, phantom experiments, and ex vivo experiments. Although the evaluation environments were not sufficiently realistic, feasibility and effects were verified preliminarily. Some potential clinical issues, including optical heterogeneity, background fluorescence, and ir-regularity of tissue surface, were discussed quantitatively. Among these issues, optical heterogeneity and background fluorescence were proved critical factors. The former can be solved by multi-modality imaging, i.e., combining a DOT or a morphological imaging modality with FMT. On the other hand, in my opinion, the rapid development of highly selective fluorescent dyes will continue to reduce the effects of

---

[10] Dependent on tissue optical coefficients, fluorophore concentration and other factors

the latter.

It is expected that the proposed system can be integrated to microscopy, thereby allowing its application in microscopic surgeries. The validation of the proposed depth perturbation under broad illumination is important. If it is validated, it can be applied to conventional fluorescent image-guided surgeries and an endoscopic environment. In addition, some concepts can be applied to improve the proposed depth perturbation method. For example, changing the incident angle of the laser beam can result in variations of optical path length, which may facilitate integration of the proposed depth perturbation method and the SDS method. In addition, for reconstruction of fluorophore bio-distribution, the workflow and parameters require further optimization.

It is my hope that this research will extend the scope of application of conventional fluorescent imaging from surface to deep issue, and that my work will contribute to early cancer diagnosis and to the field of low invasive surgeries.

A Solid Perturbator

The process to fabricate a solid thin optical phan¬tom is described. The phantom is used as a depth perturbator in the depth perturbation method. In this thesis, the perturbators described here were primarily applied in the ex vivo experiments (Chapter 6) and the optical solid phantom experiments (Chapter 5)

A.1 Introduction

The proposed depth perturbation method uses a thin scattering phantom with known optical properties to change the depth of the fluorophore inside biological tissue. The phantom was designed to be superimposed on the tissue surface; therefore, it should be nontoxic, sufficiently flexible for a non-planar irregular surface, and able to change the optical depth [1] of the fluorophore, i.e., the optical path length from the fluorophore to the surface.

A.2 Materials and Methods

PDMS was utilized as the phantom base. As a widely used silicon-based organic polymer, PDMS is optically clear, and fulfills the nontoxic, and flexible requirements [97]. Initially, PDMS (Silpot 184, Toray) is a viscous liquid, similar to honey [165], whereas after hardening [2], it becomes an elastic rubber-like solid.

To add the scattering property, white powdery TiO2 was mixed into the PDMS before hardening. Scattering occurs when light hits the TiO2 powder. The scattering coefficient of the phantom depends on the weight concentration of TiO2, as shown in Tab. A.1. Therefore, by adjusting the weight concentration of TiO2, an optical phantom with tissue-like scattering properties can be produced. The absorption coefficient of the TiO2-PDMS phantom is close to zero, which avoids unnecessary loss of emitted fluorescence. The refractive index of PDMS is 1.4 [93].

Finally, a mold was utilized to control the size of the hardened PDMS phantom. The mold was made of unilate, a hard synthetic resin material, using a cutting machine.

---

[1] Not only the physical depth

[2] PDMS hardening usually requires a hardening material, high temperature environment, and several hours.

Table A.1: Scattering Coefficient of TiO_2 in PDMS: values were measured using the OIR technique described in Appx. B

Weight Concentration (%)	Reduced Scattering Coefficient μ'_s (mm^{-1})	Absorption Coefficient μ_a (mm^{-1})
0.05	0.34±0.01	0
0.1	0.54±0.02	0
0.2	0.89±0.02	0.02

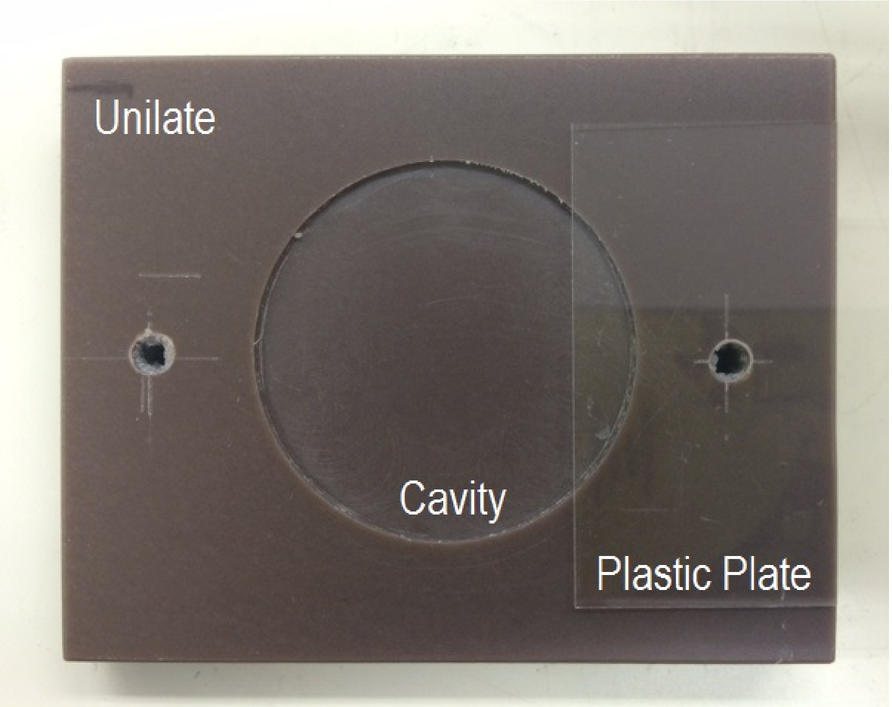

Figure A.1: Mold for the Solid Perturbator

The mold is a cuboid with a shallow cylindrical cavity (depth, 1mm; diameter, 45 mm) on the top. After pouring the liquid PDMS into the cavity, the cavity was covered by a plastic plate to remove redundant PDMS. The remaining PDMS liquid transforms to a thin phantom after hardening for several hours.

The steps involved in producing the solid perturbator are listed below.

1. Prepare liquid PDMS and hardening material with a weight ratio of 10:1.

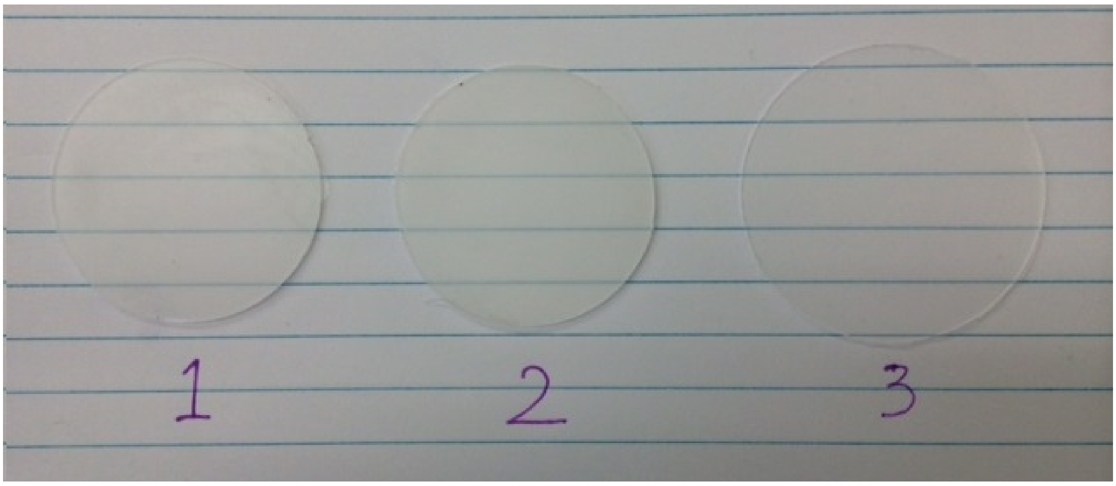

Figure A.2: Solid Perturbators

2. Add TiO2 powder to the liquid PDMS and thoroughly mix.

3. Pour a comparable volume of the PDMS-TiO2 liquid into the mold cavity and cover with a plastic plate.

4. Put the mold into an oven at high temperature (e.g., 70°C) for several hours.

5. Remove the hardened PDMS-TiO2 phantom from the oven.

A.3 Result

Three perturbators produced by the proposed method are shown in Fig.A.2. Their properties are listed in Tab.A.2. Perturbator No. 3 is the thinnest and has the lowest TiO2 concentration. Consequently, compared with No 1 and No 2, the blue lines under perturbator No. 3 are the clearest. Perturbator No. 2 is the thickest and has the highest TiO2 concentration, resulting in an obviously blurred view of the blue lines.

Table A.2: Properties of Solid Perturbators Shown in Fig. A.2

No.	Weight Concentration (%)	Thickness (mm)	Reduced Scattering Coefficient μ_s' (mm^{-1})
1	0.1	0.98	0.54
2	0.1	1.15	0.54
3	0.05	0.75	0.34

A.4 Discussion

The perturbators were produced using three different molds whose size and thickness vary slightly. The designed depth and diameter of the molds was the same; however, owing to the inadequate precision of our cutting machine, the cavity size deviated slightly. Note that this did not affect the use of the perturbators because perturbator thickness can be input as a parameter in the inverse process for localizing the fluorophore centroid (Chapter 4). The perturbator diameter would be fine only if the perturbator is larger than the FOV of the measuring system.

B In situ Measurement of Biological Tissue Optical Properties

In this thesis, an oblique-incidence reflectometry technique is used to measure tissue optical coefficients. This method was first proposed by Wang et al. [154]. In this appendix, a custom setup, phantom experiment results, and ex-vivo measured optical coefficients of several biological tissues are described.

B.1 Introduction

As inferred by its name, the oblique-incidence reflectometry (OIR) technique uses an obliquely incident laser beam as the light source. Further, OIR samples the relative profile of diffuse reflectance [86] and finally induces absorption coefficient μ_a and reduced scattering coefficient μ_s' from the profile and beam incident position. I selected this technique because it (1) enables non-contact and non-invasive measurement of tissue optical properties; (2) only requires to measurement of relative diffuse reflectance profile, which avoids the complicated calibration process required for quantitative measurements.

B.2 Principle

The principle of this technique relies on the assumption that a narrow laser beam incident on a semidefinite scattering medium is equivalent to an isotropic point source located at the extension line [1] of the beam and one transport mean free path (mfp') away from the incident position. As a result, the horizontal position of the equivalent point source deviates from the initial incident position. According to the diffusion theory, the deviation Δx can be calculated as

$$\Delta x = \frac{\sin \alpha_i}{n {\mu_t}'} \tag{B.1}$$

where α_i is the incident angle, n is the refractive index on the boundary and $\mu_t' = \mu_s' + 0.35\mu_a$ is the total attenuation coefficient [2].

---

[1] If the laser is incident on a refractive index unmatched boundary, the location is affected by Snell's law

[2] μ_t' should be defined as $\mu_t' = \mu_s + \mu_s$. However, according to Wang et, al [154], this modified equation leads to a better measurement accuracy. In this thesis, I use this modified expression only under conditions that involve optical properties measurements.

Furthermore, the diffuse reflectance profile [3] obeys the diffuse equation, and can be expressed as [86]

$$R(r) = 3D(\mu_{\text{eff}} + \frac{1}{\rho_1})\frac{\exp(-\rho_1\mu_{\text{eff}})}{\rho_1^2} + (3D + 4AD)(\mu_{\text{eff}} + \frac{1}{\rho_2})\frac{\exp(-\rho_2\mu_{\text{eff}})}{\rho_2^2} \tag{B.2}$$

where $\mu_{\text{eff}} = \sqrt{3\mu_a(\mu_a + \mu_s')}$ denotes the effective attenuation coefficient. ρ_1 and ρ_2 denote the distances from the equivalent source and its virtual negative point sources[4] respectively, to a observation point on the sample surface at a radius r from the axis of the equivalent point source; $D = 1/(3\mu_t')$ denotes the diffusion coefficient; and A is a constant determined by the reflective index. By fitting the measured diffuse reflectance values to this model, μ_{eff} and D can be estimated simultaneously. Since both D and μ_{eff} are functions of μ_s' and μ_a ,they can be deduced as

$$\mu_a = D\mu_{\text{eff}}^2 \tag{B.3}$$

$$\mu_s{}' = \frac{1}{3D} - 0.35\mu_a \tag{B.4}$$

For a detailed explanation of this technique, see Ref. [154, 86].

B.3 Method and Material

In this section, the custom setup of the oblique-incidence reflectometry system and several verification experiments are described.

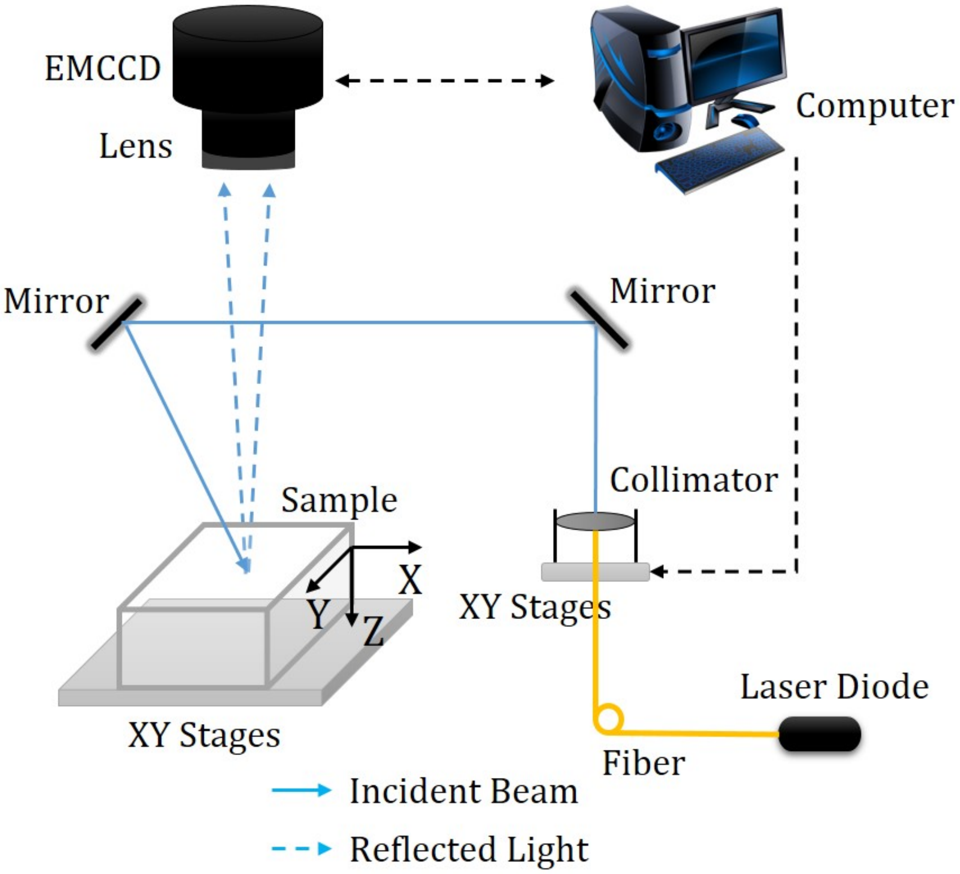

Figure B.1: Schematic of OIR System

B.3.1 Oblique-incidence Reflectometry System

Figures B.1 and B.2 show the custom OIR system schematic and setup, respectively. The setup includes many components of the ECW-FMT system, including the EMCCD camera, lens, PBS[5], fibers, collimator and laser system. Thus, it is theoretically possible to combine the two systems. The specifications of the OIR system components are given in Tabs. 3.1 and 3.2. The tilt angle of the mirror in Fig. B.2 determines the incident angle of the laser beam. Here the incidence angle is arranged to $\alpha_i = 50°$.

---

[3] More than one mfp' far from the incident point
[4] Mirrored point source to fulfill the boundary condition. For details see [157]
[5] Here it is used as a mirror

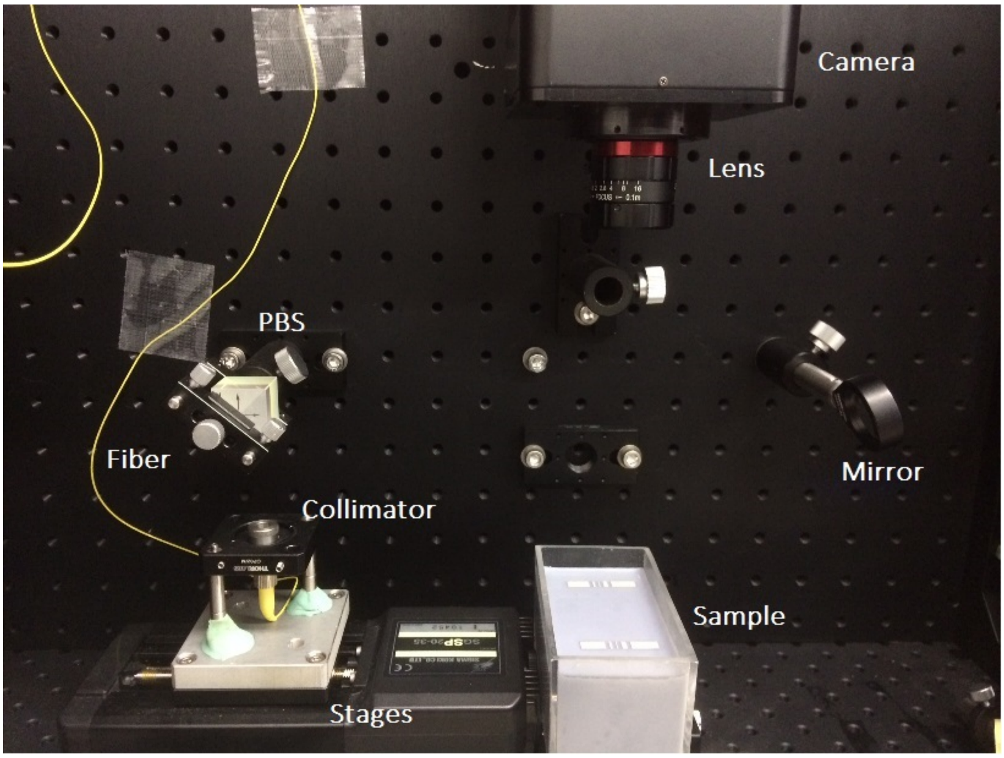

Figure B.2: Setup of the OIR System

B.3.2 Phantoms

A liquid phantom comprising intralipid (scatter), black ink (absorber), and water was used to mimic the scattering and absorption properties of biological tissues. Six phantoms with different volume concentrations of intralipid and ink were produced (Tab. B.1). The true absorption coefficient of the black ink was 0.050 $\mathrm{mm}^{-1}/(\mathrm{mL/L})$ as measured by a spectrophotometer. About the scattering coefficient of intralipid solution, many different values are reported in literatures [149, 36], which may be attributed to differences among intralipid producer. Herein, an integrated sphere method [117] was used to measure μ_s' of the intralipid solution (volume concentration, 1%) independently. The integrated sphere method is the most commonly used method in the bio-optic field. However, it is unavailable in in situ and non invasive measurements owing to the need to slice the sample thinly.

Table B.1: Phantom Composition: volume concentrations of intralipid and ink

Phantom No.	Intralipid	ink
1	0.33%	0
2	0.66%	0
3	1.00%	0
4	1.00%	0.20%
5	0.66%	0.13%
6	0.33%	0.20%

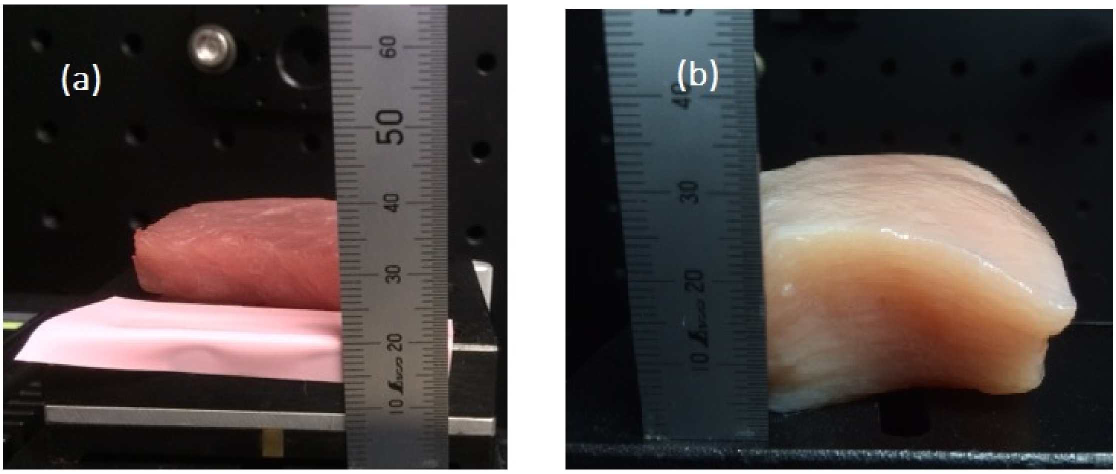

Figure B.3: Ex-vivo Samples: (a) pork chuck and (b) chicken breast

B.3.3 Tissue Samples

Two biological tissue samples were tested using the system, including chicken breast and pork chuck. Each had a thickness greater than 1 cm, and thus they can be approximated to a semi-infinite medium considering the limited penetration depth of light. For simplicity, several locations with a flat surface and without significant heterogeneity were selected. Five locations on each sample were tested.

B.3.4 Experiment Steps

In each test, the experiment was executed as:

- Obtain an image of the incident point using an extremely thin reflection plate[6] .
- Obtain an image of the diffusion reflectance with a short exposure time (typically 2 ms).
- Obtain an image of the diffusion reflectance again with a longer exposure time (typically greater than 5 ms)

The image captured with a longer exposure time always leads to saturation around the incident position, but can effectively detect the profile of the region far from the incident position. Imaging twice is a good choice for a camera with limited dynamic range.

B.3.5 Data Processing

Figure B.4 shows representative images captured by the oblique-incidence reflectometry system. To extract the optical coefficients, the centroid of the original reflected pattern is computed as the incident point (Fig. B.4(a)). Then, the saturated part on the long exposure image (Fig. B.4(c)) is replaced with data from the short exposure (Fig. B.4(b)) multiplied by the exposure time ratio to generate a complete and clear reflectance pattern (Fig. B.4(d)). The data on the central line along the X-axis is obtained and used to calculate Δx as shown in (Fig. B.4(e)). The profile is then applied to curve fitting (e.g., the trust-region method) to solve the optical coefficients.

B.4 Results

Here the estimated optical coefficients obtained the custom OIR system are provided. For comparison, some expected values and values reported in the literature

---

[6] Made of a piece of cover glass and white paint with 0.15 mm thickness

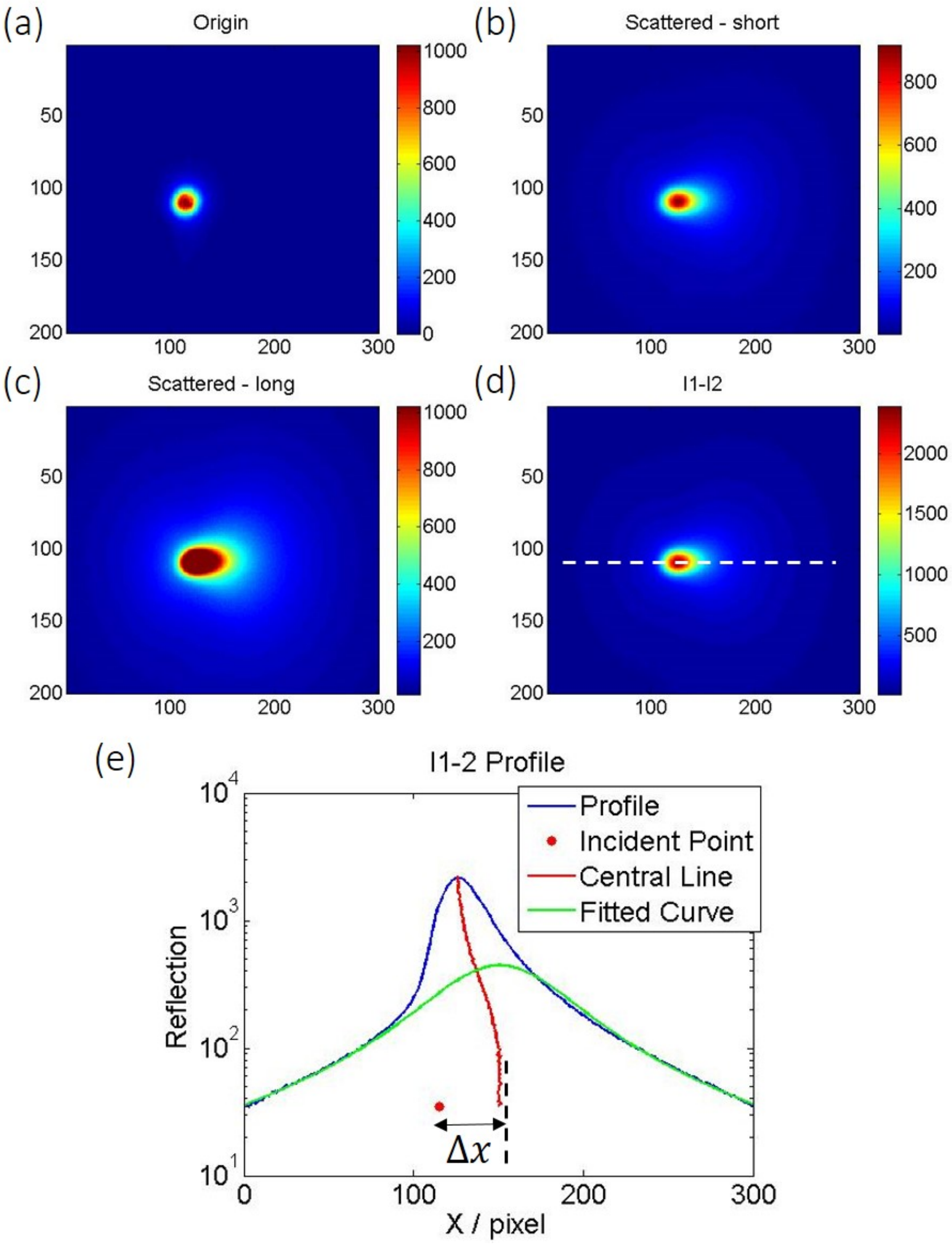

Figure B.4: Representative Images Captured by the Oblique-Incidence Reflectometry System: (a) original pattern of the incident beam; (b) diffused reflection image with a short exposure; (c) diffused reflection image with a long exposure; (d) combined images with (b) and (c); (e) profile of the white dash line on (d) are also described.

B.4.1 Phantoms

Table B.2: Estimated Optical Coefficient in Phantom Experiments(mm^{-1})

Phantom No.	Estimated μ_a	Expected μ_a	Estimated μ_s'	Expected μ_s'
1	0.000	0.002*	0.322	0.681**
2	0.003	0.002*	0.497	
3	0.004	0.002*	0.658	
4	0.116	0.100	0.600	
5	0.680	0.667	0.487	
6	0.090	0.100	0.332	

* absorption coefficient of water at the incident wavelength (785 nm)
** value provided by the integrated sphere method

As shown in Table B.2, the estimated absorption coefficients well match the expected values. The estimated μ_s' increases with intralipid concentration, and at a concentration 1% it has a value that is close to the result of the integrated sphere method .

B.4.2 Tissue Samples

Table B.3: Estimated Optical Coefficient in Ex-vivo Experiments (mm^{-1})

Phantom No.	Estimated μ_a	Estimated μ_s'
Pork Chuck	0.03 ± 0.02	0.26 ± 0.05
Chicken Breast	0.00	0.33 ± 0.05

Table B.3 shows the results of the ex-vivo experiments. Both pork chuck and chicken breast have nearly zero absorption, which is consistent with their non vessel nature. In terms of scattering, the estimated value for the pork chuck sample is 0.26 ± 0.05 mm^{-1}. The integrated sphere method provides a value of 0.21 ± 0.05 mm^{-1}. For chicken breast, the estimated μ_s' is 0.33±0.05, which is greater than the measured value (0.2 mm^{-1}) [103]. This significant deviation may be attributed to the differences in chicken breasts used. The integrated sphere method was also applied to the chicken breast sample but could not obtain a reasonable result [7].

B.5 Conclusion

This appendix has described the in situ measurement of tissue optical properties. The results of the phantom experiments indicate that the chosen method has good accuracy. The ex vivo experiments prove its ability with noninvasive measurement.

---

[7] The algorithm of the integrated sphere method did not converge

Bibliography

[1] Jarmo T Alander, Ilkka Kaartinen, Aki Laakso, Tommi Pätilä, Thomas Spillmann, Valery V Tuchin, Maarit Venermo, and Petri Välisuo. A review of indocyanine green fluorescent imaging in surgery. *Journal of Biomedical Imaging*, 2012:7, 2012.

[2] Raphael Alford, Mikako Ogawa, Peter L Choyke, and Hisataka Kobayashi. Molecular probes for the in vivo imaging of cancer. *Molecular BioSystems*, 5(11):1279–1291, 2009.

[3] Takehiro Ando. *Cell Transplantation Support System based on Intraoperative Evaluation of Cardiac Status, PhD Thesis*. the University of Tokyo, 2011.

[4] Takehiro Ando, Etsuko Kobayashi, Hongen Liao, Takashi Maruyama, Yoshihiro Muragaki, Hiroshi Iseki, Osami Kubo, and Ichiro Sakuma. Precise comparison of protoporphyrin ix fluorescence spectra with pathological results for brain tumor tissue identification. *Brain tumor pathology*, 28(1):43–51, 2011.

[5] Richard C Aster, Brian Borchers, and Clifford H Thurber. *Parameter estimation and inverse problems*. Academic Press, 2013.

[6] Johan Axelsson, Jenny Svensson, and Stefan Andersson-Engels. Spatially varying regularization based on spectrally resolved fluorescence emission in fluorescence molecular tomography. *Optics express*, 15(21):13574–13584, 2007.

[7] John A Barrett, R Edward Coleman, Stanley J Goldsmith, Shankar Vallabhajosula, Neil A Petry, Steve Cho, Thomas Armor, James B Stubbs, Kevin P Maresca, Michael G Stabin, et al. First-in-man evaluation of 2 high-affinity psma-avid small molecules for imaging prostate cancer. *Journal of Nuclear Medicine*, 54(3):380–387, 2013.

[8] Hector RA Basevi, Kenneth M Tichauer, Frederic Leblond, Hamid Dehghani, James A Guggenheim, Robert W Holt, and Iain B Styles. Compressive sensing based reconstruction in biolumi-

nescence tomography improves image resolution and robustness to noise. *Biomedical optics express*, 3(9):2131–2141, 2012.

[9] Paul Beard. Biomedical photoacoustic imaging. *Interface focus*, page rsfs20110028, 2011.

[10] Carolyn Z Behm and Jonathan R Lindner. Cellular and molecular imaging with targeted contrast ultrasound. *Ultrasound quarterly*, 22(1):67–72, 2006.

[11] Saskia Björn, Karl-Hans Englmeier, Vasilis Ntziachristos, and Ralf Schulz. Reconstruction of fluorescence distribution hidden in biological tissue using mesoscopic epifluorescence tomography. *Journal of biomedical optics*, 16(4):046005–046005, 2011.

[12] Saskia Björn, Vasilis Ntziachristos, and Ralf Schulz. Mesoscopic epifluorescence tomography: reconstruction of superficial and deep fluorescence in highly-scattering media. *Optics express*, 18(8):8422–8429, 2010.

[13] David Boas, J Culver, J Stott, and A Dunn. Three dimensional monte carlo code for photon migration through complex heterogeneous media including the adult human head. *Optics express*, 10(3):159–170, 2002.

[14] David A Boas, Dana H Brooks, Eric L Miller, Charles A DiMarzio, Misha Kilmer, Richard J Gaudette, and Quan Zhang. Imaging the body with diffuse optical tomography. *Signal Processing Magazine, IEEE*, 18(6):57–75, 2001.

[15] Reinhard Bos, Jacobus JM van der Hoeven, Elsken van Der Wall, Petra van Der Groep, Paul J van Diest, Emile FI Comans, Urvi Joshi, Gregg L Semenza, Otto S Hoekstra, Adriaan A Lammertsma, et al. Biologic correlates of 18fluorodeoxyglucose uptake in human breast cancer measured by positron emission tomography. *Journal of Clinical Oncology*, 20(2):379–387, 2002.

[16] Ben A Brooksby, Hamid Dehghani, Brian W Pogue, and Keith D Paulsen. Near-infrared (nir) tomography breast image reconstruction with a priori structural information from mri: algorithm development for reconstructing heterogeneities. *Selected Topics in Quantum Electronics, IEEE Journal of*, 9(2):199–209, 2003.

[17] Nannan Cao, Arye Nehorai, and Mathews Jacobs. Image reconstruction for diffuse optical tomography using sparsity regularization and expectation-maximization algorithm. *Optics express*, 15(21):13695–13708, 2007.

[18] J Chang, HL Graber, and RL Barbour. Improved reconstruction algorithm for luminescence optical tomography when background lumiphore is present. *Applied optics*, 37(16):3547–3552, 1998.

[19] Ian Y Chen and Joseph C Wu. Cardiovascular molecular imaging focus on clinical translation. *Circulation*, 123(4):425–443, 2011.

[20] Kun Chen, Lev T Perelman, Qingguo Zhang, Ramachandra R Dasari, and Michael S Feld. Optical computed tomography in a turbid medium using early arriving photons. *Journal of biomedical optics*, 5(2):144–154, 2000.

[21] Yu Chen, Shuai Yuan, Jeremiah Wierwille, Renee Naphas, Qian Li, Tiffany R Blackwell, PT Winnard, VT Raman, and Kristine Glunde. Integrated optical coherence tomography (oct) and fluorescence laminar optical tomography (flot). *Selected Topics in Quantum Electronics, IEEE Journal of*, 16(4):755–766, 2010.

[22] Dmitriy M Chudakov, Mikhail V Matz, Sergey Lukyanov, and Konstantin A Lukyanov. Fluorescent proteins and their applications in imaging living cells and tissues. *Physiological Reviews*, 90(3):1103–1163, 2010.

[23] Alper Corlu, Regine Choe, Turgut Durduran, Mark A Rosen, Martin Schweiger, Simon R Arridge, Mitchell D Schnall, and Arjun G Yodh. Three-dimensional in vivo fluorescence diffuse optical tomography of breast cancer in humans. *Optics express*, 15(11):6696–6716, 2007.

[24] Teresa Correia, Adam Gibson, Martin Schweiger, and Jeremy Hebden. Selection of regularization parameter for optical topography. *Journal of biomedical optics*, 14(3):034044–034044, 2009.

[25] Jan S Dam, Carsten B Pedersen, Torben Dalgaard, Paul Erik Fabricius, Prakasa Aruna, and Stefan Andersson-Engels. Fiber-optic probe for noninvasive real-time determination of tissue optical properties at multiple wavelengths. *Applied optics*, 40(7):1155–1164, 2001.

[26] Hamid Dehghani, Matthew E Eames, Phaneendra K Yalavarthy, Scott C Davis, Subhadra Srinivasan, Colin M Carpenter, Brian W Pogue, and Keith D Paulsen. Near infrared optical tomography using nirfast: Algorithm for numerical model and image reconstruction. *Communications in numerical methods in engineering*, 25(6):711–732, 2009.

[27] Hamid Dehghani, Brian R White, Benjamin W Zeff, Andrew Tizzard, and Joseph P Culver. Depth sensitivity and image reconstruction analysis of dense imaging arrays for mapping brain function with diffuse optical tomography. *Applied optics*, 48(10):D137–D143, 2009.

[28] Nikolaos Deliolanis, Tobias Lasser, Damon Hyde, Antoine Soubret, Jorge Ripoll, Vasilis Ntziachristos, M Lesaffre, F Jean, F Ramaz, AC Boccara, et al. Free-space fluorescence molecular tomography utilizing 360ˆ o geometry projections. *Optics letters*, 32(4):382, 2007.

[29] Nirupama Deshpande, Andrew Needles, and Jürgen K Willmann. Molecular ultrasound imaging: current status and future directions. *Clinical radiology*, 65(7):567–581, 2010.

[30] Kim Douma, Lenneke Prinzen, Dick W Slaaf, Chris PM Reutelingsperger, Erik AL Biessen, Tilman M Hackeng, Mark J Post, and Marc AMJ van Zandvoort. Nanoparticles for optical molecular imaging of atherosclerosis. *Small*, 5(5):544–557, 2009.

[31] Wolfgang Drexler, Mengyang Liu, Abhishek Kumar, Tschackad Kamali, Angelika Unterhuber, and Rainer A Leitgeb. Optical coherence tomography today: speed, contrast, and multimodality. *J. Biomed. Opt*, 19(7):071412, 2014.

[32] Joyita Dutta, Sangtae Ahn, Changqing Li, Simon R Cherry, and Richard M Leahy. Joint l1 and total variation regularization for fluorescence molecular tomography. *Physics in medicine and biology*, 57(6):1459, 2012.

[33] Qianqian Fang. Mesh-based monte carlo method using fast ray-tracing in plücker coordinates. *Biomedical optics express*, 1(1):165–175, 2010.

[34] Qianqian Fang and David A Boas. Monte carlo simulation of photon migration in 3d turbid media accelerated by graphics processing units. *Optics express*, 17(22):20178–20190, 2009.

[35] Jinchao Feng, Chenghu Qin, Kebin Jia, Shouping Zhu, Kai Liu, Dong Han, Xin Yang, Quansheng Gao, and Jie Tian. Total variation regularization for bioluminescence tomography with the split bregman method. *Applied optics*, 51(19):4501–4512, 2012.

[36] Stephen T Flock, Steven L Jacques, Brian C Wilson, Willem M Star, and Martin JC van Gemert. Optical properties of intralipid: a phantom medium for light propagation studies. *Lasers in Surgery and Medicine*, 12(5):510–519, 1992.

[37] Robert W Flower. Injection technique for indocyanine green and sodium fluorescein dye angiography of the eye. *Investigative Ophthalmology & Visual Science*, 12(12):881–895, 1973.

[38] Benjamin L Franc, Paul D Acton, Carina Mari, and Bruce H Hasegawa. Small-animal spect and spect/ct: important tools for preclinical investigation. *Journal of Nuclear Medicine*, 49(10):1651–1663, 2008.

[39] Masao Fujiwara, Takahide Mizukami, Ayano Suzuki, and Hidekazu Fukamizu. Sentinel lymph node detection in skin cancer patients using real-time fluorescence navigation with indocyanine green: preliminary experience. *Journal of Plastic, Reconstructive & Aesthetic Surgery*, 62(10):e373–e378, 2009.

[40] Sanjiv Sam Gambhir. Molecular imaging of cancer with positron emission tomography. *Nature Reviews Cancer*, 2(9):683–693, 2002.

[41] Melisa Gao, George Lewis, Gordon M Turner, Antoine Soubret, and Vasilis Ntziachristos. Effects of background fluorescence in fluorescence molecular tomography. *Applied optics*, 44(26):5468–5474, 2005.

[42] Ryan Gessner and Paul A Dayton. Advances in molecular imaging with ultrasound. *Molecular imaging*, 9(3):117, 2010.

[43] Anuradha Godavarty, Margaret J Eppstein, Chaoyang Zhang, Sangeeta Theru, Alan B Thompson, Michael Gurfinkel, and Eva M Sevick-Muraca. Fluorescence-enhanced optical imaging in large tissue volumes using a gain-modulated iccd camera. *Physics in Medicine and Biology*, 48(12):1701, 2003.

[44] Gene H Golub and Urs Von Matt. Generalized cross-validation for large-scale problems. *Journal of Computational and Graphical Statistics*, 6(1):1–34, 1997.

[45] Jacques Hadamard. Sur les problèmes aux dérivées partielles et leur signification physique. *Princeton university bulletin*, 13(49-52):28, 1902.

[46] Dima A Hammoud, John M Hoffman, and Martin G Pomper. Molecular neuroimaging: From conventional to emerging techniques 1. *Radiology*, 245(1):21–42, 2007.

[47] Per Christian Hansen. Regularization tools version 4.0 for matlab 7.3. *Numerical Algorithms*, 46(2):189–194, 2007.

[48] Israel Hanukoglu and Revital Rapoport. Routes and regulation of nadph production in steroidogenic mitochondria. *Endocrine research*, 21(1-2):231–241, 1995.

[49] Mukesh G Harisinghani, Jelle Barentsz, Peter F Hahn, Willem M Deserno, Shahin Tabatabaei, Christine Hulsbergen van de Kaa, Jean de la Rosette, and Ralph Weissleder. Noninvasive detection of clinically occult lymph-node metastases in prostate cancer. *New England Journal of Medicine*, 348(25):2491–2499, 2003.

[50] Xiaowei He, Yanbin Hou, Duofang Chen, Yuchuan Jiang, Man Shen, Junting Liu, Qitan Zhang, and Jie Tian. Sparse regularization-based reconstruction for bioluminescence tomography using a multilevel adaptive finite element method. *Journal of Biomedical Imaging*, 2011:4, 2011.

[51] Eugene Hecht. Optics, 4th. *International edition, Addison-Wesley, San Francisco*, 2002.

[52] L Hervé, A Koenig, A Da Silva, M Berger, J Boutet, JM Dinten, P Peltié, and P Rizo. Noncontact fluorescence diffuse optical tomography of heterogeneous media. *Applied optics*, 46(22):4896–4906, 2007.

[53] Elizabeth Hillman, David A Boas, Anders M Dale, and Andrew K Dunn. Laminar optical tomography: demonstration of millimeter-scale depth-resolved imaging in turbid media. *Optics letters*, 29(14):1650–1652, 2004.

[54] Elizabeth MC Hillman and Sean A Burgess. Sub-millimeter resolution 3d optical imaging of living tissue using laminar optical tomography. *Laser & photonics reviews*, 3(1-2):159–179, 2009.

[55] Nobuyuki Hirai, Akio Kosaka, Takakazu Kawamata, Tomokatsu Hori, and Hiroshi Iseki. Image-guided neurosurgery system integrating ar-based navigation and open-mri monitoring. *Computer Aided Surgery*, 10(2):59–72, 2005.

[56] Timon Hussain and Quyen T Nguyen. Molecular imaging for cancer diagnosis and surgery. *Advanced drug delivery reviews*, 66:90–100, 2014.

[57] Damon Hyde, Eric L Miller, Dana H Brooks, and Vasilis Ntziachristos. Data specific spatially varying regularization for multimodal fluorescence molecular tomography. *Medical Imaging, IEEE Transactions on*, 29(2):365–374, 2010.

[58] T Ido, C-N Wan, V Casella, JS Fowler, AP Wolf, M Reivich, and DE Kuhl. Labeled 2-deoxy-d-glucose analogs. 18f-labeled 2-deoxy-2-fluoro-d-glucose, 2-deoxy-2-fluoro-d-mannose and 14c-2-deoxy-2-fluoro-d-glucose. *Journal of Labelled Compounds and Radiopharmaceuticals*, 14(2):175–183, 1978.

[59] Tina Islam and Lee Josephson. Current state and future applications of active targeting in malignancies using superparamagnetic iron oxide nanoparticles. *Cancer Biomarkers*, 5(2):99–107, 2009.

[60] Steven L Jacques and Brian W Pogue. Tutorial on diffuse light transport. *Journal of Biomedical Optics*, 13(4):041302–041302, 2008.

[61] Ravi Prasad K Jagannath and Phaneendra K Yalavarthy. Minimal residual method provides optimal regularization parameter for diffuse optical tomography. *Journal of biomedical optics*, 17(10):106015–106015, 2012.

[62] Michelle L James and Sanjiv S Gambhir. A molecular imaging primer: modalities, imaging agents, and applications. *Physiological reviews*, 92(2):897–965, 2012.

[63] Siti M Janib, Ara S Moses, and J Andrew MacKay. Imaging and drug delivery using theranostic nanoparticles. *Advanced drug delivery reviews*, 62(11):1052–1063, 2010.

[64] Jsanchezd. Charge-coupled device — Wikipedia, the free encyclopedia. [Online; accessed 16-Jan-2015].

[65] Joo Hyun Kang and June-Key Chung. Molecular-genetic imaging based on reporter gene expression. *Journal of Nuclear Medicine*, 49(Suppl 2):164S–179S, 2008.

[66] Kimberly A Kelly, Jennifer R Allport, Andrew Tsourkas, Vivek R Shinde-Patil, Lee Josephson, and Ralph Weissleder. Detection of vascular adhesion molecule-1 expression using a novel multimodal nanoparticle. *Circulation research*, 96(3):327–336, 2005.

[67] Bas LJH Kietselaer, Chris PM Reutelingsperger, Guido AK Heidendal, Mat JAP Daemen, Werner H Mess, Leonard Hofstra, and Jagat Narula. Noninvasive detection of plaque instability with use of radiolabeled annexin a5 in patients with carotid-artery atherosclerosis. *New England Journal of Medicine*, 350(14):1472–1473, 2004.

[68] Dongkyu Kim, Yong Yeon Jeong, and Sangyong Jon. A drug-loaded aptamer- gold nanoparticle bioconjugate for combined ct imaging and therapy of prostate cancer. *ACS nano*, 4(7):3689–3696, 2010.

[69] Toshiyuki Kitai, Takuya Inomoto, Mitsuharu Miwa, and Takahiro Shikayama. Fluorescence navigation with indocyanine green for detecting sentinel lymph nodes in breast cancer. *Breast cancer*, 12(3):211–215, 2005.

[70] Malea Kneen, Javier Farinas, Yuxin Li, and AS Verkman. Green fluorescent protein as a noninvasive intracellular ph indicator. *Biophysical journal*, 74(3):1591–1599, 1998.

[71] Gerhard Kohl. The evolution and state-of-the-art principles of multislice computed tomography. *Proceedings of the American thoracic Society*, 2(6):470–476, 2005.

[72] Daisuke Kokuryo, Yasutaka Anraku, Akihiro Kishimura, Sayaka Tanaka, Mitsunobu R Kano, Jeff Kershaw, Nobuhiro Nishiyama, Tsuneo Saga, Ichio Aoki, and Kazunori Kataoka. Spio-picsome: Development of a highly sensitive and stealth-capable mri nano-agent for tumor detection using spio-loaded unilamellar polyion complex vesicles (picsomes). *Journal of Controlled Release*, 169(3):220–227, 2013.

[73] Kazuki Kurihara, Hiroshi Kawaguchi, Takayuki Obata, Hiroshi Ito, Kaoru Sakatani, and Eiji Okada. The influence of frontal sinus in brain activation measurements by near-infrared spectroscopy analyzed by realistic head models. *Biomedical optics express*, 3(9):2121–2130, 2012.

[74] Iina Laitinen, Antti Saraste, Eliane Weidl, Thorsten Poethko, Axel W Weber, Stephan G Nekolla, Pia Leppänen, Seppo Ylä-Herttuala, Gabriele Hölzlwimmer, Axel Walch, et al. Evaluation of $\alpha v\beta 3$ integrin-targeted positron emission tomography tracer 18f-galacto-rgd for imaging of vascular inflammation in atherosclerotic mice. *Circulation: Cardiovascular Imaging*, 2(4):331–338, 2009.

[75] ML Landsman, G Kwant, GA Mook, and WG Zijlstra. Light-absorbing properties, stability, and spectral stabilization of indocyanine green. *J. Appl. Physiol*, 40(4):575–583, 1976.

[76] Gregory M Lanza and Samuel A Wickline. Targeted ultrasonic contrast agents for molecular imaging and therapy. *Progress in cardiovascular diseases*, 44(1):13–31, 2001.

[77] Fridrik Larusson, Sergio Fantini, and Eric L Miller. Hyperspectral image reconstruction for diffuse optical tomography. *Biomedical optics express*, 2(4):946–965, 2011.

[78] F Leblond, Z Ovanesyan, SC Davis, PA Valdés, A Kim, A Hartov, BC Wilson, BW Pogue, KD Paulsen, and DW Roberts. Analytic expression of fluorescence ratio detection correlates with depth in multi-spectral sub-surface imaging. *Physics in medicine and biology*, 56(21):6823, 2011. doi: http://dx.doi.org/10.1088/0031-9155/56/21/005.

[79] Frederic Leblond, Scott C Davis, Pablo A Valdés, and Brian W Pogue. Pre-clinical whole-body fluorescence imaging: Review of instruments, methods and applications. *Journal of photochemistry and photobiology B: Biology*, 98(1):77–94, 2010.

[80] Frederic Leblond, Kathryn M Fontaine, Pablo Valdes, Songbai Ji, Brian W Pogue, Alex Hartov, David W Roberts, and Keith D Paulsen. Brain tumor resection guided by fluorescence imaging. In *SPIE BiOS: Biomedical Optics*, pages 71640M–71640M. International Society for Optics and Photonics, 2009.

[81] Daniel Richard Leff, Oliver J Warren, Louise C Enfield, Adam Gibson, Thanos Athanasiou, Darren K Patten, Jem Hebden, Guang Zhong Yang, and Ara Darzi. Diffuse optical imaging of the healthy and diseased breast: a systematic review. *Breast cancer research and treatment*, 108(1):9–22, 2008.

[82] Changhui Li and Lihong V Wang. Photoacoustic tomography and sensing in biomedicine. *Physics in medicine and biology*, 54(19):R59, 2009.

[83] Ji Li, Ahmed Chaudhary, Steven J Chmura, Charles Pelizzari, Tijana Rajh, Christian Wietholt, Metin Kurtoglu, and Bulent Aydogan. A novel functional ct contrast agent for molecular imaging of cancer. *Physics in medicine and biology*, 55(15):4389, 2010.

[84] Hongen Liao, Masafumi Noguchi, Takashi Maruyama, Yoshihiro Muragaki, Etsuko Kobayashi, Hiroshi Iseki, and Ichiro Sakuma. An integrated diagnosis and therapeutic system using intra-operative 5-aminolevulinic-acid-induced fluorescence guided robotic laser ablation for precision neurosurgery. *Medical image analysis*, 16(3):754–766, 2012.

[85] Hongen Liao, Koji Shimaya, Kaimeng Wang, Takashi Maruyama, Masafumi Noguchi, Yoshihiro Muragaki, Etsuko Kobayashi, Hiroshi Iseki, and Ichiro Sakuma. Combination of intraoperative 5-aminolevulinic acid-induced fluorescence and 3-d mr imaging for guidance of robotic laser ablation for precision neurosurgery. In *Medical Image Computing and Computer-Assisted Intervention–MICCAI 2008*, pages 373–380. Springer, 2008.

[86] Shao-Pow Lin, Lihong Wang, Steven L Jacques, and Frank K Tittel. Measurement of tissue optical properties by the use of oblique-incidence optical fiber reflectometry. *Applied optics*, 36(1):136–143, 1997.

[87] Fei Liu, Mingze Li, Bin Zhang, Jianwen Luo, and Jing Bai. Weighted depth compensation algorithm for fluorescence molecular tomography reconstruction. *Applied optics*, 51(36):8883–8892, 2012.

[88] Kathryn E Luker, Martha Hutchens, Tracey Schultz, Andrew Pekosz, and Gary D Luker. Bioluminescence imaging of vaccinia virus: effects of interferon on viral replication and spread. *Virology*, 341(2):284–300, 2005.

[89] Shenglin Luo, Erlong Zhang, Yongping Su, Tianmin Cheng, and Chunmeng Shi. A review of nir dyes in cancer targeting and imaging. *Biomaterials*, 32(29):7127–7138, 2011.

[90] Maria L Macheda, Suzanne Rogers, and James D Best. Molecular and cellular regulation of glucose transporter (glut) proteins in cancer. *Journal of cellular physiology*, 202(3):654–662, 2005.

[91] H Maeda, J Wu, T Sawa, Y Matsumura, and K Hori. Tumor vascular permeability and the epr effect in macromolecular therapeutics: a review. *Journal of controlled release*, 65(1):271–284, 2000.

[92] KP Maresca, SM Hillier, FJ Femia, D Keith, C Barone, JL Joyal, CN Zimmerman, AP Kozikowski, JA Barrett, WC Eckelman, et al. A series of halogenated heterodimeric inhibitors of prostate specific membrane antigen (psma) as radiolabeled probes for targeting prostate cancer. *Journal of medicinal chemistry*, 52(2):347–357, 2008.

[93] James E Mark. *Polymer data handbook*. Oxford University Press, 2009.

[94] Guillermo Marquez and Lihong Wang. White light oblique incidence reflectometer formeasuring absorption and reduced scatteringspectra of tissue-like turbid media. *Optics Express*, 1(13):454–460, 1997.

[95] Sebastian Marschall, Birgit Sander, Mette Mogensen, Thomas M Jørgensen, and Peter E Andersen. Optical coherence tomography—current technology and applications in clinical and biomedical research. *Analytical and bioanalytical chemistry*, 400(9):2699–2720, 2011.

[96] Noguchi Masafumi. *master Thesis*. the University of Tokyo, 204.

[97] Alvaro Mata, Aaron J Fleischman, and Shuvo Roy. Characterization of polydimethylsiloxane (pdms) properties for biomedical micro/nanosystems. *Biomedical microdevices*, 7(4):281–293, 2005.

[98] Aya Matsui, Eiichi Tanaka, Hak Soo Choi, Joshua H Winer, Vida Kianzad, Sylvain Gioux, Rita G Laurence, and John V Frangioni. Real-time intra-operative near-infrared fluorescence identification of the extrahepatic bile ducts using clinically available contrast agents. *Surgery*, 148(1):87–95, 2010.

[99] Christian M Matter, Matthias Stuber, and Matthias Nahrendorf. Imaging of the unstable plaque: how far have we got? *European heart journal*, 30(21):2566–2574, 2009.

[100] Sandra S McAllister and Robert A Weinberg. Tumor-host interactions: a far-reaching relationship. *Journal of Clinical Oncology*, 28(26):4022–4028, 2010.

[101] Donald W McRobbie, Elizabeth A Moore, Martin J Graves, and Martin R Prince. *MRI from Picture to Proton*. Cambridge University Press, 2006.

[102] Shanta M Messerli, Shilpa Prabhakar, Yi Tang, Khalid Shah, Maria L Cortes, Vidya Murthy, Ralph Weissleder, Xandra O Breakefield, and Ching-Hsuan Tung. A novel method for imaging apoptosis using a caspase-1 near-infrared fluorescent probe. *Neoplasia*, 6(2):95–105, 2004.

[103] Shinichi Miki, Seishi Tanaka, and Yoshiaki Shimomura. Determination of optical properties of chicken breast tissue using three-fiber based diffuse reflectance method. In *Biomedical Topical Meeting*, page TuI9. Optical Society of America, 2006.

[104] Mette Mogensen, Lars Thrane, Thomas Martini Jørgensen, Peter E Andersen, and GBE Jemec. Optical coherence tomography for imaging of skin and skin diseases. In *Seminars in cutaneous medicine and surgery*, volume 28, pages 196–202. WB Saunders, 2009.

[105] Monica Monici. Cell and tissue autofluorescence research and diagnostic applications. *Biotechnology annual review*, 11:227–256, 2005.

[106] Ratnakar B Mujumdar, Lauren A Ernst, Swati R Mujumdar, Christopher J Lewis, and Alan S Waggoner. Cyanine dye labeling reagents: sulfoindocyanine succinimidyl esters. *Bioconjugate chemistry*, 4(2):105–111, 1993.

[107] Haijing Niu, Fenghua Tian, Zi-Jing Lin, and Hanli Liu. Development of a compensation algorithm for accurate depth localization in diffuse optical tomography. *Optics letters*, 35(3):429–431, 2010.

[108] Vasilis Ntziachristos. Fluorescence molecular imaging. *Annu. Rev. Biomed. Eng.*, 8:1–33, 2006.

[109] Vasilis Ntziachristos, Jorge Ripoll, Lihong V Wang, and Ralph Weissleder. Looking and listening to light: the evolution of whole-body photonic imaging. *Nature biotechnology*, 23(3):313–320, 2005.

[110] Vasilis Ntziachristos and Ralph Weissleder. Experimental three-dimensional fluorescence reconstruction of diffuse media by use of a normalized born approximation. *Optics letters*, 26(12):893–895, 2001.

[111] Shinpei Okawa, Tatsuya Ikehara, Ichiro Oda, and Yukio Yamada. Reconstruction of localized fluorescent target from multi-view continuous-wave surface images of small animal with lp sparsity regularization. *Biomedical Optics Express*, 5(6):1839–1860, 2014.

[112] Emilia S Olson, Tao Jiang, Todd A Aguilera, Quyen T Nguyen, Lesley G Ellies, Miriam Scadeng, and Roger Y Tsien. Activatable cell penetrating peptides linked to nanoparticles as dual probes for in vivo fluorescence and mr imaging of proteases. *Proceedings of the National Academy of Sciences*, 107(9):4311–4316, 2010.

[113] Christopher C Paige and Michael A Saunders. Lsqr: An algorithm for sparse linear equations and sparse least squares. *ACM Transactions on Mathematical Software (TOMS)*, 8(1):43–71, 1982.

[114] YT Pan, TQ Xie, CW Du, S Bastacky, S Meyers, and ML Zeidel. Enhancing early bladder cancer detection with fluorescence-guided endoscopic optical coherent tomography. *Optics letters*, 28(24):2485–2487, 2003.

[115] Nataliya Panchuk-Voloshina, Rosaria P Haugland, Janell Bishop-Stewart, Mahesh K Bhalgat, Paul J Millard, Fei Mao, Wai-Yee Leung, and Richard P Haugland. Alexa dyes, a series of new fluorescent dyes that yield exceptionally bright, photostable conjugates. *Journal of Histochemistry & Cytochemistry*, 47(9):1179–1188, 1999.

[116] Jesung Park, Javier A Jo, Sebina Shrestha, Paritosh Pande, Qiujie Wan, and Brian E Applegate. A dual-modality optical coherence tomography and fluorescence lifetime imaging microscopy system for simultaneous morphological and biochemical tissue characterization. *Biomedical optics express*, 1(1):186–200, 2010.

[117] John W Pickering, Scott A Prahl, Niek Van Wieringen, Johan F Beek, Henricus JCM Sterenborg, and Martin JC Van Gemert. Double-integrating-sphere system for measuring the optical properties of tissue. *Applied optics*, 32(4):399–410, 1993.

[118] Brian W Pogue, Troy O McBride, Judith Prewitt, Ulf L Österberg, and Keith D Paulsen. Spatially variant regularization improves diffuse optical tomography. *Applied optics*, 38(13):2950–2961, 1999.

[119] Luís F Portugal, Joaquim J Júdice, and Luís N Vicente. A comparison of block pivoting and interior-point algorithms for linear least squares problems with nonnegative variables. *Mathematics of Computation*, 63(208):625–643, 1994.

[120] S Prahl. Everything i think you should know about inverse adding-doubling. *Oregon Medical Laser Center, St. Vincent Hospital*, 2011.

[121] Jaya Prakash and Phaneendra K Yalavarthy. A lsqr-type method provides a computationally efficient automated optimal choice of regularization parameter in diffuse optical tomography. *Medical physics*, 40(3):033101, 2013.

[122] Kun Qian, Takehiro Ando, Kensuke Nakamura, Hongen Liao, Etsuko Kobayashi, Naoki Yahagi, and Ichiro Sakuma. Ultrasound imaging method for internal jugular vein measurement and estimation of circulating blood volume. *International journal of computer assisted radiology and surgery*, 9(2):231–239, 2014.

[123] Manuel Querol and Alexei Bogdanov Jr. Environment-sensitive and enzyme-sensitive mr contrast agents. In *Molecular Imaging II*, pages 37–57. Springer, 2008.

[124] Daniel Razansky, Martin Distel, Claudio Vinegoni, Rui Ma, Norbert Perrimon, Reinhard W Köster, and Vasilis Ntziachristos. Multispectral opto-acoustic tomography of deep-seated fluorescent proteins in vivo. *Nature Photonics*, 3(7):412–417, 2009.

[125] Daniel Razansky and Vasilis Ntziachristos. Hybrid photoacoustic fluorescence molecular tomography using finite-element-based inversion. *Medical physics*, 34(11):4293–4301, 2007.

[126] J Regula, AJ MacRobert, A Gorchein, GA Buonaccorsi, SM Thorpe, GM Spencer, AR Hatfield, and SG Bown. Photosensitisation and photodynamic therapy of oesophageal, duodenal, and colorectal tumours using 5 aminolaevulinic acid induced protoporphyrin ix–a pilot study. *Gut*, 36(1):67–75, 1995.

[127] Renato M.E. Sabbatini. The cyclotron and pet. http://www.cerebromente.org.br/n01/pet/petcyclo.htm/, 1997.

[128] Antti Saraste, Stephan G Nekolla, and Markus Schwaiger. Cardiovascular molecular imaging: an overview. *Cardiovascular research*, 83(4):643–652, 2009.

[129] Joan H Schiller, David Harrington, Chandra P Belani, Corey Langer, Alan Sandler, James Krook, Junming Zhu, and David H Johnson. Comparison of four chemotherapy regimens for advanced non–small-cell lung cancer. *New England Journal of Medicine*, 346(2):92–98, 2002.

[130] JM Schmitt. Optical measurement of blood oxygenation by implantable telemetry. Technical report, Technical Report, 1986.

[131] Martin Schweiger and Simon Arridge. The toast++ software suite for forward and inverse modeling in optical tomography. *Journal of biomedical optics*, 19(4):040801–040801, 2014.

[132] Martin Schweiger, Simon R Arridge, and David T Delpy. Application of the finite-element method for the forward and inverse models in optical tomography. *Journal of Mathematical Imaging and Vision*, 3(3):263–283, 1993.

[133] Walter J Scott, John Howington, Steven Feigenberg, Benjamin Movsas, and Katherine Pisters. Treatment of non-small cell lung cancer stage i and stage ii: Accp evidence-based clinical practice guidelines. *CHEST Journal*, 132(3_suppl):234S–242S, 2007.

[134] EM Sevick-Muraca. Translation of near-infrared fluorescence imaging technologies: emerging clinical applications. *Annual review of medicine*, 63:217–231, 2012.

[135] Takeaki Shimokawa, Takashi Kosaka, Okito Yamashita, Nobuo Hiroe, Takashi Amita, Yoshihiro Inoue, and Masa-aki Sato. Hierarchical bayesian estimation improves depth accuracy and spatial resolution of diffuse optical tomography. *Optics express*, 20(18):20427–20446, 2012.

[136] Ronald I Siphanto, Roy GM Kolkman, Arjan Huisjes, Magdalena C Pilatou, Frits FM de Mul, Wiendelt Steenbergen, and Leon NA van Adrichem. Imaging of small vessels using photoacoustics: an in vivo study. *Lasers in surgery and medicine*, 35(5):354–362, 2004.

[137] Thorvald Sørensen. {A method of establishing groups of equal amplitude in plant sociology based on similarity of species and its application to analyses of the vegetation on Danish commons}. *Biol. skr.*, 5:1–34, 1948.

[138] Antoine Soubret and Vasilis Ntziachristos. Fluorescence molecular tomography in the presence of background fluorescence. *Physics in medicine and biology*, 51(16):3983, 2006.

[139] Walter Stummer, Alexander Novotny, Herbert Stepp, Claudia Goetz, Karl Bise, and Hans Jürgen Reulen. Fluorescence-guided resection of glioblastoma multiforme utilizing 5-ala-induced porphyrins: a prospective study in 52 consecutive patients. *Journal of neurosurgery*, 93(6):1003–1013, 2000. doi: http://dx.doi.org/10.1016/S1470-2045(06)70665-9.

[140] Walter Stummer, Uwe Pichlmeier, Thomas Meinel, Otmar Dieter Wiestler, Friedhelm Zanella, and Hans-Jürgen Reulen. Fluorescence-guided surgery with 5-aminolevulinic acid for resection of malignant glioma: a randomised controlled multicentre phase iii trial. *The lancet oncology*, 7(5):392–401, 2006.

[141] Johannes Swartling, Jan S Dam, and Stefan Andersson-Engels. Comparison of spatially and temporally resolved diffuse-reflectance measurement systems for determination of biomedical optical properties. *Applied optics*, 42(22):4612–4620, 2003.

[142] Johannes Swartling, Antonio Pifferi, Annika MK Enejder, and Stefan Andersson-Engels. Accelerated monte carlo models to simulate fluorescence spectra from layered tissues. *JOSA A*, 20(4):714–727, 2003.

[143] Johannes Swartling, Jenny Svensson, Daniel Bengtsson, Khaled Terike, and Stefan Andersson-Engels. Fluorescence spectra provide information on the depth of fluorescent lesions in tissue. *Applied optics*, 44(10):1934–1941, 2005.

[144] Guillermo J Tearney, Ik-Kyung Jang, and Brett E Bouma. Optical coherence tomography for imaging the vulnerable plaque. *Journal of biomedical optics*, 11(2):021002–021002, 2006.

[145] Andrey Tikhonov. Solution of incorrectly formulated problems and the regularization method. In *Soviet Math. Dokl.*, volume 5, pages 1035–1038, 1963.

[146] Susan L Troyan, Vida Kianzad, Summer L Gibbs-Strauss, Sylvain Gioux, Aya Matsui, Rafiou Oketokoun, Long Ngo, Ali Khamene, Fred Azar, and John V Frangioni. The flare™ intraoperative near-infrared fluorescence imaging system: a first-in-human clinical trial in breast cancer sentinel lymph node mapping. *Annals of surgical oncology*, 16(10):2943–2952, 2009.

[147] Gordon M Turner, Giannis Zacharakis, Antoine Soubret, Jorge Ripoll, and Vasilis Ntziachristos. Complete-angle projection diffuse optical tomography by use of early photons. *Optics letters*, 30(4):409–411, 2005.

[148] Unknown. Wikimedia commons, the free media repository. http://commons.wikimedia.org/, [Online; accessed 16-Jan-2015].

[149] Hugo J Van Staveren, Christian JM Moes, Jan van Marie, Scott A Prahl, and Martin JC Van Gemert. Light scattering in intralipid-10% in the wavelength range of 400-1100 nm. *Applied optics*, 30(31):4507–4514, 1991.

[150] Claudio Vinegoni, Ion Botnaru, Elena Aikawa, Marcella A Calfon, Yoshiko Iwamoto, Eduardo J Folco, Vasilis Ntziachristos, Ralph Weissleder, Peter Libby, and Farouc A Jaffer. Indocyanine green enables near-infrared fluorescence imaging of lipid-rich, inflamed atherosclerotic plaques. *Science translational medicine*, 3(84):84ra45–84ra45, 2011.

[151] Tuan Vo-Dinh. *Biomedical photonics handbook*. CRC press, 2010.

[152] Kateryna D Volkova, Vladyslava B Kovalska, Anatoliy L Tatarets, Leonid D Patsenker, Dmytro V Kryvorotenko, and Sergiy M Yarmoluk. Spectroscopic study of squaraines as protein-sensitive fluorescent dyes. *Dyes and pigments*, 72(3):285–292, 2007.

[153] Maureen A Walling, Jennifer A Novak, and Jason RE Shepard. Quantum dots for live cell and in vivo imaging. *International journal of molecular sciences*, 10(2):441–491, 2009.

[154] Lihong Wang and Steven L. Jacques. Use of a laser beam with an oblique angle of incidence to measure the reduced scattering coefficient of a turbid medium. *Appl. Opt.*, 34(13):2362–2366, May 1995.

[155] Lihong Wang, Steven L Jacques, and Liqiong Zheng. Mcml—monte carlo modeling of light transport in multi-layered tissues. *Computer methods and programs in biomedicine*, 47(2):131–146, 1995.

[156] Lihong V Wang and Song Hu. Photoacoustic tomography: in vivo imaging from organelles to organs. *Science*, 335(6075):1458–1462, 2012.

[157] Lihong V Wang and Hsin-i Wu. *Biomedical optics: principles and imaging*. John Wiley & Sons, 2012.

[158] Thomas D Wang, Michael S Feld, Yang Wang, Jacques Van Dam, and Stephen F Fulghum. Fluorescence imaging endoscope, June 26 2007. US Patent 7,235,045.

[159] Ralph Weissleder. Molecular imaging in cancer. *Science*, 312(5777):1168–1171, 2006.

[160] Ralph Weissleder and Mikael J Pittet. Imaging in the era of molecular oncology. *Nature*, 452(7187):580–589, 2008.

[161] Julia Welzel. Optical coherence tomography in dermatology: a review. *Skin Research and Technology*, 7(1):1–9, 2001.

[162] Michael A Whitney, Jessica L Crisp, Linda T Nguyen, Beth Friedman, Larry A Gross, Paul Steinbach, Roger Y Tsien, and Quyen T Nguyen. Fluorescent peptides highlight peripheral nerves during surgery in mice. *Nature biotechnology*, 29(4):352–356, 2011.

[163] Walter Wiesner, Koenraad J Mortelé, Hoon Ji, and Pablo R Ros. Normal colonic wall thickness at ct and its relation to colonic distension. *Journal of computer assisted tomography*, 26(1):102–106, 2002.

[164] Wikipedia. Positron emission tomography — Wikipedia, the free encyclopedia. [Online; accessed 15-Jan-2015].

[165] Wikipedia. Polydimethylsiloxane — Wikipedia, the free encyclopedia, 2014. [Online; accessed 30-Aug-2014].

[166] Lawrence E Williams. Anniversary paper: nuclear medicine: fifty years and still counting. *Medical physics*, 35(7):3020–3029, 2008.

[167] Maciej Wojtkowski, Bartlomiej Kaluzny, and Robert J Zawadzki. New directions in ophthalmic optical coherence tomography. *Optometry & Vision Science*, 89(5):524–542, 2012.

[168] Amy P Wu, Michael A Whitney, Jessica L Crisp, Beth Friedman, Roger Y Tsien, and Quyen T Nguyen. Improved facial nerve identification with novel fluorescently labeled probe. *The Laryngoscope*, 121(4):805–810, 2011.

[169] Linhui Wu, Huijuan Zhao, Xin Wang, Xi Yi, Weiting Chen, and Feng Gao. Enhancement of fluorescence molecular tomography with structural-prior-based diffuse optical tomography: combating optical background uncertainty. *Applied Optics*, 53(30):6970–6982, 2014.

[170] Fan Xia, Jingfang Mao, Jinquan Ding, and Huanjun Yang. Observation of normal appearance and wall thickness of esophagus on ct images. *European journal of radiology*, 72(3):406–411, 2009.

[171] Minghua Xu and Lihong V Wang. Photoacoustic imaging in biomedicine. *Review of scientific instruments*, 77(4):041101, 2006.

[172] Lily Yang, Hui Mao, Zehong Cao, Y Andrew Wang, Xianghong Peng, Xiaoxia Wang, Hari K Sajja, Liya Wang, Hongwei Duan, Chunchun Ni, et al. Molecular imaging of pancreatic cancer in an animal model using targeted multifunctional nanoparticles. *Gastroenterology*, 136(5):1514–1525, 2009.

[173] Baohong Yuan, Sean A Burgess, Amir Iranmahboob, Matthew B Bouchard, Nicole Lehrer, Clémence Bordier, and Elizabeth MC Hillman. A system for high-resolution depth-resolved optical imaging of fluorescence and absorption contrast. *Review of Scientific Instruments*, 80(4):043706, 2009.

[174] Baohong Yuan, NanGuang Chen, and Quing Zhu. Emission and absorption properties of indocyanine green in intralipid solution. *Journal of biomedical optics*, 9(3):497–503, 2004.

[175] Guido Zavattini, Stefania Vecchi, Gregory Mitchell, Ulli Weisser, Richard M Leahy, Bernd J Pichler, Desmond J Smith, and Simon R Cherry. A hyperspectral fluorescence system for 3d in vivo optical imaging. *Physics in medicine and biology*, 51(8):2029, 2006.

[176] Tuo Zhou, Takehiro Ando, Hongen Liao, Etsuko Kobayashi, and Ichiro Sakuma. Piecewise weighted tikhonov regularization for reconstructing fluorophore distribution in tissue using mesoscopic epifluorescence tomography. *Advanced Biomedical Engineering*, 2(0):84–94, 2013.

[177] Tuo Zhou, Takehiro Ando, Hongen Liao, Etsuko Kobayashi, and Ichiro Sakuma. A depth perturbation method for determining depth of fluorophore in tissue. In *CLEO: 2014*, page AM2P.4. Optical Society of America, 2014.

[178] Tuo Zhou, Takehiro Ando, Keiichi Nakagawa, Hongen Liao, Etsuko Kobayashi, and Ichiro Sakuma. Localizing fluorophore (centroid) inside a scattering medium by depth perturbation. *Journal of Biomedical Optics*, 20(1):017003–017003, 2015.

C Research Achievement

Journal Papers

1. **Tuo Zhou**, Takehiro Ando, Keiichi Nagakawa, Hongen Liao, Etsuko Kobayashi, Ichiro Sakuma. Localizing Fluorophore (Centroid) inside a Scattering Medium by Depth Perturbation. Journal of Biomedical Optics. 20(1), 017003 (2015).

2. **Tuo Zhou**, Takehiro Ando, Hongen Liao, Etsuko kobayashi, Ichiro Sakuma. Piecewise Weighted Tikhonov Regularization for Reconstructing Fluorophore Distribution in Tissue using Mesoscopic Epifluorescence Tomography. Advanced Biomedical Engineering. Vol(2); 2013: 84-94.

Conference Reports

1. **Tuo Zhou**, Takehiro Ando, Etsuko kobayashi, Ichiro Sakuma. Spatially varying regularization based on depth perturbation for epifluorescence tomography, 23rd Annual Conference of Japan Society of Computer Aided Surgery. Osaka, Japan, November , 2014.

2. **Tuo Zhou**, Takehiro Ando, Hongen Liao, Etsuko kobayashi, Ichiro Sakuma. A Depth Perturbation Method for Determining Depth of Fluorophore in Tissue, Conference on Lasers and Electro-Optics (CLEO), San Jose, America, June, 2014;

3. **Tuo Zhou**, Takehiro Ando, Hongen Liao, Etsuko kobayashi, Ichiro Sakuma. Reconstruction Methods for Distribution of Fluorophore Biomarker Embedded in Tissue using Mesoscopic Epifluoresecene Tomography, Japan Bomedical Engineering Society. Fukuoka, Japan, July, 2013;

4. **Tuo Zhou**, Takehiro Ando, Hongen Liao, Etsuko kobayashi, Ichiro Sakuma. Determining Depth of Fluorescent Inclusion in Tissue Based on Fluorescence Spectra Change, Asian Academic Seminar. Mumbai, Inida, December , 2012.

5. **Tuo Zhou**, Takehiro Ando, Hongen Liao, Etsuko kobayashi, Ichiro Sakuma. Fluorescence Spectra Change with the Depth of Fluorescent Inclusion in Tissue: A Simulation Study, 21st Annual Conference of Japan Society of Computer Aided Surgery. Tokushima, Japan, November , 2012 (**Conference Paper Award**).

Award

Conference Paper Award the 21st Annual Conference of Japan Society of Computer Aided Surgery.

D Acknowledgment

It is with immense gratitude that I acknowledge the support and help of my supervisor Prof. Ichiro Sakuma. Without his continuous instruction, this thesis would not have been possible.

I would like to express the deepest appreciation to Prof. Yasuhiko Jimbo, Prof. Teruo Fujii, Prof. Hiroyuki Takahashi, Prof. Eji Okada, Prof. Eji Okada, Prof. Takashi Azuma for their time and efforts on reviewing this thesis which is greatly improved by their advices.

I owe my deepest gratitude to Prof. Etsuko Kobayashi and Dr. Takehiro Ando for their daily advices.

I would like to thank Prof. Hongen Liao for his suggestions from the point of a Chinese staff's view, especially for his support when I just arrived in Japan.

I wish to thank Dr. Keiichi Nakagawa. He greatly supported me in optics, research methods, and Japanese.

It gives me great pleasure in working with Dr. Junchen Wang and Dr. Liangjing Yang. Our communication is never affected by any language barrier. I especially thank Dr. Liangjing Yang for his English proofreading on my manuscripts.

I consider it an honor to work with my colleges in Biomedical Precision Lab. I thank them for their patience and tolerance to a foreign student. I enjoy the discussion with them both on studies and on the daily life in Japan. I always feel that I stay at a big family.

I would like to express the deepest appreciation to Dr. Lihong Wang, Dr. QianQian Fang, Dr. Richard C. Aster for their sample codes which greatly facilitated my researches.

I cannot find words to express my gratitude to Ms. Maruyama. I train my Japanese with her once a week for the three years. She does not only teach me Japanese, but also shares her experiences and her ideas in Japanese culture with me.

I am indebted to my parents who encourages me to study aboard. In these three year, only two weeks per year I can stay with them.

I owe my deepest gratitude to Mrs. Jinglu Cai who makes my life happy and colorful.

This work is partly supported by a Grant for Translational Systems Biology and Medicine Initiative (TSBMI) from the Ministry of Education, Culture, Sports, Science and Technology of Japan. In the doctoral course, I receive the scholarship from the Ministry of Education, Culture, Sports, Science and Technology of Japan. I am much appreciated for these financial supports.